Spin to charge current interconversion in Rasha interfaces and topological insulators

Maxen Cosset-Cheneau

To cite this version:

Maxen Cosset-Cheneau. Spin to charge current interconversion in Rasha interfaces and topological insulators. Atomic Physics [physics.atom-ph]. Université Grenoble Alpes [2020-..], 2022. English. NNT : 2022GRALY043 . tel-03908310

HAL Id: tel-03908310
https://theses.hal.science/tel-03908310

Submitted on 20 Dec 2022

THÈSE

Pour obtenir le grade de

DOCTEUR DE L'UNIVERSITÉ GRENOBLE ALPES

École doctorale : PHYS - Physique
Spécialité : Nanophysique
Unité de recherche : Spintronique et Technologie des Composants

Conversion entre courant de spin et courant de charge dans des interfaces Rashba et des isolants topologiques

Spin to charge current interconversion in Rasha interfaces and topological insulators

Présentée par :

Maxen COSSET-CHENEAU

Direction de thèse :

Jean-Philippe ATTANE PROFESSEUR, Université Grenoble Alpes	Directeur de thèse
Laurent VILA INGENIEUR HDR, Université Grenoble Alpes	Co-directeur de thèse

Rapporteurs :

AURELIEN MANCHON
Professeur des Universités, AIX-MARSEILLE UNIVERSITE
JUAN-CARLOS ROJAS-SANCHEZ
Chargé de recherche HDR, CNRS DELEGATION CENTRE-EST

Thèse soutenue publiquement le **26 septembre 2022**, devant le jury composé de :

AURELIEN MANCHON Professeur des Universités, AIX-MARSEILLE UNIVERSITE	Rapporteur
JUAN-CARLOS ROJAS-SANCHEZ Chargé de recherche HDR, CNRS DELEGATION CENTRE-EST	Rapporteur
BART VAN WEES Professeur, Rijksuniversiteit Groningen	Examinateur
MAIRBEK CHSHIEV Professeur des Universités, UNIVERSITE GRENOBLE ALPES	Président
SERGIO VALENZUELA Professeur, Universidad Autónoma de Madrid	Examinateur

Abstract

The spin-to-charge current interconversion in non-magnetic systems is based on the spin-orbit coupling. During the past ten years, spintronics has been deeply transformed by the use of this effect. While the spin-to-charge interconversion in conventional spintronics relies on the exchange interaction, this can also be achieved using the strong spin-orbit coupling present in some ferromagnetic materials. The effect of the interplay between the exchange interaction and spin-orbit coupling on the spin transport and interconversion is however not well understood, which for now limits the use of the new functionalities offered by these materials. In addition to the study of the spin-to-charge interconversion in metals, other type of materials such as topological insulators, Rashba interfaces and ferroelectric semiconductors are being investigated. These systems are appealing for novel spin-logic concepts due to their large spin-orbit-driven spin-to-charge interconversion and multifunctional properties. This thesis focuses on the exploration of spin-to-charge interconversion effects in these materials using various techniques and devices. The first chapter presents the concepts used and developed throughout this thesis, which are the spin transport in metals with the magnetization collinear and transverse to the spin polarization, as well as the conversion of a spin current into a charge current into metals, Rashba interfaces and topological insulators. In the second chapter, the collinear and transverse spin transport properties are measured using lateral spin valves, setting the groundwork for a quantitative characterization of the spin-to-charge interconversion effects in the aforementioned systems. In the third chapter, the effect of the competition between the exchange interaction and the spin-orbit coupling on the spin-to-charge interconversion is evaluated. This is done by measuring the inverse spin Hall effect in ferromagnetic materials across their transition temperature using a spin-pumping ferromagnetic resonance technique, and by rotating the ferromagnet ISHE-material magnetization with respect to the spin current polarization using a novel design of lateral spin valve. The fourth chapter studies the spin-to-charge interconversion in two-dimensional electron gas at interfaces between $SrTiO_3$ and various metals, and in the newly discovered two-dimensional electron gas at the metal-$KTaO_3$ interface using spin-pumping measurements. Finally, the fifth chapter discuss the local detection of the interconversion in the context of recently proposed spin-logic devices. In the first part of this last chapter, the optimization of the interconversion voltage output required for magnetoelectric spin-orbit devices is studied in platinum, through interface engineering and by performing local detection of the interconversion in the topological insulator Sb_2Te_3. In the second part, the patterning of such local interconversion devices using the ferroelectric Rashba semiconductor GeTe and the two-dimensional electron gas present at the metal-$SrTiO_3$ interfaces is performed, with an opening toward their use for the recently proposed ferroelectric spin-orbit device.

Résumé

L'interconversion entre courants de spin et de charge dans les systèmes non magnétiques est basée sur le couplage spin-orbite. Au cours des dix dernières années, la spintronique a été profondément transformée par l'utilisation de cet effet. Alors que l'interconversion spin-charge dans la spintronique conventionnelle repose sur l'interaction d'échange, elle peut également être réalisée en utilisant le fort couplage spin-orbite présent dans certains matériaux ferromagnétiques. L'effet conjoint de l'interaction d'échange et du couplage spin-orbite sur le transport et l'interconversion spin-charge n'est cependant pas bien comprise, ce qui limite pour l'instant l'utilisation des nouvelles fonctionnalités offertes par ces matériaux. En plus de l'étude de l'interconversion spin-charge dans les métaux, d'autres types de matériaux tels que les isolants topologiques, les interfaces de Rashba et les semiconducteurs ferroélectriques sont étudiés. Ces systèmes sont intéressants pour la réalisation de nouveaux concepts de logique de spin en raison de leur grande efficacité d'interconversion spin-charge et de leurs propriétés multifonctionnelles. Cette thèse se concentre sur l'exploration des effets d'interconversion spin-charge dans ces matériaux en utilisant diverses techniques et dispositifs. Le premier chapitre présente les concepts utilisés et développés tout au long de cette thèse, qui sont le transport de spin dans les métaux avec une aimantation colinéaire et transverse à la polarisation du courant de spin spin, ainsi que la conversion d'un courant de spin en un courant de charge dans les métaux, les interfaces Rashba et les isolants topologiques. Dans le deuxième chapitre, les propriétés de transport de spin colinéaire et transverse sont mesurées à l'aide de vannes de spin latérales, jetant les bases d'une caractérisation quantitative des effets d'interconversion spin-charge dans les systèmes mentionnés précédemment. Dans le troisième chapitre, l'effet de la compétition entre l'interaction d'échange et le couplage spin-orbite sur l'interconversion spin-charge est évalué. Pour ce faire, nous mesurons l'effet Hall de spin inverse dans les matériaux ferromagnétiques à travers leur température de transition en utilisant une technique de résonance ferromagnétique de pompage de spin, et en faisant tourner la magnétisation du matériau ISHE ferromagnétique par rapport à la polarisation du courant de spin en utilisant une nouvelle géométrie de vanne de spin latérale. Le quatrième chapitre étudie l'interconversion spin-charge dans le gaz d'électrons bidimensionnel aux interfaces entre SrTiO3 et divers métaux, et dans le gaz d'électrons bidimensionnel nouvellement découvert à l'interface métal-$KTaO_3$ en utilisant des mesures de pompage de spin. Enfin, le cinquième chapitre traite de la détection locale de l'interconversion dans le contexte de dispositifs à logique de spin récemment proposés. Dans la première partie de ce dernier chapitre, l'optimisation de la tension d'interconversion requise pour les dispositifs spin-orbite magnétoélectriques est étudiée dans le platine, par l'ingénierie de l'interface et en effectuant une détection locale de l'interconversion dans l'isolant topologique Sb_2Te_3. Dans la deuxième partie, le modelage de tels dispositifs d'interconversion locale en utilisant le semiconducteur ferroélectrique de Rashba GeTe et le gaz d'électrons bidimensionnel présent aux interfaces métal-$SrTiO_3$ est réalisé, avec une ouverture vers leur utilisation pour une récente proposition de disposif basé sur le contrôle rémanent de l'interconversion par une polarisation ferroélectrique.

Remerciements

Mes remerciements vont premièrement à Laurent et Jean-Philippe. Tout d'abord pour m'avoir accueilli dans leur groupe, mais également pour m'avoir laissé de la liberté sur les sujets abordé au cours de ma thèse, tout en donnant des directions fortes au groupe et auxquelles j'ai eu plaisir à contribuer. Je les remercie également pour leur engagement constant au cours d'une période difficile pour tous, et qui grâce à eux a été comparativement très bien vécue dans leur équipe. Finalement, je suis très reconnaissant pour tout ce que j'ai appris à leur contact, tant du point de vue technique, que littéraire ou diplomatique. Les sorties au ski ou dans les bars, ainsi que les soirées en salle blanche me manqueront, même si je resterai toujours Cendrillon.

Bien sûr, ma thèse a été un travail d'équipe. Je remercie donc les post-doctorants et doctorants qui ont significativement contribués tant à ma thèse qu'à l'environnement de travail de mon groupe. Tout d'abord Tuong, pour ses conseils avisés et (parfois) excellentes idées, et ensuite Cécile pour ses compétences et son énergie, parfois débordante. Bien sûr je n'oublie pas Yu dont la bonne humeur et la sympathique présence a été d'une grande aide tant au labo qu'à l'extérieur. Enfin, je remercie Paul qui aura su me transmettre de manière agréable tant sa passion pour le sujet qu'une partie de ses vastes connaissances sur le pompage de spin.
Je remercie également mes collègues de bureau pour m'avoir supporté tout ce temps : Salvatore à la tête dure, et Aurélie l'auvergnate à qui je souhaite bien du courage avec les hordes italiennes. Parlant d'italien, il y a bien sûr Paolo, dont j'espère voir les goûts musicaux un jour régresser vers les miens. Vos thèses seront probablement intéressantes, et j'espère couronnées de succès. Travailler avec vous aura été un plaisir, malgré nos petits accrochages ponctuels. Indispensable à l'identité du groupe ont été les membres plus ou moins officiels de la partie japonaise de l'équipe : Ryuhei, Taro et Sambit. Je souhaite bonne chance à ceux qui n'ont pas encore soutenu, et à tous un bon retour à la civilisation. Nous ne serions pas au complet sans Michael qui lui a, d'une manière ou d'une autre, trouvé la civilisation à Grenoble.
Finalement, mon travail aurait été bien moins intéressant sans nos stagiaires, désormais doctorants par ailleurs. Tout d'abord Théo, qui j'espère progressera en nanofabrication, survie en montagne et gestion du personnel – le graphisme utilisé à plus ou moins bon escient étant déjà maîtrisé. Ensuite Nicolas, qui devrait bien s'en sortir depuis son exil parisien.
J'ai également grandement apprécié l'aide d'Alain Marty, spécialement pour ses conseils théoriques, celle de Patrick Warin et de Stéphane Auffret pour la croissance de certains matériaux utilisés au cours de ma thèse, d'Ursula Ebels pour avoir mis à notre disposition certains de ses équipements et enfin et bien sûr, Ariel Brenac dont l'indispensable aide technique me serait impossible à résumer. Finalement, une grande partie des résultats que j'ai présenté sont le fruit de nombreuses collaborations : celles de Henri Jaffrès dont le modèle a permis l'analyse des résultats de transport de spin non-locales, ainsi que Manuel Bibes et son groupe à CNRS/Thalès pour la fabrication des échantillons d'oxides mesurés en spin-pumping. Je remercie également Pierre Noé et son groupe au LETI pour leur important travail de croissance sur Sb2Te3 et GeTe : je ne doute pas que cette collaboration avec Spintec sera porteuse de résultats importants. Finalement, bien que peu décrite dans ce manuscrit, la croissance de GeTe par Fabien Cheynis et Frédéric Leroy du CINaM permettra, je l'espère, d'importantes avancées dans projets liés à GeTe.
Finalement, je remercie les rapporteurs et examinateurs pour avoir lu mon manuscrit et assisté à ma soutenance.

Enfin, je tiens à remercier mes amis, et tout spécialement Alma et Ariane, ainsi ma famille pour leur soutient tout au long de mon doctorat.

Contents

Introduction

The scaling down of the conventional CMOS technology is currently reaching physical limits, in size, speed, and in static energy consumption due to increased leakage at the most aggressive technological nodes [1]. The need to address these issues is becoming crucial, as the demand for more powerful computers increases, in particular because of new developments in domains such as the artificial intelligence and the internet of things [2]. Circumventing these limitations of the CMOS technology will require new routes to be explored. Spintronics is one of these new routes.

The birth of Spintronics, a field of research and technology devoted to the use of the electron spin in electronics, is usually identified as the discovery of the giant magnetoresistance by A. Fert and P. Grünberg [3, 4] in 1988. This effect appears for instance in a trilayer made of two outer ferromagnetic material layers, separated by a non-magnetic (NM) metal spacer. It is characterized by a resistance that depends on the relative magnetization orientation between the ferromagnetic (FM) layers. An antiparallel magnetization configuration corresponds to a high resistance state, while a parallel configuration corresponds to a low resistance. This allowed developing magnetic field sensors, and in the 90's the GMR was used in hard disk drive heads. This was quickly followed by the industrial use of the tunneling magnetoresistance, which appears in similar multilayers but where the non-magnetic spacer is replaced by a crystalline MgO barrier [5]. This so-called magnetic tunnel junction (MTJ), which allows for a several orders of magnitude increase of the resistance difference between the magnetic configurations. The MTJ is the building block that allows spintronics to compete or complement the CMOS technology to develop the next generation electronics. Indeed, the non-volatility of the magnetic order leads to the possibility to use Magnetic Random Access Memories (MRAM) for in-memory processing architectures [2], a computational paradigm that embeds computations in memory arrays . These new architectures allow overcoming the memory Wall which limits the computational power of the usual von Neumann CMOS architectures. While moving towards non-von Neumann computing architectures remains a challenge, the MRAM are already seeing applications in the microelectronic industry, mostly in embedded memories. The first MRAM device, the toggle MRAM, was commercialized in 2006 by Everspin, and met mostly niche applications for memory storage in extreme conditions. Indeed, the writing was performed using magnetic fields, thus strongly reducing the device scalability, its energy efficiency (100 pJ/bit), and its writing speed (35 ns) [6].

The next generation of MRAM was the Spin Transfer Torque MRAM, or STT-MRAM, which relies on the concept of Spin Transfer Torque introduced in 1996 by Berger [7] and Slonczewski [8]. Here, one of the two ferromagnetic layers that constitute the MTJ has its magnetization fixed using a synthetic antiferromagnet, and corresponds to a hard layer. The magnetization of the other ferromagnetic layer remains free. A charge current flowing vertically into the MTJ becomes spin polarized within the hard layer. It then transfers its spin angular momentum to the free magnetization and aligns it with its spin polarization. The STT permits a much faster writing speed (down to 5 ns), and is much more energy efficient (5-10 pJ/bit) [9]. Furthermore, it has a good scalability and can be integrated in the 14-16 nm CMOS technology nodes at the cache memory level [10]. These functionalities caught the interest of major semiconductor companies such as Samsung, TSMC, Intel and GlobalFoundries, which are commercializing embedded memories containing STT-MRAMs, for a market expected to reach several billions of dollars by 2026 [11]. Despite these successes, the envisioned use of STT-MRAM for cache level still faces important challenges. The main one concerns the important current density that must be applied for a fast switching of the free magnetization. This causes aging of the MgO barrier [12], thus reducing the reliability and cyclability of such a device, which is inconsistent with cache memory level applications that requires a large number of fast writing operations.

This challenge could be overcomed however by replacing the STT, that depends only on the exchange interaction to form the spin current, by the Spin-Orbit Torque (SOT) [13], in which the spin current is generated by the spin-orbit interaction. In the SOT-MRAM, the magnetization switching of the free layer is achieved by flowing a charge current in an adjacent material with strong spin-orbit interaction. This creates a spin current that enters the free layer, and which can induce magnetization switching for large applied charge currents. The separation between the writing and

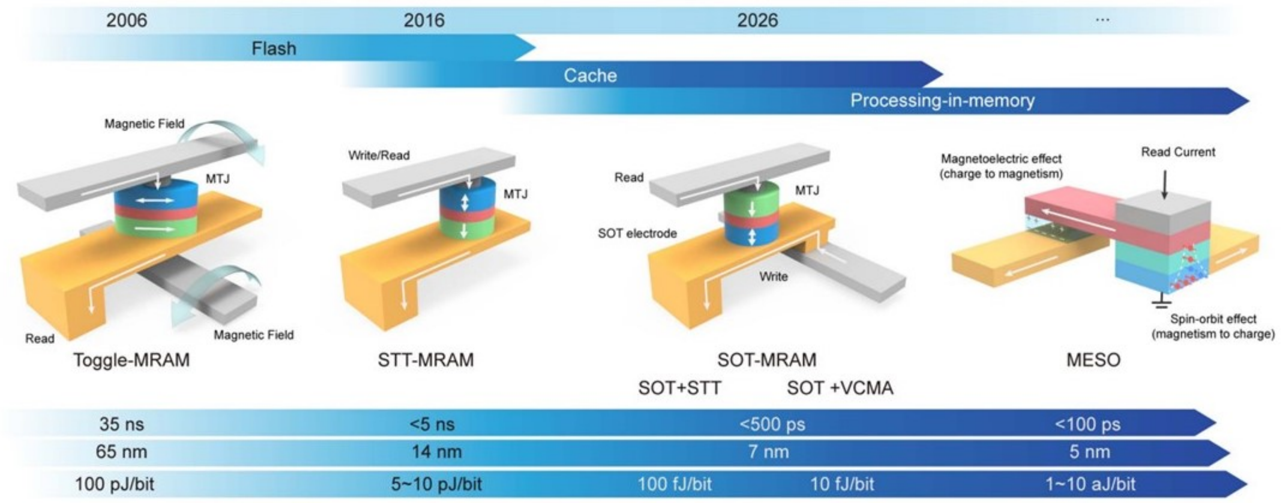

Figure 1: Schematics of the different types of MRAM, and of the MESO device with their development timeline, position in the memory hierarchy, performance and technological node integration. Image from Ref. [2].

reading paths reduces the aging problem due to the MgO barrier. Furthermore, this new switching mechanism does not rely on thermal fluctuations, and can consequently be done much faster. The functionalities offered by the SOT-MRAM have triggered a large activity on this device, with IMEC announcing in 2018 a 210 ps switching of SOT-MRAM with a 350fJ/bit operation power [14]. This potential of SOT-MRAMs attracted the attention of major foundries, who included it on their roadmaps [15]. However, several challenges need to be addressed for the SOT-MRAM to fulfill this potential. One of them is the need to increase the writing efficiency in order to decrease the power consumption. This implies producing more spin current upon the application of a given charge current in the spin-charge interconversion material.

The first SOT switching was demonstrated in 2011 in SPINTEC, using heavy metals to convert a charge current into a spin current [16], thus exploiting the important experimental work on the reciprocal process regarding the spin to charge interconversion which started in the 2000's [17]. The identification of materials with a large spin-charge interconversion efficiency, using either spin-to-charge or charge-to-spin methods, will help increase the writing efficiency in SOT-MRAM. So far, a strong focus has been put on the use of three-dimensional topological insulators [18] as a source of spin current, with the demonstration of room temperature switching at current densities lower than in heavy metals, and using large scale deposited topological insulators. In addition, two-dimensional systems including van der Waals materials [19] but also Rashba interfaces [20] might provide the high interconversion efficiency associated to a low resistivity, which reduces the power consumption of the switching [21]. Finally, the necessary presence of an external magnetic field for SOT deterministic switching leads to an increased interest in materials with a magnetic order, which can also produce a spin current using the spin-orbit coupling [22]. This led to the expansion of a new research direction that look toward the understanding of spin-charge interconversion effect in ferromagnetic and antiferromagnetic materials [23, 24, 25].

While MRAMs can complement or replace CMOS devices for memory applications, their inability to produce an output charge current makes them unable to perform logical operations . Several possibilities are being investigated to perform spin logic, based for instance on domain walls, magnons or skyrmions [26]. A spin logic device which has recently been gaining momentum is the Magneto Electric Spin Orbit (MESO) device [27] proposed by Intel. It relies on the magnetoelectric control of a nanomagnet, and is combined with a spin-orbit based read-out scheme, which produces a current accordingly to the polarization of a magnetoelectric material storing the information. The reversal of such a polarization necessitates a very low energy [28], typically in the aJ/bit range. Furthermore, the charge current produced by the spin to charge interconversion in its read-out block allows to cascade these devices. An important prerequisite for the integration of such a device into logic circuit is the optimization of the output read-out signal. This creates an important challenge, which necessitate the optimization of the interconversion, notably by exploring the conversion in topological insulators, in order to achieve the large spin to charge interconversion signal required by the MESO device. Recently, an alternative to the MESO device was proposed in my group, termed the Ferroelectric Spin Orbit (FESO) device. Similarly to the case of the MESO device, the idea is to store the information in a ferroelectric polarization, the reading being made by spin-charge interconversion. In contrast to the MESO device however, the FESO device links the sign of the spin-charge interconversion directly to the ferroelectric polarization. This removes an important issue of the MESO device, which is the need for a magnetoelectric coupling, but necessitates the identification of ferroelectric materials with large spin-charge interconversion efficiency that changes sign with the ferroelectric polarization [29, 30].

The question of the spin-charge interconversion is thus at the core of this new generation of spintronics. Beyond technological issues, this interconversion raises fundamental questions, such as the role of toplogical surface states in the conversion, or the influence on the conversion of the symmetry breaking in ferromagnets. I therefore chose to focus my PhD work on the spin-charge interconversion in three new classes of materials: ferromagnets, toplogical insulators, and ferroelectric spin-orbit materials.

This manuscript starts with a **first chapter** introducing the basis of spin dependent transport and spin-charge interconversion. The **second chapter** will consist in a measurement of the collinear and transverse spin transport parameter in metals. In the **third chapter**, I will discuss the link between the ferromagnetic order on the spin charge interconversion in the light ferromagnetic materials NiCu and NiPd. The **fourth chapter** will then be dedicated to the spin-charge interconversion in two dimensional electron gases at the surface of complex oxides. Finally, in the **fifth chapter** I will discuss the optimization of the electrical measurement in a heavy metal and a topological insulator in the context of the MESO device signal output. This will be followed by a presentation of preliminary results regarding the realization of FESO devices.

Chapter 1

Spin transport and spin to charge interconversion

The central concept on which spintronics relies is that of spin current. It corresponds to the flow of a spin angular momentum, usually carried by the spins of conduction electrons. In non-ferromagnetic materials, charge currents are usually not spin polarized, and the electrons have their spins in random directions. This current does not carry any angular momentum, so that there is no associated spin current (Fig. 1.1a). When a charge currents flows in a ferromagnet, the electron from the majority (↑) and minority (↓) spin populations have different scattering probabilities due to the higher scattering rate with the localized electronic states [31] (Fig. 1.1b). The charge current is then spin polarized and consist both in a flux of charges and a flux of angular momentum, *i.e.*, a spin current. Another situation is the case in which the spin current is not driven by a net flux of electrons. Indeed, as described in Fig. 1.1c, if a flux of electrons with ↑ spins flows in a direction opposite to a ↓ spins flux, there is not net charge flux, even though a flux of angular momentum is present. In this situation, the spin current is not accompanied by a net charge current and is called a *pure spin current*. This pure spin current can be created by flowing a charge current through the interface between a ferromagnet and a non-magnet [32, 33]. The spin orbit coupling can also interconvert spin and charge currents, as described later in this chapter. In that case a longitudinal charge current will be converted into a transverse spin current (or vice versa).

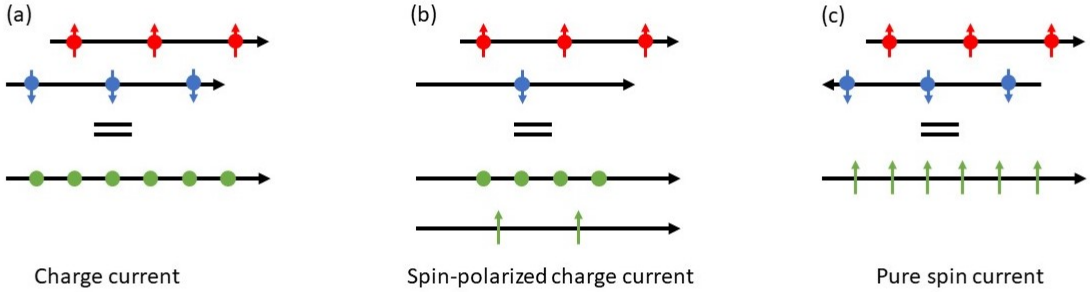

Figure 1.1: Sketches of the different type of electronic currents. (a) Non-polarized charge current. (b) Spin polarized charge current. (c) Pure spin current.

These two contributions to the electronic Hamiltonians will be at the core of the spin current generation discussed in this manuscript. The first one is based on the exchange interaction, which creates the long range magnetic order by coupling the spins of the localized electrons with those of the mobile carriers. This interaction has the effect of producing a spin current by polarizing a charge current as described in Fig. 1.1b, but can also lead to spin rotation and dephasing if a spin current with a polarization not collinear to the magnetization flows in the ferromagnet [34]. In addition to the exchange interaction, the production of the spin current, as well as its flow in ferromagnetic and non-magnetic materials, can be controlled by the spin-orbit interaction, which couples the spin of electronic carriers with their angular momentum. This coupling causes a randomization of the electronic spin and therefore a relaxation of the spin current flow. However, it also has the effect of creating a pure spin current in non ferromagnetic materials, thanks to the spin Hall and Rashba Edelstein effects.

In this chapter, I will describe the effect of both the spin-orbit interaction and the exchange interaction on spin current production and transport. I will start by describing the spin transport in metallic systems, in which the exchange interaction is responsible for the spin current production, while the role of the spin-orbit interaction will be limited to the spin current relaxation. In the second section, I will show how the exchange interaction leads to a spin current relaxation through ballistic processes, which gives rise to an anisotropic spin transport in ferromagnetic materials. Finally, in the last section I will describe how the spin-charge interconversion effects can connect the charge and spin current in absence exchange interaction, *i.e.*, in non-magnetic materials.

1.1 Spin transport and spin generation in metallic materials

In a ferromagnet with a magnetization collinear to its polarization and in non-magnets, the dynamics of the spin current is controlled by diffusive effects [35, 32]. In this section, I will introduce qualitatively the main mechanisms of spin current relaxation and their associated characteristic lengths. I will then present the Valet-Fert model [35], which describes quantitatively the spin transport in metals. Finally, I will show how a spin current can be injected from a ferromagnet into a non-magnet, with a particular focus on the role of interfacial spin transport parameters.

1.1.1 Bulk spin transport and spin current generation in metallic materials

Let us describe the electronics transport using the Drude model to illustrate the main quantities that control the spin current in metals. In this model, the electrons propagating in a material scatters on crystal defects, or on phonon/magnon modes. The average scattering time between two collisions is denoted by τ, and the mean free path between two collisions is $\lambda_t = v_F \tau/\sqrt{3}$ with v_F the Fermi velocity.
These electronic scattering events can be related to the spin transport properties using the Eliott-Yafet [36] mechanism, dominant in most metals [1] [38, 39, 40, 41, 42, 43, 44]. In this model, the Spin-Orbit (SO) coupling present in the material mixes the up and down states taken along an arbitrary axis. This results in a non-zero probability of spin-flip, with probabilities a_{ph} and a_{def} scaling with the SO strength, for scattering on phonons and impurities respectively. The spin of an electron has therefore an average lifetime τ_{sf} given by:

$$\frac{1}{\tau_{sf}} = \frac{a_{ph}}{\tau_{ph}} + \frac{a_{def}}{\tau_{def}} \tag{1.1}$$

with τ_{def} and τ_{ph} the average scattering times on impurities and phonons contributing to the scattering time as $1/\tau = 1/\tau_{ph} + 1/\tau_{def}$. The scaling relation between spin and electronic scattering time has been checked from spin transport measurements, obtaining a scattering time of $\tau_{sf} \sim 10 - 100$ ps for Cu, which corresponds to electronic scattering times in the 10^{-2} ps range, and spin-flip probabilities $a_{ph/def} \sim 10^{-3}$ [39]. From this, one can obtain the average distance $\lambda_{sf} = v_F \tau_{sf}$ over which a spin propagates before it flips. This quantity, corresponding to a spin mean free path, is however purely microscopic and will not be accessible in our measurement. A more relevant quantity is the *spin diffusion length* given in non-magnets by

$$l_{sf} = \sqrt{\frac{\lambda_t \lambda_{sf}}{3}} \tag{1.2}$$

that corresponds to the average distance the spin travels from its original position [45]. The spin diffusion ranges from a few nanometers for materials with high SO interactions such as Pt [46] to 1 μm for light metals such as Al and Cu [33]. We will see in the next section that this quantity controls the diffusion equation obeyed by the spin current.

The simple relation between the spin diffusion length and the scattering times implies that there is a link between the electrical resistivity and the spin diffusion length. The resistivity scales with the electron scattering rate as $\rho \propto 1/\tau$ so that $\rho l_{sf} \propto \sqrt{\tau_{sf}/\tau}$ [39]. If one of the two above mentioned scattering processes dominates, then $\rho l_{sf} \propto \sqrt{a_{ph/def}}$. The spin flipping coefficient being independent of the electron scattering rate, this implies that when changing the temperature or the carrier density the product ρl_{sf} is constant [39, 38]. However, the value of ρl_{sf} is not expected to remain the same when the main spin relaxation process changes.

---

[1] Another mechanism, which leads to the spin current relaxation in systems lacking inversion symmetry by spin rotation between the scattering events, has been introduced by Dyakonov and Perel' [37]. It probably contributes to the spin relaxation in some systems discussed in the chapters 4 and 5, such as the two dimensional electron gas at the surface of complex oxides and in GeTe. This mechanism will however not be described here since only the spin to charge interconversion in these materials is discussed in this manuscript.

So far, the discussion concerned non-magnetic materials. The situation in ferromagnets is not significantly different and the same relation remains, with minor modifications taking into account the presence of two opposite spin populations. In ferromagnetic materials, the electrons have their spins along the magnetization with two different orientations, with a band structure for the two populations shifted in energy by the exchange splitting. Minority spins ($\downarrow$) have a higher density of state at the Fermi surface than majority spins ($\uparrow$) [47], and therefore a lower conductivity $\sigma_\downarrow < \sigma_\uparrow$ [48]. This defines the *spin polarization* for ferromagnetic materials, defined as the conductivity asymetry between the two spin channels

$$\beta = \frac{\sigma_\uparrow - \sigma_\downarrow}{\sigma_\uparrow + \sigma_\downarrow} \tag{1.3}$$

Similarly, it is possible to define independently spin diffusion lengths $l_{sf}^{\uparrow(\downarrow)}$ for the two spin populations. A global spin diffusion length for the two spin populations can then be defined as $1/\lambda_{sf}^F = 1/\lambda_{sf}^\uparrow + 1/\lambda_{sf}^\downarrow$, so that the spin diffusion length in FMs writes $l_{sf}^F = \sqrt{1/6(1-\beta^2)\lambda_t\lambda_{sf}}$ with λ_t the electronics mean free path averaged between the two spin conduction channels [45]. The spin relaxation mechanisms in the Eliott-Yafet model are also similar to those present in non-magnets, with an additional relaxation mechanism caused by magnons modes at high temperature [49]. The estimation of these diffusive spin transport parameters is critical in spintronics, as they determine the scale at which spin-based devices or stacks have to be designed. Their measurement will be discussed in the second chapter of this manuscript.

In the next section we will use the parameters introduced above to discuss the Valet-Fert equations, which constitute the basis of the model used through this manuscript.

1.1.2 The Valet-Fert model

The transport of electrons relies on the drift-diffusion model [50, 32, 35], in which the electronic displacement is due to a drift created by the application of an electric field and to the diffusion caused by a local charge accumulation. This description is valid in the diffusive limit, in which the typical size of the system is much larger than λ_t. For generality purpose I will start from the basic equations for two spin populations, with different spin dependent transport parameters. This will allow describing ferromagnetic materials. Retrieving the case of non-magnets is then straightforward by taking $\sigma_\uparrow = \sigma_\downarrow$. As described above, the current of electrons with spin $s = \uparrow$ or $\downarrow$ in the presence of an electric field $\boldsymbol{E} = -\partial_{\boldsymbol{r}} V$ and charge accumulation n_s writes:

$$\boldsymbol{j}_s = -\sigma_s \boldsymbol{E} - eD_s \partial_{\boldsymbol{r}} n_s \tag{1.4}$$

with $D_s = 1/3 v_F \tau_s$ the diffusion constant for s polarized spins. The quantity that described the accumulation of spins with respect to the equilibrium condition is the spin electrochemical potential $\mu_s = eD_s/\sigma_s n_s - V$ with units of an electrical potential. The spin dependent conductivity is given by the Einstein relation $\sigma_s = e^2 N_S D_s$, N_s being density of states at the Fermi energy of the s polarized electron. The current of s spins $\boldsymbol{j}_s$ can then be written as a generalized Ohm law:

$$\boldsymbol{j}_s = -\sigma_s \partial_{\boldsymbol{r}} \mu_s \tag{1.5}$$

By introducing the average potential $\mu_m = (\mu_\uparrow + \mu_\downarrow)/2$, the spin accumulation $\mu = (\mu_\uparrow - \mu_\downarrow)/2$, the charge current $\boldsymbol{j}_c = \boldsymbol{j}_\uparrow + \boldsymbol{j}_\downarrow$ and the spin current $\boldsymbol{j} = \boldsymbol{j}_\uparrow - \boldsymbol{j}_\downarrow$, we can write using the previously introduced parameters [52]:

$$\boldsymbol{j}_c = -\sigma \partial_{\boldsymbol{r}} (\mu_m + \beta \mu) \tag{1.6}$$

for the charge current, with $\sigma = (\sigma_\uparrow + \sigma_\downarrow)/2$ the average of the conductivity of both spin species corresponding to the total conductivity of the material. The spin current can be written:

$$\boldsymbol{j} = -\sigma^\star \partial_{\boldsymbol{r}} \mu + \beta \boldsymbol{j}_c \tag{1.7}$$

$\sigma^\star$ being equal to $\sigma(1-\beta^2)$. Note that both the spin and charge currents are in Ampères, with possibility to recover a unit of momentum flux for the spin current using a multiplication by $\hbar/2e$, e being the electron charge. The average potential and spin accumulation are expressed in Volts. Both these terms contain a drift term, corresponding to the usual electrical response to a field for the charge current, including the asymmetry β of the conductivity between the electrons species for the spin current, and a diffusion term that depends on the gradient of the spin accumulation.

As discussed above, while the charge current is conserved with $\partial_{\boldsymbol{r}} \cdot \boldsymbol{j}_c = 0$, the spin current is not conserved due to the spin relaxation processes discussed in the previous section:

$$\partial_{\boldsymbol{r}} \cdot \boldsymbol{j} = \frac{1-\beta^2}{\rho l_{sf}} \mu \tag{1.8}$$

Finally, when combining these equations, we obtain the diffusion equation obeyed by the spin accumulation:

$$\Delta \mu = \frac{\mu}{l_{sf}^2} \tag{1.9}$$

with $l_{sf}^2 = D\tau_{sf}$ as discussed before. D is a function of the diffusion coefficient and densities of states at the Fermi level for the two spin species. One can retrieve the equations for the non-magnetic metals simply by taking $\beta = 0$. The consequence of this equation is that an excess of electron in one of the spin channels will be attenuated exponentially along the spin diffusion.

The remaining question is how to produce a spin accumulation in the first place. There exist several methods for the generation of a spin accumulation, such as the Spin Pumping by FerroMagnetic Resonance [53] (SP-FMR) or the Spin Hall effect [51]. For now, we will consider the simplest one, relying on the electrical injection of an electrical current from a ferromagnet into a non-magnetic material [32]. This method involves however interfacial effects which will be described in the next section.

1.1.3 Spin transport at metal/metal interfaces

In this section, I will solve the Valet-Fert equation for a simple ferromagnet/non-magnet bilayer using different boundary conditions, taking into account the interface resistance, spin polarization and spin memory loss (SML) at the interface. I will illustrate the effect of these interfacial terms on the spin current injection in the non-magnet. These analytic results are also used to benchmark a Finite Element resolution of the Valet-Fert equations that will be useful to compute the solution to the Valet-Fert equations in complex geometries. Both the analytical calculations and the formulation of the Finite Element Simulations are detailed in the appendix.

Spin injection at the interface between ferromagnetic and non-magnetic materials

Let us consider a bilayer composed of a non-magnet (spin diffusion length l_{sf}^N, resistivity ρ_N, polarization $\beta_N = 0$) and of a ferromagnetic material (spin diffusion length l_{sf}^F, resistivity ρ_F and polarization β_F), with thicknesses larger than their spin diffusion lengths. A charge current perpendicular to the plane (Z direction) is flown across the interface ($z = 0$) between these two materials, from the ferromagnet to the non-magnet (Fig. 1.2a). We start by assuming a transparent interface, i.e., a continuity of the spin accumulation and charge current across the interface. Due to the non-zero polarization of the ferromagnet, the charge current is spin polarized. This leads to a more important transfer of spin ↑ than spin ↓ into the non-magnet. Since at equilibrium the two spin populations need to be equal in the non-magnet, this leads to a spin accumulation $\mu(0)$ at the interface, and thus to the flow of spin currents from the interface into the FM and into the NM:

$$j_s^N = \frac{\mu_{|0+}}{R_N}, \; j_s^F = -\frac{\mu_{|0-}}{R_F} \tag{1.10}$$

in which $R_{F/N} = l_{sf}^{F/N} \rho^{F/N}/(1-\beta_{F/N}^2)$ are the spin resistances, which quantify the capacity of a material to relax the spin currents. The spin accumulation $\mu_{|0+(-)}$ is taken at the NM (FM) side. In this system, j_s^N corresponds to the spin current injected from the FM into the NM, while j_s^F is a spin backflow term, which represents the relaxation of the interface spin accumulation into the ferromagnet. The spin accumulation at the interface $\mu(0)$ can be computed from the spin resistor model [52] and its evolution in the bulk is obtained by solving eq. 1.9. The evolution of $\mu(z)$ and $j(z)$ in the system are given in Fig. 1.2b for a transparent interface. The spin accumulation created at the interface vanishes exponentially in the FM and NM over their respective spin diffusion lengths. The spin current displays a different behavior. It is constant in the bulk of the FMs as the charge current is spin polarized since β_F is non zero, and decreases at the interface due to the spin backflow term. The injected spin current in the NM decreases exponentially over its spin diffusion length. The solution obtained using Finite Element Simulations is also given in the Fig. 1.2b and matches perfectly the analytical solution.

The transparent interface approximation is commonly used in spintronics, as it allows to reduce the number of parameters introduced in the models, and because it is difficult to measure spin-dependent interface parameters. A

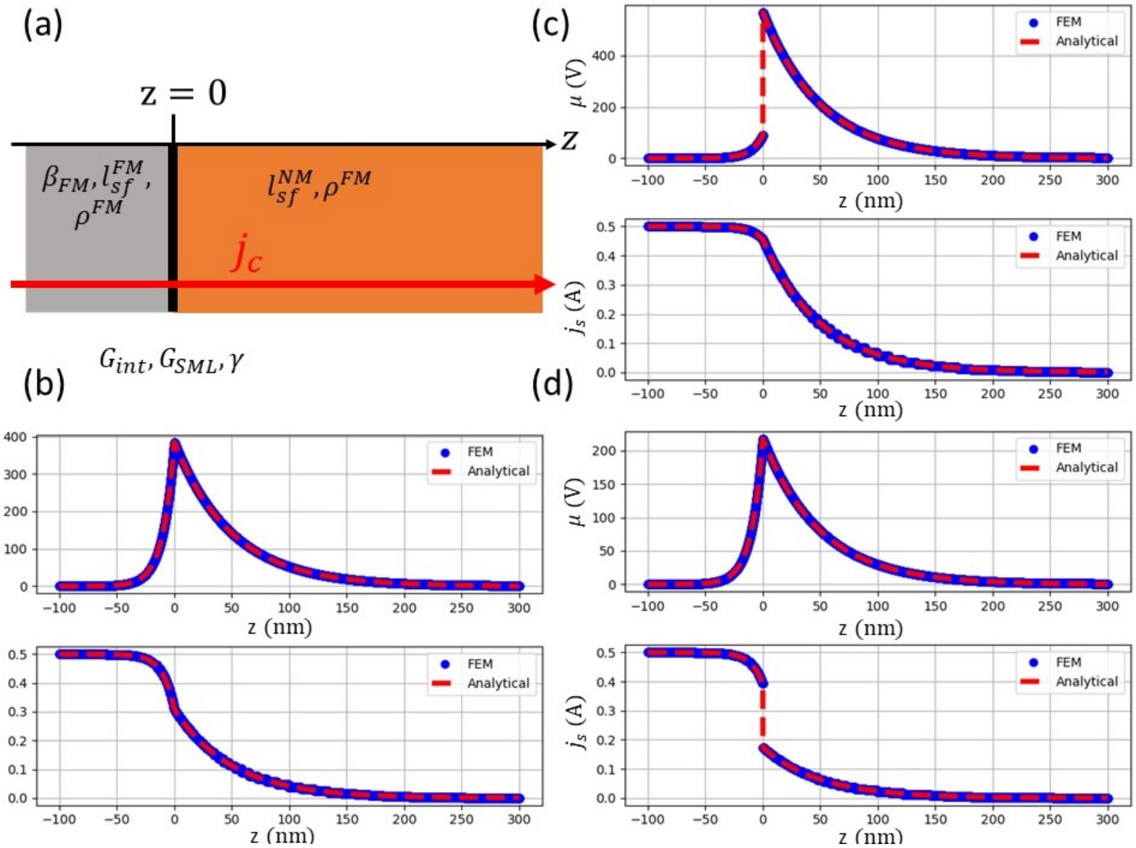

Figure 1.2: (a) FM/NM bilayer used for the calculations. (b) Spin accumulation (top) and current (bottom) map with a transparent interface between the FM and NM, obtained by FEM simulations and analytical calculations. (c) Spin accumulation and current map for a polarized resistive interface described by eq. 1.11. (d) Spin accumulation and current map for an interface with SML described with eq. 1.12. In (b), (c) and (d), $z = 0$ corresponds to the interface between the FM ($z < 0$) and the NM ($z > 0$).

number of experiments have however demonstrated that in general, a sizeable interface resistance exists at metal-metal interfaces [54], and that the spin current polarization can experience relaxation processes due to spin-orbit coupling at the interface [46]. Finally, the interface resistance can be different for spin species with opposite orientations, giving rise to an interfacial polarization [55]. In the next paragraph, I will discuss the effect of these interfacial parameters on the electrical injection from a ferromagnet into a non-magnet.

Spin transport parameter at non-magnet/ferromagnet interfaces

As will be discussed in Chapter 5, the interface resistance and the interface polarization play a crucial role in the injection of a spin current into a non-magnetic material [56]. The associated boundary conditions can be written:

$$\begin{pmatrix} j_c \\ j_s \end{pmatrix} = G_{int} \begin{pmatrix} 1 & \gamma \\ \gamma & 1 \end{pmatrix} \begin{pmatrix} \mu_{m|0^-} - \mu_{m|0^+} \\ \mu_{|0^-} - \mu_{|0^+} \end{pmatrix} \tag{1.11}$$

in which G_{int} is the interface conductance, corresponding to the inverse of the resistance area RA [54]. These boundary conditions will create a discontinuity in the potential and spin accumulation profiles. γ corresponds to an interfacial polarization, given by $\gamma = (G_\downarrow - G_\uparrow)/(G_\downarrow + G_\uparrow)$ with $G_{\uparrow(\downarrow)}$ the interfacial conductance of the spin $\uparrow$ ($\downarrow$) species. The presence of both an interface resistance and an interface polarization will increase the spin accumulation and injected spin current at the interface, since the spin backflow from the NM to the FM is cancelled by the interface resistance. This more efficient spin injection from the FM into the NM from a polarized interface is shown in Fig. 1.2c, with the results of the analytical calculations based on the spin resistor model and FEM simulations taking into account the boundary conditions (see the appendix for more details on the calculations). Again, we find a perfect agreement between the FEM simulations and analytical calculations. The presence of an interface resistance keeps the continuity of the spin current across the interface. This means that we have so far neglected the Spin Memory loss across the interface.

In a non-ideal interface, the possibility for an electron to loose the memory of its spin when crossing the interface needs to be considered. Indeed the symmetry breaking at the interface, associated with spin-orbit coupling, can cause an important interfacial spin current relaxation called the Spin Memory Loss which can strongly complexify the evaluation of the spin transport properties [55, 46]. This spin memory loss at the interface generates a discontinuity of the spin current and is modeled using the boundary conditions at each side of the interface [57]:

$$\begin{pmatrix} j_{c|0^{+(-)}} \\ j_{s|0^{+(-)}} \end{pmatrix} = G_{SML} \begin{pmatrix} 0 & 0 \\ 0 & 1 \end{pmatrix} \begin{pmatrix} \mu_{m|0^{+(-)}} \\ \mu_{|0^{+(-)}} \end{pmatrix} \tag{1.12}$$

The effect of this interfacial term is shown in Fig. 1.2d, with a non-resistive interface ($G_{int} \to \infty$) for clarity. As shown in Fig. 1.2d, the spin current on the NM side decreases with the presence of SML, which is therefore detrimental to the spin injection efficiency. It is worth noting that this description of the interfacial spin transport is distinct from the one introduced by Bass and Pratt, which model the interface as a layer with a finite thickness t_I and spin diffusion length l^I_{sf} [58] in addition to the resistance area and a polarization γ. The spin memory loss is then modelled by a spin flip parameter $\delta = t_I/l^I_{sf}$ describing the spin relaxation *inside* the interface. This model can be mapped into the one which uses G_{SML} to describe the spin-memory loss since they both describe the interfacial spin transport using three parameters. However, it seems that no simple analytical correspondence can be made between the two in the general case. In this manuscript I use the spin memory loss model that relies on the G_{SML} parameter since it is much more simple to implement in FEM simulations than the one of Bass and Pratt.

For simplicity, in this section I have illustrated separately the effect of a polarized interface resistance and the spin memory loss. In practice, both these effects coexist with additional spin-charge and spin-spin interconversion (spin swapping) [59] contributions as well as possible non-collinear effects. Although these interfacial effects can be described using FEM simulations, they will not be presented in this manuscript. The effect of the interface resistance on the spin transport at a ferromagnet-non magnet interface will be discussed in Chapter 2, and the interface polarization will be measured in Chapter 5 in the context of the spin-charge interconversion.

1.2 Non-collinear spin transport in ferromagnetic materials

So far, we have considered spin transport in lateral spin valves in a situation in which the spin current polarization is always collinear with the ferromagnet's magnetization. In this section, I will give the basis of non-collinear magnetoelectronics, in order to describe the spin transport in non-collinear systems.

1.2.1 Quantum mechanical description

The aim of this paragraph is to provide a brief quantum mechanical overview of the non-collinear spin transport at the interface between a ferromagnet and a non-magnet, which has been introduced in Refs. [60, 61]. The spin quantification axis is taken along the magnetization of the ferromagnet ($\hat{y}$). For illustration purpose, I will start by describing a single electron scattering on the interface between the non-magnet and the ferromagnet. In this section, I will use the Bloch representation of an electron spin going from the non-magnet into the ferromagnet, with a wave vector $\boldsymbol{K} = k_z\hat{z} + \boldsymbol{q}$, $\hat{z}$ being the normal to the interface and $\boldsymbol{q}$ a vector that belongs to the xy plane. The spin $|\sigma\rangle$ part of the electronics wave function is described in the Bloch representation as:

$$|\sigma\rangle = \cos\frac{\theta}{2}\mathrm{e}^{-i\phi/2}\,|\uparrow\rangle + \sin\frac{\theta}{2}\mathrm{e}^{i\phi/2}\,|\downarrow\rangle \tag{1.13}$$

with θ the polar angle and ϕ the azimutal angle with respect to the spin quantification axis $\hat{y}$. For simplicity, let us consider the situation of an incident electron with its spin along $\hat{z}$ so that $\theta = \pi/2$ and $\phi = 0$. The incident wave function then writes:

$$\psi_{in} = \frac{1}{\sqrt{2}}[|\uparrow\rangle + |\downarrow\rangle]\mathrm{e}^{ik_z z}\mathrm{e}^{i\boldsymbol{q}\cdot\boldsymbol{r}} \tag{1.14}$$

with $(z, \boldsymbol{r})$ the spatial variable. Due to the exchange energy in the ferromagnet, the $|\uparrow\rangle$ (minority) and $|\downarrow\rangle$ (majority) component of the incident spin do not have the same probability R_σ of being transmitted and reflected at the interface. The $|\downarrow\rangle$ spin have indeed to overcome a larger energy barrier than the $|\uparrow\rangle$ to enter the ferromagnet, so that its probability of being reflected is higher and $|R_\uparrow| > |R_\downarrow|$. The reflected wave function writes:

$$\psi_R = \frac{1}{\sqrt{2}}[R_\uparrow \left|\uparrow\right\rangle + R_\downarrow \left|\downarrow\right\rangle]\mathrm{e}^{-ik_z z}\mathrm{e}^{i\boldsymbol{q}\cdot\boldsymbol{r}} \tag{1.15}$$

So that the reflected spin takes a component antiparallel to the magnetization $\theta_R > \pi/4$. Furthermore, the reflection coefficients are in general not real, so that the spin rotates partially around the magnetization direction, and $\phi_R \neq 0$ (Fig. 1.3a). Importantly, R_σ depends on $\boldsymbol{q}$ so that the spin rotation upon reflection will depend on its angle of incidence on the interface.

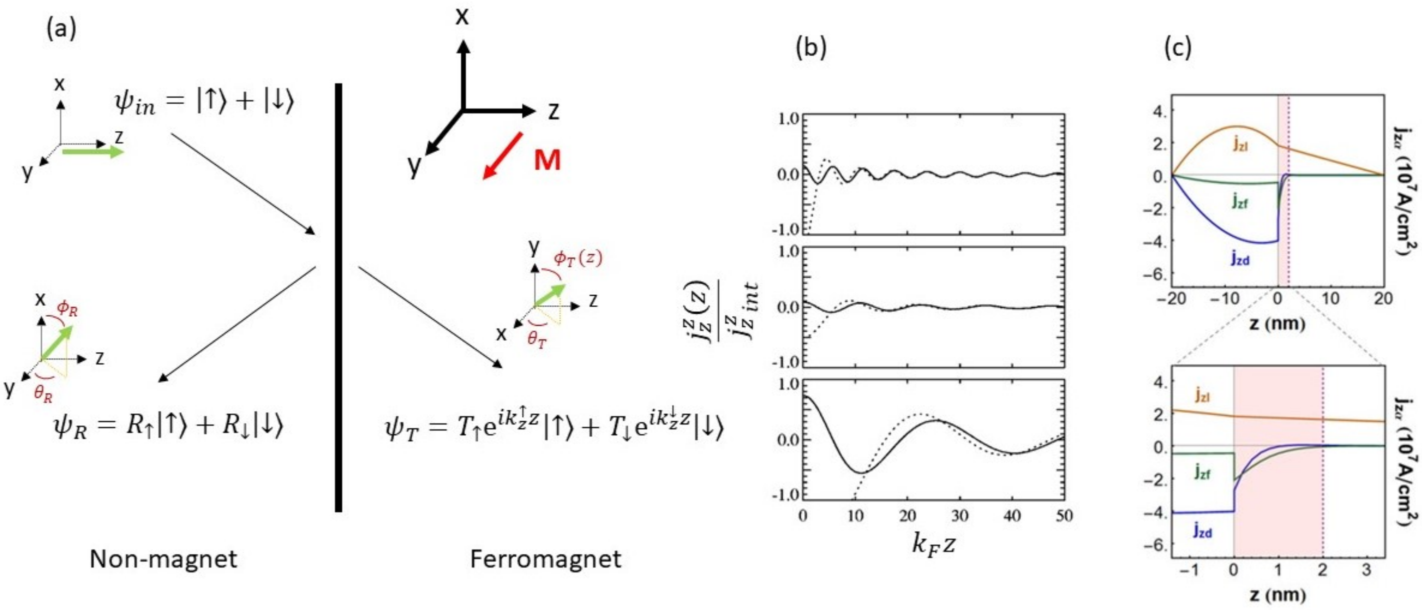

Figure 1.3: (a) Sketch of the non-collinear processes experienced by an electronic spin along $\hat{z}$ (green arrow) scattering at the interface between a non-magnet and a ferromagnet with a magnetization along $\hat{y}$. (b) Evolution of the $\hat{z}$ component of the polarization when flowing into a ferromagnet with magnetization along $\hat{y}$ and an exchange coupling J increasing from the top to the bottom panel. Image from ref [62]. (c) Relaxation and rotation processes of the spin current polarization component (j_{zl}, j_{zf}, j_{zd}, in the ($\hat{l}$,$\hat{f}$,$\hat{d}$) basis) flowing from a non-magnet into a ferromagnet, with magnetization along the $\hat{l}$ direction. Image from [63].

Similarly to the case of the reflection, the spin transmission probability amplitudes T_σ for minority and majority spins are different with $T_\uparrow > T_\downarrow$. Furthermore, the $\uparrow$ and $\downarrow$ propagate in the ferromagnet with different wave vectors $k_z^\uparrow$ and $k_z^\downarrow$ so that the transmitted wave function writes:

$$\psi_T = \frac{1}{\sqrt{2}}[T_\uparrow \mathrm{e}^{ik_z^\uparrow z} \left|\uparrow\right\rangle + T_\downarrow \mathrm{e}^{ik_z^\downarrow z} \left|\downarrow\right\rangle]\mathrm{e}^{i\boldsymbol{q}\cdot\boldsymbol{r}} \tag{1.16}$$

This causes the spin to partially align with the magnetization ($\theta_T < \pi/4$), while it also rotates around it due to the different propagation wave vectors of the two spin components. This means that ϕ_T depends on z. Similarly to the reflection case, the transmission coefficients, but also the propagation wave vectors k_F^σ depend on $\boldsymbol{q}$, so that the phase amplitude $\phi_T(z)$ depends on the incident electron state position on the non-magnetic material Fermi surface.

The spin current probed in the experiment do not concern only one electron but all the electronic states on the non-magnetic material Fermi contour with $k_z > 0$. This means that one has to sum the Fermi contour states for $|\boldsymbol{q}| \in [0, k_F]$ with $k_z > 0$ to obtain the transmitted and reflected spin current [62]. As previously mentioned, the angle taken by the reflected spin depends on $\boldsymbol{q}$. This causes a phase averaging of the reflected spin current, which decreases its polarization. The case of the transmitted spin current is slightly more complex since the phase of the electron evolves with its position in the ferromagnetic material. The polarization of the spin current is then a result of the spin dynamics and depends on its propagation distance into the ferromagnet. As shown in Fig. 1.3b, the polarization of the spin current rotates around the magnetization. At the same time, its amplitude decreases due to the phase averaging between the different transmitted electronic states that takes place when going deeper into the ferromagnet. The speed of the rotation and of the phase averaging depends on the ferromagnet's exchange interaction, since it controls the splitting between $k_F^\uparrow$ and $k_F^\downarrow$ as $|k_F^\uparrow - k_F^\downarrow| \propto J$ [34]. This leads to a spin precession length $l_L \propto 1/J$ [64]. For a large exchange interaction, the polarization along Z at $z = 0$ is small, due to the large difference between $T_\uparrow$ and $T_\downarrow$. The large mismatch between $k_F^\uparrow$ and $k_F^\downarrow$ then causes a fast precession and phase averaging, over a few Angstrom into the ferromagnet for 3d ferromagnets such as Co, CoFe and NiFe [64]. Upon decreasing the exchange interaction and consequently the Fermi vector splitting, the transmitted spin current polarization increases, and so does the oscillations period, with a much larger phase averaging length. We will see in the third chapter that in some materials it can become as large as the spin diffusion length.

In the next paragraph, we will see how the non-collinear spin transport can be described in a diffusive equation framework, through the generalization of the Valet-Fert model described in section 1.1.2.

1.2.2 Non-collinear spin transport modelling

The Valet-Fert model describes the spin current as two counter propagating ↑ and ↓ polarized charge currents along an arbitrary spin quantification axis, so that only one direction of spin polarization is allowed. In this case, the spin current is a vector in the three dimensional real space, while the spin accumulation is a scalar. As previously described however, the non-collinear spin transport requires the spin polarization to take arbitrary directions. The spin current must then be described as a 3x3 tensor $\boldsymbol{j} = (\boldsymbol{j}_\alpha)_{\alpha\in\{x,y,z\}}$, where $\boldsymbol{j}_\alpha$ represent the flow of spin current in the direction α, and the vector components give the direction of the spin current polarization. The spin accumulation will now be a vector $\boldsymbol{\mu}$ of the three dimensional spin space. A generalization of the Valet-Fert equations in the non-collinear configuration has been provided in several publications, either taking into account the effect of spin-orbit interaction in the bulk [65], or at the interface [66, 59]. For simplicity, I will here focus on the case in which only the effect of the exchange interaction is taken into account, which as been described in Ref. [64].
Let us start with the bulk non-collinear spin transport effects. The flux equation for the charge current j_α^c flowing in the α direction writes:

$$-\sigma^\star \partial_\alpha \mu_m = j_\alpha^c - \beta \boldsymbol{m} \cdot \boldsymbol{j}_\alpha \tag{1.17}$$

Which is similar to the case of the Valet-Fert equation (eq. 1.6), and simply takes into account the fact that the spin current polarization is not necessarily collinear with the magnetization in the second right hand side term. The generalization of the spin flux equation (eq. 1.7) corresponds to:

$$-\sigma^\star \partial_\alpha \boldsymbol{\mu} = \boldsymbol{j}_\alpha - \beta j_\alpha^c \boldsymbol{m} + \frac{\lambda_t}{l_\perp}(\boldsymbol{m} \times \boldsymbol{j}_\alpha) \times \boldsymbol{m} - \frac{\lambda_t}{l_L}(\boldsymbol{m} \times \boldsymbol{j}_\alpha) \tag{1.18}$$

which takes into account the spin precession and the spin phase averaging through the lengths l_L and $l_\perp$. The conservation equations for the charge current still writes $\partial_\alpha j_\alpha^c = 0$, while that of the spin current is the generalization of eq. 1.8:

$$\partial_\alpha \boldsymbol{j}_\alpha = -\frac{\sigma^\star}{l_{sf}^2}\boldsymbol{\mu} - \frac{\sigma^\star}{l_\perp \lambda_t}(\boldsymbol{m} \times \boldsymbol{\mu}) \times \boldsymbol{m} + \frac{\sigma^\star}{l_L \lambda_t}(\boldsymbol{m} \times \boldsymbol{\mu}) \tag{1.19}$$

With new terms that describe the effects of spin rotation and the transverse spin relaxation by phase averaging. From these equations, it is possible to derive a diffusion equation for the different components of the spin accumulation. While the collinear component of the spin accumulation simply follows eq. 1.9, the transverse spin accumulation needs to be written as a complex number $\tilde{\mu} = \mu_1 + i\mu_2$, where μ_1 and μ_2 correspond to the two components of the transverse part of the spin accumulation $\boldsymbol{\mu}_\perp = (\boldsymbol{m} \times \boldsymbol{\mu}) \times \boldsymbol{m}$. This allows to write the diffusion equation in the form [64]:

$$\Delta \tilde{\mu} = \frac{\tilde{\mu}}{l_{mx}^2} \tag{1.20}$$

with the complex transverse spin relaxation length:

$$\frac{1}{l_{mx}^2} = (\frac{1}{\lambda_t} + \frac{1}{l_\perp} - \frac{i}{l_L})(\frac{\lambda_t}{l_{sf}^2} + \frac{1}{l_\perp} - \frac{i}{l_L}) \tag{1.21}$$

For 3d ferromagnetic materials at room temperature such as Co, Cofe and NiFe, the strong exchange interaction causes a fast spin precession and phase averaging. The ballistic relaxation processes of the transverse spin current therefore happen on less than one nanometer scale, which is shorter than the electronic mean free path and spin diffusion lengths in these materials [64, 67]. This corresponds to the clean limit (l_L, $l_\perp \ll \lambda_t$, l_{sf}) where the diffusive spin relaxation processes can be neglected. The transverse spin relaxation length then reduces to:

$$\frac{1}{l_{mx}} = \frac{1}{l_\perp} - \frac{i}{l_L} \tag{1.22}$$

However, for materials with a low exchange interaction, which is for instance the case of dilute magnetic alloys composed of magnetic atoms in a non-magnetic matrix such as NiCu, NiPd and FePt, this may not be the case anymore, meaning that the transverse relaxation lengths could be larger than the spin diffusion lengths. In this case, the transverse spin current relaxation processes of the diffusive regime dominate the ballistic ones. As a consequence, it is possible to achieve $l_{mx} \sim l_{sf}$ in this class of materials. The situation in which the clean limit is expected to hold will be studied experimentally in the second chapter of this manuscript, while the case of dilute magnetic alloys will be explored in Chapter 3.

The interfacial processes, namely the reflection with spin rotation described by R_σ and the spin filtering during the transmission (T_σ), are represented using the following boundary conditions [64]:

$$\boldsymbol{j}^a_\alpha \cdot \boldsymbol{n}_\alpha = \mathrm{Re}(G^T_{\uparrow\downarrow})\Delta\boldsymbol{\mu} - \mathrm{Im}(G^T_{\uparrow\downarrow})\boldsymbol{m} \times \Delta\boldsymbol{\mu} + \epsilon^a[\mathrm{Re}(G^R_{\uparrow\downarrow})\boldsymbol{\mu}^a - \mathrm{Im}(G^R_{\uparrow\downarrow})\boldsymbol{m} \times \ \boldsymbol{\mu}^a] \tag{1.23}$$

In which the superscript $a = f/n$ refers to a quantity on the FM or NM side of the interface. $\Delta\mu$ is the difference of spin accumulation between each side of the interface, while $\epsilon^f = -\epsilon^n = 1$ for an interface normal $\boldsymbol{n}$ pointing towards the FM. The quantity $G^T_{\uparrow\downarrow}$ corresponds to the spin *transmitted* mixing conductance, its real (imaginary) part describing the transfer of spin current without (with) rotation across the interface. $G^R_{\uparrow\downarrow}$ is the *reflected* spin mixing conductance, with a real part describing the relaxation of the spin current at the interface, due to the spin dependent reflection and phase averaging, and an imaginary part corresponding to the rotation of the incident electron spin upon reflection. The effect of these boundary conditions can be seen in Fig. 1.3c, where they create a discontinuity of the transverse polarization of the spin current which flows from the non-magnet into the ferromagnet. The effect of the spin mixing conductance imaginary part is to create a spin current with polarization perpendicular to both the magnetization and to the incident spin current polarization transverse to the magnetization.

In the limit where the thickness of the FM is much larger than l_L and $l_\perp$, it is possible to strongly reduce the number of parameters describing the transverse relaxation processes. Indeed, the rotation and relaxation induced by l_L and $l_\perp$ have an effect similar to the one of the imaginary and real parts of the spin mixing conductance, respectively. By redefining the interface as the thickness of the ferromagnet in which the transversely polarized spin current relaxes (Fig. 1.3c), it is possible to redefine the transmitted and reflected spin-mixing conductances by setting $G^T_{\uparrow\downarrow} = 0$ and include the effect of $l_{L/\perp}$ in $G^R_{\uparrow\downarrow}$ which is then replaced by $G_{\uparrow\downarrow}$. The spin current flowing from the non-magnet into the ferromagnet with a transverse polarization will then simply be expressed as [63]:

$$\boldsymbol{j}^a_\alpha \cdot \boldsymbol{n}_\alpha = \mathrm{Re}(G_{\uparrow\downarrow})\boldsymbol{\mu} - \mathrm{Im}(G_{\uparrow\downarrow})\boldsymbol{m} \times \boldsymbol{\mu} \tag{1.24}$$

with $\boldsymbol{\mu}$ the spin accumulation at the interface on the side of the non-magnet, and $G_{\uparrow\downarrow}$ the *spin mixing conductance.* The real part of this quantity describes the relaxation of the transversely polarized spin current that enters into the ferromagnet and takes into account both the interfacial and bulk relaxation effects. Its imaginary part reflects the rotation of this spin current at the interface between the non-magnet and the ferromagnetic material.

Finally, the value at the FM/NM interface of a spin current with an arbitrary polarization direction writes, taking into account the collinear relaxation processes:

$$\boldsymbol{j}^a_\alpha \cdot \boldsymbol{n}_\alpha = G_s(\boldsymbol{m} \cdot \mu)\boldsymbol{m} + \mathrm{Re}(G_{\uparrow\downarrow})\boldsymbol{m} \times (\boldsymbol{\mu} \times \boldsymbol{m}) \tag{1.25}$$

in which we neglected the imaginary part of the spin mixing conductance, since we will consider in the following only metal-metal interfaces [34]. In this case, $G_{\uparrow\downarrow}$ represent the efficiency of the transversely polarized spin current relaxation and is given by the sum of an interfacial and a bulk term:

$$\frac{1}{G_{\downarrow\uparrow}} = \frac{1}{G^R_{\uparrow\downarrow}} + \frac{1}{\rho_{FM}\min(l_L, l_\perp)} \tag{1.26}$$

which will help interpret the results of transversely polarized spin current relaxation processes at metal-metal interfaces later on in this manuscript.

The spin mixing conductance introduced by the non-collinear spin transport processes is a central parameter in spintronics, as it controls the transfer of angular momentum from an incoming spin to the local magnetization. It is therefore crucial for the study of STT [62] and SOT [68]. A direct measurement of this quantity is not straightforward, and in particular, very few observations of the spin relaxation anisotropy predicted by eq. 1.25 have been made so far [69]. In Chapter 2, I will present a measurement method used for the extraction of the spin mixing conductance at the interface between Cu and 3d ferromagnets.

1.3 Spin-charge interconversion

The SO interaction does not only have the effect of relaxing the spin current that flows in a non-magnet. It also allows for the formation of a spin current from a charge current through the Spin Hall Effect (SHE), or to the conversion of a spin current into a charge current through its Onsager reciprocal effect. While the SHE drives the interconversion in bulk metallic materials, an interconversion effect called the Edelstein Effect (EE) is also present in two dimensional electronic systems.

1.3.1 Spin Hall effect in metals

In metallic materials, the SO interaction couples the spin of a conduction electron to its momentum [70]. This coupling can be made either trough the skew scattering [71], in which the impurity generates an effective magnetic field that depends on the spin of the incident electron (Fig. 1.4a), leading to a momentum modification depending on the electron spin. Another mechanism linking the electronic displacement with the spin is the side jump [72], that couples a lateral displacement of the electron incident on an impurity with its spin direction (Fig. 1.4b). One last mechanism is the so called intrinsic mechanism [73] in which the electron experiences a spin dependent anomalous velocity, due to the effect of the SO interactions on the band structure.

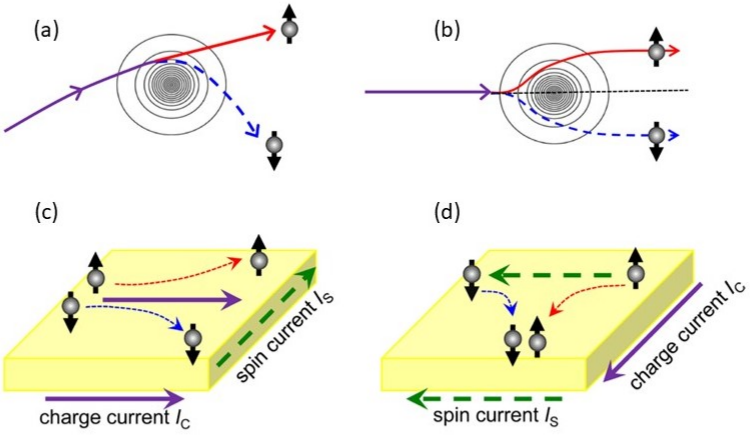

Figure 1.4: (a) Sketch of the skew scattering process. (b) Sketch of the side jump process. (c) Principle of the Spin Hall Effect. (d) Principle of the Inverse Spin Hall Effect. Image from [74].

All these SO-based effects have the consequence of generating a spin current from a charge current. Indeed, when a non-polarized charge current flows in a material, its electrons have a random polarization. The three above mentioned mechanisms will deviate the electrons trajectories according to their spin, thus creating a spin current transverse to the charge current through the Spin Hall Effect [74]. When considering bulk non-magnets, the rotational invariance of the materials constrains the polarization of the produced spin current to be transverse to both the charge and spin current flows [75], so that the spin current $\boldsymbol{j}_s^{SHE}$ with polarization $\boldsymbol{\sigma}$ generated by a charge current $\boldsymbol{j}_c$ can be written:

$$\boldsymbol{j}_s^{SHE} = \theta_{SHE}(\boldsymbol{j_c} \times \boldsymbol{\sigma}) \tag{1.27}$$

where θ_{SHE} is the Spin Hall Angle (SHA), giving the ratio of the produced spin current over the applied charge current. A simplified illustration of the SHE is presented in Fig. 1.4c, in which only one spin polarization is considered. Note that in general, all polarization directions $\boldsymbol{\sigma}$ must be considered, so that $\boldsymbol{j}_s^{SHE}$ should take a tensorial form, as described in the appendix. The SHE possesses a reciprocal effect. A pure spin current of polarization σ is constituted of electrons with opposite spins moving in opposite directions (Fig. 1.4d). The spin dependent scattering processes presented in Fig. 1.4a and Fig. 1.4b will cause these electrons to be deviated in the same direction. As shown in Fig. 1.4d, this creates a charge current both transverse to the spin current flow and spin polarization. This effect is the Inverse Spin Hall Effect (ISHE), described phenomenologicaly by:

$$\boldsymbol{j}_c^{ISHE} = \theta_{SHE}(\boldsymbol{j_s} \times \boldsymbol{\sigma}) \tag{1.28}$$

The SHE is a charge to spin conversion effect, while the ISHE describes a spin to charge conversion. These effects are Onsager reciprocal [76] and therefore quantified by the same figure of merit θ_{SHE}.

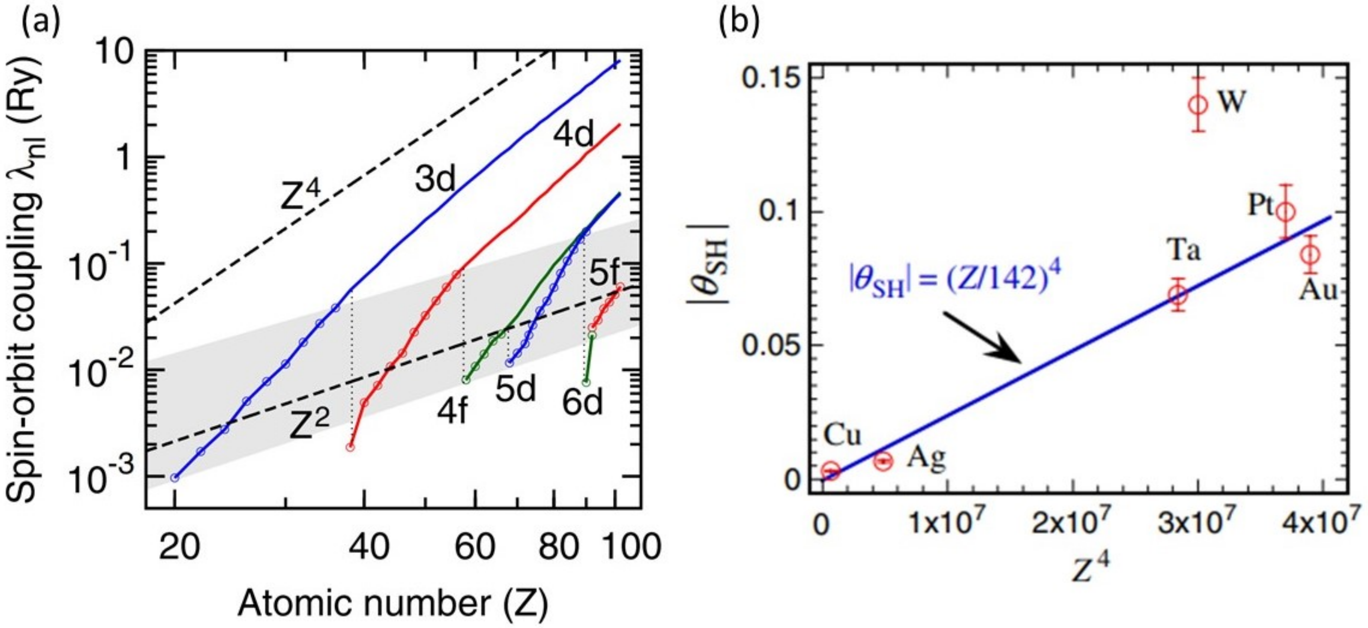

Figure 1.5: (a) Evolution of the spin orbit interaction strength λ versus the atomic number in the different series of the periodic table, from 3d to 5f. Image from Ref. [77]. (b) Spin Hall angle versus the atomic number for some representative materials. Image from Ref. [78].

The SO interaction is the driving force behind the SHE. Its hamiltonian writes $H_{SO} = \lambda \boldsymbol{L} \cdot \boldsymbol{S}$ with $\boldsymbol{L}$ the angular momentum and $\boldsymbol{S}$ the electronic spin. Its scaling factor is $\lambda \propto \partial_r V(r)$ [77] with $V(r)$ the potential created by the atomic nucleus. Consequently, it is expected that $\lambda \propto Z^2$ with Z the atomic number for the electrons of the outer shell. The elements made of atoms from the heavy series will then have a larger SO interaction than the ones from the lighter series. Even though it depends on the resistivity of the material [79, 74] and of details of the orbital filling [38], this is overall expected to lead to a larger spin Hall angle for the heavier than for the lighter elements [78] as shown in Fig. 1.5b. The consequence for the overall research regarding the spin Hall effect has been a strong experimental focus on the heavy elements such as the 4d (Pd [80]) or 5d (Ta [81], W [82], Pt [79], Au [83]) series, or on alloys made of a light matrix with heavy impurities [70, 84, 85] using a variety of FMR-based [86, 87, 46], optical [88] and electrical methods [89]. In these methods, large spin Hall angles of up to 10 % have been observed in Pt, W and Ta. However, this Z^2 dependence of the SO interaction strength is verified only when moving from one series to the other (Fig. 1.5a). The overall increase of the SO interaction with Z also depends on the principal quantum number of the outer electronic shell, so that it is monotonic only inside a series, where it varies roughly as Z^4. Consequently, atoms of the light 3d series can have a SO interactions comparable to the ones of the 5d series (Fig. 1.5a), so that we can expect large spin Hall angles in some light elements. Despite some exceptions [91], the lighter 3d serie has been mostly ignored in spin Hall effect measurements. This is in particular the case for the 3d ferromagnets (Co, Fe and Ni). These materials have been little studied despite the interesting implication of the magnetization induced symmetry breaking on the SHE, and have only recently started to receive theoretical [92, 93, 94] and experimental [95, 96] attention. This question of the spin-Hall effect in light ferromagnetic materials will be discussed in Chapter 3.

The metals discussed in this paragraph, whether they are magnetic or not, have the particularity of matching a very strong symmetry constraint, which is the space reversal symmetry. Indeed, their bulk is invariant by rotation of space, so that their Hamiltonian does not change when performing the transformation $k \to -k$. This has a strong impact on their band structure, since this constrains states with opposite wave vectors to have the same spin expectation values. This is discussed in more details in the next paragraph, where I will also show the effect of the space reversal symmetry breaking on the band structure and spin-charge interconversion properties of some systems studied in this manuscript.

1.3.2 Edelstein effect at Rashba interfaces and in topological surface states

Spin texture at Rashba interfaces and surface of topological insulators

The band structures in solids are strongly constrained by symmetries. Here, we will focus on two of them: the Time Reversal Symmetry (TRS), and the Space Reversal Symmetry (SRS). Their effect on the band structure will be illustrated by considering the eigen-energies $E_{k\sigma}$ of an Hamiltonian, k being the wave vector and $\sigma =\uparrow$ ($\sigma =\downarrow$) the spin. Reversing the time corresponds to the transformation $\sigma \to -\sigma$ and $k \to -k$, so that the TRS imposes $E_{k\sigma} = E_{-k-\sigma}$. Reversing the space, on the other hand, leaves the spin untouched and causes the transformation $k \to -k$ only. This means that the SRS imposes $E_{k\sigma} = E_{-k\sigma}$. Lifting the TRS allows opposite spins with the same wave vector to be non-degenerate, while keeping the SRS imposes the band structure to be symmetric with respect to $k = 0$. This is linked to the apparition of a ferromagnetic order. Here, we will focus on non-magnetic interfaces, where the TRS is conserved, while the SRS is broken. The band structure shown in Fig. 1.6a is then allowed by symmetries, since it has the relation $E_{k_x\sigma} = E_{-k_x-\sigma}$ imposed by the TRS, while $E_{k\sigma} = E_{-k\sigma}$ does not need to hold. Now, I will consider an interface perpendicular to the $\hat{z}$ direction, the k-space of its localized states spam over the plane (k_x, k_y). Due to the SRS breaking, the band structure presented in Fig. 1.6b, with inner and outer Fermi surfaces presenting a spin texture coupled to the momentum with opposite chiralities, is now allowed by symmetries. Such a spin-split band structure has been observed at metallic surfaces and interfaces such as gold ([97] and Fig. 1.6c), Ag/Bi [98] and at metal-insulator interfaces such as Cu/BiO$_x$ [99].

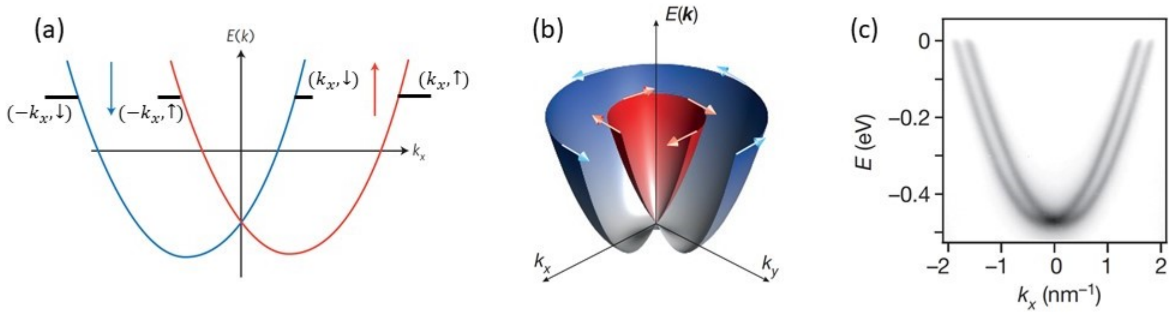

Figure 1.6: (a) Band structure along the X-direction allowed by the space reversal symmetry breaking. The states discussed in the text are given by the black lines. Image modified from Ref. [100]. (b) Band structure with two Fermi contours and opposite spin chiralities allowed by the space reversal symmetry breaking. (c) ARPES measuerement of the bands measured at the surface of Au(111), displaying the two Fermi contours allowed by the space reversal symmetry breaking. Images modified from Ref. [101].

Even though such Rashba-split band structures are allowed by symmetries at interfaces, they cannot be obtained simply by the SRS breaking. A sizeable spin-orbit coupling must indeed be involved to obtain such a splitting. Once this condition is met, a minimal Hamiltonian around $\hat{\boldsymbol{k}} = 0$, which predicts the spin texture due to the Rashba splitting can be written [100]:

$$H_R = \alpha_R \hat{\boldsymbol{\sigma}} \cdot (\hat{\boldsymbol{k}} \times \hat{z}) \tag{1.29}$$

with α_R the Rashba parameter which depends on the SO interactions and on the electric field induced by the symmetry breaking at the interface, $\hat{\boldsymbol{\sigma}}$ the Pauli matrix vector, and $\hat{z}$ the normal to the interface. When added to the kinetic energy part of the Hamiltonian, this Rashba Hamiltonian gives the dispersion relation:

$$E_{\uparrow\downarrow} = \frac{\hbar^2 k^2}{2m^\star} \pm \alpha_R k \tag{1.30}$$

with $m^\star$ the effective mass of the electron, which reproduces well the simple band structure observed with ARPES at the surface of Au (Fig. 1.6c). When considered in the 2D (k_x, k_y) plane of the interface, H_R gives the band structure with spin-momentum locking shown in Fig. 1.6b. In Chapter 4, I will give the physical origin of this spin-momentum locking in the two dimensional electron gas at the surface of $SrTiO_3$. Despite being the most studied systems for the spin-charge interconversion, metal-metal and metal-insulator interfaces are not the only systems in which such a spin texture can be observed. In Chapter 4 of this manuscript, I will present a Rashba interface between two insulating materials, while in Chapter 5, I will present GeTe, a system where the spin-momentum-locked band structure is present in the bulk of the material.

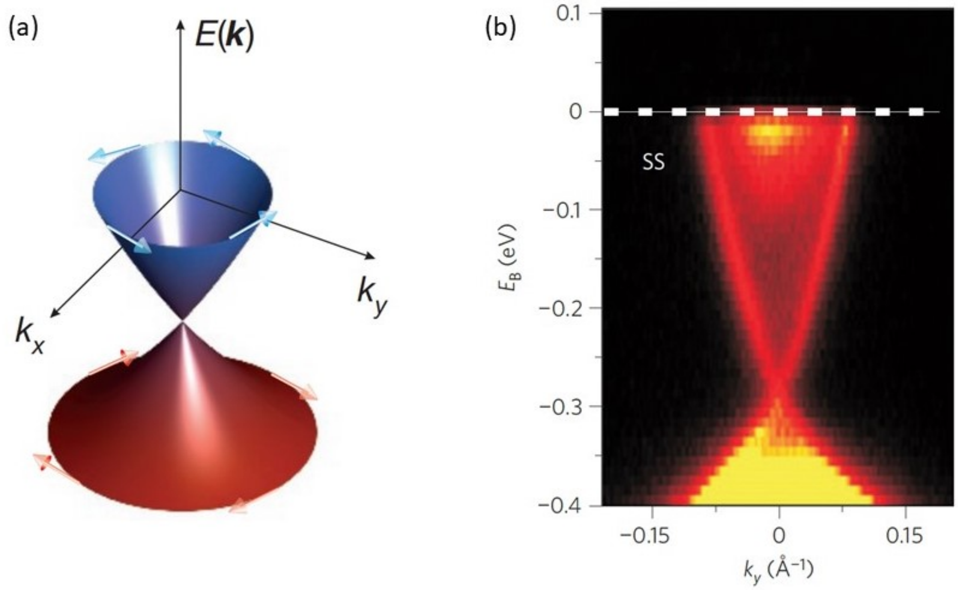

Figure 1.7: (a) Sketch of the Dirac cone of a topological surface state with spin momentum locking. Image from Ref. [101]. (b) ARPES measurement of the topological surface states in Bi_2Se_3. The brighter zones at the top and bottom of the Dirac cone correspond to the bulk conduction and valence bands. Here, the Fermi level lies at the bottom of the conduction band. Image from Ref. [102].

Finally, the phenomenon of spin-momentum locking has also been observed in a different class of materials with different band structures, that of three dimensional topological insulators.

These materials are the subject of an intense interest in spintronics, due to the presence of topologically protected surface states. In these materials, the presence of a strong SO interaction creates an anticrossing between the top of the valence and the bottom of the conduction bands. This leads to the formation of topological states consisting in a gapless Dirac cone (Fig. 1.7) [102, 103]. Importantly for spin-charge interconversion effects, this Dirac cone exhibits a spin momentum locking which allows to perform the spin-charge interconversion. The spintronics activity on these materials have so far mostly been concerned with high quality materials deposited by molecular beam epitaxy such as HgTe [104], Bi_2Se_3 [105], $(Bi_{1-x}Sb_x)_2Te_3$ [106]. In these materials, the interconversion measurements have mainly been performed using FMR-based methods, with some report of electrical potentiometric measurements [107]. More recently, topological insulators deposited on a large scale by magnetron sputtering have displayed high spin to charge interconversion efficiencies [108] at room temperature, even though the structural quality of these materials is still low, with a high number of defects and a poor stochiometry. The challenge of fabricating spin logic devices from high quality materials grown on a large surface by industry compatible processes still needs to be addressed, and will be discussed in Chapter 5 of this manuscript.

The main interest of electron systems with spin momentum locking is their high spin-charge interconversion efficiency when compared to that of metals. This interconversion is due to the spin-momentum locking of the surface states, through the so-called Edelstein Effect that I will describe in the next section.

Edelstein effect at Rashba interfaces and in topological surface states

The charge to spin interconversion has been described by a simple model that assumes the presence of two dimensional bound states at an interface represented by the (x, y) plane, thus constituting a two dimensional electron system [98]. This electron system has one (topological surface states) or several (Rashba interfaces) Fermi contours with spin-momentum locking (Fig. 1.6 and Fig. 1.7). In the following, we assume these Fermi contours to be circular, even though this is not true in general. Similarly to the case of the Spin Hall Effect, the spin-charge interconversion can be a charge to spin (Direct Edelstein Effect) or a spin to charge (Inverse Edelstein Effect) conversion. In the direct Edelstein effect, applying an electric field parallel to the surface shifts the Fermi contours in the reciprocal space (Fig. 1.8a and 1.8b). This causes the appearance of a spin accumulation, with a sign that depends on the Fermi contour chirality. In the case of a Rashba interface with opposite spin chiralities, the inner Fermi contour produces a spin accumulation opposite to the outer one. Since the Fermi wave vectors of these two Fermi contours are different, they host a different number of electronic states. The two dimensional electron system at the Rashba interface then hosts a net spin accumulation (Fig. 1.8a). The case of the topological insulator is similar, but simpler, since it has no inner Fermi contour that counterbalance the spin accumulation created by the shift in the reciprocal space. In the case of the inverse Edelstein effect, a spin current is absorbed by the electronic states at the interface, thus creating a spin accumulation that shifts the Fermi contours accordingly to their spin chirality. In the case of a Rashba interface where the two concentric Fermi contours have opposite spin chiralities, these will be shifted in opposite directions (Fig. 1.8c), leading to the appearance of right and left propagating electronic states. Similarly to the case of the direct Edelstein effect however, the difference in Fermi wave vectors of the two Fermi contours leads to the appearance of a net charge current. The case of the topological surfaces states is similar but with only one Fermi contour. In the rest of this paragraph, I will give more details regarding the Inverse Edelstein Effect (IEE), since it will be experimentally explored in this manuscript.

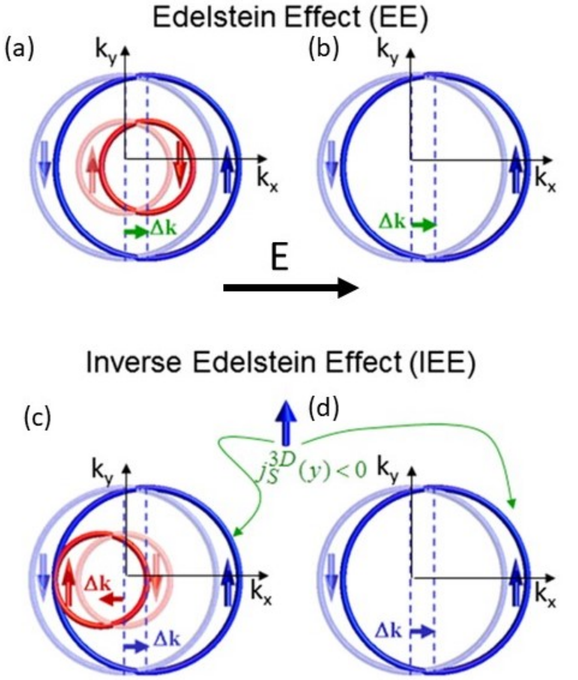

Figure 1.8: (a) and (b) Principle of the Direct Edelstein effect at Rashba interfaces (a) and in the surface states of topological insulators (b). The Fermi contours are shifted by an applied electric field E (black arrow). (b) and (c) Principle of the Inverse Edelstein effect in topological insulators (d) and Rashba interfaces (c). The injection of a $\hat{y}$-polarized spin current creates a chirality dependent shift of the Fermi energies, which in turn generates a charge current at the interface. Image from Ref. [109].

Let us focus on the case of a Rashba interface. When a spin current with polarization $\uparrow$ along the $\hat{y}$ direction is being injected into the 2DEG, the two Fermi surfaces are shifted in opposite directions, in order to accommodate the $\uparrow$-oriented spin accumulation induced in the system. The shifts write $\Delta k_x^{out} = -\Delta k_x^{in} = \Delta k_x$ and, since $k_F^{in} < k_F^{out}$, this causes an excess of electronic states moving to the right in Fig. 1.8c and 1.8d, leading to the apparition of a charge current in the 2DEG. The charge currents produced by the inner and outer Fermi surfaces indeed write $j_{in/out}^c \propto \pm k_F^{in/out} \mu_\uparrow^{in/out}$, so that the total charge current $j_c = j_{in}^c + j_{out}^c$ is non zero. It is related to the spin accumulation $\delta\mu$ injected by the spin current through:

$$j_c = \frac{\epsilon_0}{\tau} \delta\mu \tag{1.31}$$

the spin accumulation being expressed in Volts. τ corresponds to the electronic scattering time into the 2DEG. The spin accumulation produced by the injected spin current j can be evaluated by assuming a momentum-independent transmission of the electronic states into the 2DEG [98]:

$$j_s = \frac{\hbar \epsilon_0}{\tau^2 \alpha_R} \delta\mu \tag{1.32}$$

Here, the spin current density j_s is three dimensional, and is in $\mathrm{A \cdot m^{-2}}$. The link between the injected spin current and detected charge current then writes:

$$j_c = \frac{\alpha_R \tau}{\hbar} j_s = \lambda_{IEE}\, j \tag{1.33}$$

where $\lambda_{IEE} = \alpha_R \tau / \hbar$ is the Inverse Edelstein length, which represents the efficiency of the spin to charge interconversion. The interconversion efficiency in these two systems therefore depends on two main parameters. The first is the Rashba parameter α_R, which controls the amplitude of the splitting between the inner and outer Fermi contours. The second one is the mean scattering time τ, which is linked to the interconversion, as it controls the shift Δk_x of the Fermi contours. This 2D picture is of course very simplistic for metal-metal and metal-insulator interfaces, which necessitate a three dimensional treatment to take into account the charge and spin transport in the directions transverse to the interface [59, 63, 66]. The case of the topological insulator is somehow similar, except that due to the presence of a unique Fermi contour, the Edelstein length simply writes [110]:

$$\lambda_{IEE} = v_F \tau \tag{1.34}$$

with v_F the Fermi velocity of the topological surface states, so that in topological insulators the Edelstein length is equal to the mean free path, because of the carrier backscattering protection provided by the presence of a single Fermi contour.

It is important to note that this picture of the Inverse Edelstein Effect is strongly simplified, and causes an overestimation of the Edelstein length. Indeed, it applies only to the case of an isolated 2DEG, or for topological insulators with a fully insulating bulk, which is not the case in general since the Fermi level lies in the bulk states for most topological insulators Fig. 1.7b [111]. In practice however, the electronic states are coupled to their environment. This is due either to the presence of nearby metallic bulk states Rashba metal-metal and metal-insulator interfaces, and of conductive bulk states for topological insulators, which are present in most of the studied materials [104]. In the case of the insulator-insulator interface discussed in Chapter 4, the 2DEG electronic states are still coupled with the ferromagnetic material used to inject the spin current, which opens a new scattering channel upon tunneling through an insulating interface. All these external scattering events causes a decrease of the Edelstein length in both the case of the topological insulators and Rashba interfaces, where the scattering time τ needs to be replaced by [104, 112]:

$$\tau_{eff} = \frac{\tau}{1 + \frac{2\tau}{\tau_t}} \tag{1.35}$$

with τ_t representing the characteristic time of the electronics states outside of the 2DEG. The modulation of the interconversion through electronic scattering outside of the 2DEG will be discussed in Chapter 4 of this manuscript.

Chapter 2

Electrical measurement of the spin relaxation anisotropy in ferromagnetic materials

When a spin current enters a ferromagnetic material, it relaxes and transfers its angular momentum through different processes depending on the relative orientation of its polarization with the magnetization. If the polarization is collinear with the magnetization, it relaxes through diffusive processes, when electron scatters on impurities with spin orbit coupling, in a process well described by the Valet-Fert model [35]. In this case, the angular momentum is transferred to the lattice and does not affect the magnetization. On the other hand, the component of the polarization which is transverse to the magnetization relaxes on a very short (ballistic) length scale. As seen in the previous chapter, this is associated to the Larmor precession of the conduction electron spins around the strong *s*-*d* exchange field of the ferromagnet [64]. This leads to decoherence, and to the transfer of angular momentum to the magnetization, i.e., to spin transfer torques [60, 61, 113].

This angular momentum transfer to the magnetization plays a central role in spintronics. Indeed, an important part of current research focuses on the possibility to switch magnetization using a spin current, either generated by another ferromagnet (or domain) such as for the Spin Transfer Torque, or by a nearby non-magnet through the Spin Hall effect [70] or Rashba-Edelstein effect for the Spin Orbit Torque [13, 114]. This approach allows measuring the resulting torques, associated to this momentum transfer. The reciprocal process, involving the transfer of an angular momentum from a ferromagnet to another material by either Spin Pumping Ferromagnetic Resonance [115] or by Spin Seebeck Effect [116] provides ways to access the spin transport [117] and spin-charge interconversion properties [87, 118]. This makes the understanding of these non-collinear spin current relaxation processes fundamental in spintronics, both from an applied and fundamental perspectives.

So far, most of the methods aiming at evaluating the transfer of a transverse spin current to the magnetization have relied on radio frequency based methods [86, 119]. Despite their apparent simplicity, these methods face several spurious mechanisms such as the presence of microwave dephasing in broadband FMR experiments [120] and two-magnon scattering [57]. They are also not able to access the transverse spin current relaxation parameters at interfaces between FMs and materials with low spin relaxation efficiency such as copper due to important spin backflow effects [121]. Furthermore, it is not possible using these methods to perform a comparison between the efficiencies of the collinear and transverse processes, making them unable to benchmark these results with the important literature existing on the spin current relaxation through diffusive processes [67, 74, 83, 122, 123]. This final limitation would cause them to miss several interfacial effects such as spin memory loss [124, 55] and interfaces resistance [125], crucial for the transfer of angular momentum across the interface between the ferromagnet and the non-magnet [56, 126, 127].

In this chapter, I will present a measurement method based on lateral spin valves for the measurement of spin current relaxation into a ferromagnet, with a magnetization transverse to the spin current polarization. I will first describe the working principle of these lateral spin valves, that involve in their simplest form only the collinear spin transport. The characterization of the diffusive spin transport process will then be described, with the extraction of associated parameters (polarization β, spin diffusion length l_{sf} and resistivity ρ). Finally, I will show how we performed the measurement of the spin mixing conductance, which controls the transfer of angular momentum from the spin current to the magnetization (see section 1.2 of Chapter 1), at the interface between Cu and 3d ferromagnetic materials.

2.1 Spin transport using lateral spin valves

Lateral spin valves are devices which allow to produce and detect a pure spin current using d.c. electrical measurements. As such, they have been an important tool for the study of spin current, both from the point of view of spin transport and interconversion characterization. In this chapter, they will be used only for spin transport characterization measurements, while we will see how they can be used for interconversion measurements in the next chapter. The results presented in this section are a summary of two studies published in Physical Review B, for which I contributed by making measurements [67], or data analysis with Finite Element simulations [33].

2.1.1 A device for the study of pure spin current effects

Spin transport measurements in a lateral spin valve: Lateral Spin valves (LSVs) are made of two ferromagnetic electrodes bridged by a non-magnetic channel (Fig. 2.1a). One of these electrodes is used to inject the spin current and is called the injector, while the other is used to probe the spin current density and is called the detector (reversing the role of the two electrodes leads to the exact same signals). The pure spin current is generated in the channel by flowing a charge current between the injector and one end of the channel (Fig. 2.1b). As seen in section 1.1.3 of Chapter 1, this has the effect of creating a spin accumulation at the interface between the channel and the injector, with a polarization along the injector magnetization. The generated spin accumulation will then diffuse along the channel, toward the detector, as illustrated by the iso-surfaces represented in Fig. 2.1c. This gradient of spin accumulation will produce a spin current in the channel. As evidenced in Fig. 2.1b, the charge and spin currents are not present in the same regions of the device, so that lateral spin valve generates a pure spin current. The produced spin accumulation and spin current relaxe over the spin diffusion length in the copper channel. According to eq. 1.6, the charge current writes as the gradient of an electric-like potential $V = \mu_m + \beta\mu$, β being the polarization of the detector. For simplicity, we assume a transparent interface so that μ_m and μ are continuous across the interface. Since the polarization is zero in the copper channel, V is therefore not continuous. Indeed, denoting $V_{FM(NM)}$ the electric-like potential at the detector (channel) side of the interface, the potential drop across the interface is:

$$V_s = V_{FM} - V_{NM} = \beta\mu_{|detector} \tag{2.1}$$

with $\mu_{|detector}$ the spin accumulation at the interface between the channel and the detector. The sign of the spin accumulation reverses when reversing the magnetization of the injector, while the sign of the polarization changes when reversing the magnetization of the detector. This means that the potential drop changes sign when reversing the relative orientation between the spin current polarization and the magnetization direction. In practice, this corresponds to a change in the relative orientation of the magnetization directions of the two electrodes when going from the parallel (P) to the antiparallel (AP) configuration. In real devices however, the potential drop V_s does not change sign when going from the P to the AP configuration, because of thermal and geometrical effects that create a temperature dependent baseline superimposed to V_s [128], which only vanishes at low temperature. The spin accumulation is therefore probed by measuring V_s in the parallel ($V_s(P)$ and antiparallel ($V_s(AP)$) configurations, and is given by the spin signal:

$$\Delta R = \frac{V_s(P) - V_s(AP)}{I_c} = \frac{2\beta\mu_{|detector}}{I_c} \tag{2.2}$$

with I_c the bias charge current flowing from the injector to the channel. The P and AP configurations of the electrodes are accessed by sweeping a magnetic field in their easy magnetization axis. As the electrodes are designed to have different switching fields, one can access the two configurations and deduce the spin signal ΔR as described in Fig. 2.2a.

The value of the spin signal can be evaluated in a simple way using a one dimensional model, assuming (i) a uniform spin accumulation at the interface between the channel and the electrodes, and (ii) a uniform spin accumulation on the thickness of the channel, outside of the spin injection and detection zones. As shown in Fig. 2.1c, this assumption holds for the dimensions of the devices discussed in this section. In this framework, the spin signal writes when assuming in addition that the interfaces between the electrodes are transparent [33]:

$$\Delta R = \frac{4R_N(\beta R_F)^2}{(R_N + 2R_F)^2 e^{L/l_{sf}^N} - R_N^2 e^{-L/l_s f^N}} \tag{2.3}$$

with β the polarization of the ferromagnetic electrodes, L the distance between the electrodes, $l_{sf}^{N(F)}$ the spin diffusion length of the FMs (F) and of the channel (N), and $\rho_{N(F)}$ their resistivities. By defining the sections $A_N = W_N \times t_N$ and $A_F = w_F \times w_N$, one can write $R_N = \rho_N l_{sf}^N / A_N$ and $R_F = \rho_F l_{sf}^F / A_F(1 - \beta^2)$.

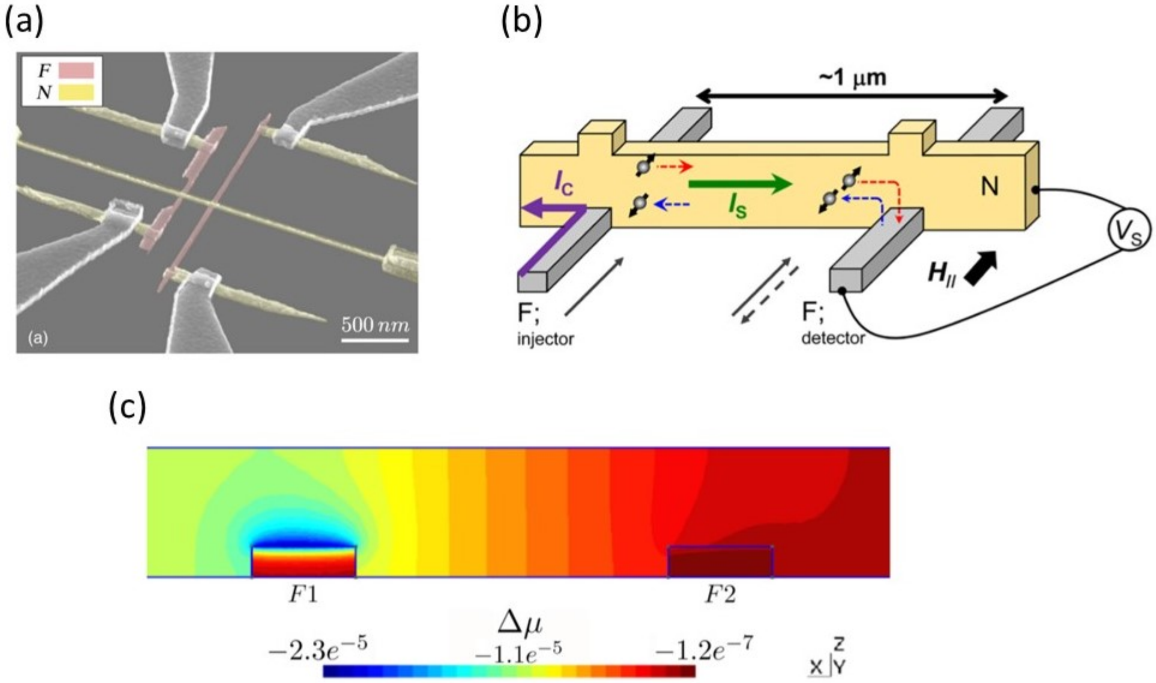

Figure 2.1: (a) Scanning Electron Microscopy (SEM) image of a lateral spin valve with the FM in red and the NM in yellow. (b) Working principle of a LSV. The charge current (in purple) injected between the Cu channel and the FM injector produces a pure spin current (in green) that flows in the Cu channel and relaxes in the detector, creating a potential drop between it and the channel. (c) Map of the spin accumulation obtained by FEM simulations. The spin accumulation profile is homogeneous in the channel thickness and at its interfaces with the electrodes, this homogeneity validates the 1D model used to describe this device.

In equation 2.3, the polarization of the ferromagnetic electrode sets the amplitude of the measured signal, while the spin diffusion length of the channel can be extracted through the signal dependence with the distance between electrodes. In the following paragraph, which is a shortened version of a study we published in Physical Review B [33], we will extract these two quantities by varying the geometry of the device.

2.1.2 Measurement of the spin diffusion length in Cu, Al and Au

The devices used for the measurement of the spin diffusion length of the channel material were fabricated using a multilevel electron-beam lithography process. The ferromagnetic 50 nm wide and 15 nm thick Py electrodes were deposited in a first step, followed by that of a 50 nm wide and 80 nm thick Cu channel in a second step. The distance between the electrodes was varied from 150 nm to 1 μm to study the change in spin signal associated with the spin current relaxation. Microscopic Ti(5 nm)/Au(100 nm) contact electrodes are used to connect the device to the measurement system.

The measurement of the spin signals have been carried out at 300K and 77K using a standard lock-in technique with a 79 Hz and 100 μA bias current. The spin signals obtained using the procedure described in Fig. 2.2a, for the devices with different distances L between the electrodes are reported in Fig. 2.2b. As expected from eq. 2.3, the spin signal decreases exponentially when increasing the distance between the electrodes. After measuring electrically the resistivities of Cu and NiFe in nanowires, and using literature spin diffusion length values of the spin for Py [122, 129, 67], only two parameters remain unknown: β and l_{sf}^{Cu}. These two parameters can be extracted independently from the ΔR evolution presented in Fig. 2.2b, as β controls the maximum amplitude of the spin signal and l_{sf}^{Cu} its exponential decrease.

Additionally, in order to check the relevance of the 1D model in this non-strictly 1D geometry, we reproduce the experimental data using the FEM simulations described in the appendix. The calculated values are shown in table 2.1, and are in very good agreement with the 1D model when taking some very minor corrections to extracted β and l_{sf}^{Cu} values.

A similar procedure has been used for the extraction of the FM polarization and of the NM spin diffusion length for channels made of Al and Au. The results are given in table 2.1 at room temperature and 77 K. The extracted data matches well with the existing literature on this type of devices [83, 39, 129], with a larger spin diffusion length for Al, followed by those of Cu and Au. Furthermore, it is worth noting that the polarization of Py is found to depend on the material constituting the NM channel. This is most likely because, as discussed in section 1.1.3, the interface is in general not transparent, and the measured polarization is an effective one taking into account the Py/NM interface polarization, SML and interface resistance [130, 56]. In any case, these effective parameters are sufficient to estimate the spin current injected in LSV channels, and will be used throughout the rest of this chapter.

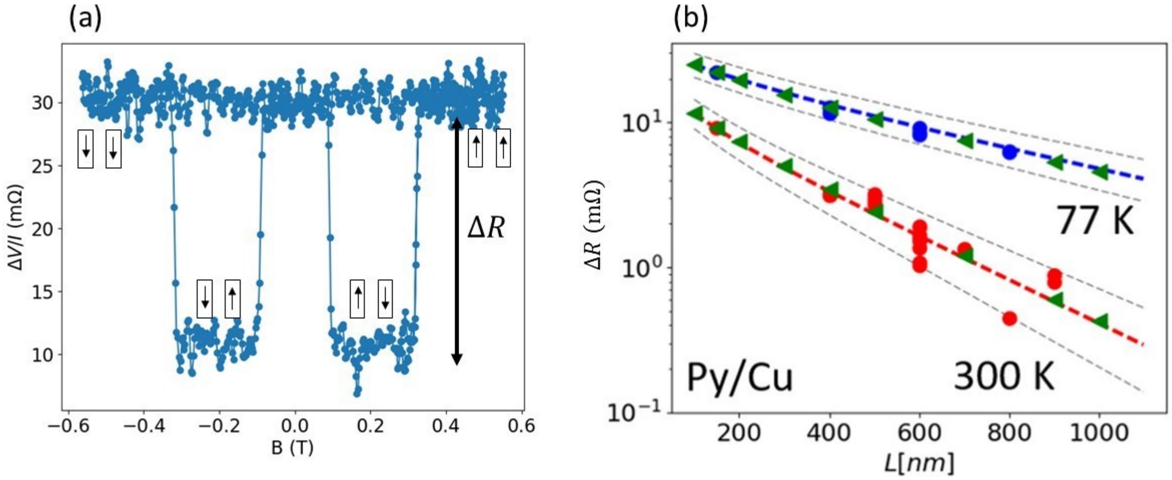

Figure 2.2: (a) Typical shape of the non-local signal, obtained at room temperature in a lateral spin valve with a copper channel and CoFe electrodes. The rectangles represent the injecting and detecting electrodes and the arrows their magnetization direction. At high magnetic field, the two magnetizations are aligned. Upon decreasing the magnetic field toward negative values, the magnetization of the electrode with the lower coercive field switches. The electrode magnetizations are then in an antiparallel configuration. At lower magnetic field, the magnetization of the electrode with the larger coercive field switches as well, so that the magnetizations come back in a parallel configuration. A similar behavior is observed upon increasing the magnetic field. The difference between the two configurations is the spin signal ΔR. (b) Evolution of the spin signal when increasing the distance between Py electrodes separated by a copper channel, while keeping all other geometrical parameters constant. The dotted lines correspond to a fit using the 1D analytical modelling, while the green triangles are the results of FEM calculations using the parameters given by the analytical fit.

Material	β	l_{sf} (nm)	ρ ($\Omega\cdot$ nm)	T (K)
Py/Al	0.22 ± 0.01	450 ± 90	30	300
	0.32 ± 0.01	110 ± 30	15	77
Py/Cu	0.22 ± 0.01	300 ± 60	35	300
	0.31 ± 0.03	900 ± 80	25	77
Py/Au	0.26 ± 0.01	140 ± 30	27 ± 3	77

Table 2.1: Extracted effective polarization β at the interface between Py and Al, Cu and Au and collinear spin transport parameter in Al, Cu and Au.

Additionally, this work exemplifies the limitations of the 1D model validity. The essential parameter is the comparison between the spin diffusion length and the characteristic sizes of the device sections: the spin diffusion lengths must allow the spin accumulation to be homogeneous across each contact section to ensure the validity of the modelisation by a punctual contact. This issue will be discussed in more detail in the following section, corresponding to a study published in Physical Review B [67].

2.1.3 Spin diffusion length and polarization in 3d ferromagnets

The main ferromagnetic materials used for spintronics devices are Co, CoFe and Py. These materials are also those used for spin injection in lateral spin valves. The knowledge of their spin diffusion length and polarization is central to the characterization of the spin current formed in lateral spin valves. Furthermore, in the context of our study of the spin transport anisotropy, a proper characterization of the collinear spin transport properties in ferromagnetic materials provides a useful reference for the measurement of non-collinear spin transport parameters such as the spin mixing conductance.

In the previous section, we showed how to calibrate the spin injection in a LSV by measuring the spin signal evolution when increasing the distance between the injector and the detector. This methods work well for materials with large spin diffusion lengths, but is not applicable for short l_{sf} (less than 50 nm) due to limitations in the e-beam lithography techniques [74]. As 3d ferromagnetic materials have spin diffusion lengths smaller than 50 nm, another technique is needed to extract this parameter. Here, we used the spin absorption technique in lateral spin valves [122]. This method relies on the use of an additional relaxation channel in the LSV, made by adding an absorbing wire made of the studied material in-between the electrodes (Fig. 2.3a and 2.3b). This extra wire will absorb a part of the spin current that flows into the channel, reducing the amount of spin current that reaches the detector, and therefore decreases the spin signal (Fig. 2.4d).

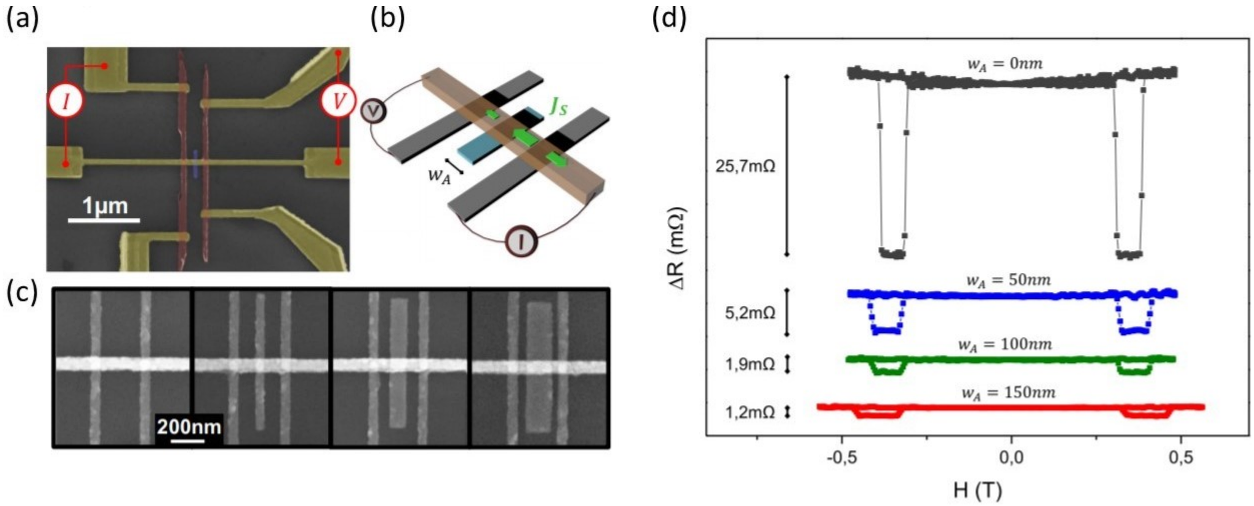

Figure 2.3: (a) SEM image of a lateral spin valve with a CoFe absorbing wire between the two electrodes. (b) Schematic of the device with the measurement configuration used for the spin absorption measurements. (c) SEM image of the reference LSV without absorber, and of LSVs with absorbers of increasing widths used to study the decrease of spin signals presented in (d).

We used this method to extract the polarization and spin diffusion lengths of 3d ferromagnetic materials. note that this method can also be used to study non magnetic materials with small spin diffusion length, for example with large spin-orbit coupling. The lateral spin valves were made using the method described in the previous section. The only difference is that now, the ferromagnetic electrodes used for the spin current injection and detection are not only made of Py, but can also consists of Co or CoFe wires. A requirement of this technique is that the same material should be used for the electrode and the absorber. This indeed allows to deconvolute in the spin resistance of the studied FMs the role of the spin polarization and spin diffusion length. The sample used for the measurement and the spin signals obtained for a CoFe absorber are displayed in Fig. 2.3c. The insertion of a 50 nm absorbing wire has the effect of strongly decreasing the spin signal. It is then further decreased by an increase of the width of the absorber as shown in Fig. 2.3d. These experiments clearly show that, contrarily to what has been done for most spin-absorption experiments so far [74], the above-described 1D model cannot be used directly, as it gives a spin diffusion length that depends on the width of the absorber as shown in ref. [123]. Indeed, while the 1D model correctly takes into account the volume of relaxation it does not take into account the finite width of the absorber. As discussed in the previous section, this 1D model assumes a homogeneous spin accumulation at each interface, which is not the case here for the interface between the channel and the absorber in presence of a strong absorption, as it will be discussed below.

A way to solve the issue of the non-uniform spin accumulation is to define locally the boundary conditions for the spin current relaxation at the interface between the copper channel and the absorber. The expression of the spin current j_s^z that flows vertically toward the absorber is:

$$j_s^z(x) = G_s \mu(x) \tag{2.4}$$

In which $\mu(x)$ is the spin accumulation at the interface between the spin current and the absorber. This quantity depends on its position along the absorber (x-axis). The spin relaxation at the interface between the channel and the absorber is controlled by the effective spin conductance $G_s = (1/G_{abs} + 1/G_{int})^{-1} + G_{SML}$. The terms G_{int} and G_{SML}

have been defined in section 1.1.3, and $G_{abs} = (1-\beta_A^2)\tanh(t_A/l^A_{sf})/\rho_A l^A_{sf}$ corresponds to the spin conductance of the absorber (which is simply the inverse of the spin resistance defined in paragraph 1.2), responsible for the bulk spin current relaxation effects. For simplicity, we neglect the spin memory loss term ($G_{SML} = 0$), and consider that the interface between the channel and the absorber is transparent ($G_{int} \gg G_{abs}$), so that $G_s = G_{abs}$ and only bulk effects contribute to the spin current relaxation.

This additional boundary condition results in a correction of the spin diffusion length of copper, where the absorber lays underneath the channel (Fig. 2.4a). This region can therefore be treated as a new material with a spin relaxation in parallel in the Cu channel and in the absorber. Its resistivity is ρ_{Cu} and it has a spin diffusion length given by [123]:

$$l^{\star}_{sf} = \frac{l^{Cu}_{sf}}{\sqrt{1 + G_s \frac{\rho_N (l^{Cu}_{sf})^2}{t_N}}} \tag{2.5}$$

The resulting effective system is displayed in Fig. 2.4a. As the spin accumulation is now homogeneous at the interface between the copper channel without absorber underneath, and in the newly effective material, it becomes possible to use a 1D model. This allows computing an analytical expression for the spin signal, similar to eq. 2.3, with additional terms originating from the absorber presence [123]. This expression allows fitting the experimental results, as illustrated in Fig. 2.4b for a CoFe absorber with CoFe injecting electrodes, β_{CoFe} and l^{CoFe}_{sf} being the fitting parameters. This expression allows to reproduce the exponential decrease of spin accumulation above the absorber due to the spin sink. Note that the direct application of the 1D model without definition of an effective spin diffusion length would produce a decrease at a much smaller rate, inversely proportional to the width of the absorber as can be seen from the definition of the spin resistance. As mentioned above, the use of the same material for the absorber and the ferromagnetic electrodes allows disentangling the spin polarization and spin diffusion length from the spin resistance of the FM material. Indeed, this reduces the number of material parameter, but also reveals differently the respective roles of the spin diffusion length and polarization. The relaxation of the spin current in the absorber is controlled by the global parameter G_{abs}, entangling β_A and l^A_{sf}. The amplitude of the spin signal without absorber, on the other hand, depends on $G_{abs} = 1/R_F$ (eq. 2.3), but also in a separate way of β_A. The data points displayed in Fig. 2.4b illustrate how to separate the extraction of the spin diffusion length and polarization of the FM electrodes. The slope of the absorption over the absorber width depends more on the spin diffusion length of the FM, while its amplitude depends more on its polarization. The results obtained for the studied 3d FMs are given in table 2.2. I also added the spin diffusion length of Pt that we measured using the same method [67], as this material will we be used as a reference in Chapters 4 and 5 of this manuscript. From these results, the effective spin diffusion length $l^{\star}_{sf}$ can be estimated and is of the order of 30 nm for the studied material. This means that the 1D model, using a point contact for the junction between the channel and the absorber, is as expected unable to describe this kind of spin absorption experiments. As the width of the absorber (50 to 150 nm) is larger than the effective spin diffusion length, this does not permit the presence of an homogeneous spin accumulation at the interface between the absorber and the channel. Finally, it is important to keep in mind that the non-zero interface resistance and SML could play a significant role in these results [124, 56]. We will however see later that both the interface resistance and SML can be deemed as negligible at Cu/3d-FMs interfaces.

Material	ρ (Ω·nm)	β	l_{sf} (nm)	T (K)
CoFe	200 ± 13	0.48 ± 0.02	6.2 ± 0.5	300
	150 ± 9	0.48 ± 0.03	8.3 ± 1	10
NiFe	300 ± 30	0.22 ± 0.05	5.2 ± 1	300
	220 ± 12	0.4 ± 0.1	5.8 ± 1	10
Co	250 ± 24	0.17 ± 0.05	7.7 ± 2	300
	150 ± 16	0.18 ± 0.09	12.3 ± 3	10
Pt	180 ± 7	/	3.8 ± 0.5	300
	130 ± 4	/	4.8 ± 0.5	10

Table 2.2: Extracted diffusive spin transport parameters in CoFe, Co, NiFe and Pt at room temperature and 10 K, using spin absorption in lateral spin valves.

As described in the section 1.1.1 of the first chapter, the spin relaxation processes described in this section are driven by spin-orbit coupling trough diffusive processes. In the next section, we will explore experimentally a situation in which the spin current relaxation is due to ballistic processes related the exchange coupling in ferromagnetic materials.

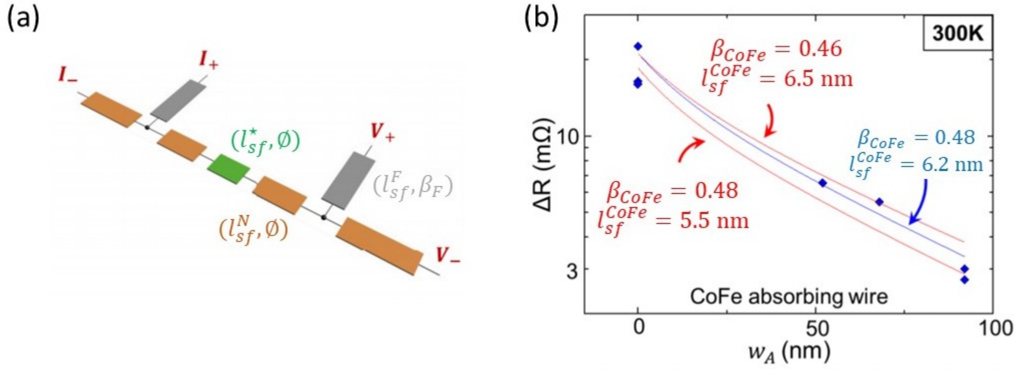

Figure 2.4: (a) Sketch of the equivalent device obtained when using the analysis of the spin absorption experiment described in section 2.1.3. The section of the channel on top of the absorber is now described by a material with an effective spin diffusion length given by eq. 2.5. (b) Evolution of the spin signal when increasing the width of the CoFe absorber. The blue lines represent fits from the model described in section 2.1.3. This procedure allowed for the extraction of the parameters reported in table 2.2

2.2 Non-collinear spin transport in ferromagnetic materials

In the section 2.1 of the first chapter, I described the relaxation of a spin current flowing in a ferromagnet with a magnetization transverse to its polarization. These relaxation processes are due to the spin rotation and dephasing around the exchange field, and are expected to take place on a much shorter length scale than the diffusive relaxation processes, at least in high Curie temperature ferromagnetic materials such as CoFe, Co and NiFe [64]. In section 2.2 of Chapter 1, I showed that in the case where the thickness of the ferromagnet is much larger than the transverse spin relaxation length, the relevant parameter for the estimation of the non-collinear spin relaxation is the spin mixing conductance $G_{\uparrow\downarrow}$. In the present section, I will describe a design of lateral spin valve which allows the exploration of non-collinear spin current relaxation processes. I will then show how we measured experimentally the spin relaxation anisotropy in 3d ferromagnets, before extracting the spin mixing conductance at the interface between Cu and Co, CoFe and NiFe.

2.2.1 Observation of the spin relaxation anisotropy in 3d ferromagnets

The spin relaxation lengths for the non-collinear spin relaxation processes are even smaller than the spin diffusion lengths in ferromagnetic materials. This means that a spin absorption method will have to be used, similarly to the case of the spin diffusion length method extraction presented previously. The method presented in the paragraph 1.3 of this chapter is however not directly applicable. Indeed, according to eq. 1.18, the polarization of the spin current created by flowing a charge current at the interface between a ferromagnet and a non-magnet is along the magnetization direction. The easy magnetization axis of the absorbing wire used in the device presented in Fig. 2.3 is along the one of the injection electrode. This means that its magnetization is always along the polarization of the spin current, so that only the relaxation of a spin current with a polarization collinear with the magnetization can be probed using this device geometry. The difficulty in observing the non-collinear relaxation processes in lateral spin valves has thus been a long-standing issue. Different methods have been proposed to measure it, with modified injecting electrode designed to change the spin current polarization [69], or by using the Hanle effect to rotate the spin current polarization around an external magnetic field during its diffusion into the non-magnetic channel [131, 132]. The issues with these methods are a limited control over the spin current polarization direction, due to the complex geometry of the ferromagnetic electrodes in Ref. [69], and to a large increase of fitting parameters in ref. [131, 132]. It is also not possible using this method to observe directly the difference in relaxation efficiency between the collinear and non-collinear situations. Alternatively, methods such as the Spin Hall Magnetoresistance [133] rely on the anisotropy of the spin current relaxation in a ferromagnet. However, the need for a spin-charge interconversion material strongly complexifies the analysis, while the presence of a charge current flowing in the active part of the device generates strong parasitic signals unrelated to the spin current transport [134]. Finally, the main method used for the measurement of the non-collinear spin transport parameters are FMR based methods such as spin-pumping [135], however without possibility to compare the spin relaxation efficiency in the collinear and non-collinear situations, and strong spin-backflow effects which make impossible the measurement of the spin mixing conductance at the interface between 3d-ferromagnets and low spin conductance materials such as copper. Indeed the effective spin conductance measured using these methods includes the spin back flow, without any possibility to estimate it separately.

Here, in order to overcome these limitations, we used a modified design of lateral spin valve for spin absorption presented in Fig. 2.5a. Here, the absorbing wire has been replaced by a nanodisk-shaped absorber. Thanks to the absence of shape anisotropy, the magnetization of the absorber can then be rotated in the plane of the device using a very weak external magnetic field, that leaves the magnetization of the injecting electrode, and therefore the polarization of the spin current, unmodified. Furthermore, this geometry allows for the measurement of the spin current relaxation for a magnetization both collinear and transverse to the spin current polarization. It is then possible (i) to observe electrically the spin relaxation anisotropy and (ii) to calibrate on a single device the measured spin-mixing conductance with the spin conductance measured in the first section of this chapter.

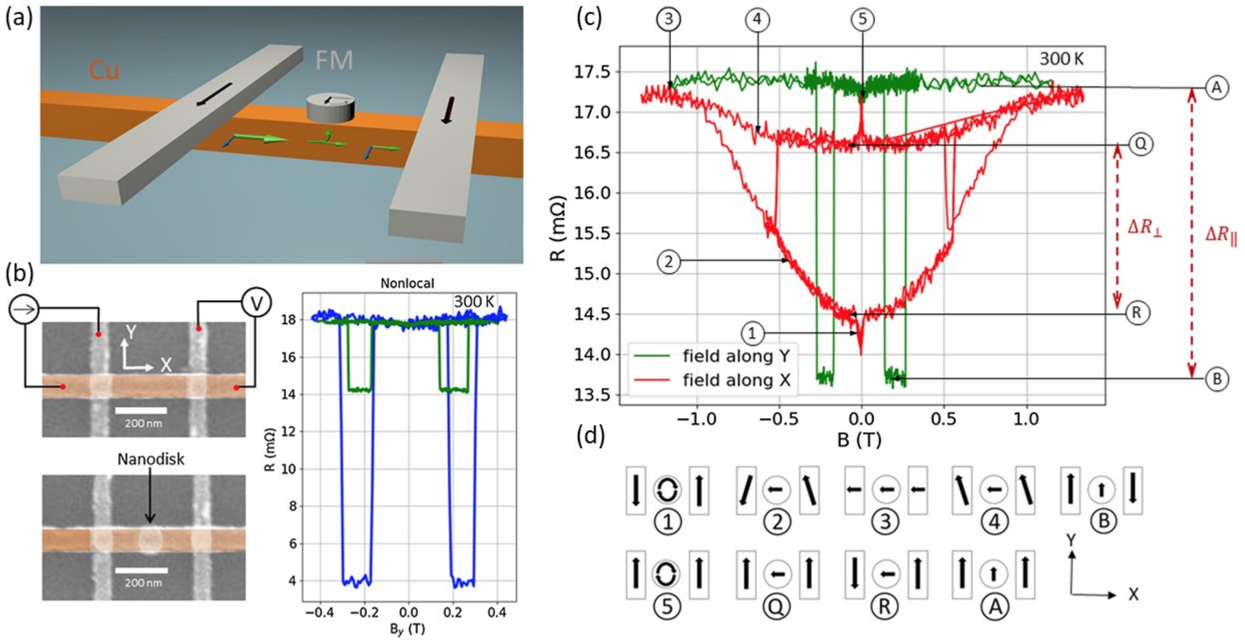

Figure 2.5: (a) Magnetization (black and grey arrows) and spin current (green arrows) in the LSV, with the Cu in orange and the ferromagnetic material in grey. The blue arrows correspond to the polarization of the spin current. The two perpendicular arrows on this absorber indicate two possible magnetization orientations, collinear or transverse to the injected spins. (b) Colored scanning electron microscopy (SEM) image of a reference LSV (top), i.e., without absorber, and with the absorber (below). The orange part corresponds to the Cu channel, and the grey one to the ferromagnetic electrodes. The associated spin signal shows the strength of the spin relaxation by the absorber in the collinear configuration, e.g. with a magnetic field along the Y direction (green versus blue curves, for absorber versus reference signals respectively). (c) Nonlocal measurement of the LSV with a Py absorber when applying a magnetic field along the Y (green) and X axis (red). (d) Magnetic configurations of the injector, absorber, and detector.

The lateral spin valves presented in this study have been fabricated in a process similar to that which was presented in section 1 of this chapter. The first step is the deposition of the nanodisk-shaped made of CoFe, NiFe or CoFe. Then, the CoFe injecting and detecting electrode were deposited. Finally, the Cu channel was added on top of the electrodes, after cleaning the interfaces with Ion Beam Etching. The most difficult part is to target overlay alignment better than 10 nm in the device fabrication. Indeed the Cu channel should be placed exactly on top of the nanodisk. As the dimension of the channel that we use is around 50-80 nm, the realignement between the dot and channel fabrication levels requires a precision better than 10 nm. This is made possible by precisely locate the alignment marks present on the substrate when performing the electron beam lithography steps, and to recalibrate for each device the deflexion of the electron beam. The measurement of the non-local signal was carried out using standard low frequency a.c. lock-in techniques, with a bias current of 300 μA.

The ability of the nanodisk-shaped absorber to relax the spin current flowing in the channel was first checked by comparing the spin signal obtained in a reference lateral spin valve, with a 300 nm gap between the electrodes to that of a lateral spin valve with the same geometry, except for the insertion of a 80 nm of diameter absorber between the electrodes (Fig. 2.5b). The spin signal is reduced by 70 to 80% (Fig. 2.5b), in good agreement with previous studies (section 2.1.3). This proves the good transparency of the interface between the Cu channel and the nanodisk, which allows a large part of the spin current to flow into the absorber. In order to measure the spin absorption anisotropy, we swept a magnetic field along the X and Y direction described in Fig. 2.5b. The X direction corresponds to a direction transverse to the electrodes easy magnetization axis, while Y refers to the collinear direction. The measurements acquired for magnetic fields applied along these two directions are shown in Fig. 2.5c. At zero field, the nanodisk magnetization is in a vortex states, as expected from OOMF simulations [136], and as confirmed by the low field peaks observed on the cycle obtained for a field along the x-axis (Fig. 2.5d). At a magnetic field of 0.1 T, the magnetization of the nanodisk saturates in the direction of the field, while the magnetization of the injecting and detecting electrodes is left unchanged. When the magnetic field is along Y, the parallel and antiparallel configurations of the two electrodes can easily be reached as described in section 2.1.2, corresponding to the magnetic states A and B in Fig. 2.5d. For a field along the X-direction, the magnetization of the electrodes progressively rotates toward X, with a saturation at 1 T, where the non-local signal equals the value obtained for the field along the Y direction. The parallel and antiparallel configurations for an absorber magnetization along the X direction are accessed by taking advantage of the slight misalignment of the field with the X-direction, which allows for a high field switching of the electrodes (see Ref. [137] for details on the measurement sequence). The parallel and antiparallel states then correspond to the low field states Q and R of Fig. 2.5d, in which the magnetization of the nanodisk is saturated, but the electrodes magnetization are along their easy magnetization axis. The spin signals in the transverse and collinear configurations then correspond respectively to the difference of the non-local resistances between states Q - R and A - B, so that the *transverse* spin signal writes $\Delta R_{\perp} = R_Q - R_R$ and the *collinear* spin signal is $\Delta R_{||} = R_A - R_B$.

The change in the absorber magnetization orientation results in a large modulation of the spin signal, by about $(\Delta R_{||} - \Delta R_{\perp})/\Delta R_{||} \sim 40$ % (Fig. 2.6a). A similar measurement sequence was reproduced on several devices and different nanodisks made of CoFe, Co and NiFe. The contrast between the transverse and collinear spin signals remain of the same order of magnitude, with always a more efficient spin current relaxation in the transverse configuration (Fig. 2.6b). Importantly, the results remain the same at low and high temperature, ruling out the contributions of thermal magnons, and we controlled that these results could not originate from a Hanle effect (more details in Ref. [137]) due to the stray field generated by the nanodisk, or to the externally applied magnetic field.

This variation of spin signal between the transverse and collinear configurations is a clear manifestation of the spin absorption anisotropy in ferromagnets. For all the studied ferromagnetic materials, we systematically find the absorption to be more efficient in the transverse configuration. This means that the spin current relaxation is more efficient when due to spin rotation around the exchange field of CoFe, NiFe and Co. In the next paragraph, I will describe more quantitatively these effects by extracting the spin mixing conductance at the interface between Cu and CoFe, NiFe and Co.

2.2.2 Measurement of the spin mixing conductance at the Cu/3d-FM interface

We analyzed our results by using a method combining analytical calculations and numerical simulations. This is a generalization by Henri Jaffrès of his previous work [138], that describes the multicontact magnetoresistance obtained in LSVs in a pure collinear magnetic configurations. Here, the model describes the absorber as a collection of multiple ferromagnetic contacts to the Cu channel, as already illustrated in ref. [123], but also taking into account the most general non-collinear magnetic configuration. For each contact, the three components of the spin polarization are intertwined through a local rotation of the frame attached to each contact. This allows to fully describe the spin current evolution by taking into account the spin relaxation through the spin conductance and real part of the spin mixing conductance, and the spin rotation through its imaginary part (eq. 1.24). The main novelty of this approach when compared to previous modelling [139, 140] lies in the possibility to take into account both the collinear and non-collinear spin relaxation effects, for an arbitrary direction of the spin current polarization with respect to the magnetization. It is then possible to reproduce the experimental measurement of the non-local signal evolution Fig. 2.6b and 2.6d. The details of the calculation will not be described in this manuscript, but the interested reader can refer to the supplementary information of ref. [137] for more information. Here, I will illustrate the results of this model, and compare them in Fig. 2.7 with those of finite element simulations. In this figure, the magnetization of the injecting electrode is along the $\hat{y}$-axis, and the absorber magnetization is along the $\hat{x}$-axis. The injection of a bias charge current through the detector then creates a spin accumulation along the $\hat{y}$ direction, which diffuses into the channel Fig. 2.7b. This creates a spin current that

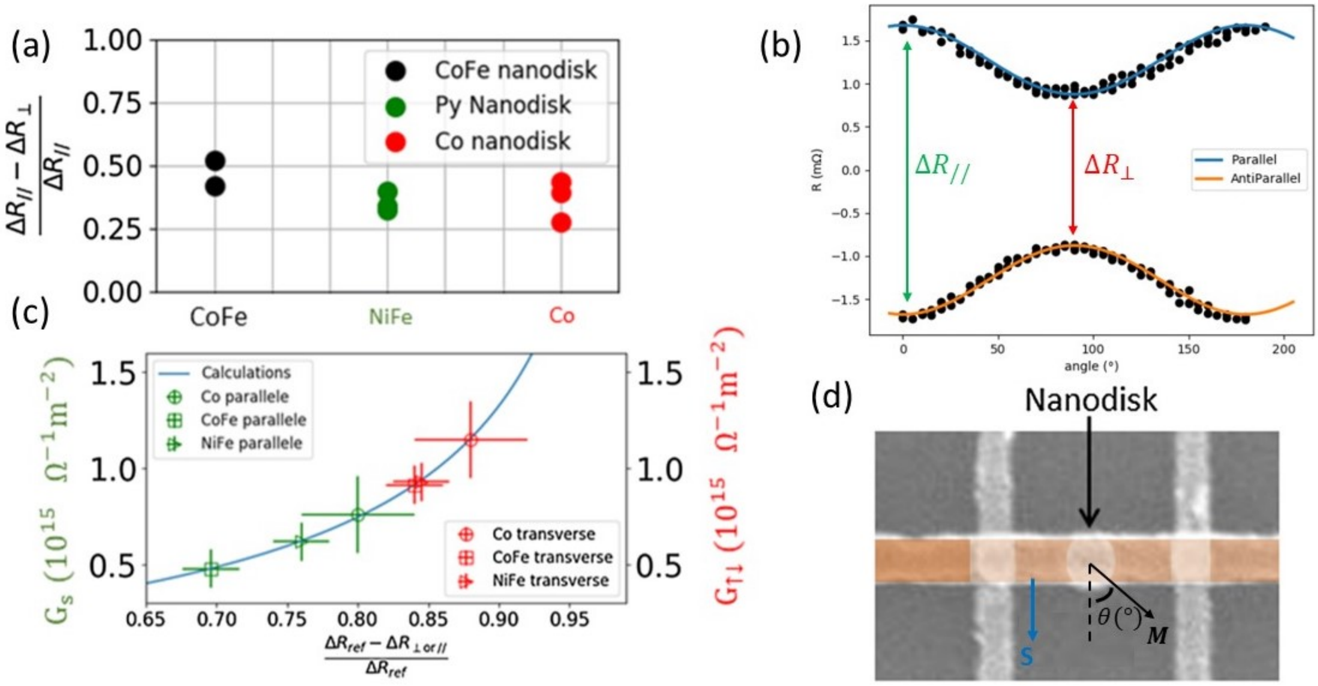

Figure 2.6: (a) Relative decrease of the nonlocal spin signal amplitude between the parallel and the transverse configuration for CoFe, NiFe and Co absorbers. Each symbol corresponds to a single device. (c) Relative variation of the spin signal amplitude when inserting an absorber, as a function of the interface conductance $G = G_s$ (in the collinear case, in green) or $G_{\uparrow\downarrow}$ (in the transverse case, in red). Different symbols correspond to different materials. The blue curve has been obtained with the model introduced in section 2.2.2, and is valid for both the collinear and transverse cases. The absorption values are experimental data. The error bars reflect the experimental dispersion of the absorption from device to device. (b) Evolution of the spin signal when rotating the magnetization of the absorber, with respect to the spin polarization. (d) The black curves of (b) correspond to the predictions of our models (lines), and reproduce well the experimental data points (symbols).

flows in the $\hat{x}$-direction, while decaying slowly over the large spin diffusion length of Cu. Upon arriving in the channel region where the absorber is present, the decay rate of the spin current strongly increases because of the large spin relaxation rate of the absorber, associated to a large spin-mixing conductance. The remaining spin current then reaches the detecting electrode, creating the detected non-local spin signal. In the region of the absorber that is close to the the injecting electrode, a spin polarization appears along the $\hat{z}$-direction, which in turn diffuses toward the injecting and detecting electrode. This is due to the spin current rotation around the $\hat{x}$-axis, caused by the imaginary part of the spin-mixing conductance. Finally, two sources of spin current polarized along the $\hat{x}$-axis appears at the edges of the injecting and detecting electrodes (Fig. 2.7a), due to the rotation of the $\hat{z}$-polarized spin polarization around their magnetization, also caused by the imaginary part of the spin-mixing conductance. This illustrates the good qualitative agreement of the model we developed in [137] with Finite Element Simulations. The advantage of this model relies on its low required computing power, while the small spin relaxation scales involved in the non-collinear relaxation processes require a refined meshing and therefore a large computing power, which caused some numerical difficulties. Importantly, the spin current with a polarization transverse to the magnetization of the detecting electrode is not detected, so that the effect of the imaginary part of the spin mixing conductance cannot be measured. In the following, accordingly to eq. 1.25, I will consider that the spin mixing conductance is a real quantity since its imaginary part is one order of magnitude smaller than its real part [141].

This model was used to extract G_s and $G_{\uparrow\downarrow}$ at the copper/FM interface from our measurements of ΔR, as described in Fig. 2.6c. The only free parameters are G_s and $G_{\uparrow\downarrow}$. The spin diffusion length, resistivity and polarization of the copper channel and FM electrodes are taken from previous measurements in lateral spin valves, described in section 2.1.3.

To this end, we evaluated the amount of the spin current absorbed by the nanodisk when its magnetization is collinear

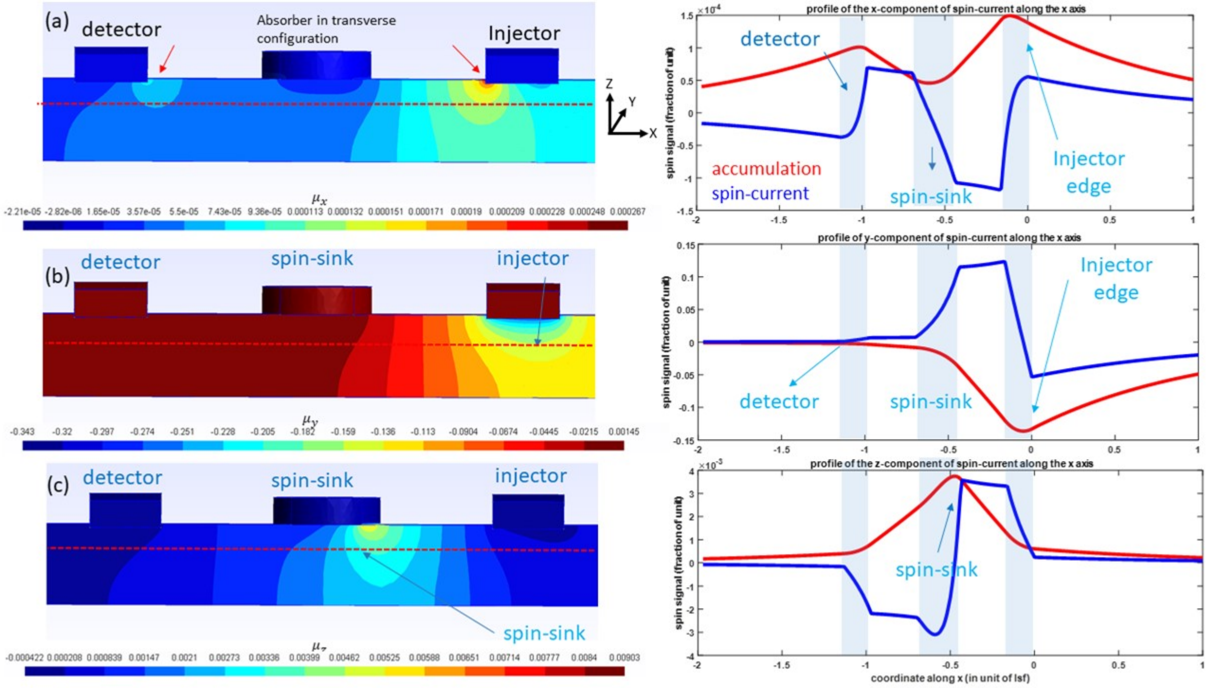

Figure 2.7: (a) Map of the spin accumulation polarized along the X-axis in the structure, obtained using FEM simulations in the left panel, and from our semi-analytical modelling in the right panel. (b) and (c) correspond to evolution of the spin accumulation polarized along Y, i.e., along the electrode magnetization, and Z, respectively. Note that the spin current is injected in the right of the structure.

with the spin current polarization:

$$\frac{\Delta R_{ref} - \Delta R_{||}}{\Delta R_{ref}} \tag{2.6}$$

and when it is transverse to it:

$$\frac{\Delta R_{ref} - \Delta R_{\perp}}{\Delta R_{ref}} \tag{2.7}$$

with ΔR_{ref} the reference spin signal amplitude for a lateral spin valve without absorber. As shown in Fig. 2.6c, between 70% (NiFe) and 80% (Co) of the spin current flowing in the channel is absorbed in the collinear configuration, while in the transverse one between 85 and 90 % of the spin current is absorbed. We then plotted the evolution of the amount of absorbed spin current with the spin(-mixing) conductance, using the above-described model. The variations of $(\Delta R_{ref} - \Delta R_{||})/\Delta R_{ref}$ on G_s and of $(\Delta R_{ref} - \Delta R_{\perp})/\Delta R_{ref}$ on $G_{\uparrow\downarrow}$ predicted by our model are found to be identical. These variations are thus represented by the single blue curve in Fig. 2.6c. This particular feature may be understood by reminding that the imaginary part of $G_{\uparrow\downarrow}$ has been neglected, and that the absorber thickness is larger than the relaxation lengths. The position of the symbols along the abscissa corresponds to the measured absorption efficiency. For the collinear configuration $(\Delta R_{ref} - \Delta R_{||})/\Delta R_{ref}$, one can access from the blue curve to the corresponding value of G_s in our system. Similarly, $G_{\uparrow\downarrow}$ can be deduced from the absorption $(\Delta R_{ref} - \Delta R_{\perp})/\Delta R_{ref}$ acquired in the transverse case. The absorption being enhanced in the transverse configuration, $G_{\uparrow\downarrow}$ is larger than G_s. The values extracted are gathered in table 2.3. In the collinear case, we will conclude that G_s is similar to what was measured previously in section 2.1.3. In the transverse configuration, the values of $G_{\uparrow\downarrow}$ extracted are of the same range of magnitude as the few existing data, either given by spin pumping [135] or by Hanle effect experiments [132]. Let us now compare the experimental conductances to the theoretical predictions, by considering a simplified picture based only on the relaxation lengths proposed in [69]. The main hypotheses are the following: (i) the interface is purely transparent, (ii) the relaxation of the collinear spin component is controlled by the rate of spin-flip, which is scaling with the inverse of the spin diffusion length of the absorber [35, 123], and (iii) the relaxation of the transverse spin component is mainly controlled by the Larmor length l_L and the transverse spin relaxation length $l_\perp$ [64]. In these hypotheses, G_s depends on l_{sf}^F, the spin diffusion length of the absorber. Here, the thickness of the absorber is much larger than the typical spin diffusion length l_{sf}^F of 3d ferromagnets [67]. Consequently, in the collinear case the efficiency of the absorption scales with the spin conductance, $G_s = 1/R_s = (1-\beta_F^2)/\rho_F l_{sf}^F$, where β_F is the absorber polarization and ρ_F its resistivity. Using data from previous experiment [67], G_s is deduced to be close to $0.61^{+0.26}_{-0.20} \times 10^{15}$, $0.62^{+0.05}_{-0.08} \times 10^{15}$, and $0.5^{+0.25}_{-0.16} \times 10^{15}\ \Omega^{-1}\,\mathrm{m}^{-2}$ for NiFe, CoFe and Co, respectively. As one may note, these values are consistent with those obtained here using the blue curve of Fig. 2.6c. On the other hand, if one neglects the presence of interfacial contributions to the spin mixing conductance, as in [69], the spin mixing conductance writes $G^L_{\uparrow\downarrow}$ (where L stands for Larmor) and may be estimated as $G^L_{\uparrow\downarrow} \approx 1/\min(l_L, l_\perp)\rho_F$ if $l^F_{sf} \gg l_L, l_\perp$, as described previously. According to *ab initio* calculations [64], this would lead to $G^L_{\uparrow\downarrow}$ values ranging from $3 \times 10^{15}\Omega^{-1}\mathrm{m}^{-2}$ for NiFe to $13 \times 10^{15}\Omega^{-1}\mathrm{m}^{-2}$ for Co. In the absence of computed values for l_L and $l_\perp$ in CoFe, no prediction can be made for the values of $G^L_{\uparrow\downarrow}$ for this material. However, by considering the values given for Co and Fe in ref. [64], it seems safe to assume that its $G^L_{\uparrow\downarrow}$ is larger than $3 \times 10^{15}\Omega^{-1}\mathrm{m}^{-2}$.

Interface	$G_s\ (10^{15}\Omega^{-1}m^{-2})$	$G_{\uparrow\downarrow}\ (10^{15}\Omega^{-1}m^{-2})$
Cu/Co	0.76 ± 0.1	1.1 ± 0.2
Cu/CoFe	0.48 ± 0.2	0.91 ± 0.1
Cu/NiFe	0.62 ± 0.1	0.93 ± 0.1

Table 2.3: Extracted spin conductance and spin mixing conductance at the interface between Cu and Co, CoFe and NiFe.

This simplified approach, in which the sole transport lengths determine the spin absorption, predicts values of G_s close to our measurements. However, those predicted for $G^L_{\uparrow\downarrow}$ values appear to be much larger than the experimental ones, which goes in favor of additional contributions to the spin diffusion, Larmor precession and transverse decoherence lengths. Our results suggest that, even at room temperature, one needs to consider ballistic contributions. As the density of conduction channels in Cu is finite, the transverse spin absorption is somehow limited. The physical quantity associated to this quantum limitation of the interface conductivity is the Sharvin conductance [142], a key parameter of transport, rarely taken into account in spintronics experiments [126]. Up to a small correction that characterizes the spin dependence of the reflection at a given interface, the spin mixing conductance is expected to be rather close to the Sharvin conductance [34]. Here, our experimental values of $G_{\uparrow\downarrow}$ are indeed comparable to the Sharvin conductance $G_{sh} = 1.2 \times 10^{15}\Omega^{-1}\mathrm{m}^{-2}$ of 3d FM-Cu interfaces obtained by *ab initio methods* [34].

We can thus explain our results in a simplified manner by taking into account in series both the Sharvin conductance G_{sh} and the real part of the spin-mixing conductance $G^L_{\uparrow\downarrow}$ within the relaxation lengths picture, so that the overall spin-mixing conductance writes *in fine* $1/G_{\uparrow\downarrow} = 1/G_{sh} + 1/G^L_{\uparrow\downarrow}$. According to previous ab initio calculations [34], the Sharvin conductance is typically 3–10 times smaller than the estimations of $G^L_{\uparrow\downarrow}$, i.e. $G^L_{\uparrow\downarrow} \gg G_{sh}$. The spin absorption in the transverse case is thus actually limited by the Sharvin conductance, and the experimental values of $G_{\uparrow\downarrow}$ remain close to the values of G_{sh} in Cu.

To conclude this chapter, we measured the collinear spin transport properties in the most widely used non-magnets (Al, Cu and Au) and ferromagnets (Co, CoFe and NiFe) in spintronics using lateral spin valves. We then measured the non-collinear spin transport properties in ferromagnetic materials and measured the spin mixing conductance at the interface between Cu and Co, CoFe and NiFe. Our observations show that the spin relaxation in these materials is much faster in the transverse than in the collinear situation, and that it is limited only by the finite number of conduction channels at the interface, *i.e.* by the Sharvin conductance.

Chapter 3

Spin-charge interconversion in ferromagnetic materials

In the previous chapter, I have shown how the exchange and the spin-orbit interactions act on the spin current transport in lateral spin valves. In these devices, the exchange interaction can be used to generate a spin current by flowing a charge current through the interface between a ferromagnetic and a non-magnetic material. It also allows the transfer of angular momentum from the spin current to the magnetization through ballistic non-collinear processes. The spin-orbit coupling on the other hand, only leads to spin-relaxation due to scattering off impurities, e.g. through diffusive processes.

In the first chapter however, I mentioned that the spin-orbit interactions can also produce a spin current into heavy non-magnetic materials, thanks to the spin Hall effect. More recently, a sizeable spin Hall effect has been observed in lighter elements, and in particular in 3d ferromagnets. Indeed, despite their smaller atomic number [231], large Spin Hall angles, comparable to that of Pt, have also been obtained in these materials [232, 78, 233, 234]. In addition to the spin-charge interconversion properties, the spin-orbit coupling is at the origin of specific transport properties in ferromagnets. Its interplay with magnetism gives rise to the anisotropic magnetoresistance [201] and the anomalous Hall effect [216]. However the link between the SHE and the magnetic order is unclear. Indeed, the modifications of the band structure at the phase transition [202, 203, 204], such as the band shift associated with the vanishing of the exchange splitting [220], could lead to a change in the spin-charge interconversion properties. A way to investigate that point, which we developed during my PhD, is to perform spin-Hall effect measurements both in the paramagnetic and ferromagnetic phases, to provide insights about the relation between the magnetic order and the spin Hall effect. Secondly, in addition to the modification of the band structure, the ferromagnetic order breaks the space rotational symmetry by introducing a magnetization vector. We saw in the previous chapter that this has important consequences on the spin transport properties. It is thus also expected that the spin-charge interconversion should be modified by this symmetry breaking [75].

Investigations on the link between the ferromagnetic order and the spin Hall effect have been started only recently and the results are so far mostly conflicting. Indeed, some studies report an effect of the magnetic order only around the Curie temperature in magnetic alloys such as $\mathrm{Ni}_{0.09}\mathrm{Pd}_{0.91}$ [214] or $\mathrm{Fe}_{0.25}\mathrm{Pt}_{0.75}$ [235]. Other studies in SrRuO_3 report a strong [261] or very weak [269] effect of the phase transition on the SHE. The studies concerned with the SHE anisotropy in ferromagnetic materials are also rare and controversial, showing different results for similar materials. Indeed, observations of a moderate anisotropy in Py [265], a large one in CoFe [264], and an isotropic behaviour in Co [233] have been reported, some of them contradicting theoretical predictions [92]. This could result from differences in-between material properties, but also from the fact that a precise measurement of this anisotropy remains challenging. Indeed, several techniques have been used so far to study the SHE in ferromagnetic materials such as second harmonic [270, 235], spin Seebeck effect [233, 250], non-local magnon transport [265, 264, 276], lateral spin valves [214], spin-torque ferromagnetic resonance [269] and spin-pumping ferromagnetic resonance [261]. Observing the SHE anisotropy in FMs using these methods is not straightforward, as it requires controlling independently the magnetization of two different FMs in direct contact [250, 232, 243, 233, 269, 270]. Techniques involving a charge current flowing into the Ferromagnetic-Spin Hall Effect (FM-SHE) material are complicated because of the contamination by spurious effects such as the Planar Hall effect [274] and the Anomalous Hall Effect (AHE) [275], while the methods based on non-local magnon transport that allowed the observation of an anisotropic SHE in FMs [265, 264] involve the direct contact between the magnetic insulator and the studied FM material, which could render complex the interpretation of these results [276].

In this chapter, I will explain in a first section why the transition from a paramagnetic to a ferromagnetic order is expected to have a strong effect on the SHE, and how the presence of a magnetization vector can lead to an anisotropy of the SHE. In a second section, I will present a measurement of the SHE across the Curie temperature in the dilute ferromagnetic material NiCu using a spin-pumping ferromagnetic resonance method. In the last section, I will explore the anisotropy of the SHE in the ferromagnetic phase of NiCu and NiPd.

3.1 Spin-charge interconversion in ferromagnetic materials

In this section I will discuss from a theoretical point of view the effect of the paramagnetic-ferromagnetic phase transition on the band structure in ferromagnetic materials and its possible influence on the spin-charge interconversion. I will then show how the symmetry breaking by the magnetization vector can induce an anisotropy of the spin-charge interconversion.

3.1.1 Ferromagnetic band structure and intrinsic spin Hall effect

The ferromagnetism of isolated ions originates from the combined effects of the Coulomb interaction and the Pauli exclusion principle, which create an effective coupling, named the exchange interaction, between the spins of the electrons populating the outer electronic shell of the atom, which translates into the Hund's rule in the orbital filling of the ion [277].

In ferromagnetic metals, this electron-electron interaction can provide a simplified model for the origin of the ferromagnetic order, with however the complicating aspect of the large delocalization of the conduction electrons expected to support the magnetism. Furthermore, since the spin direction of an electron depends on the one of all the other electrons, ferromagnetism is a many-body problem which leads to important theoretical challenges and an important body of theoretical proposals for its origin [278]. Here I will focus on the case of the 3d series, where light 4sp and heavy 3d electrons are present at the Fermi level. In this series, the two pictures proposed to describe ferromagnetism are the itinerant electron (Stoner) model, and a partially localized model of the electronic transport [279]. In the Stoner model, the 4sp and 3d electrons are considered to be fully itinerant. The ferromagnetism then originates from a mechanism similar to the Hund rule, with two electrons of opposite spin experiencing a larger Coulomb repulsion due to their higher probability of being present at the same point in space. Aligning the electronic spins consequently lowers the energy of the system, thus giving rise to a net magnetic moment in the metal [277]. Although this model is too complicated to give quantitative results, molecular field approximations predict a rigid shift of the opposite spin bands. The second partially localized model includes both the localized features of the initial Heisenberg model of ferromagnetism, and the presence of itinerant electrons. In this model, the 3d electrons are considered as being localized on the atoms and give rise to the magnetic order through intra-atomic Coulomb interactions, while the 4sp electrons are delocalized with their spin coupled to the local 3d moment by an exchange interaction [218]. This exchange would create the spin polarization of a charge current flowing in a ferromagnetic material, as well as the non-collinear spin transport effects discussed in Chapters 1 and 2. Importantly, the spin transport effects in ferromagnets studied in Chapter 1 and Chapter 2 do not depend on the origin of the ferromagnetism as only the itinerant electrons are being probed by transport measurements. In this chapter, we will however see that the localized or delocalized nature of the ferromagnetism can have important consequences on transport properties such as the spin Hall effect.

Regardless of the origin of the ferromagnetism in 3d ferromagnets, its appearance leads to an important modification of the electronic band structure, that is expected to have a dramatic effect on the intrinsic spin Hall effect. Indeed, the intrinsic spin Hall effect originates from the spin-orbit driven splitting of the band structure at high symmetry points. This is particularly the case in Pt, where the presence of such splitting at the Fermi level in the X and L points (Fig. 3.1a) leads to the appearance of a large spin Hall angle [73], (see Fig. 3.1b). According to tight binding calculations reported in Ref. [203], the spin Hall effect in paramagnetic Ni is predicted to have an intrinsic origin, due to the strong resemblance of its band structure with that of Pt, including the splitting at the X and L points (Fig. 3.1c). In the ferromagnetic phase of Ni however, the spin-orbit induced splitting at the Fermi level vanishes (Fig. 3.1d), so that no intrinsic spin Hall effect is expected in ferromagnetic Ni. This means that the ferromagnetic-paramagnetic transition could have a dramatic effect on the spin-charge interconversion in ferromagnetic materials. Similar conclusions are expected to hold in NiCu, as the calculations reported in Ref. [203] indicate that the band structure of NiCu and Ni are similar, despite a broadening in NiCu due to the disorder introduced by the alloying.

In addition to the band structure modification induced by the ferromagnetic-paramagnetic phase transition, other

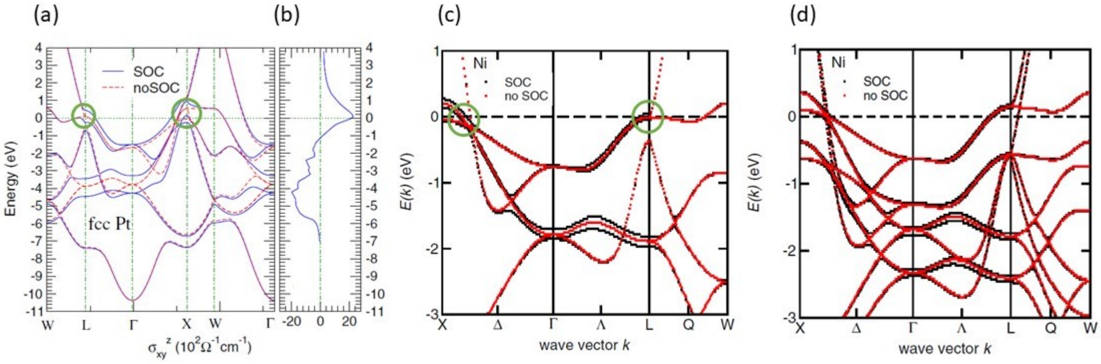

Figure 3.1: (a) Band structure of Pt and (b) computed intrinsic spin Hall conductivity. Modified from Ref. [73]. The green circles indicate the spin-orbit split bands at the Fermi energy at points L and X. (c) Band structure of paramagnetic and (d) ferromagnetic Ni. The spin-orbit splitting at the Fermi energy in points X and L vanishes in the ferromagnetic phase of Ni. Modified from Ref. [203].

effects could induce a change in the spin-charge interconversion properties of ferromagnetic materials. Indeed, the interplay between the exchange coupling and the spin-orbit interaction is expected to produce an important anisotropy of the spin-charge interconversion.

3.1.2 Anisotropy of the spin-charge interconversion in ferromagnetic materials

Historically, the first known consequences of the interplay between the spin-orbit interaction and the magnetization are the Anomalous Hall Effect (AHE) [216] and the Anisotropic Magnetoresistance [266]. Both these effects are known to produce a charge-charge interconversion by introducing non-diagonal terms in the conductivity tensor. This produces a charge current that flows perpendicularly to the applied one. As explained in the section 1.1.2, a charge current flowing in a ferromagnetic material is necessarily accompanied by a spin current, because of the presence of a spin conductivity asymmetry β. The AHE consequently produces a spin current polarized along the magnetization with a flow transverse to the applied charge current. Furthermore, as discussed in the chapter 2, the component of the spin current polarization transverse to the magnetization is expected to vanish over a very short length scale. Consequently, the initial models describing the spin-orbit driven spin-charge interconversion effects in ferromagnetic materials neglect the spin polarization component transverse to the magnetization. In this approximation, the spin and charge flux equations of the Valet-Fert model can be generalized as [215]:

$$\boldsymbol{j}_c = \sigma\,\partial_{\boldsymbol{r}}\mu_m + \beta\sigma\,\partial_{\boldsymbol{r}}\mu + \sigma^{AHE}\,\boldsymbol{m}\times(\partial_{\boldsymbol{r}}\mu_m + \xi\partial_{\boldsymbol{r}}\mu) + \sigma^{AMR}\,\boldsymbol{m}[\boldsymbol{m}\cdot(\partial_{\boldsymbol{r}}\mu_m + \eta\partial_{\boldsymbol{r}}\mu)] \tag{3.1}$$

and

$$\boldsymbol{j}_s = \sigma\partial_r\mu + \beta\sigma\,\partial_{\boldsymbol{r}}\mu_m + \sigma^{AHE}\,\boldsymbol{m}\times(\partial_{\boldsymbol{r}}\mu + \xi\partial_{\boldsymbol{r}}\mu_m) + \sigma^{AMR}\,\boldsymbol{m}[\boldsymbol{m}\cdot(\partial_{\boldsymbol{r}}\mu + \eta\partial_{\boldsymbol{r}}\mu_m)] \tag{3.2}$$

with σ^{AHE} and σ^{AMR} the non-diagonal conductivity tensor terms associated to the AHE and to the AMR (most often termed planar Hall effect in this context). Here, μ refers to a spin accumulation polarized along the magnetization vector $\boldsymbol{m}$. ξ and η correspond to the polarizations associated to the AHE and planar Hall effects, respectively, and are not necessarily related to β [237]. The two first terms of eq. 3.1 and 3.2 are due to the drift-diffusion terms of the Valet-Fert model. The two other terms describe the above mentioned charge-charge interconversion effects, but also related the spin-charge interconversion effects. Here, I will focus on this spin-to-charge interconversion, but similar considerations also apply to the charge-to-spin process.

Let us consider the injection of a spin current $\boldsymbol{j}_z$ flowing in the $\hat{z}$ direction, with a polarization along $\hat{x}$ into a ferromagnetic material with a magnetization $\boldsymbol{m}$ (Fig. 3.2a). Following the approach developed in the chapter 2 of this manuscript, I will consider that the spin current polarization transverse to the magnetization relaxes at the interface, so that only its component collinear to the magnetization flows into the ferromagnetic material. The spin current flowing in the ferromagnetic materials writes $\boldsymbol{j}_z \cdot \boldsymbol{m} = \sigma\partial_{\boldsymbol{r}}\mu$. Introducing the Anomalous and Planar Hall angles $\theta^{AHE} = \sigma^{AHE}/\sigma$ and $\theta^{PH} = \sigma^{AMR}/\sigma$, the resulting charge current writes at the first order in these two angles:

$$\boldsymbol{j}_c = \beta(\boldsymbol{j}_z\cdot\boldsymbol{m})\hat{z} + \xi\theta^{AHE}(\boldsymbol{m}\times\hat{z})(\boldsymbol{j}_z\cdot\boldsymbol{m}) + \eta\theta^{PH}\boldsymbol{m}(\boldsymbol{m}\cdot\hat{z})(\boldsymbol{j}_z\cdot\boldsymbol{m}) \tag{3.3}$$

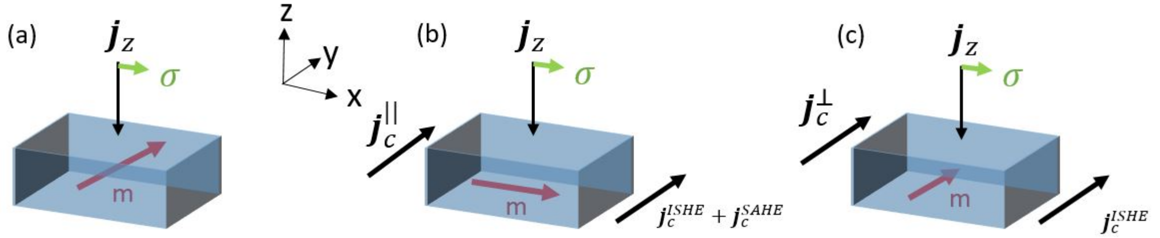

Figure 3.2: (a) Injection of a spin current in a ferromagnet with a magnetization not collinear with the spin current polarization. (b) When the magnetization is along $\boldsymbol{\sigma}$, the injected spin current is converted into a charge current $\boldsymbol{j}_c^{||}$ along $\hat{y}$, which corresponds to the sum of the contributions of the spin Hall effect and of the spin anomalous Hall effect $\boldsymbol{j}_c^{ISHE} + \boldsymbol{j}_c^{SAHE}$. (c) When the magnetization is perpendicular to $\boldsymbol{\sigma}$, the injected spin current is converted into a charge current $\boldsymbol{j}_c^{\perp}$ along $\hat{y}$, corresponding to solely $\boldsymbol{j}_c^{ISHE}$.

While the first term of eq. 3.3 simply corresponds to the conductivity asymmetry-driven charge current, the second term shows that the injected spin current can produce a charge current in a direction transverse to its flow, thereby leading to an inverse spin Hall-like interconversion effect. The third term leads to the generation of a charge current flowing along the $\boldsymbol{m}$ direction. For simplicity, I will here assume that the magnetization lies in the (x,y) plane, so that the contribution of the Planar hall effect to the interconversion will be disregarded, even though it has already been considered for the generation of spin-orbit torques for field-free magnetization switching, due to the new degree of freedom offered by its dependence on the magnetization direction [215, 238]. This results in the interconversion of the spin current into a charge current denoted:

$$\boldsymbol{j}_c^{||} = \theta_{||}(\boldsymbol{m} \times \hat{z})(\boldsymbol{j}_z \cdot \boldsymbol{m}) \tag{3.4}$$

with $\theta_{||} = \xi\theta^{AHE}$. Here, the symbol "||" refers to the fact that this interconversion takes place only when the polarization of the spin current is collinear to the magnetization (Fig. 3.2b). As a consequence, the interconversion driven by the anomalous Hall effect is highly anisotropic, since the direction of the produced charge current depends on the magnetization direction, while its amplitude depends on the relative orientation between the spin current polarization and the magnetization, with a cancellation of the effect when they are transverse due to the fast relaxation of the spin current in this situation.

This picture of a total cancellation of the spin-charge interconversion has however been challenged by band structure calculations, which predict that the spin-orbit interaction in ferromagnetic materials can cause the spin eigenstates to be misaligned with the magnetization at the crossing between majority and minority spin bands [92, 219]. This leads the relaxation of the transverse spin current polarization to occur on a substantially larger length scale than when taking into account only the effect of the exchange interaction [205]. Therefore, a spin current with a polarization transverse to the magnetization could exist in the bulk of a ferromagnetic material, with a spin-orbit interaction comparable in strength to the exchange coupling [252]. As a consequence, it could be possible for a spin current $\boldsymbol{j}_z$ polarized transversely to the magnetization to generate a charge current (Fig. 3.2c):

$$\boldsymbol{j}_c^{\perp} = \theta_{\perp}(\boldsymbol{m} \times (\boldsymbol{j}_z \times \boldsymbol{m})) \times \hat{z} \tag{3.5}$$

with $\theta_{\perp}$ the spin Hall angle of the interconversion between a transversely polarized spin current and a charge current. A more physically correct picture is to separate the interconversion into two contributions [92]. One is the magnetization dependent Spin Anomalous Hall Effect with an angle $\theta^{SAHE} = \theta_{||} - \theta_{\perp}$, which originates from the Anomalous Hall effect as described in eq. 3.1 to 3.4. The other is the isotropic Spin Hall Effect quantified by $\theta^{SHE} = \theta_{\perp}$. The charge current produced by the spin-to-charge interconversion in a ferromagnetic material is then given by the sum of an anisotropic and an isotropic terms with respect to the angle between the spin current polarization and the magnetization (Fig. 3.2b and 3.2c):

$$\boldsymbol{j}_c = [\theta^{SAHE}\boldsymbol{m}(\boldsymbol{j}_z \cdot \boldsymbol{m}) + \theta^{SHE}\boldsymbol{j}_z] \times \hat{z} \tag{3.6}$$

Measuring the relative importance of these two contributions could thus provide a critical information on the relative importance of the exchange interaction and the spin-orbit interaction in ferromagnetic materials on the spin transport properties. Indeed, observing a fully anisotropic signal would indicate that the transverse spin polarization component relaxes very quickly upon entering the ferromagnet, and that the exchange interaction dominates the spin transport. On the other hand, the second term of eq. 3.6 is a sign of ferromagnetic band structure modification by the spin-orbit interaction. This would thus allow providing a better understanding of the relative importance of the AHE and SHE-driven interconversion processes in ferromagnetic materials.

In the second section of this chapter, I will address the question of the link between the ferromagnetic order and the SHE by perfoming spin-pumping measurements of the spin to charge interconversion in NiCu through its Curie temperature.

3.2 Link between the magnetic phase and the spin to charge interconversion in NiCu

In this section, I will start by describing the SP-FMR technique, used for several studies presented in this manuscript, and illustrate it with the spin-charge interconversion in Pt. I will then move on to the measurement of the spin-charge interconversion in NiCu. First I will show that despite being a light metal, the spin Hall angle at room temperature is similar to that of Pt. I will then present measurement of the spin-charge interconversion in NiCu across its transition temperature, in order to see whether or not a strong modification of the NiCu band structure occurs. This study on NiCu has been published in Physical Review Letters [243], and the paragraph 2 of this section can be considered as an extended version of this publication.

3.2.1 Spin injection and interconversion measurement using SP-FMR

The SP-FMR methods [87, 281, 224], also called spin pumping, is a powerful and widely used tool for the study of spin to charge interconversion in a variety of materials, including heavy metals [46], topological insulators [109] and oxide-based two dimensional electron gases [20] (see chapter 4). It allows interconversion measurement on microscopic devices without the need for nanofabrication. In this section, I will describe the SP-FMR technique, illustrating it with the simple example of the ISHE measurement in Pt.

The Ferromagnetic resonance

When placed in a magnetic field $\boldsymbol{H_{ext}}$, the magnetization follows the direction of the electron spins put into precession around $\boldsymbol{H_{ext}}$ by the Zeeman interaction. It is however observed that the magnetization does not precess indefinitely and eventually aligns on the direction of the local effective field. This is described by the Landau-Lifshitz-Gilbert (LLG) equation [221]:

$$\partial_t \boldsymbol{m} = -\gamma(\boldsymbol{m} \times \boldsymbol{H}_{eff}) + \alpha_G(\boldsymbol{m} \times \partial_t \boldsymbol{m}) \tag{3.7}$$

with $\boldsymbol{H}_{eff}$ the effective magnetic field in the material, in general not collinear to $\boldsymbol{H}_{ext}$, γ the gyromagnetic ratio and α_G the Gilbert damping. The first term on the right hand side describes the rotation of the magnetization around $\boldsymbol{H}_{eff}$, while the second term describes the damping of the magnetization precession toward its equilibrium position along $\boldsymbol{H}_{eff}$, due to the spin-orbit interaction that allows dissipating the magnetic energy to the lattice [222] (even though Eddy currents can also contribute to the damping [222, 280]).

When the FM is additionally submitted to an oscillating magnetic field of amplitude $\boldsymbol{h}_{rf}$ and perpendicular to $\boldsymbol{H}_{eff}$, it is possible to observe a Ferromagnetic Resonance (FMR) for a given value of the static magnetic field called the resonance field H_{res}. At these FMR conditions, the magnetization will then sustain rotations around $\boldsymbol{H}_{res}$ as seen in Fig. 3.3a, and the power provided by the oscillating field compensates the power dissipated by the damping.

In the linear regime where $H_{res} \gg h_{rf}$, the resonance results in a Lorentzian evolution of the imaginary part of the magnetic susceptibility χ'', that links the m_z component of the magnetization to the oscillating field according to y: $m_z = \chi'' h_{rf}^y$, using the coordinates of Fig. 3.3a. This creates a maximum of χ'' at a resonance field $\boldsymbol{H}_{res}$, with a finite linewidth ΔH proportional to the Gilbert damping Fig. 3.3b.

The relation between the applied magnetic field H_{ext} and the pulsation ω_{res} of h_{rf} at which the material resonates is given by the Kittel formula [223]:

$$\omega_{res} = \gamma\sqrt{(\mu_0 M_s + H_{ext} + H_{uni})(H_{ext} + H_{uni})} \tag{3.8}$$

with μ_0 the vacuum magnetic permeability, M_s the effective magnetization saturation value, and H_{uni} the magnetic anisotropy contribution to the effective applied field. Here M_s is in $\mathrm{A \cdot m^{-1}}$ while H_{ext} and H_{uni} are expressed in Teslas.

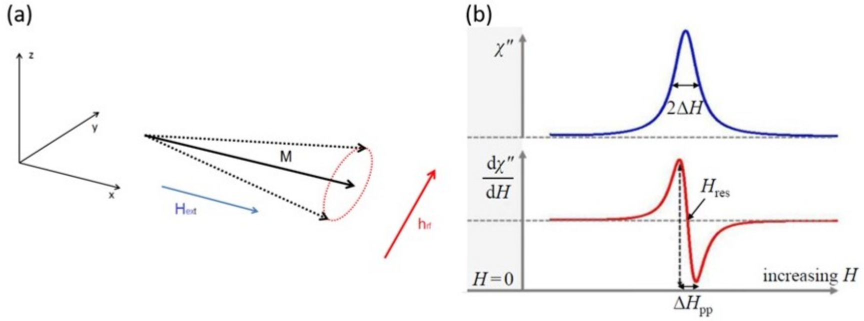

Figure 3.3: (a) Orientation of the static and variable magnetic field applied to the ferromagnetic film during a FMR experiment. (b) Schematics of a FMR signal. At the resonance, the imaginary part of the magnetic susceptibility reaches a maximum, with a lorentzian shape around the resonance field. The detected signal is the derivative of the susceptibility with respect to the applied static magnetic field, so that the FMR signal has the shape of an antilorentzian. Image from Ref. [169].

Let us now consider a thin ferromagnetic field submitted to an in-plane static magnetic field and to a radiofrequency field at fixed frequency ω. When the applied field H_{ext} is scanned in amplitude, the system eventually reaches the FMR conditions given by eq. 3.8. In practice, the variation of the FMR susceptibility is measured using a lock-in technique in a braodband set-up, so that we actually obtain the derivative of the susceptibility versus the applied static field $\partial\chi''/\partial H$ which has the shape of an antilorentzian as shown in the bottom panel of Fig. 3.3b. The width of the resonance is then measured by the peak to peak linewidth ΔH_{pp} linked to the half width at half maximum ΔH by $\Delta H_{pp} = 2/\sqrt{3}\Delta H$ which depends on the LLG parameters following [115]:

$$\Delta H_{pp} = \Delta H_0 + \frac{2}{\sqrt{3}}\left(\frac{\omega}{\gamma}\right)\alpha_G \tag{3.9}$$

The ΔH_0 term is a frequency independent linewidth broadening due to the material inhomogeneities [267]. It does not depend on the frequency of h_{rf}, so it can be easily separated from the damping dependent term in broadband measurements, *i.e.* in FMR measurements in which it is possible to change the frequency of the *r.f.* field.

In the following, I will describe how a spin current can be generated using FMR in a ferromagnetic thin film in contact with a non-magnet.

Spin injection at the ferromagnetic resonance

At the FMR conditions in a 3d FM, the Gilbert damping term transfers angular momentum from the d-localized electrons to the s-conduction electrons. This causes the apparition of an out of equilibrium spin accumulation in the FM [115]. When put in contact with a non-magnet, the spin accumulation diffuses into this neighbouring material, creating a pure spin current with polarization collinear to the instantaneous magnetization of the FM (Fig. 3.4a). This spin current can be expressed in units of $\mathrm{A\cdot m^{-2}}$ by [224]:

$$\boldsymbol{j}_{pump}(t) = \frac{\hbar}{4\pi} g^{eff}_{\uparrow\downarrow}[\boldsymbol{m}(t)\times\partial_t\boldsymbol{m}(t)]\left(\frac{2\mathrm{e}}{\hbar}\right) \tag{3.10}$$

with $g^{eff}_{\uparrow\downarrow}$ the effective spin mixing conductance, in units of m^{-2}. This quantity includes the spin backflow term due to the relaxation into the FM of the spin accumulation produced by the spin pumping (Fig. 3.4a) in the neighbouring material [53]. The backflow term causes a modification of the bare spin mixing conductance $g_{\uparrow\downarrow}$ at the interface between a ferromagnet and a perfect spin-sink described in the chapter 1, thus decreasing the amount of spin-current injected from the ferromagnet into the neighbouring material. The effective spin mixing conductance writes [121]:

$$g^{eff}_{\uparrow\downarrow} = \frac{g_{\uparrow\downarrow}}{1+\frac{g_{\uparrow\downarrow}}{g_s}} \tag{3.11}$$

with $g_s = (\mathrm{h}/\mathrm{e}^2)\tanh(t_{NM}/l^{NM}_{sf})/(l^{NM}_{sf}\rho^{NM})$ the spin conductance of the material in which the spin current is injected, with l^{NM}_{sf} and ρ^{NM} its spin diffusion length and resistivity. e is the charge of the electron and h is the Planck constant.

Note that here the notations $g_{s/(\uparrow\downarrow)}$ used for the spin (mixing) conductances are different from the ones used in Chapters 1 and 2: $G_{s/(\uparrow\downarrow)}$. This is to evidence the difference in units between the quantities typically used to express them in SP-FMR (m^{-2}) and in transport experiment ($\Omega^{-1}\mathrm{m}^{-2}$). The link between the two can be made through the expression $G = (\mathrm{e}^2/\mathrm{h})g$. This spin backflow correction to the injected spin current plays a very important role, especially when injecting a spin current in materials with a low spin conductance such as Cu and Al.

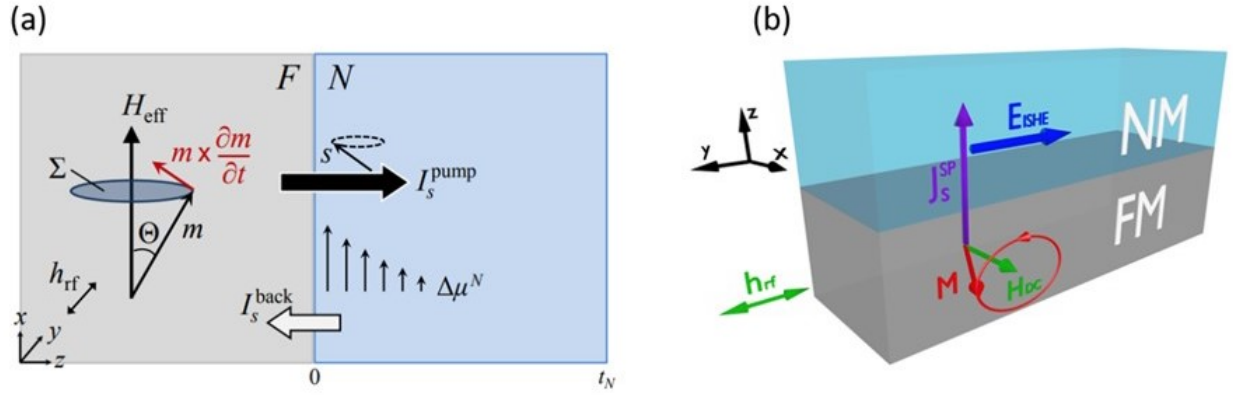

Figure 3.4: (a) Schematics of the spin pumping experiment. The magnetization $\boldsymbol{m}$ of the ferromagnet rotates around the static field $\boldsymbol{H}_{eff}$, with an angle Θ that depends on the amplitude of the rf field $\boldsymbol{h}_{rf}$. The transfer of angular momentum from the localized to the mobile electrons creates a spin accumulation that diffuses into the non-magnet, creating a spin current with a rotating polarization around $\boldsymbol{H}_{eff}$. This additional dissipation process results in an increase of the effective Gilbert damping. The spin accumulation at the FM/MN build-up is partly re-absorbed into the ferromagnet by a back-flow spin current (Image from Ref. [90]). (b) Typical stack used in spin pumping experiments, with the spin current created in the NM by the FM at the FMR conditions converted into a charge current, or rather in an electric field $\boldsymbol{E}_{ISHE}$ in open circuit conditions. The potential drop V_{ISHE} is measured at the two short ends of the system.

A consequence of this spin current flow from the FM into the neighbouring non-magnet is the opening of an additional relaxation channel for the out of equilibrium spin accumulation created by the magnetization precession, that will add up to the one modeled by the Gilbert damping α_G and writes [126]:

$$\alpha_{F/N} = \alpha_G + \frac{\hbar\gamma}{4\pi M_s t_F} g_{\uparrow\downarrow}^{eff} \tag{3.12}$$

with t_F the thickness of the ferromagnetic film. Experimentally, this will translate into an increase of the FMR resonance linewidth when a non-magnetic material is placed in contact with the FM when compared to the linewidth of a single layer FM.

This spin current injection mechanism will play a crucial role in the following section, as it allows for the measurement of spin to charge interconversion effects. I will firstly illustrate how the SP-FMR method can be used to measure the spin to charge interconversion in a heavy metal.

Measurement of the ISHE in heavy metals

Let us consider a FM/HM bilayer stack submitted to a static field in the X-direction, and to an oscillating one in the Y-direction. At the FMR conditions, the rotation of the FM magnetization around the static field will produce a spin current flowing into the non-magnet (Fig. 3.4b). As mentioned before, the polarization of the spin current follows the instantaneous magnetization of the FM. However, since in most spin pumping experiments the oscillating field frequency is in the tens of GHz range, interconversion effects linked with the polarization precession will not be detected. Taking the average $j_{pump} = \omega/2\pi \int_0^{2\pi/\omega} j_{pump}(t)\mathrm{d}t$ value of the spin polarization is then an acceptable approximation. The spin current polarization is therefore along the static field direction, and depends on the precession angle Θ of the magnetization. This precession angle is itself a function of the parameters M_s, γ, $g_{\uparrow\downarrow}^{eff}$ and $\alpha_{F/N}$ introduced in the previous section, so that the spin current at the interface between the ferromagnet and the non-magnet writes [87]:

$$j_{pump} = \frac{\hbar\omega}{4\pi} g_{\uparrow\downarrow}^{eff} \sin^2(\Theta) \left(\frac{2\mathrm{e}}{\hbar}\right) = \frac{g_{\uparrow\downarrow}^{eff} \gamma^2 \hbar (\mu_0 h_{rf})^2}{8\pi\alpha_{F/N}} \left[\frac{\mu_0 M_s \gamma + \sqrt{(\mu_0 M_s \gamma)^2 + 4\omega^2}}{(\mu_0 M_s \gamma)^2 + \omega^2}\right] \left(\frac{2\mathrm{e}}{\hbar}\right) \tag{3.13}$$

The thickness-dependent spin current into the heavy metal is then deduced from the Valet-Fert equations:

$$j(z) = j_{pump}\frac{\sinh[(t_{HM} - z)/l_{sf}^{HM}]}{\sinh[t_{HM}/l_{sf}^{Pt}]} \tag{3.14}$$

where the Z axis is normal to the interface between the FM and the HM. Since the flow direction of the spin current (along Z) and its polarization (along X) are perpendicular, a charge current per unit of surface j_c along Y is created by the ISHE in the HM (Fig. 3.4b):

$$j_c = \theta_{SHE}\int_0^{t_{HM}} j(z)\frac{\mathrm{d}z}{t_{HM}} = \theta_{SHE}j_{pump}\frac{l_{sf}^{HM}}{t_{HM}}\tanh\left(\frac{t_{HM}}{2l_{sf}^{HM}}\right) \tag{3.15}$$

Since the measurements are carried out in open circuit conditions, as seen in Fig. 3.4b, the actual charge current is zero, so that the measured potential drop V_{ISHE} is linked to the produced charge current by:

$$j_c = \frac{1}{wt_{HM}}\frac{V_{ISHE}}{R} \tag{3.16}$$

with R the resistance of the bilayer between the two potential measurement points and w the bilayer width. Using eqs. 3.15 and 3.16, the spin Hall angle of the heavy metal can then be expressed as:

$$\theta_{SHE} = \frac{1}{R\tanh(t_{HM}/2l_{sf}^{HM})}\frac{V_{ISHE}}{wl_{sf}^{HM}j_{pump}} \tag{3.17}$$

It is important to note here that a direct consequence of this set of equations is that for a large heavy metal thickness ($t_{HM} \gg l_{sf}^{HM}$), the ISHE-produced potential drop and charge current depend on the spin Hall angle and on spin diffusion length as $j_c \propto \theta_{SHE}l_{sf}^{HM}$. This feature will be important for comparing the spin to charge interconversion efficiency between bulk and two dimensional materials [200], as discussed in the next chapter.

The goal of our spin pumping measurements is to extract the spin Hall angle of a given material using eq. 3.17. The resistance R is straightforward to obtain, and V_{ISHE} can be extracted from the electrical measurement described in Fig. 3.4b at the FMR conditions. More difficult to evaluate, however, is the spin current pumped from the ferromagnet into the normal metal, as it depends on the magnetization M_s and on the parameters of the LLG equation (γ, α_G and $g_{\uparrow\downarrow}^{eff}$). In order to illustrate the spin Hall angle extraction procedure in a simple case, I will present the measurement of the spin Hall angle of platinum using a Py/Pt bilayer deposited on SiO_2.

Measurement of the Spin Hall angle of Pt

We fabricated a bilayer of NiFe(15 nm) and Pt(20 nm) by electron beam evaporation. The permalloy was deposited first on a Si/SiO_2 substrate, followed by the deposition of Pt. We also deposited a reference sample of 15 nm Py on SiO_2, and capped the samples with two nanometers of aluminium. The samples were then cut into macroscopic samples of $0.4 \times 2.4\,\mathrm{mm}^2$.

We firstly evaluate the spin current j_{pump} by measuring the LLG equation parameters using broadband measurements. The sample is placed between two Helmholtz coils on a gold waveguide. The coils provide a static field corresponding to $\mathbf{H}_{ext}$ of eq. 3.8, while a radiofrequency field $\mathbf{h}_{rf}$ perpendicular to the plane of the bilayer is created by the waveguide, with frequencies ranging from 4 to 24 GHz (see [268] for more details on this set-up). The *r.f.* power transmitted by the waveguide is measured by a lock-in. The static field is swept in amplitude for a given frequency of the *r.f.* field. At the FMR conditions, a part of the power transmitted by the waveguide is absorbed by the sample. This corresponds to an increase of χ'', the imaginary part of the magnetic susceptibility χ, which takes a Lorentzian shape around the resonance field (Fig. 3.3b). The lock-in detection compares the loss of power with the reference power applied to the wave guide and measures $\partial\chi''/\partial H_{ext}$. We can then extract the peak to peak linewidth ΔH_{pp} and resonance field H_{res} by fitting a curve similar to that of the bottom panel of Fig. 3.5c. The extracted H_{res} and ΔH_{pp} are shown in Fig. 3.5b and 3.5a.

The evolution of the linewidth with respect to the frequency of the *r.f.* field is shown in Fig. 3.5a. As expected from eq. 3.9, ΔH_{pp} depends linearly of the *r.f.* field frequency, with a baseline due to the inhomogeneous broadening ΔH_0. The slope for the Py/Pt stack is larger than for the Py thin film, which indicates a larger damping in the LLG equation, corresponding to the extra damping of eq. 3.12.

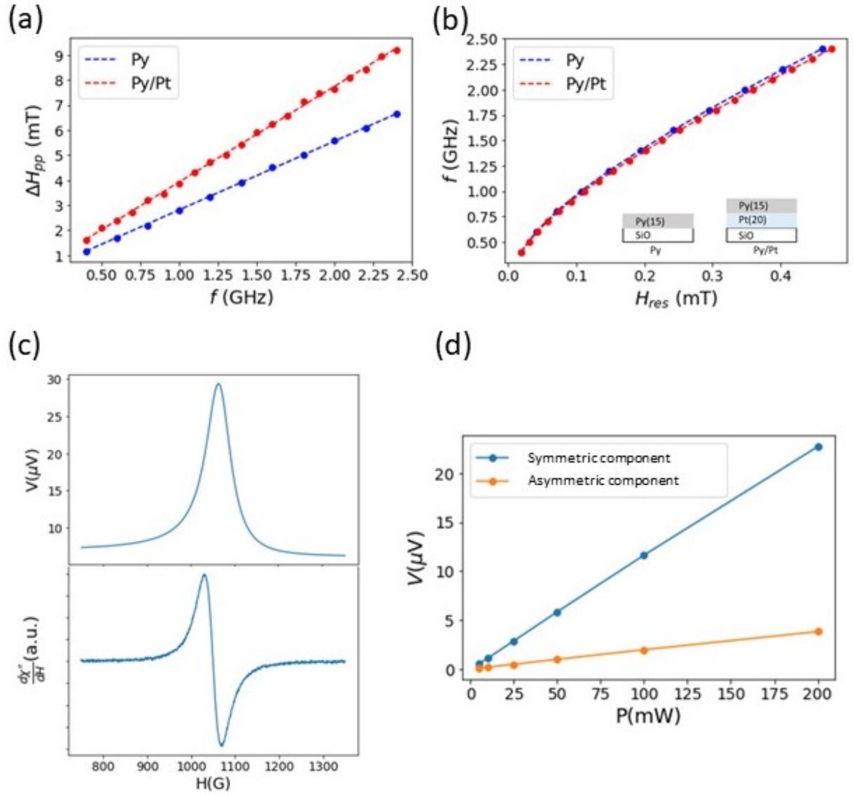

Figure 3.5: (a) Evolution of the peak to peak FMR linewidth with the *r.f.* magnetic field frequency, for a Py thin film and a Py/Pt bilayer. The dotted lines correspond to fits using eq. 3.9. The difference of slope between the two systems is a direct indication of the extra damping induced by the spin pumping from Py into Pt. (b) Change of resonance field with the *r.f.* wave frequency for the Py thin film and the Py/Pt bilayer. The dotted lines are fitted using the Kittel equation eq. 3.8 and are used for the extraction of the gyromagnetic ratio γ and the effective magnetization M_s of Py. (c) Typical shape of the electrical signal obtained by SP-FMR measurements in cavity. The FMR signal (bottom) is an anti-Lorentzian. The electrical signal is the combination of a Lorentzian and an anti-Lorentzian. Both signals have the same resonance field, indicating that the FMR drives the electrically detected signal. (d) Linear increase of the amplitudes of the Lorentzian and anti-Lorentzian components of the electrical signal displayed in the top panel of (c). The linear evolution indicates that in this range of *r.f.* powers the system remains in its linear response regime.

The magnetization M_s and gyromagnetic ratio γ are extracted by fitting the data displayed in Fig. 3.5b using eq. 3.8. Here we neglected the effect of H_{uni}. The damping, inhomogeneous broadening, Landé factors and magnetizations for the Py and Py/Pt stacks are displayed in Table 3.1. The magnetization and Landé factor of Py are mostly independent of the presence of Pt. As mentioned before, the damping increases due to the spin pumping into Pt, while the inhomogeneous broadening is larger for Py deposited directly on SiO$_2$. From these parameters we can extract the spin current j_{pumped} injected into Pt from the Py layer, which is equal to $6.12 \cdot 10^6\ \mathrm{A \cdot m^{-2}}$.

The ISHE is measured by placing the sample in a MS5 3loop–2gap resonant cavity [268]. This cavity contains standing *r.f.* electromagnetic waves. The center of the cavity corresponds to a node of electric field and to an antinode of the magnetic one. This allows to minimize the charge related spin rectification effects [217, 225] which usually complicate the analysis of SP-FMR experiments [226]. The sample is also submitted to a static magnetic field. When sweeping the amplitude of this d.c. field, we eventually reach the FMR conditions. The resonance is observed by the lock-in detection of the *r.f.* power resonating off the cavity, which gives a measurement of $\partial\chi''/\partial H_{ext}$, similarly to the case of broadband set-up (Fig. 3.5c). At the resonance field, the electrical measurements of the ISHE signal, Fig. 3.5c, gives a Lorentzian signal with a maximum at the FMR conditions indicated by the FMR signal of Fig. 3.5c bottom panel. The electrical signal is mostly symmetric with respect to the resonance field, but also possesses a small antisymmetric component resulting from the planar Hall effect [226]. The symmetric shape could actually originates from rectifications effects or thermal effects rather than from ISHE, and its origin needs to be carefully evaluated. To keep the description of the

FMR technique in a reasonable length, these rectification effects and the process used to disentangle them from the ISHE signals will not be described here, as they have been detailled in previous publications from my group [227, 226, 268]. To cite a few: symmetry of the electrical signal around the resonance field and angular dependencies are of great importance in that respect.

	α_G	ΔH_0 (mT)	g	M_s ($\mathrm{kA \cdot m^{-1}}$)
SiO_2/Py	$7.04 \cdot 10^{-3}$	0.063	2.13	748
SiO_2/Py/Pt	$9.79 \cdot 10^{-3}$	0.104	2.11	724

Table 3.1: FMR characteristic quantities extracted for SiO_2/Py and SiO_2/Py/Pt stacks using the broadband measurements described in Fig. 3.5a and 3.5b. The Landé factror g gives the gyromagnetic ratio $\gamma = g\mu_B/\hbar$, with μ_B the Bohr magneton.

In the case of our stack, the maximum of this electrical signal corresponds to V_{ISHE}. This signal varies linearly with the applied field power, which indicates that the ISHE response remains in the linear regime (Fig. 3.5d). At 200 mW, we detected $V_{ISHE} = 22.7\,\mu V$. To obtain a generated ISHE voltage independent of the *r.f.* power, we normalize it by the resistance and the amplitude of the *r.f.* field $h_{rf} = 2\sqrt{PQ/\kappa}$ with $\kappa = 500\,\mathrm{A \cdot kg^{-1}}$, an expression given by the constructor of the cavity. The quality factor of the cavity is directly calibrated on the set-up. For a power of 200 mW and a quality factor Q=500, the *r.f.* field amplitude is $h_{rf} = 0.89$ G. Finally, the only missing parameter to extract the spin Hall angle of Pt is its spin diffusion length, estimated to be 3.3 nm [67] using the non-local transport measurements described in the Chapter 1. From this analysis, we obtained a spin Hall angle $\theta_{SHE} = 0.04 \pm 0.01$, which is close to the value found commonly in literature on platinum with similar resistivity [228].

One must note here that the analysis described here is a rather rough estimation of the spin Hall angle of platinum, used to illustrate the spin pumping technique. As previously mentioned, rectifications effects such as the planar Hall effect, anomalous Hall Effect and thermal effects such as the Spin Seebeck effect and the anomalous Nernst effect can also contribute to the electrical signal measured in spin pumping. The planar Hall effect can be disentangled from the spin to charge interconversion signal, using a careful symmetry analysis of the measured voltage with respect to the resonance field and by rotating the static field direction. The thermal effects, however, have symmetries similar to the ISHE signal. In a study we published in Journal of Applied Physics, which I will not detail here, we have shown that these thermal contributions are negligible in the Py/Pt system, by analysing the static field sweep speed dependence of the electrical signal [227].

3.2.2 Independence of the Inverse Spin Hall Effect with the Magnetic Phase in Thin NiCu Films

In this paragraph I will discuss the link between the magnetic order and the spin-charge interconversion in NiCu. First, I will demonstrate that, despite being a light metal, NiCu harbors a large spin-Hall angle, comparable to that of platinum. Second, I will present measurements of the spin-charge interconversion in NiCu across its transition temperature. This study has been previously published in Physical Review Letters, and the following section can be considered as an extension of this publication [243].

NiCu: a light metal with a large spin Hall angle

The spin-charge interconversion in NiCu was measured by SP-FMR experiments in cavity, using the set-up described in section 3.2.1. To this end, we used $Co_{53}Fe_{27}B_{20}$ (CFB) as a spin injector, because its Gilbert damping, magnetization, and resistivity are nearly temperature independent in the studied temperature range [239], and since its self-induced SHE is small [240]. Using magnetron sputtering, we grew a 15 nm thick CFB layer onto a Si/SiO_2 substrate. The NiCu layer was sputtered on top, directly from $Ni_{60}Cu_{40}$ and $Ni_{50}Cu_{50}$ targets. The samples were further protected from oxidation by a 3 nm Al layer. To compare the spin to charge conversion efficiency of NiCu with that of platinum, we also grew a CFB(15)/Pt(15)/Al(3) sample (the numbers in parenthesis indicate the thicknesses in nm), using the same deposition chamber. The samples were cut into slabs of length L = 2.4 mm and width W = 0.4 mm prior to the interconversion measurement.

The high ISHE signal in paramagnetic NiCu was first confirmed by performing the SP-FMR measurement in the CFB/NiCu/Al and CFB/Pt/Al stacks, as well as in a reference CFB(15)/Al(3) bilayer at room temperature. Remarkably, the spin-pumping signal in CFB/NiCu has the same sign and a similar amplitude as that of the CFB/Pt sample, as can be seen in Fig. 3.6a. The signal is dominated by a symmetric contribution V_{sym}, suggesting that it originates from the ISHE, as further confirmed by out-of-plane angular dependence measurements of the interconversion [225, 226].

We also performed broadband FMR measurements from 4 to 24 GHz using a broadband stripline with lock-in

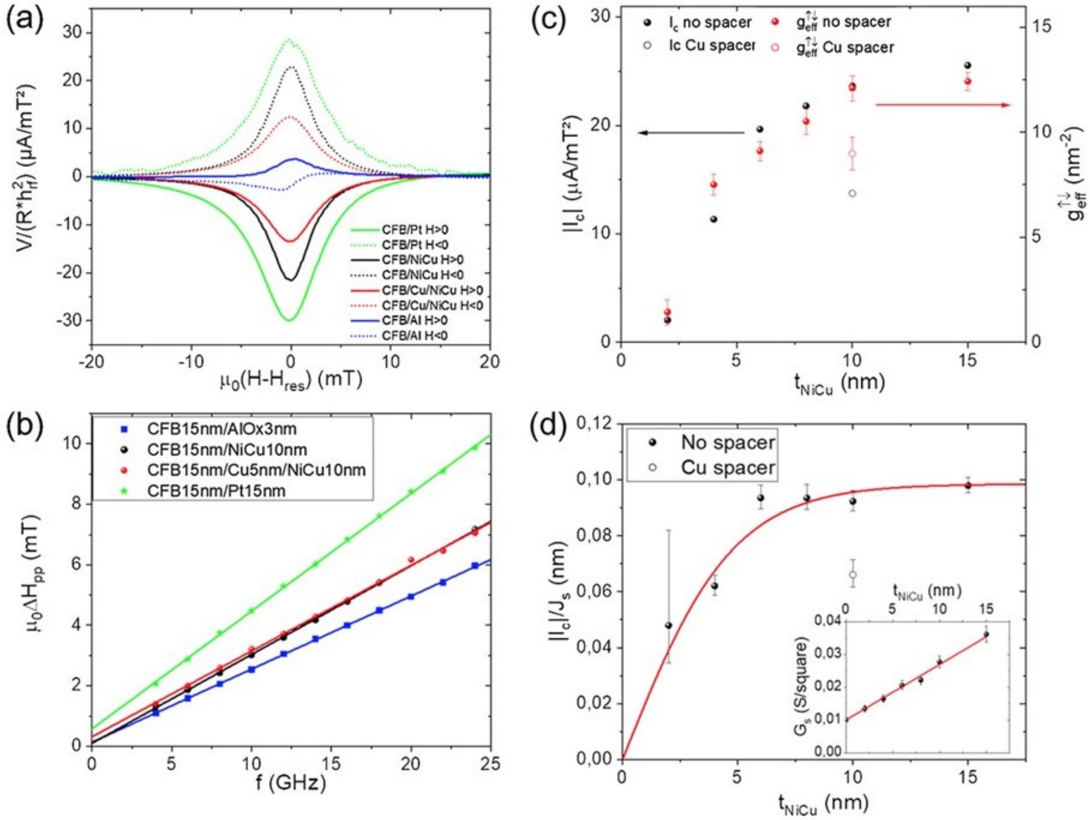

Figure 3.6: (a) Spin-pumping signals in CFB(15)/Pt(15), CFB(15)/Ni$_{60}$Cu$_{40}$(10), CFB(15)/Cu(5)/Ni$_{60}$Cu$_{40}$(10), and in the CFB(15)/Al(3) reference sample. The signals are given in the parallel (H > 0) and antiparallel (H < 0) configurations. (b) Broadband measurements of the FMR linewidth of CFB(15)/Pt(15), CFB(15)/Ni$_{60}$Cu$_{40}$(10), CFB(15)/Cu(5)Ni$_{60}$Cu$_{40}$(10), and in the CFB(15)/Al(3) samples. (c) Effective spin mixing conductance and absolute value of the charge current production, as a function of the NiCu film thickness t_{NiCu}. (d) Thickness dependence of the absolute value of the charge current production divided by the spin current. The fit in red is performed using Eq. (2). The inset shows the thickness dependence of the sheet conductance. The measurements were performed at room temperature, all thicknesses are in nm.

detection. By applying the Kittel formula (eq. 3.8), we extracted the magnetic properties of the CFB film. The obtained values are close to previous observations in Co$_{53}$Fe$_{27}$B$_{20}$, with an effective magnetization of 890 ± 20 kA/m and a gyromagnetic ratio of $(1.870 \pm 0.005) \times 10^{11}\mathrm{rad\,s^{-1}T^{-1}}$ ($g = 2.130 \pm 0.005$). We extracted the Gilbert damping from the frequency dependence of the peak-to-peak linewidth ΔH_{pp} (eq. 3.9). As can be seen from the different slopes of ΔH_{pp} in Fig. 3.6b, an enhancement of the damping is observed from $(6.64 \pm 0.03) \times 10^{-3}$ in CFB(15)/Al(3) to $(8.05 \pm 0.05) \times 10^{-3}$ in the CFB(15)/Ni$_{60}$Cu$_{40}$(10) or $(1.070 \pm 0.006) \times 10^{-2}$ in CFB(15)/Pt(15). The extra-damping indicates the existence of spin injection via spin pumping, and possibly to other effects such as magnetic proximity [207] and spin memory loss [46].

We performed cavity spin pumping as well as broadband measurements as a function of the thickness of the Ni$_{60}$Cu$_{40}$(10) layer (from 2 to 15 nm), to evaluate both the spin diffusion length l_{sf} and the spin Hall angle (SHA) θ_{SHE} of NiCu. The broadband FMR measurement at room temperature shows that the extracted magnetic properties of the CFB are unaffected by the NiCu layer, except for the damping that increases with the NiCu thickness, saturating at 10 nm (Fig. 3.6c). The slow increase of the damping in ultrathin NiCu layers as a function of its thickness is not compatible with a large SML or proximity effect. We also grew a sample with a 5 nm insertion of Cu between the CFB and NiCu in order to suppress any magnetic proximity effects. The spin signal is lowered with the Cu spacer as can be seen in Fig. 3.6a, possibly because of SML at the CoFeB/Cu interface. The damping is slightly reduced from $(8.05 \pm 0.05) \times 10^{-3}$ to $(7.75 \pm 0.05) \times 10^{-3}$, as shown in Fig. 3.6c, showing evidence of the minor role of the magnetic proximity effect in the damping enhancement. From the broadband FMR measurement we calculate the effective spin mixing conductance $g_{eff}^{\uparrow\downarrow}$. The obtained values of $g_{eff}^{\uparrow\downarrow}$ as well as the absolute value of the charge current production at resonance

$$I_c = \frac{V_{sym}(H > 0) - V_{sym}(H < 0)}{2Rh_{rf}^2}$$

are plotted in Fig. 3.6c, with and without the Cu spacer. The small contribution of CFB to the spin-pumping signal was separately determined on a CFB(15)/Al(3) layer (Fig. 3.6a) and subtracted from the signal. The spin mixing conductance and spin-pumping signal saturate at 10 nm, with values of $12.4 \pm 0.4\,\mathrm{nm}^{-2}$ and $25\,\mu\mathrm{A/mT}^2$, respectively. Owing to the apparent minor role of magnetic proximity effect and SML in the CFB/NiCu bilayers [46], the spin current is evaluated using the conventional spin-pumping model described in section 3.2.1, using eq. 3.13.

The resistivity ρ of the NiCu layer is $60 \pm 3\,\mu\Omega\,\mathrm{cm}$, and independent on the thickness (cf. inset of Fig. 3.6d), in line with the short mean free path in this alloy [208]. We can thus assume a constant spin diffusion length and spin Hall angle for the different NiCu thicknesses. Combining eq. 3.11 and 3.17, it is then possible to extract l_{sf} and θ_{SHE}. From the fit in Fig. 3.6d we obtained $l_{sf} = 2.4 \pm 0.3\,\mathrm{nm}$ and $\theta_{SHE} = 4.1^{+0.6}_{-0.4}$ %. Contrary to Ref. [203], we did not observe any remarkable SML or magnetic proximity effect, which might explain why our estimated SHA is much lower. The value of I_c/j_s is 32% smaller with the Cu interlayer, compared to the case of the direct contact. This is likely due to the SML, which is typically of 20% to 30% at the CoFe/Cu [209] and Co/Cu [210] interfaces. These results demonstrate the possibility to obtain a high spin Hall angle, comparable to the one of platinum in a light material.

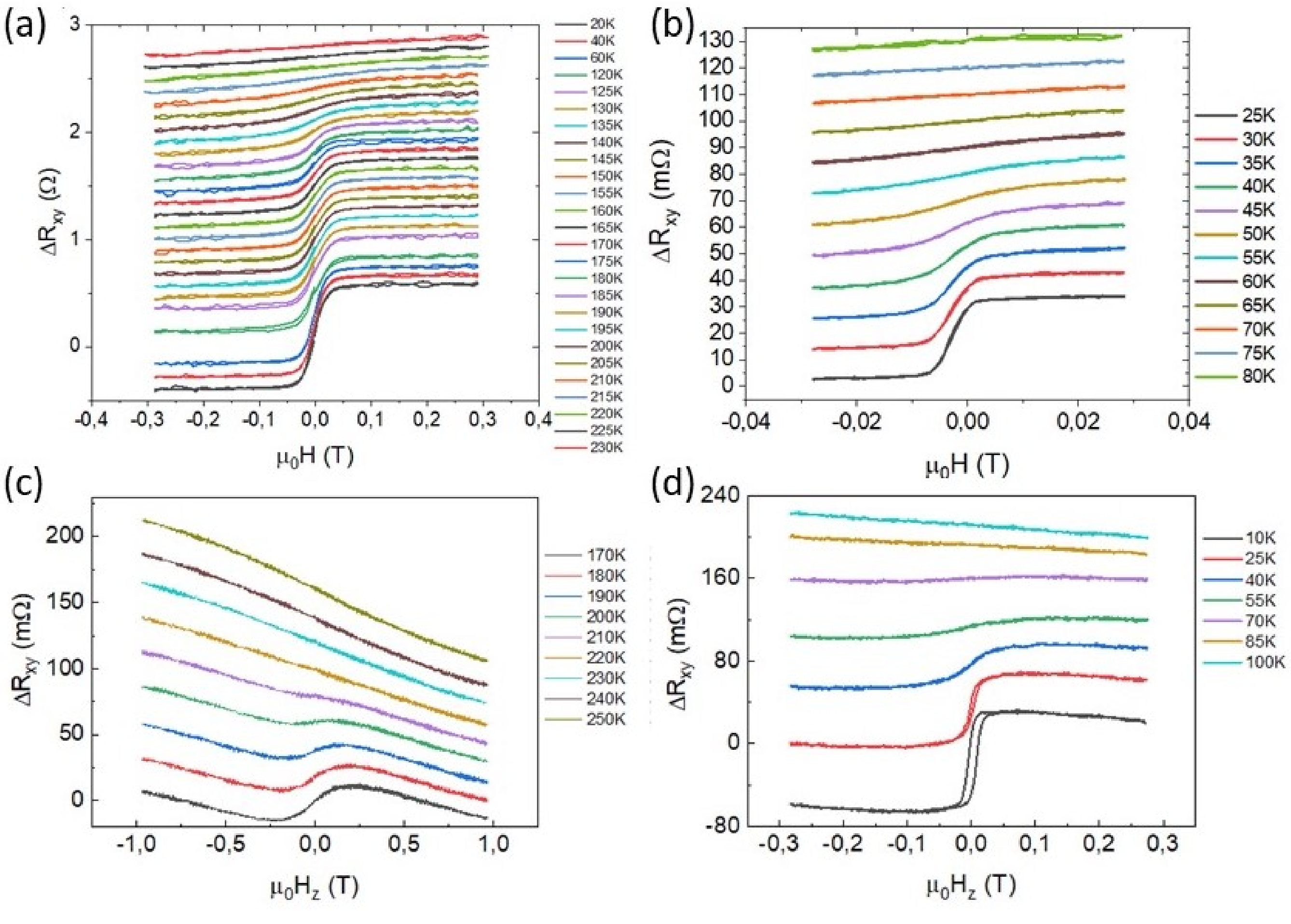

Figure 3.7: (a) Temperature dependence of the Hall resistance ΔR_{xy} versus the external magnetic field H in (a) $\mathrm{Ni}_{60}\mathrm{Cu}_{40}$ and (b) $\mathrm{Ni}_{50}\mathrm{Cu}_{50}$ (c) CFB(15)/Cu(5)/$\mathrm{Ni}_{60}\mathrm{Cu}_{40}$(10), (d) CFB(15)/Cu(5)/$\mathrm{Ni}_{50}\mathrm{Cu}_{50}$(10) thin films deposited on SiO_2. The curves are shifted along the vertical axis for clarity.

Measurement of the spin-charge interconversion in NiCu across its transition temperature

In order to investigate the effect of the NiCu paramagnetic-to-ferromagnetic phase transition on the spin Hall effect, we performed a temperature dependent measurement of the spin-charge interconversion. This has been done in 10 nm thick NiCu film with 60:40 and 50:50 compositions, with and without Cu insertion.

First, we checked the values of the critical temperatures of $Ni_{60}Cu_{40}$ and $Ni_{50}Cu_{50}$, which are expected to be below room temperature for these two materials. We performed R_{xy} measurement in a Hall configuration, in squared macroscopic devices of NiCu deposited on SiO_2, and with an out of plane applied magnetic field (Fig. 3.7a and 3.7b). At low temperature one observes the characteristic Anomalous Hall Effect signal, with two different values for positive and negative fields. When increasing the temperature, only remains a linear evolution, characteristic of the normal Hall effect, which indicates the transition from the ferromagnetic to the paramagnetic phase at 60 K for $Ni_{50}Cu_{50}$ and 210 K for $Ni_{60}Cu_{40}$. We performed similar measurements on CFB/NiCu bilayers, in order to make sure that the critical temperature is not modified by the proximity effect with CFB. The results are shown in Fig. 3.7c and 3.7d. The trend in the AHE modification is the same as in the NiCu-only thin films, with an AHE signal disappearing at similar temperatures. The magnetization of CFB is not saturated at 1 T, so that its AHE appears as a straight line above the Curie temperature of NiCu. These results confirm that the Curie temperature of the film is not modified by the proximity with CFB or the Cu interlayer. This also evidences a limited interdiffusion when avoiding high temperature baking [206].

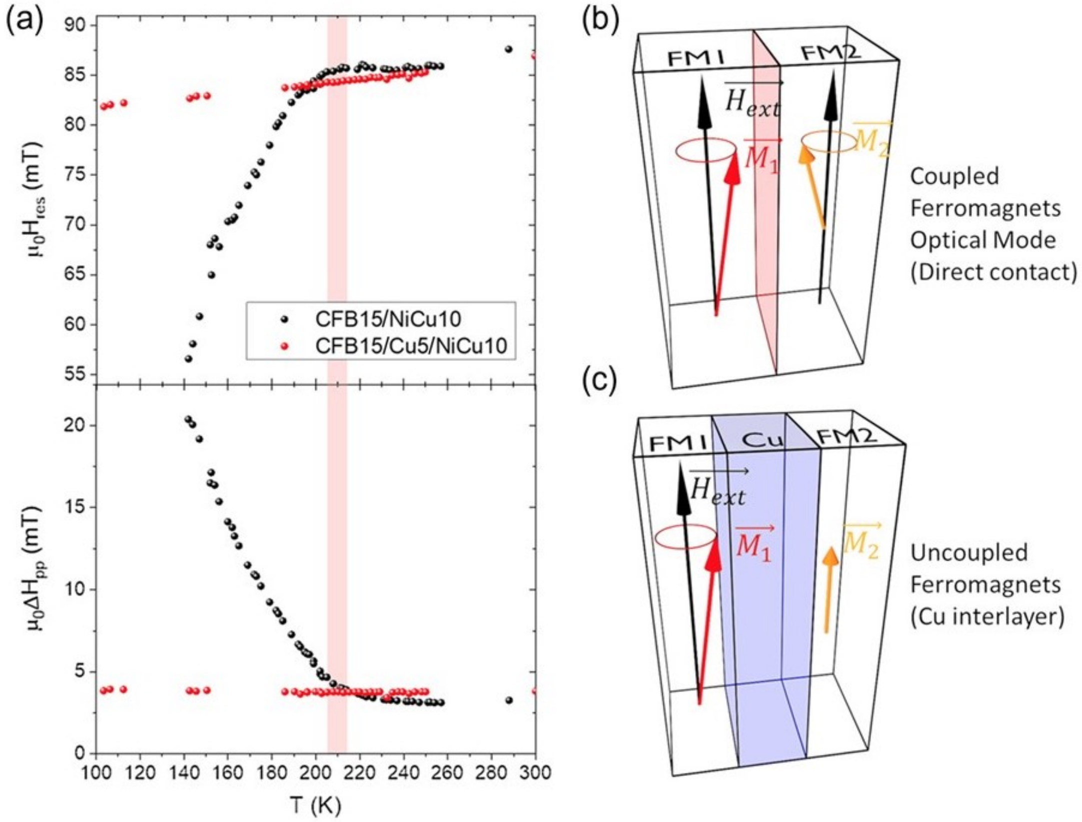

Figure 3.8: (a) Resonance field and linewidth of CFB as a function of the temperature in $CFB(15)/Ni_{60}Cu_{40}(10)$ and $CFB(15)/Cu(5)/Ni_{60}Cu_{40}(10)$. The red shaded area depicts the Curie temperature T_c $(210 \pm 5$ K) of $Ni_{60}Cu_{40}$. (b) In direct contact at resonance both magnetization vectors of FM1 (CFB) and FM2 (NiCu) precess out of phase for the optical mode. (c) When the ferromagnets are decoupled using a thick enough Cu interlayer, only FM1, here CFB, is excited at its resonance.

We then performed temperature dependent SP-FMR measurements of the spin-charge interconversion, starting with an analysis of the FMR parameter of the $CFB/Ni_{60}Cu_{40}$ and $CFB/Cu/Ni_{60}Cu_{40}$ stacks. Fig. 3.8a clearly shows that the resonant properties of both samples are similar around room temperature, but their behaviors at low temperature are strikingly different. In the absence of the Cu interlayer, the resonance field decreases below 210 K, while the linewidth increases. These effects are not observed with the 5 nm Cu spacer. Importantly, this change occurs around the paramagnetic to ferromagnetic transition temperature of $Ni_{60}Cu_{40}$, so that it can be explained by the exchange coupling between the two adjacent CFB and NiCu layers.

Indeed, when CFB is in direct contact with NiCu and below T_c, an exchange coupling between the two layers arises, so that the magnetization vectors of the two ferromagnets precess together either in phase (acoustic mode) or out of phase (optical mode). The spin transport can be of a magnonic nature and is not limited to electrons, leading to strong modifications of the resonance field and linewidth [211, 212]. The lowering of the resonance field in Fig. 3.8a is associated to the optical mode (out of phase precession) depicted in Fig. 3.8b. Such a decrease becomes larger when the temperature is lowered, due to both the increased magnetization of NiCu and the strengthening of the exchange coupling. With the 5 nm Cu spacer the coupling is suppressed and the electronic transport prevails. The suppression of the coupling is revealed by the absence of any noticeable change of the resonance field and linewidth around the Curie temperature seen in Fig. 3.8a. As the two magnetic layers are not coupled, when CFB is at resonance the magnetization of NiCu is out of resonance (*i.e.*, static) as depicted in Fig. 3.8c, so that the dynamical properties remain unaffected [212]. We could not observe the resonance of $Ni_{60}Cu_{40}$ in the uncoupled case or the acoustic mode in direct contact, either using the lock-in detection of the spectrometer or the electrical detection. This is likely due to the broad linewidth of the resonance peak of NiCu [253].

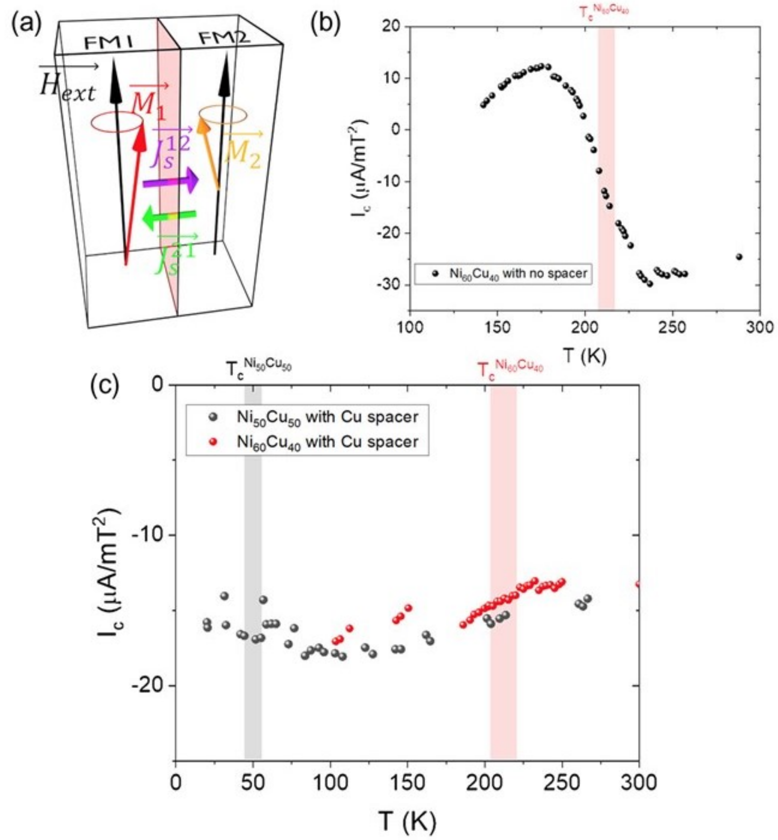

Figure 3.9: (a) Schematic representation of the spin-pumping process below Tc (optical mode) for the direct contact. Spin currents are injected from FM1 to FM2 (J_s^{12}) and from FM2 to FM1 (J_{12}^{x}) with a 180° phase shift. (b) Spin-pumping signal in a coupled bilayer without Cu spacer. In red the T_c of $Ni_{60}Cu_{40}$. (c) ISHE signal as a function of temperature in CFB(15)/Cu(5)/$Ni_{60}Cu_{40}$ and CFB(15)/Cu(5)/$Ni_{50}Cu_{50}$ samples with different Curie temperatures (${T_c}^{Ni_{60}Cu_{40}}$ shown in red and ${T_c}^{Ni_{50}Cu_{50}}$ in grey).

The charge current production at resonance I_c as a function of the temperature was measured with and without Cu insertion. As can be seen in Fig. 3.9b in the exchange-coupled system (without the Cu insertion), I_c is negative above the Curie temperature. When lowering the temperature however, the current production is abruptly modified around T_c, and even changes sign below 200 K. Without further measurements, one might conclude that the SHE is strongly affected by the ferromagnetic transition, and changes sign on a narrow temperature range. However, in the case of the direct contact, the strong modification of the resonance properties across the magnetic phase transition makes it impossible to accurately evaluate the spin current injected at resonance. Moreover, the CFB and NiCu layers are coupled and both precessing at resonance, so that a spin current is injected from CFB toward NiCu and from NiCu toward CFB, as depicted in Fig. 3.9a. The exact spin accumulation profile cannot be evaluated, and a non-negligible ISHE signal from CFB could start contributing [234]. For these reasons, to properly evaluate the ISHE in NiCu below the Curie temperature it is necessary to perform the same measurement in the CFB/Cu/NiCu trilayer, to verify that such a sign change is not due to spurious effects related to the coupling. In this decoupled system, I_c is constant and does not change sign at T_c, as can be seen in Fig. 3.9c. Similarly to what is observed at room temperature, the reduced value of the produced charge current with the Cu spacer is likely due to the SML. The absence of any noticeable effect on the transition is also observed for the stoichiometry $Ni_{50}Cu_{50}$ (T_c = 60 K). In these trilayers the spin signal as well as the resonant properties of the CFB layer are independent of the temperature: the same spin current injection and charge current production are observed in both the paramagnetic and the ferromagnetic states. We could not observe any anomaly around the Curie temperature evidencing the SHE mechanism differs from that of NiPd [214]. Therefore, the large ISHE in NiCu alloys in the paramagnetic phase is equal to the that in the ferromagnetic phase, and thus unrelated to the magnetic order. This feature is supported by the observation that the spin Hall angle is positive while the anomalous Hall angle is negative, in agreement with the calculations of the intrinsic effects in ferromagnetic Ni [254, 92, 219]. This suggests that the two mechanisms in NiCu are dominated by the intrinsic contribution. It also confirms previous observations by Omori et al. in Ref. [96] that the anomalous and spin Hall effects can be of opposite sign. For both $Ni_{60}Cu_{40}$ and $Ni_{50}Cu_{50}$, the figure of merit of the spin to charge current conversion $\theta_{SHE} l_{sf}$ is of 0.1 nm, independently on the stoichiometry, as expected for alloys of similar resistivity [72]. This value is comparable to that of Pt (0.18 nm) [46, 79], thereby allowing for an efficient detection of spin currents.

The large SHA in paramagnetic NiCu was previously explained by similarities between the calculated band structure of paramagnetic nickel and platinum around the Fermi level (section 3.1.1) [203], while the calculated band structure of ferromagnetic nickel in Ref. [203] does not resemble to that of Pt. This is not compatible with our observation of a large magnetic-phase-independent ISHE in NiCu. On the contrary, our observations suggest that the band structure is not particularly affected by the phase transition, or that these possible changes do not reflect in modification of the spin Hall effect properties. The modifications of the band structure occurring at the ferromagnetic transition, and in particular the shift of the bands associated with the collapse of the exchange splitting are still debated with conflicting results for nickel [255, 220, 256]. The ferromagnetic-paramagnetic transition is characterized by the loss of the long-range ferromagnetic order but is not necessarily associated with the collapse of exchange splitting that occurs at higher temperature, as observed in $SrRuO_3$ or Fe [257, 258]. Indeed, while the transition from the ferromagnetic to paramagnetic state occurs due to single particle excitation in the Stoner model, which leads the energy shift between the two spin populations to disappear, this is not necessarily the case for the partially localized model. In this second case, the local magnetic moments are not quenched, but are randomized by thermal magnons, so that even though the total magnetization averaged out to zero above the critical temperature, the band structure of the material is not modified [204]. The observation of a phase independent SHE therefore indicates that the itinerant Stoner model of ferromagnetism does not describe well the ferromagnetic-paramagnetic phase transition in NiCu. The observed behavior points toward a Heisenberg-like localized character of the magnetism supported by 3d electrons in NiCu alloys, in line with previous experimental and theoretical results showing that local moments associated to the nearest neighbor environment of nickel atoms are at the origin of magnetism [259, 260]. Thus, our experimental results could be explained by the similarity of the band structure of NiCu in the paramagnetic and ferromagnetic phase.

In summary, using spin-pumping FMR in CFB/Cu/NiCu with two different stoichiometries, we measured a large positive spin Hall angle in NiCu, comparable to that of Pt. The SHA is insensitive to the magnetic phase when magnetization and injected spins are aligned. This suggests that, in NiCu, the effect of the ferromagnetic-paramagnetic transition on the SHE has to be understood using a localized Heisenberg picture. These results also emphasize the importance of avoiding direct contact to properly measure the ISHE in a ferromagnet for resonance measurements. Direct contact leads to drastic changes in the dynamic response that are hard to estimate. This might explain the discrepancy between measurements of the spin Hall effect in the same material but in contact with different ferromagnets [236, 261]. Moreover, our results show that the ferromagnetic order does not necessarily play a key role in the large spin Hall effect of ferromagnets. A large variety of alloys composed of Ni, Co, or Fe in the ferromagnetic or paramagnetic phase could therefore be explored as spin current generators and detectors, extending the number of possible light metal systems with a large SHE.

In addition to the conclusion that the ferromagnetic order plays no role on the SHE in NiCu, these results provide important information regarding the anisotropy of the interconversion. As mentioned in section 3.1.2, the spin Hall angle in FMs has two contributions. One, denoted θ_{SHE} is independent of the magnetization direction, while the other,

θ_{SAHE} provides an interconversion that depends on it. The component θ_{SAHE} is expected to vanish when the material is in its paramagnetic phase, since it is expected to originate from the polarization of the charge current produced by the AHE. Since the charge current measured by the SP-FMR methods is proportional to the interconversion efficiency $(\theta_{SHE}+\theta_{SAHE})l_{sf}$ (eq. 3.6 and 3.17), its independence with the magnetic order indicates that $\theta_{SAHE} \ll \theta_{SHE}$ in NiCu, so that the spin Hall angle in NiCu is independent with the magnetization direction. However, the isotropy of the spin Hall angle does not mean that the interconversion is isotropic in this material. Indeed, as shown in the first chapter, the spin relaxation length in FMs depends on the relative angle between the spin current polarization and the magnetization direction. For a polarization collinear with the magnetization, the efficiency of the interconversion will therefore write $(\theta_{SHE}+\theta_{SAHE})l_{sf}$, while in a transverse situation it will write $\theta_{SHE}\lambda_{\perp}$ with $\lambda_{\perp}$ the transverse spin relaxation length introduced in the first chapter.

In SP-FMR measurements, the polarization of the spin current is always collinear with the magnetization of NiCu, because of the d.c. applied magnetic field that saturates the magnetization of both CFB and NiCu in the same direction, so that the anisotropy of the interconversion could not be investigated using this set-up. In the next section of this chapter, I will present a measurement of the spin-absorption isotropy in NiCu using a modified design of lateral spin valve, which allows an independent control of the injected current polarization and of the magnetization direction of the ferromagnet.

3.3 Isotropy of the Inverse Spin Hall Effect in dilute 3d ferromagnets

Lateral spin valves have been extensively used for the measurement of the spin Hall effect in various materials, including ferromagnets. However, the currently used geometry allows only the measurement of the interconversion for a spin current polarization collinear to the FM-SHE material magnetization. In the next section, I will expose the basic principle of SHE measurements in lateral spin valves, and highlight their limitations for the measurement of the spin-charge interconversion anisotropy in 3d FMs. I will then present a new geometry of lateral spin valves which overcomes these limitations, and describe the measurement of the spin-charge interconversion anisotropy in NiCu and NiPd, two dilute low T_c 3d ferromagnets with a large spin-orbit coupling.

3.3.1 Spin-Charge interconversion anisotropy measurements using lateral spin valves

The LSVs presented in Chapter 2 and used to study spin transport phenomena also permit to measure the SHE in metals, using the geometry presented for spin absorption experiments in the section 1.3 of the first chapter. This is achieved by replacing the non-local measurement configuration (Fig. 3.10b) by the SHE measurement configuration (Fig. 3.10a). If the spin current, flowing into the absorber along the Z-direction, has a spin polarization along the X-direction, a charge current is produced along the Y-direction and measured as a potential drop between the two ends of the absorber. The advantage of measuring the interconversion on lateral spin valves lies in the possibility to combine these two measurement configurations to obtain a d.c. electrical measurement on both the spin-charge interconversion signal (Fig. 3.10b) and the spin transport parameters in the absorber (Fig. 3.10a), in the same device. Despite being somewhat difficult to fabricate, the simplicity of the measurement method and the absence of serious spurious effects on the measured signal caused these devices to be extensively used for the measurement of the ISHE and SHE in various non-magnetic and magnetic systems. However, they do not allow to measure the anisotropy of the spin charge interconversion in ferromagnetic materials presented in the section 1.2. This comes from the fact that the polarization of the spin current that flows into the SHE material is along the magnetization of the injecting electrode. At low fields, the spin current is therefore polarized along the Y-direction, so that the ISHE in the absorber does not generate a potential drop along the Y-direction. The SHE in lateral spin valves is then measured by applying a magnetic field along the X-direction, that saturates the magnetization transverse to the injector easy magnetization axis, setting the spin polarization along X, so that a ISHE-driven potential drop can be measured in the SHE wire. Since the injector in LSVs is typically 50 to 100 nm wide, a large field is required to saturate the magnetization along the X-direction. A typical ISHE signal from Ref. [96], obtained using a Py wire for the SHE material, is displayed in Fig. 3.10c. From this measurement of the interconversion in Py, one can see why this LSV geometry is not suited for the measurement of the SHE anisotropy in FMs. Indeed, the magnetic field will saturate both the injector and the FM-SHE material in the same direction, so that the interconversion can be measured only when the spin polarization and the FM-SHE material magnetization are collinear.

The anisotropy of the spin-charge interconversion in ferromagnetic materials cannot be measured using the geometry presented in Fig. 3.10b, due to the impossibility to control independently the polarization of the spin current and the magnetization direction of the ferromagnetic absorber. In order to overcome this limitation, I propose a new geometry of

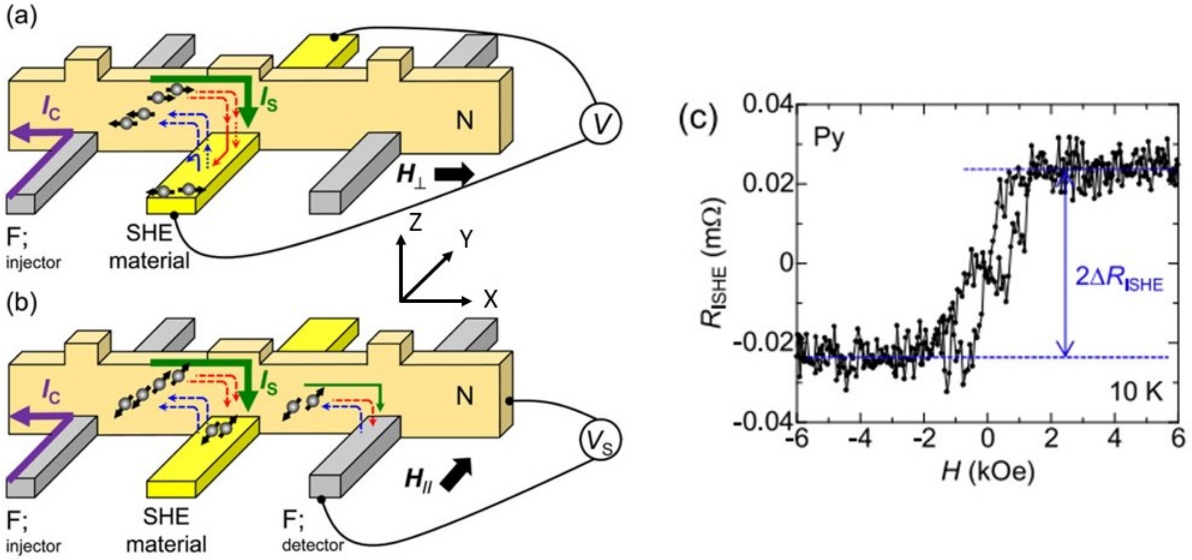

Figure 3.10: (a) Measurement configuration of the ISHE and (b) of the non-local signal (image from Ref. [74]). (c) Typical ISHE signal obtained using the ISHE measurement configuration presented in (a) using a Py wire as a SHE material (image from Ref. [96]).

lateral spin valves, which allows to perform low-field measurement of the ISHE. The geometry of the device is presented in Fig. 3.11a. Here, the easy magnetization axis of the injecting and detecting electrodes are rotated by 90 degrees with respect to the geometry of Fig. 3.10, so that the low field spin polarization is geometrically constrained to be along the X-direction at zero field. The ISHE can then be measured during a low field sweep. The non-local measurement configuration for a device without absorber is displayed in Fig. 3.11b. The corresponding non-local signal is shown in Fig. 3.11e with the associated magnetic configurations of the ferromagnetic electrodes in Fig. 3.11f, which shows the signal obtained for a parallel and antiparallel configurations of the injecting and detecting electrodes. The insertion of an absorber, here made of Py (Fig. 3.11c), reduces the amplitude of the non-local signal and allows to observe the non-collinear relaxation processes already described in the Fig. 3.11g of chapter 2. The magnetic states associated with the field sweep are shown in Fig. 3.11h. When starting at a high negative magnetic field, the injector, detector and Py absorber are saturated in the -X direction. We are then in the collinear configuration that corresponds to the state A. Increasing the field to a zero value leads to the state B, where the absorber is transverse to the injector magnetization and therefore to the spin current polarization, so that the system is in a transverse configuration. When the field goes toward positive values, the Py absorber magnetization saturates toward +X and the detecting electrode magnetization switches, leading to the collinear antiparallel state C. Further increase the field brings the magnetic configuration back to a collinear parallel state (D). When the field decreases, the magnetic configuration goes back to the transverse parallel configuration (E), with an absorber magnetization in the opposite direction due to the slight magnetic field misalignment with the device. At negative fields, the detecting electrode switches, putting the system in the collinear antiparallel configuration F. The field is then swept back directly to zero, in order to go to the antiparallel transverse configuration G. The signal difference between A and F therefore corresponds to the parallel spin signal $\Delta R_{||}$, while the difference between B and G is the transverse spin signal $\Delta R_{\perp}$, following the notations of Chapter 2. As expected, $\Delta R_{||} > \Delta R_{\perp}$ due to the higher efficiency of the transverse spin relaxation processes. The signal shown in Fig. 3.11g shows that it is possible to independently control the spin current polarization and the injector magnetization, which corresponds to what has been achieved in the second chapter. However, by changing the contacts of the measurement configuration described in Fig. 3.11d, it is now additionally possible to measure the spin to charge interconversion anisotropy in the FM, by extracting independently θ_{SHE} and θ_{SAHE}.

In the context of the device introduced in Fig. 3.11a, the charge current $\boldsymbol{j}_c$ produced by the spin to charge interconversion process in a ferromagnetic material can be obtained for a SHE material magnetization rotating in the xy plane, and a spin current polarization sets along the X-direction. The spin current flowing into the absorber in the Z-direction is polarized along $\hat{x}$ so that it writes $\boldsymbol{j}_z = j_z\hat{x}$. The direction of the absorber magnetization writes $\hat{m} = \cos\phi\hat{x} + \sin\phi\hat{y}$, so that the charge current produced in the $\hat{y}$ direction given by eq. 3.6 writes:

$$-\boldsymbol{j}_c \cdot \hat{y} = j_{zx}(\theta_{SAHE}\sin^2\phi + \theta_{SHE})$$

For an absorber magnetization transverse to the spin current polarization ($\phi = 0$ or π), only θ_{SHE} contributes to the interconversion. Furthermore, when reversing the magnetization direction of the injector from $\hat{x}$ to $-\hat{x}$, one changes the polarization direction of the spin currents without changing its amplitude, so that $j_{z-x} = -j_{zx}$, and the sign of the produced charge current reverses. In the parallel configuration, ($\phi = \pm\pi/2$), both θ_{SHE} and θ_{SAHE} contribute to the interconversion. Furthermore, since the sinus is squared, the sign of the SAHE contribution to the signal depends only on the injected spin current polarization direction. The SAHE contribution will then produce a signal with opposite signs at positive and negative high fields, and will not contribute to the interconversion at low fields. The SHE contribution will give a non-zero signal at low and high fields. Finally, the interconversion signal between high and low fields will change depending on the amplitude and sign of the SAHE, that will add up to the SHE at high field.

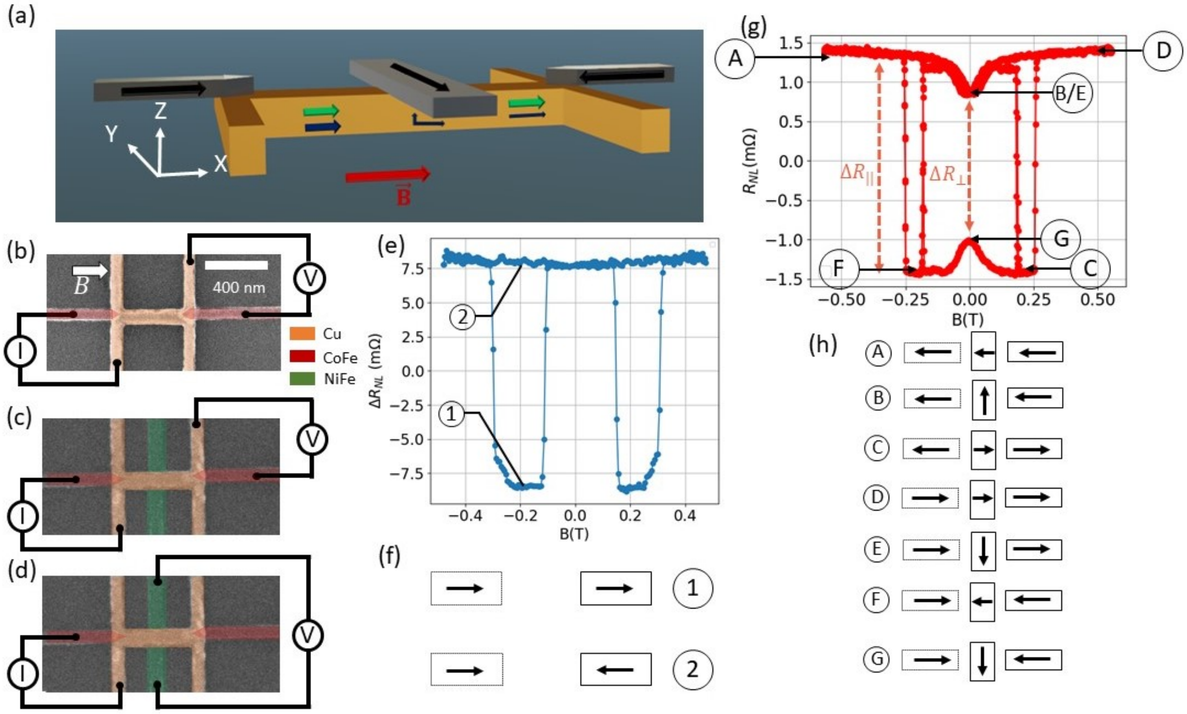

Figure 3.11: (a) Device geometry, with the FM parts in grey, and the Cu in orange. The black arrows in the FM parts represent the magnetization directions. The dark blue and green arrows within the channel represent the spin current flow direction and its polarization, respectively. The LSV has been represented with the FMs on top for the sake of clarity, but in the actual device they lie below the Cu channel to ensure a well-defined micromagnetic configurations within the electrodes and in the absorber. (b) Colored SEM image of a reference LSV without absorber, in the non-local measurement configuration. (c) Colored SEM image of a LSV with absorber, in the non-local measurement configuration. (d) Colored SEM image of a LSV in the ISHE measurement configuration. (e) Non-local signal at 12 K for a reference LSV and (f) associated magnetization state of the injector (right) and detector (left). (g) non-local signal obtained using a 100 nm wide Py absorber and (h) associated magnetic state of the injector (left), absorber (middle) and detector (right).

In the rest of the section, I will present the measurement of the interconversion anisotropy, using the device presented in Fig. 3.11, in two low critical temperature 3d FM: NiCu and NiPd.

3.3.2 Measurement of the spin-charge interconversion anisotropy in NiCu and NiPd

$Ni_{60}Cu_{40}$ (NiCu) and $Ni_{16}Pd_{84}$ (NiPd) are dilute 3d ferromagnetic materials with a large spin-orbit interaction and a small exchange coupling J. The case of NiCu has been discussed in the previous subsections. Its large spin-orbit interaction is demonstrated by a high spin Hall angle, originating from intrinsic interconversion effects, and a small spin diffusion length. The spin-orbit in NiPd originates from the presence of the heavy 4d Pd matrix, and a relatively large spin Hall angle originating from extrinsic effects has been observed in previous studies [214]. Similarly to the case of NiCu, a relatively low critical temperature ~ 200 K in NiPd indicates an exchange interaction smaller than in conventional high T_c FMs, such as NiFe, CoFe and Co. As NiCu and NiPd are paramagnetic at room temperature and ferromagnetic at low temperatures, it is thus possible to measure if the appearance of ferromagnetism leads to a SHE anisotropy.

We used CoFe injecting and detecting electrodes, and Cu for the channel of the LSV device, in order to take advantage of its long spin diffusion length and of its small interface resistance with CoFe [241, 33]. The measurements of the spin-charge interconversion anisotropy were performed in devices with absorbers made of NiCu and NiPd. As these materials are paramagnetic at room temperature and ferromagnetic at low temperatures, it is thus possible to measure if the appearance of ferromagnetism leads to an interconversion anisotropy. The devices were patterned on PMMA, by conventional e-beam on a SiO_2 substrate. The Cu, CoFe and Py wires were deposited by physical vapor deposition, while the NiCu was deposited by sputtering from a $Ni_{60}Cu_{40}$ target followed by a lift-off. $Ni_{16}Pd_{84}$ was codeposited from a Ni and a Pd targets. The CoFe electrodes were deposited in a first step, followed by the ISHE wire, and finally by the copper channel in a third step. We cleaned the interfaces *in situ* by Ion Beam Etching, prior to the deposition of the copper channel.

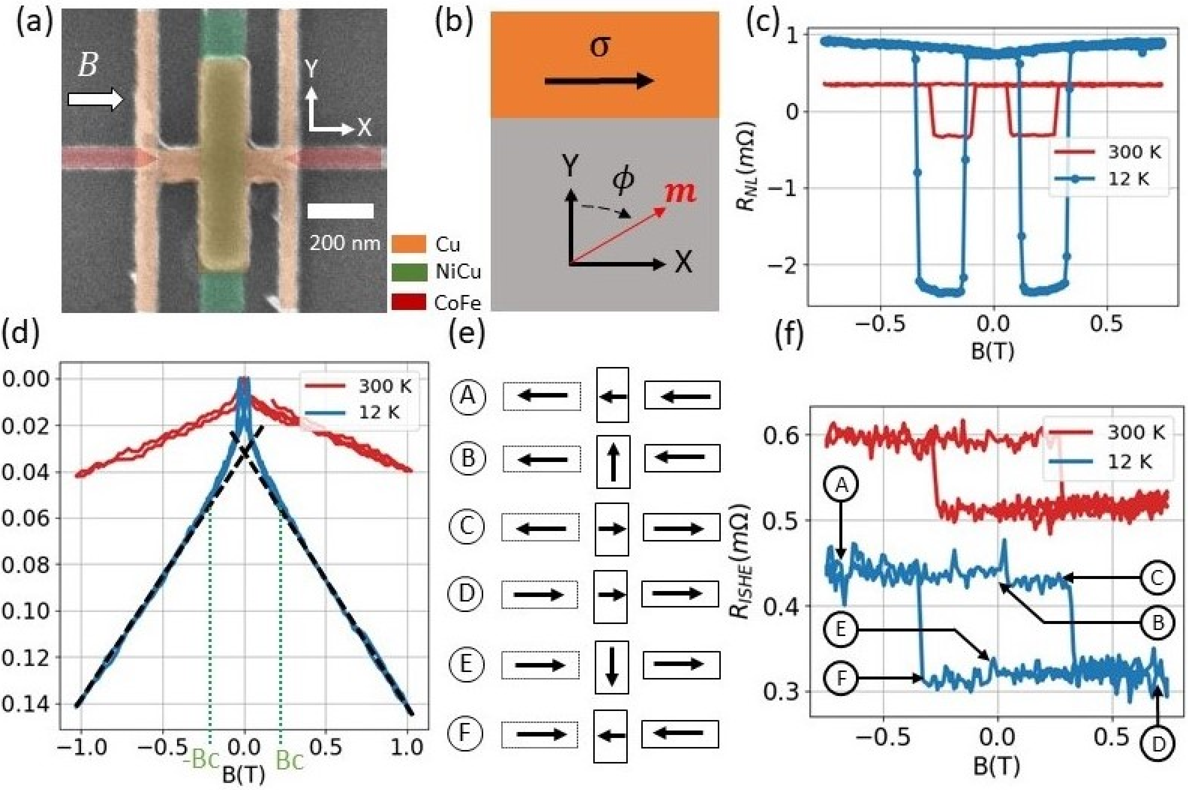

Figure 3.12: (a) Colored SEM image of a LSV with a NiCu absorber. The central part of the device is additionally covered with a Cu thin film, to avoid spurious magnetoresistive contributions to the signal. (b) Relative orientation between the spin current polarization σ and the magnetization of the absorber at low ($\phi = 0$) and high ($\phi = \pi/2$) fields. (c) Non-local signal at room temperature (red) and at 12 K (blue) using a 100 nm wide NiCu absorber. (d) Two probe magnetoresistance of the 100 nm wide NiCu absorber measured at 12 K (blue) and at room temperature (red), for a magnetic field transverse to its easy magnetization axis. (f) ISHE measurement in a NiCu absorber, made simultaneously to the non-local measurement shown in (c), and (e) scheme of the corresponding magnetic configurations.

We performed both non-local measurements (cf. Fig. 3.12c) and ISHE measurements (Fig. 3.12f) in the device presented in Fig. 3.12a. As discussed in section 3.1, the signals can be here measured at low fields, allowing the control of the angle ϕ between the absorber magnetization and the spin current polarization (cf. Fig. 3.12b). This gives access to the range of transverse and magnetic configurations presented in Fig. 3.12e, controlled by AMR measurements in Fig. 3.12d. At low fields, the magnetization of the absorber is along Y, and thus transverse to the spin current polarization, which is along X. At high fields along X, the magnetization of the absorber is along X, and thus collinear to the spin current polarization.

Before moving to the analysis of the interconversion signals presented of Fig. 3.12f, I will analyse the spin transport properties at the Cu/NiCu interface.

Extraction of the spin transport parameter at the Cu/NiCu interface

Let us firstly focus on the non-local measurements. Using the measurement configuration of Fig. 3.11c, a clear non-local signals can be obtained for devices with NiCu absorbing wire, both in the ferromagnetic and the paramagnetic phase (cf. Fig. 3.12c). Adding the absorbing NiCu wire to the LSV leads to a strong decrease of the non-local signal (going from 15 mΩ to 3.3 mΩ, cf. Fig. 3.11e vs. 3.12c), as expected for the results of chapter 2. The presence of the absorbing wire between the injecting and detecting CoFe electrodes indeed causes a partial absorption of the spin current flowing into the channel. The absorbed spin current is denoted j_z^x, as it flows in the Z direction and has a spin polarization along X. Its expression is given by the relation [133]:

$$j_z^x = G_{eff}(\hat{m})\mu^x$$

with $\hat{m}$ the magnetization direction of the absorber and μ^x the spin accumulation along the X-direction at the interface between the Cu channel and the absorber. G_{eff} is treated as an effective parameter taking into account the spin conductance $G_s = 1/\rho l_{sf}$, equal to the inverse of the spin resistance [242] (for $\hat{m} = \hat{x}$), or the spin mixing conductance $G_{\uparrow\downarrow}$ ($\hat{m} = \hat{y}$ or $\hat{z}$) [34, 242], as well as the interface resistance R_{int} (inverse of the G_{int} of eq. 1.11) and the spin memory loss term G_{SML}. The interface resistance R_{int} prevents the spin from flowing into the absorber, while the spin memory loss provides an additional relaxation channel for the spin current modeled by the conductance G_{SML}. All these terms have the effect of correcting the spin conductance of the absorbing wire, so that the spin current relaxation is controlled by an effective spin conductance [126]:

$$G_{eff} = \left(R_{int} + \frac{1}{G_s}\right)^{-1} + G_{SML}$$

Knowing the effective spin conductance and the interface resistance is central in the evaluation of the spin Hall effect, as it allows knowing the amount of spin current that flows into the absorber. In order to extract the effective spin conductance, we computed the non-local signal with FEM simulations using the GetDP-GMSH software [245, 246] (Fig. 3.13a-c). The absorber was modeled by an interfacial spin absorption zone, using the interface relaxation term described in Chapter 1 in order to take into account all the contributions previously mentioned. As expected, the non-local signal drops when increasing the value of the effective spin conductance Fig. 3.13c. This quantity was then extracted by comparing the computed non-local signal with the measured one. The extracted G_{eff} reported in table 3.2 was subsequently used to extract the interface resistance R_{int} between NiCu and Cu, by comparing it to the spin conductance G_s measured in section 3.2.2. To this end, the spin memory loss term must be neglected. The spin diffusion length l_{sf} of NiCu has previously been evaluated in section 3.2.2 by thickness dependent broadband FMR measurements. These results give a value of $l_{sf} = 2.4\,\mathrm{nm}$, and a resistivity $\rho = 600\,\Omega\cdot\mathrm{nm}$. This corresponds to a spin conductance $G_s = 0.69\cdot10^{15}\,\Omega^{-1}\cdot\mathrm{m}^{-2}$. This quantity is independent of the temperature for the Elliott-Yafet relaxation mechanism of the spin current, dominant in metals [45, 38]. In the case of a perfectly transparent interface and in the absence of spin memory loss between copper and NiCu, G_s corresponds to G_{eff} for $\hat{m} = \hat{x}$. However, such a transparent interface does not exist, since there always exists a minimum interface resistance given by a Sharvin resistance of $0.8\,f\Omega\cdot m^2$ at Cu/FM interface [242], corresponding in general to a much higher interface resistance [244]. Comparing this measured G_s with our extracted G_{eff}, we could therefore extract the interface resistance R_{int} given in the table 3.2. This large interface resistance has the effect of screening any variation of the spin relaxation between the transverse and collinear configuration, possibly explaining the very small anisotropy of spin absorption in the transverse and collinear configuration, which contrasts with the results of the first chapter and those presented in Fig. 3.11g. In addition, this large interface resistance strongly changes the interconversion signal output by acting on the shunting effect [228].

Measurement of the spin-charge interconversion anisotropy

Now that the absorbed spin current is known, let us focus on the ISHE. We firstly measured the dependence of the magnetization direction of the NiCu wire as a function of the field applied along X, by performing two probe magnetoresistance measurements (Fig. 3.12d). The magnon magnetoresistance contribution [247, 248] dominates the signal in both the paramagnetic and ferromagnetic phases. In the ferromagnetic phase, the magnetoresistance also displays at low fields a deviation from the linear behavior, corresponding to the expected anisotropic magnetoresistance. This allows measuring the saturation field of the NiCu wire ($B_c = 0.2$ T) along the X axis ($\phi = \pi/2$).

We then measured the ISHE signal using the configuration of Fig. 3.11d. The ISHE has been measured both at 12K and at 300K, knowing that the Curie temperature of $\mathrm{Ni_{60}Cu_{40}}$ has been measured to be around 220 K for a material

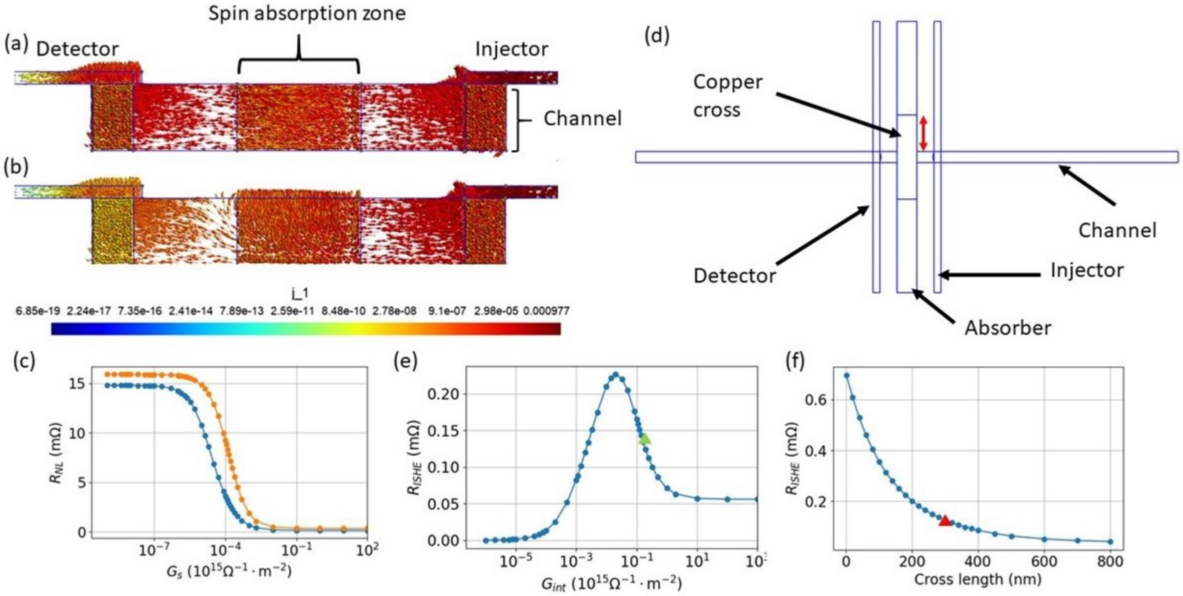

Figure 3.13: (a) FEM simulation of the spin current flow with $G_{eff} = 0$ and (b) $G_{eff} = 1 \cdot 10^{15}\Omega^{-1}\cdot\mathrm{m}^{-2}$ in the spin absorption zone. (c) Evolution of the non-local signal when increasing G_s in the spin absorption zone. (d) Geometry of the FEM simulations. The red arrow indicates the length of the copper cross. (e) Evolution of the ISHE signal when increasing the interface conductance G_{int}. The green triangle corresponds to a resistance of $7\, f\Omega \cdot m^2$. (f) Evolution of the ISHE signal with the length of the copper cross. The red triangle corresponds to a copper cross length of 270 nm.

made in the exact same conditions (see section 3.2.2). The ISHE signal, shown in Fig. 3.12f, is a square loop in both the paramagnetic and ferromagnetic phases. The observed square loop reflects the change of sign of the absorbed spin current polarization when reversing the injecting electrode magnetization. The symmetry and shape of the signal correspond to what can be expected from the ISHE symmetries, and from the switching fields measured in the non-local configuration. The parallel and transverse ISHE signals can then be obtained as $\Delta R^{\perp}_{ISHE} = R^B - R^E$ and $\Delta R^{||}_{ISHE} = R^A - R^D$, following the discussion of Fig. 3.11g and 3.11h, and R^i being the interconversion signal obtained in state i reported in Fig. 3.12e. The key finding is that at 12K, the signal is constant in the [-0.2 T; 0.2 T] field zone, where the magnetization of the absorber rotates from the X to the Y direction, so that $\Delta R^{\perp}_{ISHE} = \Delta R^{||}_{ISHE}$. This means that the spin-charge interconversion in ferromagnetic NiCu is independent of the direction of the absorber magnetization.

The spin-Hall angle was then extracted by computing the ISHE signal using the formulation described in the appendix, taking into account the interface conductance $G_{int} = 1/R_{int}$. The ISHE signal was evaluated in the geometry given in Fig. 3.13d using the 12 K parameters for NiCu given in the table 3.2, while changing the value of the interface conductance (Fig. 3.13e). We observe a peak in the interconversion signal when changing the interface conductance. The non-monotonic behavior of the ISHE signal versus the interface conductance is probably due to the fact that this parameter has an effect both on the spin transport across the interface and on the ISHE-produced charge current lines. Indeed, starting from a high interface conductance, increasing this parameter leads to a decrease of the shunting [228] induced by the copper channel, while it does not prevent the spin current from flowing into the absorber, thus increasing the measured voltage. When further increasing the value of the interface resistance, the spin conductance becomes larger than the interface conductance, so that the spin current cannot flow into the absorber. This leads to a drop of the ISHE signal which progressively goes to zero. Note that this ISHE optimum could not have been seen using 1D analytical modelling in lateral spin valves [74, 79], which underlines the relevance of FEM simulations for complex lateral spin valves geometries. The importance in taking into account the interface resistance for a proper evaluation of the spin Hall angle and for the interconversion signal optimization will be discussed in more details in chapter 5. This shows that FEM simulations are a crucial tool for an accurate evaluation of the spin Hall angle in lateral spin valves, and that a perfectly transparent interface is not necessarily the recipe for an optimal ISHE signal.

	300K	12K
G_{eff} ($10^{15}\,\Omega^{-1}\cdot\mathrm{m}^{-2}$)	0.3	0.13
R_{int} ($f\Omega\cdot\mathrm{m}^2$)	1.9	7
$\theta_{\|\|}$ (%)	1	2.5
θ_{AHE} (%)	/	2

Table 3.2: Extracted effective spin conductance in the collinear configuration. The AHE angle θ_{AHE} was measured in a simple Hall cross.

The SHA $\theta_{||}$ in the collinear configuration was extracted by comparing the measured interconversion signal with the previously described FEM simulations (Fig. 3.13e), using the interface resistance reported in table 3.2. At room temperature we used the resistivity and spin diffusion length obtained in [243]. We measured the resistivity versus temperature of NiCu using a Hall cross geometry, to evaluate the resistivity and extract the spin diffusion length at 12 K, using the independence of G_s with the temperature. The evaluated $\theta_{||}$ at 12K and room temperature are given in table 3.2. The obtained $\theta_{||}$ value of 2.5% is close to previous measurements using spin pumping [243], but slightly smaller, possibly because of the highest spin memory loss present in our ex-situ interfaces.

Finally, in order to obtain a guideline for future optimization of our device, we computed the evolution of the ISHE signal with the length of the copper cross used in the device of Fig. 3.12a, and given by the red arrow of Fig. 3.13f. This cross is used to prevent a deformation of the interconversion signal due to possible domain wall pinning after transverse saturation. The ISHE signal drops significantly when increasing the extension of the cross. This indicates that in order to observe the ISHE signal in materials with an interconversion efficiency lower than that one of NiCu, such as Co, CoFe and Py, one must reduce the extension of the cross while keeping it long enough to avoid parasitic effects.

Similar measurements were also made using a 15 nm thick $Ni_{16}Pd_{84}$ ferromagnetic absorber. Contrarily to NiCu, this material is known to display an extrinsic contribution to the spin Hall effect, due to the Ni impurities [214]. We characterized the magnetization orientation and magnetic order by performing AHE measurements on a macroscopic NiPd thin film (Fig. 3.14c). The amplitude versus temperature of the AHE measured by applying an out of plane magnetic field to the sample is displayed in Fig. 3.14e, with a low temperature anomalous Hall Angle of around 4 %. At 230 K, the AHE signal goes to zero, indicating a ferromagnetic to paramagnetic phase transition. Below 150 K, the NiPd layer has an out of plane easy magnetization axis, as shown in Fig. 3.14c. The coercive field goes to zero at 150 K, as the remanence, so that the magnetization of the film goes from out of plane to in plane above this temperature. We performed measurements of the non-local and ISHE signals for a in plane and out of plane easy magnetization axis. When the magnetization is in plane, its angle with the injected spin current polarization is parameterized by ϕ, as in the case of NiCu (Fig. 3.12b). For an out of plane magnetization, their relative orientation is parameterized by θ (Fig. 3.14a), with $\theta = 0$ at low field and $\theta = \pi/2$ at high field, which corresponds to the transverse and collinear configurations, respectively. Finally, the field necessary to saturate the magnetization in plane was evaluated by measuring the AHE in the NiPd film while applying an in plane magnetic field (Fig. 3.14f). At 20 K, the AHE signal branches rejoin at 0.5 T during the sweep, which corresponds to the in-plane saturation field. This field then progressively decreases upon increasing the temperature, until reaching zero at 150 K with the onset of the NiPd phase with an in-plane magnetization. We first measured the non-local signal (Fig. 3.14b) and the interconversion signal at 12 K (Fig. 3.14d), in the out of plane phase. Similarly to the case of NiCu, the non-local signal shows an isotropic spin absorption. The interconversion signal however has a non-squared shape, which can be due to the fact that the NiPd phase with an out of plane easy axis is associated to the presence of magnetic domains [249], that might deform the interconversion signal. In order to recover a mono-domain magnetic phase, we performed these measurements at 150 K (Fig. 3.14b and 3.14d) with an in-plane easy magnetization. In this case, we recover the square loop of the interconversion signal observed in NiCu. Since we could not evaluate the spin diffusion length and therefore the spin conductance of NiPd, the interface resistance between Cu and NiPd could not be evaluated. We consequently do not know if the isotropy of the non-local signal can be in this case attributed to the high interface resistance. However, the interconversion measurement at 150 K indicates that similarly to the case of NiCu, the interconversion is isotropic in NiPd with a spin Hall angle $\theta_{||}$ of around 1 %.

Interplay between the exchange and the SO interaction in weak ferromagnetic materials

The ISHE thus appears to be isotropic both for NiCu and NiPd in their ferromagnetic phase. This result is rather surprising in view of the discussion of section 3.1.2 and of the large AHE angles measured in NiCu and NiPd (2% and 4% respectively), which are comparable or larger than the extracted SHAs in these materials (2.5% and 1%). These AHE angles would indeed be expected to induce a strong anisotropy of the interconversion, provided that the polarization ξ introduced in eq. 3.3 is non-zero. This is also in contradiction with theoretical studies which have predicted a

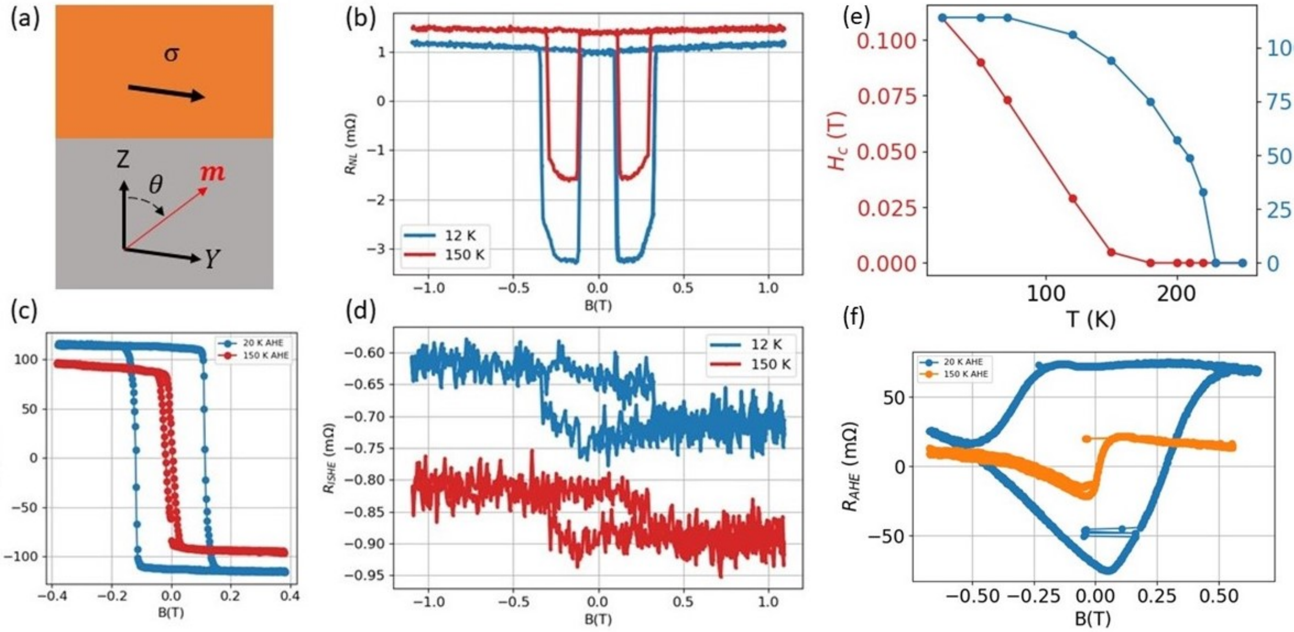

Figure 3.14: (a) Relative orientation between the spin current polarization σ and the magnetization of the absorber at low (m_z) and high (m_x) fields. Non-local (b) and ISHE (d) signals measured during the same magnetic field sweep, at 150 K and 12 K, using a 100 nm wide NiPd absorber. (c) AHE signal measured with an out-of-plane magnetic field on a 15 nm thick NiPd film. (e) Out of plane coercive field and AHE signal versus temperature measured on a 15 nm thick NiPd film. (f) AHE signal measured while applying an in-plane magnetic field at 20 K and 150 K.

sizeable modulation of the interconversion when rotating the magnetization [92, 219], even though it was done in high T_c ferromagnets such as Co, Fe and Ni.

Let us now look at the links between this isotropy of the signal and the spin transport parameters. The absorbed spin current Jc is converted into a charge current J_s according to $J_c = \theta J_s$. Importantly, θ is not the sole figure of merit of the ISHE. The conversion indeed occurs only over a limited material thickness, roughly equal to the spin relaxation length, after which the spin current, which is not conserved, vanishes. The produced signal is thus actually proportional to the product of the spin Hall angle by the spin relaxation length. If the incoming spins are collinear to the magnetization, this product is $\theta_{||} l_{sf}$, where $\theta_{||}$ is the spin Hall angle in the collinear situation. If the incoming spins are transverse to the magnetization, this product becomes $\lambda_\perp$ times $\theta_\perp$. The isotropy of the ISHE signal suggests that in our experiments:

$$\theta_{||} l_{sf} \sim \theta_\perp \lambda_\perp \tag{3.18}$$

In principle, it is possible to measure separately l_{sf} and $\lambda_\perp$, as they affect the spin absorption [242]. l_{sf} has been measured in NiCu [243] and is equal to 2.4 nm at room temperature. The measurement of $\lambda_\perp$ is more complex. The presence of a large interface resistance prevents here the observation of the spin absorption anisotropy in our devices. Extracting $\lambda_\perp$ would require thickness dependence measurements [250] with all the spurious effects linked to film thickness reduction, such as resistivity change [251]. An estimation of $\lambda_\perp$ can be however obtained by considering that it is inversely proportional to the exchange interaction J between the 3d and 4sp electronic states [64]. Indeed, assuming that all the magnetic energy constants, *i.e.* the 3d-3d and 3d-4sp exchange energies scale in the same way with the Curie temperature [262], one can estimate the transverse relaxation length by comparing the T_c of our materials to the one of a material for which $\lambda_\perp$ is know. By taking as reference material Py, which has a Tc of 800 K [263] with $\lambda_\perp^{Py} \sim 1$ nm [64, 242], $\lambda_\perp$ in NiCu can be estimated to be $\lambda_\perp^{NiCu} \sim 4$ nm. The transverse relaxation length due to ballistic effects in NiCu is therefore larger than its spin diffusion length. This means that the transverse spin current relaxes over the spin diffusion length through diffusive processes and that $\lambda_\perp^{NiCu} = l_{sf}$. $\theta_{||}$ has been estimated to be 2.5 %, which would lead according to our experimental result of equation 3.18 to the same value for $\theta_\perp$, meaning that the polarization ξ which allows the AHE to contribute to the spin-charge interconversion is equal to zero. The case of NiPd is more difficult to analyse, since we do not have values of the spin diffusion length in this material. However, the combination of the large SO interaction, evidenced by the out of plane magnetic anisotropy at low temperature, and of the small exchange interaction, evidenced by the low Curie temperature, makes us expect a similar relation between the transverse spin relaxation and the spin diffusion lengths.

In light of these results, it appears that the isotropy of the absorption is to be expected in low Tc FMs with strong spin-orbit coupling, since the low exchange interaction drives the transverse spin relaxation length to be equal to the spin diffusion length. Hence, from our experiments and eq. 3.18 we can conclude that the spin Hall angle in NiCu and NiPd is isotropic, and that the spin Hall effect is fully independent of the anomalous Hall effect. Note that the picture in high Tc FMs is however more contrasted. Indeed, it has been established that a strong anisotropy of the absorption exists in these materials [242]. The isotropy of the ISHE signal has been observed in CoFe [264] and Py [265], where the relation given by eq. 3.18 does not seem to hold [250], while it does in Co [232]. According to theoretical studies [92], the details of the SOC effect on the band structure of these materials would provide the explanation for these behaviors with in particular the presence of spin-eigenstates not collinear to the magnetization, which allows the presence of a transverse spin current to exist in the bulk of a ferromagnet. We believe that the device described in this chapter can provide an tool for a systematic investigation of these phenomena.

To conclude, this device allows for the measurement of the anisotropy of the spin-charge interconversion in ferromagnetic materials. Although the paramagnetic/ferromagnetic transition is associated to symmetry breaking, the ISHE signal in NiCu and NiPd remains surprisingly independent of the magnetization direction in the ferromagnetic phase. In terms of spin transport properties, this implies that the product of the SHA by the spin relaxation length is the same in the collinear and transverse configurations. In the studied low T_c materials, this can be understood by considering the relatively long transverse relaxation length, which causes the spin current to relax during scattering on SO impurities, and is therefore equal to the spin diffusion length. Finally, the observation that $\theta_{||} = \theta_{\perp}$ shows that the spin Hall angle is isotropic in weak ferromagnets.

In this chapter we observed that the spin Hall angle is independent with the ferromagnetic order, and that it is isotropic in two weak ferromagnets: $Ni_{60}Cu_{40}$ and $Ni_{16}Pd_{84}$. Furthermore, we observed that the spin current relaxation in these two materials in the ferromagnetic phase is also isotropic, in contradiction to the results obtained in Chapter 2 in the room temperature ferromagnetic materials Co, CoFe and NiFe. In addition, an anisotropy of the spin Hall effect has been predicted [92] and observed [264, 265] in these room temperature ferromagnetic materials (with the exception of Co, where an isotropic SHE has been reported). The main difference between the Co, CoFe, NiFe group and the weak ferromagnets NiCu and NiPd is the relative strength of their exchange interaction with respect to the spin-orbit interaction, as evidenced by their difference in Curie temperature as well as the smaller spin diffusion lengths and larger spin Hall angles in NiCu and NiPd. It is therefore likely that the effect on the magnetic order on the SHE will depend on the competition between the exchange and spin-orbit interactions [92]. The NiCu and NiPd alloys provide a convenient way to study such an interaction. Indeed, by progressively increasing the concentration of Ni in these alloys, it is to be expected that the exchange would become larger than the spin-orbit interaction in these materials. This would in principle results in an increase of the anisotropy of the spin to charge interconversion. A more systematic study of the composition dependence of the SHE anisotropy in this class of materials using the device presented in the last section of this chapter, would consequently provide crucial information for the understanding of the spin transport and interconversion effects in ferromagnetic materials.

Chapter 4

Spin-charge interconversion at Rashba interfaces

The symmetry breaking at an interface is known to induce modification of the band structure of interfacial states [100]. This has led to the observation of large spin-charge interconversion efficiencies at metal/metal interfaces [98], but also at metal/insulator interfaces [143] thanks to the Rashba-Edelstein effect [144]. The discovery of bound states constituting a two-dimensional electron gas at the interface between two insulators strongly increased the magnitude of these interconversion effects [168]. Indeed, the spin-charge interconversion depends on the strength of the electric field induced at the interface. However, as mentioned in Chapter 1, it also depends on the strength of the spin-orbit interaction and of the surface state electronic scattering rate, which is strongly reduced in such a two-dimensional electron gas. In this chapter, we will see how the modulation of these two parameters changes the spin to charge interconversion efficiency in two dimensional electron gases at the surface of complex oxides.

I will start to present a simple toy model, which shows how the combination of symmetry breaking and spin-orbit interaction leads to the presence of the spin-momentum locking. This will help understanding the origin of the Rashba-Edelstein effect at the surface of complex oxides. In a second section, I will describe the band structure of the two dimensional electron gas at the surface of $SrTiO_3$ (STO) with 001 orientation. I will then show how such a two dimensional electron gas can be obtained at the surface of STO(001) by simple reactive metal deposition, and describe the modulation of the spin-charge interconversion efficiency in this system by application of a backgate voltage. We will then see how the modification of the effective scattering time of the electronic surface states leads to a change in the spin to charge interconversion efficiency. Finally, I will present the fabrication of a two dimensional electron gas at the surface of $KTaO_3$, a complex oxide with a large spin-orbit interaction, and the measurement of the interconversion in this system.

4.1 Origin of the Rashba-split bands at interfaces: a toy model

The symmetry considerations presented in the chapter 1 are too general to derive an expression for the Hamiltonian that would allow to understand in details the band structure of systems with SRS breaking. In this section, I will describe a tight binding toy model proposed by A. Manchon *et al.* in Ref. [145], which presents in a simple way the physical origin of the band structures presented in the section 1.3.2 of Chapter 1. This model can be seen as a simplified version of those used to explain the spin-charge interconversion in complex Rashba multi-orbital systems that will be presented over the course of this chapter.

The model considers a chain of atoms along the X direction, hosting p_z and p_x orbitals, p_y being omitted for simplicity. Such a system respects the time and space reversal symmetries, so that its band structure will simply follow a parabolic shape controlled by the hopping integral between the neighbouring atoms. The SRS of the system is then broken by coupling this first chain of atoms with another atomic chain, which hosts only p_z orbitals. The system is shown in Fig. 4.1a and 4.1b. The original chain being on the bottom, its orbitals will be denoted p_z^b and p_x^b, while the orbital of the top chain is denoted p_z^t. As also described in Fig. 4.1a and 4.1b, the addition of this top chain opens a hopping path between p_z^b and p_x^b, which was previously forbidden by symmetries. In the basis $\{p_z^t, p_z^b, p_x^b\}$, the Hamiltonian of the system now writes:

$$H_{chain} = \begin{pmatrix} \epsilon_k^t & V_{zz} & V_{zx} \\ V_{zz} & \epsilon_k^b & 0 \\ V_{zx}^\star & 0 & \epsilon_k^b \end{pmatrix} \tag{4.1}$$

with ϵ_k^t the kinetic energy of p_z^t. The bottom orbitals p_z^b and p_x^b are assumed to have the same kinetic energies ϵ_k^b. The terms $V_{zz} = (V_\sigma + V_\pi)\cos k_x a/2$ and $V_{zx} = -i(V_\sigma - V_\pi)\sin k_x a/2$ describe the coupling between the two chains parameterized by the Slater-Koster hopping integrals. The eigenstates $\{|0\rangle, |-\rangle, |+\rangle\}$ are therefore a combination of the $\{p_z^t, p_z^b, p_x^b\}$ orbitals with:

$$|0\rangle = \alpha(-V_{zx}|p_z^b\rangle + V_{zz}|p_x^b\rangle) \tag{4.2}$$

with α a normalization term. This first band is simply a linear combination of the bottom chain orbitals and has a linear dispersion relation $\epsilon_k^0 = \epsilon_k^b$. The two other eigenstates $|+\rangle$ and $|-\rangle$ have energies:

$$\epsilon_k^\pm = \frac{\epsilon_k^t + \epsilon_k^b}{2} \pm \frac{1}{2}\Delta_k \tag{4.3}$$

with $\Delta_k = \sqrt{(\epsilon_k^t + \epsilon_k^b)^2 + 4(|V_{zz}|^2 + |V_{zz}|^2)}$. They can be written:

$$|+\rangle = \cos\chi\,|p_z^t\rangle + \alpha\sin\chi(V_{zz}|p_z^b\rangle + V_{zx}^\star|p_x^b\rangle) \tag{4.4}$$

$$|-\rangle = -\sin\chi\,|p_z^t\rangle + \alpha\cos\chi(V_{zz}|p_z^b\rangle + V_{zx}^\star|p_x^b\rangle) \tag{4.5}$$

The parameter χ is given by $\cos 2\chi = (\epsilon_k^t - \epsilon_k^b)/\Delta_k$. It controls the degree of hybridization between the top and bottom chain orbitals and therefore will play a crucial role in the onset of a spin texture. The hybridization of the p orbitals allows the formation of an orbital momentum odd in k_x. Indeed, the isolated p_z and p_x orbitals do not host any orbital angular momentum $\boldsymbol{L}$ by construction while, by using the relation $\langle p_x^b|\boldsymbol{L}|p_z^b\rangle = i\hat{y}$, the orbital angular momentum of the $|0\rangle$, $|+\rangle$ and $|-\rangle$ bands can be computed as:

$$\langle 0|\boldsymbol{L}|0\rangle = -\beta\sin k_x a\,\hat{y} \tag{4.6}$$

$$\langle +|\boldsymbol{L}|+\rangle = \beta\sin^2\chi\sin k_x a\,\hat{y} \tag{4.7}$$

$$\langle -|\boldsymbol{L}|-\rangle = \beta\cos^2\chi\sin k_x a\,\hat{y} \tag{4.8}$$

with $\beta(V_\sigma, V_\pi)$ a function of the Slater-Koster integrals. Importantly, this shows that the bands now host an orbital momentum that is odd in k_x, meaning that it can be seen only when applying a electric field. This effect has been described theoretically in realistic systems and named the Orbital Hall Effect [146] or Orbital Edelstein Effect [147]. It must be noted that this orbital momentum can exist only in the presence of a sizeable mixing of the top and bottom orbitals. Indeed, if the top and bottom chain orbitals are far in energy ($\epsilon_k^t - \epsilon_k^b \gg 4(|V_{zz}|^2 + |V_{zz}|^2)$), the mixing parameter χ will vanish. $|0\rangle$ and $|+\rangle$ would then reduce to a linear combination of the bottom p orbitals, while $|+\rangle = |p_z^t\rangle$. The orbital angular momentum of $|+\rangle$ would then goes to zero, while the ones of $|0\rangle$ and $|-\rangle$ compensate. The degree of orbital hybridization will play a crucial role in the understanding of the interconversion in the systems presented later on in this chapter.

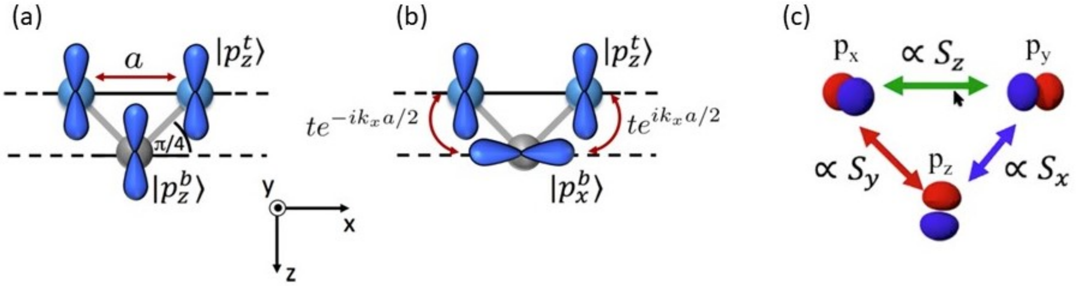

Figure 4.1: (a) and (b) Sketch of the system used for the model. The top chain hosts only p_z orbitals while the bottom one hosts both p_z and p_x orbitals. The hopping parameter between the bottom orbitals of different symmetries are zero, and the electron for both orbitals symmetries can hop on the top p_z orbitals. (c) spin momentum generated by the combination of spin-orbit coupling and hybridization between orbitals of different nature (Image from ref. [145]).

The orbitals obtained by breaking the SRS do not have any spin texture, despite it being now allowed by symmetries. This is because one interaction is still missing, which is the spin-orbit interaction $\lambda\boldsymbol{s}\cdot\boldsymbol{L}$. Now that a non zero $\boldsymbol{L}$ exists, the spin states $\boldsymbol{s}$ will align with it for a non-zero λ, generating an odd in k_x spin texture. This new interaction generates a non-diagonal contribution to the now 6-band hamiltonian in the basis $\{|0\rangle, |+\rangle, |-\rangle\} \otimes \{\uparrow, \downarrow\}$:

$$< \xi \boldsymbol{L} \cdot \boldsymbol{s} >= M_{SO} F(V_\sigma, V_\pi) \sin(k_x a)\, \hat{\sigma}_y \tag{4.9}$$

with F a function of the Slater-Koster integrals whose expression can be found in ref. [145], $\hat{\sigma}_y$ a Pauli matrix and $M_{SO} = \lambda\, \mathrm{diag}(-1, \sin^2\chi, \cos^2\chi)$. This additional term to the Hamiltonian couples the momentum k_x to the electron-spin along $\hat{y}$, leading to a spin-momentum locking. The extension of the model to the two dimensional (x, y) plane is straightforward, and taking into account the other p orbitals permits the formation of a spin momentum in all three directions of space (Fig. 4.1c). In the low k_x limit, the Spin-Orbit interaction term given by eq. 4.9 reduces to the usual minimal Rashba hamiltonian [100]:

$$H_R = \alpha_R \hat{\boldsymbol{\sigma}} \cdot (\boldsymbol{k} \times \hat{\boldsymbol{z}}) \tag{4.10}$$

with $\hat{\boldsymbol{z}}$ the normal to the plane, $\hat{\boldsymbol{\sigma}}$ the Pauli matrix vectors, and α_R the Rashba parameter which depends on the spin-orbit coupling strength, but also on the degree of orbital mixing, which itself depends on the details of the interface and on the position of the Fermi level in the band structure. This term results in a lifting of the degeneracy of the two opposite spin states, with a Rashba spin splitting energy expressed as $\Delta = 2\alpha_R k_F$ around the $k = 0$ point, with k_F the Fermi wave vector. The Rashba splitting energy is therefore both proportional to the strength of the spin-orbit coupling and to the degree of orbital hybridization induced by the symmetry breaking.

This toy model highlights the basic contributions necessary to generate a spin momentum locked band structure with Rashba splitting: a symmetry breaking that allows the presence of an out of equilibrium orbital atomic momentum, due to orbital mixing, and the presence of spin-orbit coupling which forces the electronic spin along the orbital momentum. In the next section, I will present the realization of such a two dimensional electronic system, with space reversal symmetry breaking, at the surface of STO with 001 orientation.

4.2 Spin-charge interconversion in $\mathrm{SrTiO_3}$ two dimensional electron gases

In this section, I will show how an extremely large interconversion efficiency with respect the metal-metal interfaces can be achieved in a two dimensional electron gas (2DEG) at the surface of STO with (001) orientation. In a first part, the relevant properties of STO crystallographic and electronic structures will be presented. I will then describe the band structure of a two dimensional electron gas (2DEG) based on STO, and present how the multi-orbital nature of the electronic transports leads to a highly efficient and tunable Rashba-Edelstein effect in this system. The fabrication of a 2DEG by deposition of a thin layer of aluminium, and previous SP-FMR interconversion measurements at the STO/$\mathrm{AlO_x}$ interface will be quickly reviewed. I will then present an alternative way of fabricating a 2DEG by depositing various metals at the surface of STO, as well as the SP-FMR based spin-to-charge interconversion measurements performed in these interfaces.

4.2.1 STO bulk crystal: crystallographic and electronic structure

$\mathrm{SrTiO_3}$ is a widely used material that exhibits a cubic perovskite structure at room temperature, with a large dielectric constant ϵ of $2 \cdot 10^4$ at low temperature due to its quantum paraelectric nature [148]. The 001 orientation, that we will focused on for now, is composed of neutral $\mathrm{TiO_2}$ and SrO planes, which makes this material non-polar [149]. Each Ti atom is surrounded by an oxygen octahedron (Fig. 4.2a), which causes titanum to have a 4+ valence state, while strontium is in a 2+ state. STO is a band insulator with a bandgap of 3.25 eV between a valence band made of the oxygen atoms 2p states, which are therefore weakly hybridized with the Ti 3d states that constitute the bottom of the conduction band [150]. The Ti 3d states of STO are split in two groups t_{2g} and e_g by the crystal field produced by the oxygen octahedron. The low energy group t_{2g} contains the d_{xy}, d_{zx} and d_{yz} orbitals, while the e_g group is made of $d_{x^2-y^2}$ and $d_{3z^2-r^2}$ orbitals (Fig. 4.2b). The energy separation between these two groups is of 2 eV, much larger than all the energy scales involved in the conduction band, so that only the t_{2g} group will be considered in the following. The t_{2g} group experiences a further splitting due to the Ti-3d spin-orbit coupling $\Delta_{SO} = 10 - 30$ meV. Finally, a structural distorsion below 100 K also leads to a t_{2g} group splitting of 2 meV, which is negligible compared to the previously mentioned energy scales.

The symmetries of the t_{2g} orbitals creates a highly anisotropic band structure. For all these orbitals, the electron hopping between Ti sites takes place through the p orbitals of oxygen atoms. Since hopping between t_{2g} orbitals of different nature is forbidden by symmetries, the different band retain their orbital character, with effective electronic masses depending on the k-space direction. Let us consider the d_{xy} orbital for illustration. As schematically shown in

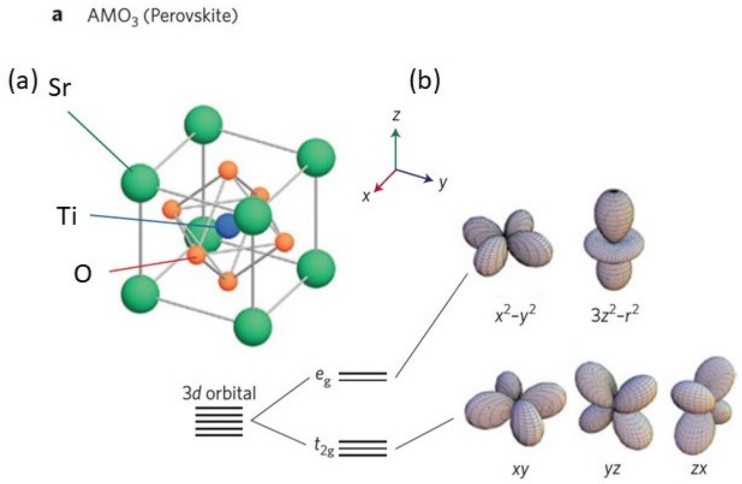

Figure 4.2: (a) Unit cell of an ABO3 perovskite. The Ti atom (blue) is surrounded by an oxygen octahedron that splits its 3d orbitals into a t_{2g} and a e_g groups (b). (Image from ref. [151]).

Fig. 4.3a, the d_{xy} orbitals possess a small overlap along the Z direction and a large one along the X and Y directions. This causes the associated band to be heavy along $\hat{z}$, with an effective mass $m_z^\star \sim 2-3m_e$ (m_e being the mass of the free electron), and light in the xy plane ($m_{x/y}^\star \sim 0.7m_e$) [150, 152]. Similar considerations apply to d_{yz} and d_{zx} so that, along say the Y direction of the k-space, the d_{xy} and d_{yz} bands will be light and the d_{zx} band heavy (Fig. 4.3b). In the (k_x, k_y) plane of the reciprocal space, this translates for the band structure at a given energy in two ellipsoids that correspond to the d_{yz} and d_{zx} bands, and a circle which is the d_{xy} band (Fig. 4.3c).

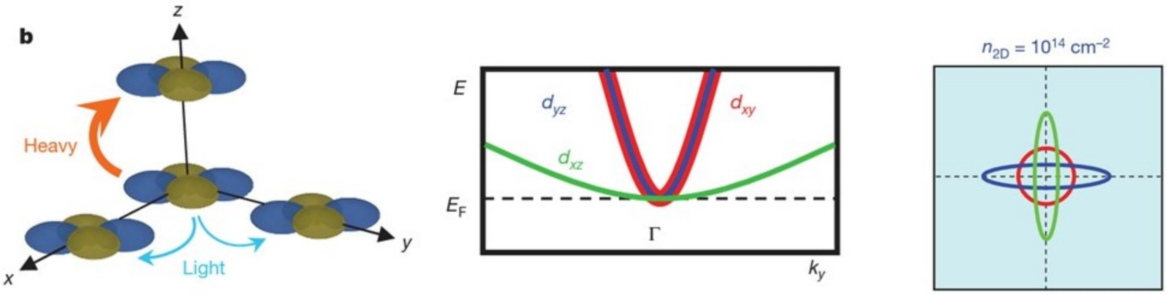

Figure 4.3: (a) Sketch of the hopping processes between d_{xy} orbitals, which creates a light band along the X and Y directions, and heavy in the Z direction. This results in bands of different masses along the Y direction. Here, the effect of the SOC has not been included, which results in a band degeneracy around the Γ point. (c) Fermi contours of the bands created by the t_{2g} orbitals in the xy plane for a carrier density of $n_s = 10^{14}\,\mathrm{cm}^{-2}$ (Image from ref. [152]).

In the next section, I will discuss how the presence of a space reversal symmetry at the interface reconstructs the band structure. This, in addition to the spin-orbit coupling, provides a system with a large and tunable spin-to charge interconversion by the inverse Edelstein Effect.

4.2.2 Orbital ordering and Rashba splitting at the surface of STO

The presence of a conducting interface at the surface of STO(001) has been demonstrated as early as 2004 [153] by depositing a thin layer of the large band gap insulator $LaAlO_3$ on the surface of Ti-terminated STO. Several other methods achieved the formation of a 2DEG at the surface of STO, including cleaving in vacuum [154] and reactive metal deposition [155]. Interestingly, the conducting interface obtained for each of these methods displayed similar features probed by ARPES measurements. Firstly, they do not have a dispersion along the $\hat{z}$ axis perpendicular to the interface, which indicates a two dimensional nature of the electron system [156]. Secondly, they possess below the Fermi level a multi-orbital subband structure of intersecting heavy and light bands, as shown in Fig 4.4a. This band structure has been attributed to an orbital reconstruction at the interface, due to the presence of a triangular shaped potential well of depth $\sim$ 300 meV[152] (inset of Fig 4.4b). This well causes a band bending at the interface, which places the conduction band below the Fermi level. The confinement causes a discretization of the STO conduction band, resulting in multiple bands with the same orbital character but shifted in energy. It also lifts the degeneracy of the t_{2g} group (Fig 4.4b). The energy of the d_{xy} orbital will then be lowered with respect to those of the d_{zx} and d_{yz} orbitals, due to the lower effective mass along the Z-direction. The typical energy difference between the lowest subbands is of $\sim$ 100 meV.

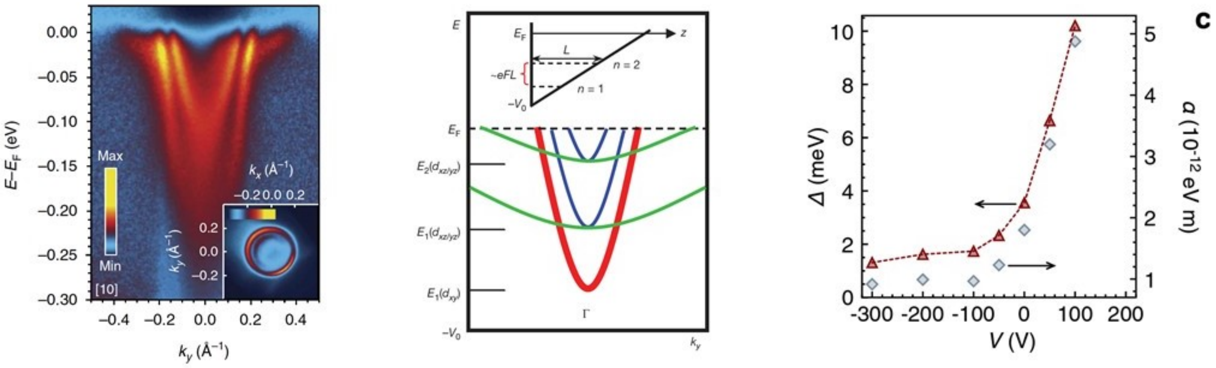

Figure 4.4: (a) ARPES measurement at the surface of a vacuum cleaved STO with 001 orientation (Image from ref. [157]). (b) Orbital reconstruction of the band structure (along k_y) created by the interfacial potential well shown in the inset. The green bands correspond to orbital with a d_{zx} symmetries, while blue and red correspond to d_{yz} and d_{xy} orbital symmetries respectively. Here, the SOC has been neglected, so that no avoided crossing can be observed (image from Ref. [152]). (c) Modulation of the Rashba splitting Δ and effective Rashba parameter α_R when moving the Fermi level in the band structure of the 2DEG by applying a back gate voltage (Image from ref. [158]).

In addition to its 2D nature and peculiar band structure, this two dimensional electron gas was demonstrated to host a tunable Rashba spin-orbit interaction through magnetotransport measurements. It is indeed possible to tune the position of the Fermi level in this 2DEG by a back gate voltage [159], thanks to the large dielectric constant of STO at low temperature. By performing magnetotransport measurements, the authors of Refs. [158, 160, 161] demonstrated the presence of a sizeable Rashba parameter in the 2DEG at the surface of STO, with a Rashba splitting of up to 10 meV, despite the low spin-orbit coupling expected in the light Ti element. The fact that the Rashba parameter depends on the position of the Fermi level in its band structure (Fig 4.4c) opens possibilities for a gate tunable interconversion efficiency since $\lambda_{IEE} \propto \alpha_R$.

The presence of a Rashba splitting in the 2DEG at the interface of STO can be understood in the framework of tight binding models [162, 163, 164] qualitatively similar to the model presented in section 4.1. In these models, the considered hopping sites are the Ti t_{2g} orbitals group. The presence of a large electric field ($\sim 83\,\mathrm{MV \cdot m^{-1}}$ [152]) at the interface of STO provides the way to open a symmetry violating hopping process between the t_{2g} orbitals of the Ti sites. This electric field E can have two effects. One is to polarize the d orbitals with a response γ_1 [163], as illustrated in (Fig. 4.5a). This deformation of the orbitals creates common symmetries elements between the orbitals of the t_{2g} group, and therefore opens additional hopping channels with amplitude [162]:

$$\gamma = \gamma_1 E \frac{t_{pd}}{\Delta_{pd}}$$

where t_{pd} refers to the hopping integral between d Ti orbitals and the oxygen p ones, while Δ_{pd} is the energy difference between these two. It is also possible that the electric field causes a ionic displacement between the Ti and oxygen atoms of the TiO_2 plane (Fig. 4.5b), with an predicted 4% deformation of the unit cell [162]. This generates an angle n between the Ti-Ti and Ti-O bonds, allowing for instance the opening of a hopping channel between d_{yz} and p_y orbitals, that would be forbidden otherwise. Since an electron can go from p_y to d_{xy}, this means that a hopping channel between d_{yz} and d_{xy} is now open with an amplitude [162]:

$$\gamma = n \frac{t_{pd}^2}{\Delta_{pd}}$$

The symmetry breaking is therefore responsible for a parity violation hopping process, that allows the hybridization of the t_{2g}-d orbital with different characters. As it was discussed in the first section, this hybridization is responsible for the apparition of an odd in k atomic orbital texture (OAM) (Fig. 4.5c). Introducing the spin-orbit coupling term $\lambda \boldsymbol{L} \cdot \boldsymbol{s}$ forces the spin to antialign with the OAM, creating a chiral spin texture shown in Fig. 4.5c.

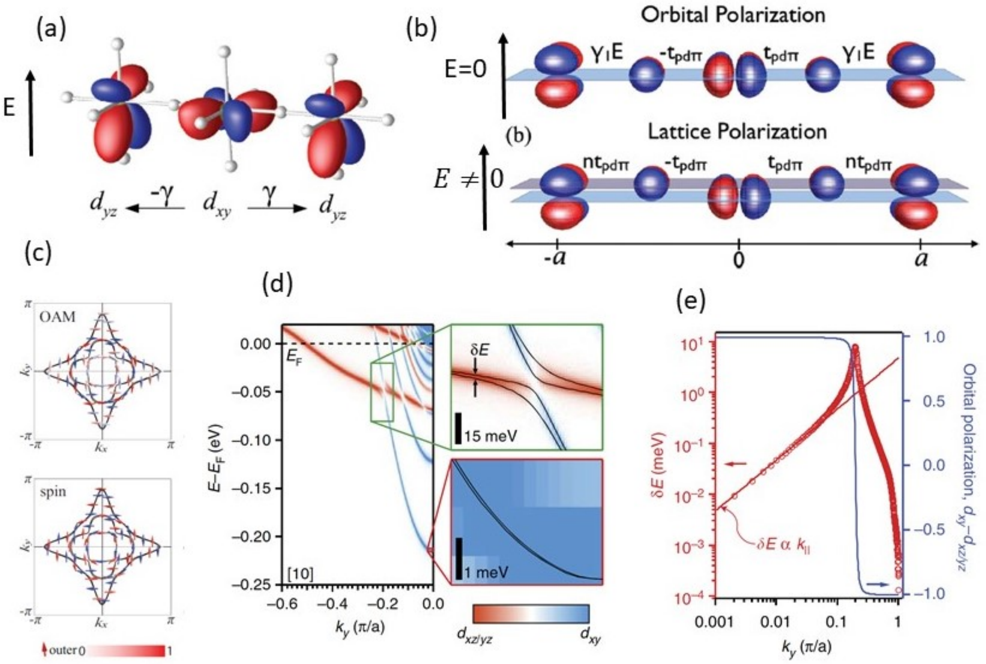

Figure 4.5: (a) Symmetry violation hopping process allowed by the t_{2g} polarization by the electric field E perpendicular to the interface (Image from Ref. [163]). (b) Symmetry violation hopping produced by the ionic displacement due by the electric field (Image from ref. [162]). (c) Calculated orbital atomic texture in the 2DEG at the surface of STO, and the resulting spin texture originating by the inclusion of the SOC Hamiltonian [164]. (d) Orbital mixing and Rashba splitting of the spin bands at the avoided crossing between 2DEG bands of different symmetries. (e) k-dependence of the Rashba splitting δE as a function of k_y. The splitting is maximum at the avoided crossing when the bands of different masses hybridize (Image from ref. [157]).

An additional complexity arises in the 2DEG due to the energy dependent orbital hybridization. In the first section, we saw that the OAM depends on the level of orbital hybridization. In the case of the 2DEG with the band structure shown in Fig. 4.4a and 4.4b, the orbital hybridization is strongly energy dependent. When the atomic orbitals are far in energy, they do not hybridize strongly. This is the case at the Γ ($k_y = 0$) point of the d_{xy} bottom band (Fig. 4.5d). Here, the electronic states have a mostly d_{xy} character, and a linear in k Rashba splitting (Fig. 4.5e). In this case, the Rashba parameter is given by $\alpha_R = 2a\lambda\gamma/\Delta_I$ where the energy splitting between the d_{xy} bottom band and the $d_{yz/zx}$ bands is noted $\Delta_I \sim 100 - 300\,\text{meV}$ [163, 157]. The term γ/Δ_I consequently corresponds to the degree of orbital hybridization between these bands around the Γ point. Since the hopping integral γ is in the order of $20\,\text{meV}$ [163], the orbitals are weakly hybridized, giving a small Rashba splitting between the inner and outer Fermi contour (Fig. 4.5e). The presence of heavy d_{yz} and d_{zx} bands shifted upward in energy with respect to the lighter d_{xy} band however allows for an energy dependent orbital hybridization. Indeed, when these bands reach their crossing points, they strongly hybridize, leading to an avoided crossing with a mixed orbital character (Fig. 4.5d). This strongly increases the OAM and results in an extremum of the Rashba splitting with a non-linear in k dependence (Fig. 4.5e) that causes the increase of the effective Rashba parameter observed in Fig. 4.4c.

This analysis, despite being somewhat simplistic due to the need to consider the spatial extension of the 2DEG over several unit cells in the depth of STO [157], provides crucial information on the origin of the spin texture in oxide surface-based 2DEGs. First, the interplay between the two symmetry violating hopping terms could provide important information regarding the interplay between spin-charge interconversion and ferroelectricity in 2DEG fabricated on the top of ferroelectric materials [29, 165, 166]. Secondly, it allows for a detailed understanding of the gate modulation of the spin-charge interconversion measured in these 2DEGs that will be described in the next paragraph.

4.2.3 Two dimensional electron gas formation on STO(001) by metal deposition

Spin to charge interconversion at $\mathrm{AlO_x}$/STO interfaces

Early 2DEGs have been obtained at oxide-oxide hetererostructure interfaces, which requires complex PLD techniques [153] for their growth. The spin-charge interconversion in STO/$\mathrm{LaAlO_3}$, which belongs to this class of system, has also been studied, and the modulation of its Inverse Edelstein Length was found to qualitatively correlate with the modulation of the effective Rashba parameter when moving the Fermi level in the band structure [167, 168]. Later on, another much simpler way of obtaining 2DEGs at the surface of STO(001) has been demonstrated by Rödel *et al.* [155]. It involves depositing a few Å thick aluminium layer on top of Ti-terminated STO (Fig. 4.6a). This causes a reduction of the Ti atoms close to the interface, leading to the appearance of a quantum well and the creation of a 2DEG hosted by the reduced Ti sites. A study of the fabrication and interconversion in such a system has been previously published in Nature Materials [20]. The oxido-reduction reaction at the origin of the formation of the 2DEG at the surface of STO has been monitored by X-ray Photoemission Spectroscopy (XPS) measurements that probe the binding energies of the Ti and Al $2p$ states, which depends on the valence states of these atoms. The XPS signal measured on bare STO and on STO with a 9 Å thick aluminium layer deposited on top are shown in Fig. 4.6b. On the bare STO susbtrate, only the $2p_{1/2}$ and $2p_{3/2}$ peaks associated with the Ti^{4+} valence states are visible. Upon deposition of aluminum, peaks associated with Ti^{3+} and Ti^{2+} states appear, which indicates the reduction of Ti sites. An angle dependent XPS measurement further indicated that this reduction takes place only on a few $\mathrm{TiO_2}$ planes close to the interface. Similar measurements indicate a partial oxidation of the Al layer, with a 75% transformation of it in $\mathrm{Al_2O_3}$. This process has been confirmed by Energy-dispersive X-ray spectroscopy maps (Fig. 4.6c) of the atomic species repartition on the Scanning Electron Tunnelling Microscopy image of Fig. 4.6a. This shows a migration of oxygen atoms from STO to the Al film, without any transfer of Ti and Sr atoms. This leads to the formation of oxygen vacancies that creates an energy well at the interface between STO and $\mathrm{Al_2O_3}$.

The conductive nature of the so-created potential well was controlled by transport experiments in $\mathrm{AlO_x}$/ NiFe(2.5 nm)/−Al(0.9 nm)/STO and $\mathrm{AlO_x}$/NiFe(2.5 nm)/STO stacks (Fig. 4.6d). While the stack without Al(0.9 nm) insertion between the NiFe layer and STO shows a less than 10% variation of its sheet resistance with temperature, a significant drop in resistance at low temperature is observed in the full stack. This indicates the presence of an additional conduction channel at the Al/STO interface. Considering NiFe and the 2DEG present at the Al(0.9 nm)/STO interface as two independent conduction channels, it is possible to extract the 2DEG sheet resistance, which shows an order of magnitude drop when decreasing the temperature, consistently with a metallic behavior of the 2DEG. This resistance decreases, associated to ARPES measurements (not discussed here) signals the presence of a 2DEG at the interface between the oxidized aluminium and STO. Its multiband structure is further confirmed by magnetotransport measurements, with the presence of a light band with density $n_s^1 = 1.8 \cdot 10^{12}\,\mathrm{cm^{-2}}$ and mobility $\mu_1 = 3300\,\mathrm{V \cdot cm^{-2} \cdot s^{-1}}$, and a heavy one ($n_s^2 = 1.0 \cdot 10^{14}\,\mathrm{cm^{-2}}$, $\mu_2 = 160\,\mathrm{V \cdot cm^{-2} \cdot s^{-1}}$) upon application of a 200 V backgate voltage [169]. Furthermore, it was also possible to modulate the carrier density with the backgate voltage, which shows that the position of the Fermi level can be electrically tuned in the band structure of the 2DEG [20].

The spin-charge interconversion in this 2DEG was measured using the SP-FMR technique described in section 3.2.1. A back-gate voltage was applied when carrying out these measurements (Fig. 4.7a). The results of these interconversion measurements at different gate voltages are shown in Fig. 4.7b, in which large interconversion signals were measured. The amplitude of these signals, and even their sign can be changed when applying a back gate voltage, a feature already observed in STO/$\mathrm{LaAlO_3}$ based 2DEG [168], although with smaller amplitudes and a reduced number of sign change. The IEE length λ_{IEE} was extracted by measuring the produced charge current and injected spin current, following the method described in section 3.2.1. The modulation of λ_{IEE} with the back gate voltage is shown in Fig. 4.7c. In ref. [168], the IEE efficiency modulation was attributed qualitatively to the band structure of the 2DEG, with a change of sign linked to the population of bands with opposite splitting signs, while the maxima were due to the maximum of effective Rashba parameter at the avoided crossings, as discussed in section 2.2. A similar analysis, backed by tight binding calculations fitted on ARPES data was carried out, to explain the results of Fig. 4.7c. It consists in evaluating à κ_{xy} parameter which links the obtained transverse spin accumulation $\boldsymbol{s}$ under an in-plane electric field $\boldsymbol{E}$, by the relation $\boldsymbol{s} = \hat{\kappa}\boldsymbol{E}$. This parameter changes with the position of the Fermi level in the band structure as described in Fig. 4.7d. At low gate voltage, only the low energy d_{xy} bands with a relatively small splitting are populated. The population of other d_{xy} bands increases the interconversion efficiency, with a maximum at the avoided crossing point between the light and heavy bands. The interconversion sign then changes due to the alternating sign of the spin splitting between the d_{xy} and $d_{yz/zx}$ bands. Similar avoided crossing and change of splitting signs leads to the series of extrema and changes of sign κ_{xy}. The behavior of κ_{xy} is observed to match closely the one of the measured λ_{IEE}.

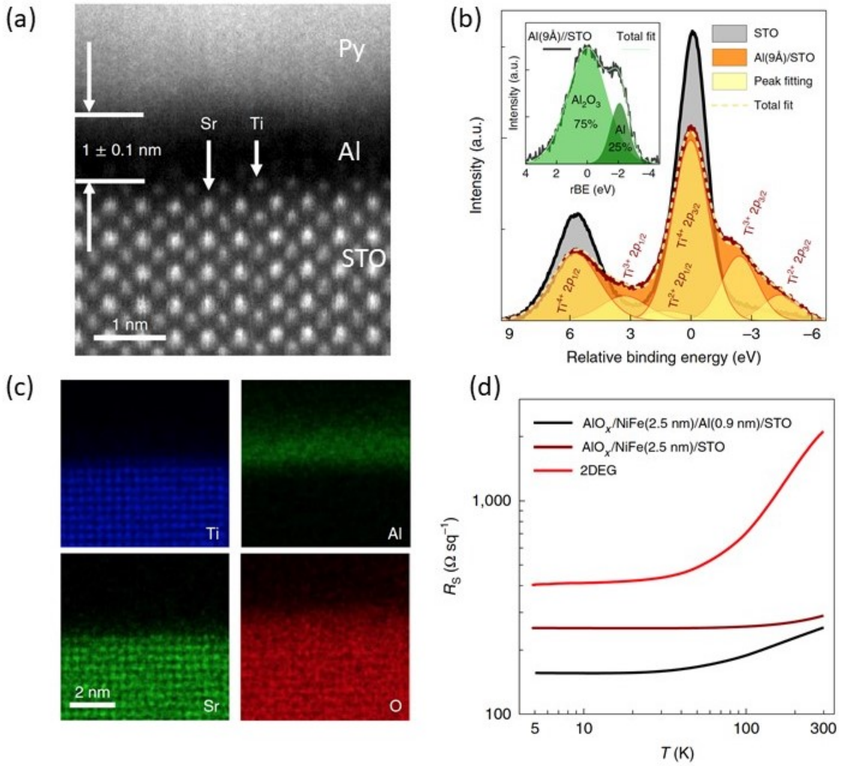

Figure 4.6: (a) Scanning TEM micrograph of the STO/Al/NiFe stack used to study the 2DEG, showing the Al layer and the Ti termination of STO(001). (b) XPS spectroscopy measurement showing the apparition of Ti atoms with reduced valence states upon deposition of a thin Al layer. (c) EDX map of the oxygen migration into the structure presented in (a), showing the oxidation of the Al layer. (d) Measurement of the sheet resistance versus the temperature of the STO/A(0.9)/Py(2.5)/AlO_x (dark) and STO/Py(2.5)/AlO_x (brown) stacks, which allows the extraction of the 2DEG resistivity evolution versus temperature (red) (Images from [20]).

The inverse Edelstein length extracted at the AlOx/STO interface goes up to 30 nm, which is more than two order of magnitude larger than the 0.2 nm estimated at the Ag/Bi and Cu/Au interfaces [98, 170] despite the larger Rashba parameters α_R observed at these interfaces (0.5 eV· Å for Ag/Bi [171] versus (0.01 eV· Å for 2DEGs at the surface of STO [158]). As discussed in the section 3.2.2 of chapter 1, this can be explained by the scattering of the interfacial states outside of the 2DEG. The Edelstein length is indeed proportional to $\alpha_R \tau_{eff}$ with $\tau_{eff} = (1/\tau + 2/\tau_{esc})^{-1}$, τ being the scattering time of the electronic states in the isolated 2DEG while τ_{esc} is the scattering time in the neighboring metallic elements. At metal-metal interfaces, we may expect that $\tau_{esc} \ll \tau$ as the electrons can easily scatter outside the 2DEG. At the interface between STO and Al_2O_3 however, the scattering of the electrons outside of the 2DEG takes place only in the nearby NiFe layer. To access this layer the electrons have to tunnel through the Al_2O_3 barrier which severely reduces τ_{esc}, thus increasing λ_{IEE} at the STO/Al_2O_3 interface with respect to Ag/Bi, despite a smaller Rashba parameter in the former [20]. In the next paragraph, I will discuss this effect in more details, by showing the formation of 2DEGs at the surface of STO by Ta and Y deposition allowing for a modulation of τ_{esc}, which increases the range of application possibilities of the STO-based 2DEG systems. The following section contains a summary of a research work done in collaboration with the group of Manuel Bibes in CNRS/Thales and published in Physical Review Materials [172]. The growth and XPS characterization and the samples have been performed by Luis M. Vicente-Arche and Srijani Mallik in CNRS/Thales. I performed the SP-FMR interconversion measurements in SPINTEC, and participated to the analysis.

Spin-charge interconversion at metal/STO interfaces

As mentioned earlier, the formation of a 2DEG on STO(001) by aluminium deposition appears to originate from the interfacial Ti reduction, due to the oxidation of the Al layer. It should in principle be possible to achieve this 2DEG formation by depositing other reactive metals on STO, provided that they verify the thermodynamic criterion $\Delta H_{f,ox} <$

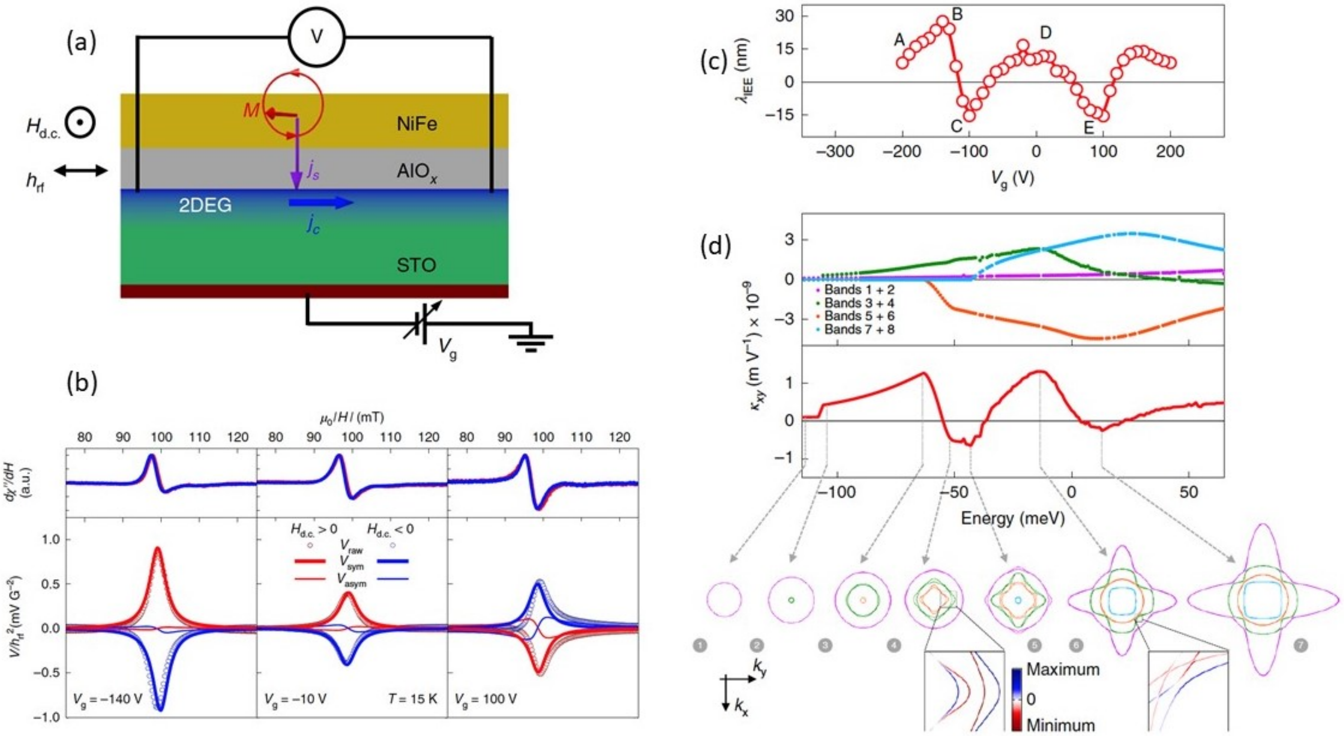

Figure 4.7: (a) SP-FMR configuration used for the interconversion measurements, with a back gate applied to tune the Fermi level position into the 2DEG. M corresponds to the magnetization of the NiFe layer. (b) FMR curve (top) and interconversion signal (bottom) measured at three different gate voltages for a positive (red) and negative (blue) magnetic field. The symmetric and asymmetric component have been separated, showing the strong domination of the former. While the amplitude of the interconversion signal strongly depends on the gate voltage, the FMR curve does not change, showing that the gate has no influence on the FMR but strongly modifies the interconversion efficiency and even changes its sign. (c) Experimental evolution of the Edelstein length with the gate voltage. (d) Theoretical contribution of the different bands to the interconversion, showing the effect of the multi-orbital transport and of the avoided crossings on the interconversion. (Images from ref. [20]).

$-250\,kJ/molO$ which means that the oxidation of the metal overlayer is favoured over that of the STO. Here, we focus on three different metals: Aluminium, Yttrium and Tantalum. The reduction of STO by these metals was monitored by XPS measurements, with varying metals thicknesses. This showed that Ti sites reduces differently depending on the deposited metal, and that a minimum metal thickness must be deposited to form the 2DEG and to protect it from the ambient conditions. The oxidation state of the metallic layer was also measured by XPS, which provided important information regarding the presence of unoxidized metallic pocket in the system, which would reduce the 2DEG mobility by opening additional scattering channels. The presence of the 2DEG and its transport properties are then controlled by transport measurement. Finally, I performed measurement of the interconversion with SP-FMR measurements in STO/X/Py systems (X=Al, Y and Ta), in which the different interconversion efficiencies observed for the studied systems were attributed to the different escape times of the electrons through the metal insertion between STO and Py.

Let us start with the STO Ti atoms reduction by the metal layers. The evolution of Ti valence states is plotted in Fig. 4.8a as a function of the metal thicknesses for all the samples, measured in situ, without breaking the vacuum of the deposition chamber (open circles), as well as after being exposed to air (filled circles). Increasing the thickness of the deposited reactive metal results in a decrease in the fraction of high-valence Ti^{4+} states of STO, which eventually saturates after depositing a few Å of metal. The minimum thickness to reach this point is larger for Y, then for Al and for Ta. Furthermore, Fig. 4.8a also reflects the critical thickness needed to preserve the reduced Ti from reoxidation by the air. This critical thickness can be defined as the point where the in situ and ex situ curves for the Ti^{4+} valence state meet. The two data sets meet around 1.3–1.7 nm for Al, 1–1.3 nm for Ta, and beyond 1.6 nm for Y. This observation can be well correlated with the oxygen diffusion coefficients of Y_2O_3, Ta_2O_5, and Al_2O_3. It is known that the oxygen diffusion coefficient for Ta_2O_5 and Al_2O_3 are of similar order of magnitude whereas it is higher for Y_2O_3 [173]. Therefore, even if Y shows the highest reduction of STO, it is not a good candidate to protect the reduced metal/STO interface (and thus the 2DEG) in comparison with Al and Ta. From these data, we also determine the thickness of the oxide formed by the reduction of the STO by metal deposition, which corresponds to the point where the concentration of Ti^{3+} becomes constant, *i.e.*, ∼0.9 nm for Al, ∼0.3 for Ta, and ∼1.2 nm for Y. In principle, for each system the sum of these two critical thicknesses indicates the deposited metal thickness above which the presence of non-oxidized metallic regions may be expected. This thickness is thus around 2.6 nm for Al, 1.6 nm for Ta, and 2.8 nm for Y, and correspond to the maximum thickness at which the metal is fully oxidized: its bottom by the reduction of STO, and its top by reaction with air. In addition, we also studied the evolution of the metal valence states after each deposition. The relative fraction of oxides and non-oxidized metal contributions obtained ex-situ for different materials are shown in Fig. 4.8b as a function of the metal thicknesses. By increasing the metal thickness, one observes the non-oxidized metal contribution for Al and Y along with their corresponding oxide valence state (Al^{3+}, Y^{3+}). In contrast, in the case of Ta, we firstly observe the appearance of reduced valence states of Ta, related to the formation of intermediate oxides (Ta^{4+}, Ta^{2+}, Ta^{1+}) which exhibit maxima depending on the thickness of the deposited Ta layer. By further increasing the thickness we observe a contribution of metallic Ta. It should be noted that the appearance of a non-oxidized metal is observed in *ex situ* XPS spectra above the thickness of the metal layers required to saturate the STO reduction. Ideally, this contribution appears when no further oxidation of the metal is possible between the oxide layers formed by the oxidation from STO and from the air.

It can be observed in Fig. 4.8b that the minimum thickness at which the non-oxidized metal appears is similar for the Al and Ta cases (∼1.5 nm), while in the case of Y it is notably higher (∼5 nm). This can be explained by considering two phenomena happening simultaneously. The first is the stronger oxidation of Y upon reducing STO, as observed in Fig. 4.8b. The second is the higher oxygen diffusion coefficient [173, 174, 175] and thicker metal oxide layer thickness for Y when exposed to air. This is also confirmed by the metal oxide layer thicknesses (t_{ox}) obtained by means of XRR on thicker samples exposed to air, which are $t_{ox,\mathrm{Y_2O_3}} = 3.8$ nm, $t_{ox,\mathrm{Al_2O_3}} = 1.8$ nm, $t_{ox,\mathrm{Ta_2O_5}} = 1.6$ nm. These numbers correspond to the passivation thickness of air-exposed Ta, Y and Al. Further, by increasing the thickness of the metal up to ∼60 nm, the trends evolve towards the saturation of contributions from the non-oxidized metal and oxides where only the native oxide and non-oxidized metal underneath are detected (as shown by the crossed circle in Fig. 4.8b). Finally, we note that for the Al and Y cases, the metallic contribution is detected in XPS at different thicknesses from those estimated from Fig. 4.8a. For the Al case, this metallic contribution is detected before reaching the critical thickness of 2.6 nm of Al. This may be explained by considering the relatively higher roughness observed by AFM on Al-based samples, with the apparition of grain with a height of up to 4 nm for films thicker than 1.7 nm. Thus, it is likely that after depositing a nominal thickness of 1.7 nm of Al some regions are thicker than 2.6 nm, favoring the presence of a metallic phase underneath. On the other hand, for the Y case, the thickness above which this metallic contribution is detected is much larger (5.1 nm) than that estimated from Fig. 4.8a (2.9 nm). This difference is possibly due to an underestimated Y thickness oxidized by STO (1.2 nm), due to the insufficient probing depth of XPS to access the whole 2DEG thickness. The evolution of the sheet resistance R_s versus temperature with different metal thicknesses is displayed in Fig. 4.8c. We observed a variation of R_s by one order of magnitude, which cannot be ascribed to the metallic capping. This implies the existence of an additional path for conduction related to the formation of a 2DEG when the STO is reduced, which is consistent with XPS data. The sheet resistance at 2 K decreases when the metal thickness increases due to the opening of an additional electronic conduction path when non-oxidized metallic areas start to appear. The sheet resistance drops when decreasing the temperature is also larger for thinner metallic capping, since in this case only the 2DEG takes part in the electronic conduction. Furthermore, we observed that the samples become insulating below ~ 1 nm as the oxide layer is not enough to protect the 2DEG region from re-oxidation by air. The carrier density of the different 2DEGs have been extracted by performing Hall measurements at 2K. A general trend is that the carrier density increases with the deposited metal thickness, until it saturates for different thicknesses depending on the metal: $n_{Al} = 9 \times 10^{13}\mathrm{cm}^{-2}$, $n_{Ta} = 7 \times 10^{13}\mathrm{cm}^{-2}$ and $n_Y = 4.5 \times 10^{13}\mathrm{cm}^{-2}$. In addition, we also observe that the carrier density saturates at different thicknesses depending on the deposited metal. This occurs when there is no further reduction of STO by increasing the metal thickness. For Al, Ta, and Y the saturation of carrier densities occurs at 1.6, 1.2, and 1.8 nm, respectively. These thicknesses match well with the critical metal thicknesses obtained from XPS. By comparing the carrier densities of each system, it can be observed that Al shows the highest carrier density while Y exhibits the lowest. However, we observed from the XPS data that the reduction of STO was maximum for Y. So, it was expected to have higher carrier densities in Y. Therefore, it has not been possible to correlate the concentration of Ti^3 into the STO with the transport properties of the 2DEG present at the interface between the different oxides. As reflected in this study, a higher concentration of oxygen vacancies in STO does not necessarily lead to higher densities of mobile carriers. The formation of 2DEGs is a complex process, and the ionic and electronic transports through the oxide layer seem to be the determinant factor in the final properties of the 2DEG. Also, the role of metal-induced gap states, defects, and fixed charges has probably to be considered.

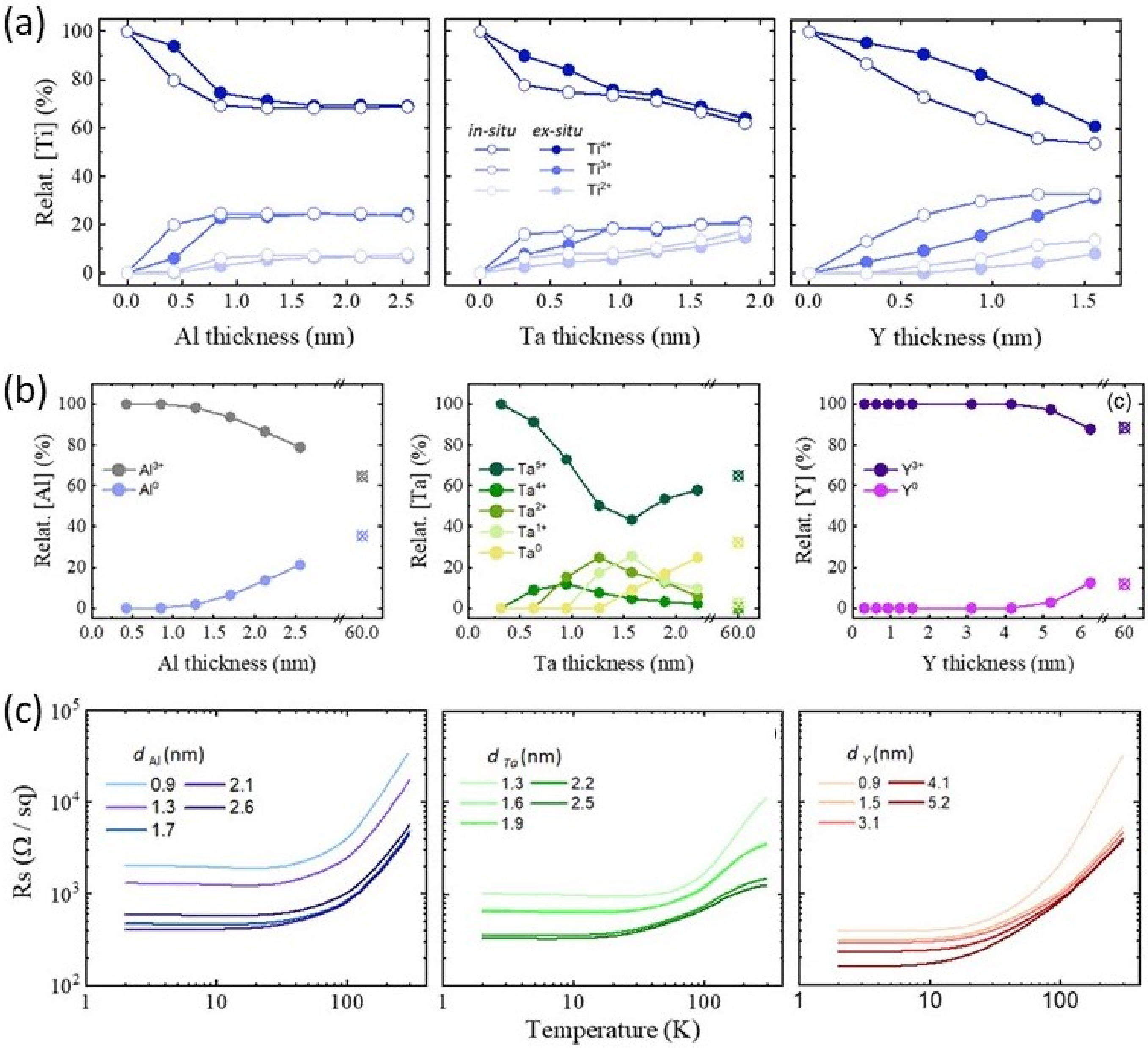

Figure 4.8: (a) Ti valence states evolution when increasing the thickness of Al, Ta, and Y. The open circles correspond to the spectra collected in situ. The filled circles correspond to the spectra collected for the same samples after being exposed to air. (b) Relative fractions of oxide and metals for Al, Ta, and Y as a function of the metal thickness. (c) Temperature dependence of the sheet resistance of the samples when varying the thickness of the Al, Ta and Y layers.

Finally, in order to assess the role of the different metals in the interconversion, we performed spin pumping measurements in STO/X(1 nm)/Py(20 nm) stacks with X=Al, Ta and Y. The spin pumping stacks where capped with 2 nm of Al, which does not play any role in the transport and in the interconversion since it is fully oxidized, and has the effect of protecting the Py film from oxidation by air. Prior to the interconversion measurements, the 2DEGs obtained in these stacks were characterized by measuring the carrier densities. This was done by performing magnetotransport measurement in STO/X(1 nm)/Py(2.5 nm) stacks, in which the Py thickness was reduced to minimize its influence on the measurement. The carrier densities are 6.66×10^{13}, 9.22×10^{13} and $10.5 \times 10^{13}\,\mathrm{cm}^{-2}$ for Ta, Al and Y, respectively, which matches with the Ti^{3+} fraction measured by XPS. This indicates that the Py prevents the reoxidation of the STO after exposure to air, while the Y, Al and Ta layer are still fully oxidized according to the results presented in Fig.

4.8a.

The figure 4.9 presents the results of the SP-FMR experiments on three STO/metal/NiFe samples with 0.9-nm-thick metal layers. Similarly to the results presented in the previous section, the interconversion signals exhibit a strong gate voltage dependence, with maxima and sign changes that correspond to the onset of conversion in bands having opposite signs for their spin-charge conversion efficiencies, or to specific avoided crossing points as described in Fig. 4.7d. The maxima occur at slightly different gate voltage values for Ta, Al, and Y samples, which reflects slight differences in the position of the Fermi energy across the band structure, as carriers are accumulated or depleted into the 2DEG by the gate voltage. This is expected since the carrier densities in the ungated case are different for each metal. Also, the difference in gate voltage positions between the two negative maxima varies between samples, being around 200 V for Al and Y but closer to 300 V for Ta. This may reflect different efficiencies in the electrostatic gating, for instance, due to different built-in electric fields in the 2DEG.

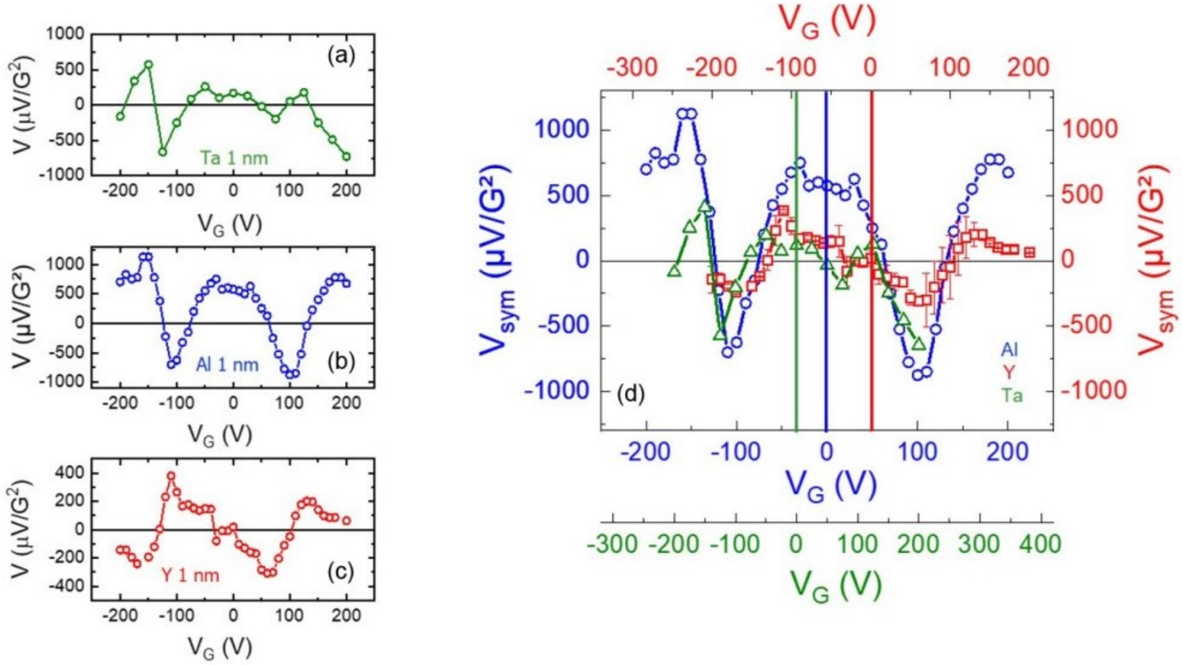

Figure 4.9: Gate dependence of the transverse voltage measured during SP-FMR experiments for STO/metal(1 nm)/NiFe(20 nm) samples for Ta (a), Al (b), and Y (c). (d) Same data replotted by shifting and/or expanding the gate voltage axis for better comparison (see text for details). The vertical lines indicate the zero gate position for the three systems.

Fig. 4.9d replots the data from Fig. 4.9a-4.9c with the same vertical scale, but with the horizontal axes slightly shifted and/or stretched to match the position of the two negative maxima. The rescaling of the back-gate dependence of the interconversion may be explained by the different spatial extensions of the 2DEGs obtained by sputtering Al, Ta and Y on STO. Indeed, the transport measurements performed on these 2DEGs revealed a larger mobility for the Y-formed 2DEG than for the Al and Ta-formed ones. This can be due to the smaller scattering probability of the electrons constituting the 2DEG for STO/Y stacks, thus indicating a larger vertical extension of 2DEG the when compared with Al and Ta-formed 2DEGs [177] that might be due to the more efficient Ti oxidation by Y deposition. From electrostatic considerations [176], it is expected that a large vertical spatial extension of the 2DEG will reduce the backgate induced carrier density modulation. Consequently, the possibility to tune the spin to charge interconversion efficiency by moving the Fermi level in the band structure is reduced for Y-formed 2DEG. This means that, when compared to the case of Al and Ta-formed 2DEG, the Fermi level energy shift for a given backgate voltage variation is reduced. This idea is supported by two observations regarding the spin to charge interconversion modulation (Fig. 4.9). First, the width of the extrema obtained using Y are wider than for Ta and Al. Second, the extrema are shifted downward in the Y-case as compared when Ta and Al. Since at the maximum backgate voltage the Fermi level lies at the top edge of the quantum well that hosts the 2DEG [178], the +200 V backgate point corresponds to a common position of the Fermi energy in the 2DEG band structure for the three systems. When decreasing the backgate voltage however, the downward shift of the

Fermi level for the 2DEG formed by Y is smaller than for the one formed by Ta and Al. This would result in a shift of the extrema to lower backgate voltages for the former system. Finally, band structure modifications induced by the different Ti oxidation level are also expected to be present [179], which would explain some slight modifications in the backgate dependence of the spin to charge interconversion. While the main features of the spin-charge conversion efficiency as a function of gate voltage can be explained by band structure effects and subtle variations in the carrier density between samples, the absolute amplitude of the conversion differs between STO/Al, STO/Ta, and STO/Y 2DEGs. This is a priori surprising if the various maxima observed in the gate dependencies correspond to the same points in the band structure for all three systems. In fact, another ingredient is needed: as mentioned above, the conversion efficiency is proportional to the (effective) Rashba coefficient α_R and to the effective scattering time τ_{eff}. This scattering time accounts for the possibility for electrons to leak out of the 2DEG through the metal oxide —acting as a tunnel barrier— , to quickly scatter in the NiFe (the scattering time in metals is in the fs range, while it is in the ps range in the 2DEG). In fact, Al, Ta, and Y oxide tunnel barriers have different tunneling transparencies, quantified by their resistance area (RA) product, and may thus result in various effective τ_{eff} values. We can relate the escape time to the RA product through $\tau_{esc} = \frac{RAe^2m^\star}{2\pi\hbar^2}$ with e the electron charge and $m^\star$ the effective mass, and thus calculate the effective scattering time. While $\sim$ 1-nm thick $\mathrm{AlO_x}$ and $\mathrm{TaO_x}$ barriers have relatively high RA values, in the order of 1 $\mathrm{M\Omega \cdot \mu m^2}$, corresponding to τ_{esc} values in the ns range or longer. The scattering rate τ in the 2DEG is consequently much larger than that in Py, so that $\tau_{eff} \sim \tau$. On the other hand, $\mathrm{YO_x}$ barriers are less resistive, with RA values closer to 1 $\mathrm{k\Omega \cdot \mu m^2}$ [180, 181, 182], leading to a τ_{esc} in the ps range. Since τ_{2DEG} is also in the ps range, significant leakage is expected to occur in the Y sample, leading to the reduction of the spin-charge conversion efficiency observed experimentally.

The results presented in this paragraph show that the formation of a 2DEG on STO with (001) orientation is achievable not only with Al, but also with Ta and Y. Furthermore, the 2DEG formation mechanism is the same for all these three materials, with quantitative differences that depend on the details of their oxidation enthalpies. The gate dependence of the interconversion for these different systems is also qualitatively similar, with differences due to the different carrier concentrations of the 2DEGs and to the properties of the tunneling barriers. This highlights the universality and simplicity of the fabrication method of 2DEG by metal capping.

Using these results, we developed in SPINTEC a process for the fabrication of 2DEGs at the surface of STO(001), using a MgO capping on top of the Ta(0.5) layer deposited on STO, to avoid re-oxidization by air. We also developed and characterized new 2DEG systems, by obtaining a 2DEG on top of STO(001) when depositing a thin layer of Mg, which opens possibilities for the fabrication of out-of-plane ferromagnetic thin films in close proximity to the 2DEG, that could be used for efficient SOT-switching. Furthermore, we obtained 2DEGs by Ta deposition on STO with 111 and 110 orientations, which has not been achieved so far, and will be used to study the effect of orbital hierarchy modification on the interconversion in these systems [183, 184]. The considerations developed in this study also provide guideline for the electrical detection of the interconversion in STO-based system, using two central results: (1) the resistance area of the 2DEG controls the spin tunneling time of the electron through the oxide and (2) the 2DEG fabricated using a less than 1 nm thick metal capping are unstable in air. An efficient electrical spin injection in a 2DEG can therefore be achieved only through the thinnest oxidized metal capping layer, even though the barrier must be resistive enough in order to minimize the scattering time outside of the 2DEG. This problematic is similar to that of the spin injection in semi-conducting materials [127]. In addition, the devices based on spin-charge interconversion in 2DEGs will have to be protected from the ambient conditions, owing to the re-oxidization by air or thin metallic barriers. Processes following these guidelines for the nanofabrication of devices for local detection of the spin-charge interconversion will be described in the next chapter.

In this second section, I have focused on the spin-charge interconversion in metal-capped STO(001). I have shown that in these systems, it is possible to modulate the spin-charge interconversion by changing the capping material used for the formation of the 2DEG. In the next section, I will discuss another direction of research, which aims at modulating the interconversion properties by fabricating 2DEG electron gases on other complex oxide materials.

4.3 Spin-charge interconversion in two dimensional electron gases at the surface of $\mathrm{KTaO_3}$

Most studies related to the physics of 2DEGs at the surface of transition metal oxides are based on STO. This material is however not the only one onto which a two 2DEG can be fabricated since 2DEGs also have been obtained at the surface of $\mathrm{KTaO_3}$, a transition metal oxide parent to STO [185]. Furthermore, the large interconversion efficiencies observed on 2DEGs at the interfaces of STO/Al and STO/LAO have been observed thanks to the large escape time of the electronic states in these systems, and despite the small spin-orbit coupling of the light Ti site that hosts the 2DEG. A natural idea to increase the efficiency of the interconversion would be to combine the long spin lifetime of electrons with a large spin-orbit coupling. This can be achieved in $KTaO_3$ (KTO), where the heavy Ta atoms has a large spin-orbit coupling. In this section, I will start by highlighting the similarities and differences between STO and KTO. I will then describe the consequences of the large spin-orbit coupling of bulk and 2DEG band structures, before showing our results on the 2DEG formation and measurement of the Inverse Edelstein Effect at the KTO/AlO_x interface.

The paragraph 2 of this section then contains the summary of a research work done in collaboration with the group of Manuel Bibes in CNRS/Thales and published in Advanced Materials [186]. The growth, XPS, and ARPES characterization and the samples have been performed by Luis M. Vicente-Arche, Julien Bréhin and Sara Varotto in CNRS/Thales, while I performed the SP-FMR interconversion measurements in SPINTEC.

4.3.1 $KTaO_3$: a STO-like complex oxide

$KTaO_3$ (KTO) is, similarly to STO, a large bandgap ($E_g = 3.64$ eV [187]) quantum paraelectric insulator, with a large dielectric constant ($\epsilon = 4500$ [188]) at low temperature. It has a perovskite structure ABO_3, with the oxygen octahedron surrounding the Ta atoms, giving them a 5+ valence state. In contrast with STO (001) however, KTO with (001) orientation is a polar material with alternating K^+O^{2-} (charge $-e$) and $Ta^{5+}O^{2-}$ planes ($+e$) alternating along the 001 direction. Its band structure also shares several similarities with that of STO. Its valence band is indeed composed of oxygen 2p states, weakly hybridized with the 5d Ta states that compose the bottom of the conduction band [189]. The oxygen octahedron splits these 5d states into e_g and t_{2g} groups separated by a several eV energy difference. These similarities make KTO a compound parent to STO. The main difference between KTO and STO comes from the presence of the heavy Ta element, which generates a spin-orbit interaction of 400 meV [190], much larger than the 10 to 30 meV introduced by Ti in STO. This results in a strong k-dependent hybridization of the t_{2g} orbital close to the Γ point in bulk KTO [191]. These orbitals split into two doubly degenerate low lying bands with, along for instance the k_y direction, a light band with mass $0.24\,\mathrm{m_e}$ with a majority contribution of d_{xy} and d_{yz} orbitals, and a heavy band ($0.66\,\mathrm{m_e}$) composed in majority of d_{xz} orbitals [191]. The split-off band with an intermediate mass ($0.35\,m_e$) lies 400 meV above these two bands, and is an equal mixture of all the t_{2g} orbitals (Fig. 4.10a).

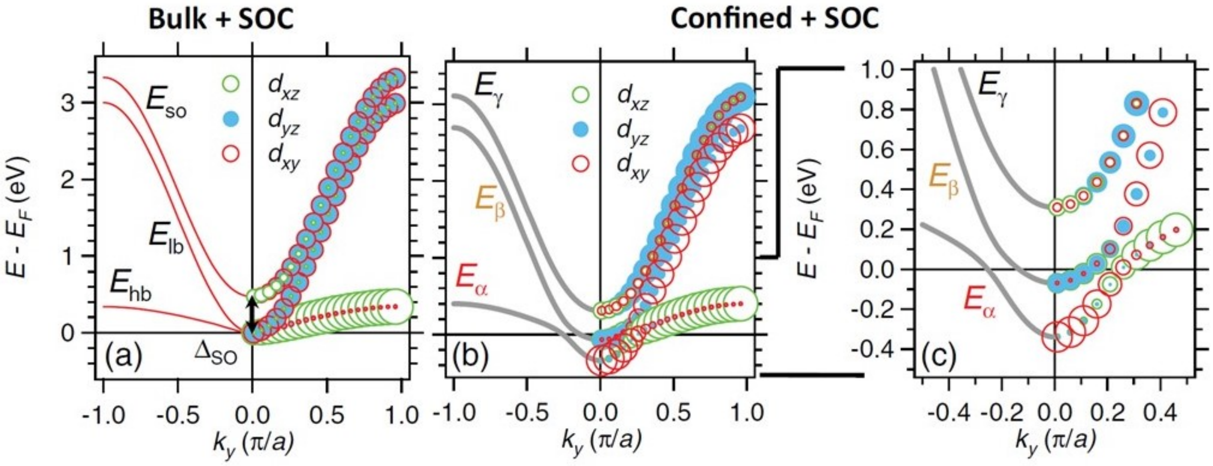

Figure 4.10: (a) Tight binding calculation of the bulk KTO bottom conduction bands. The colored dots and circles give the relative weights of the t_{2g} orbital characters. (b) and (c) Effect of the confinement on the three bulk bands (Image from ref. [191]).

Importantly, it has been demonstrated that KTO (001) can host a two dimensional electron gas, either by cleaving a KTO crystal in vacuum [193], or at the interface with oxides such as EuO, LVO or LAO [192], which creates a potential well of around 500 meV hosting the 2DEG at the surface of KTO [191]. These 2DEGs have demonstrated high mobilities up to $10^4\,\mathrm{cm^2 \cdot V^{-1} \cdot s^{-1}}$ and low carrier densities from 10^{12} to $10^{15}\,\mathrm{cm^{-2}}$, which are ranges of values similar to those obtained for 2DEGs at the surface of STO. Furthermore, magnetotransport effects have demonstrated the presence of a large SOC in KTO-based 2DEGs [187], and the inverse Edelstein effect at the KTO/EuO interface has been measured using thermal methods, with however a small generated charge current and no evaluation of the interconversion efficiency [195]. The specificity of the band structure on the surface of KTO has however been highlighted by ARPES measurements on cleaved samples [194]. Similarly to the case of STO, let us define z as the normal to the interface. Due to the strong

SOC in KTO, the t_{2g} orbital-based band have components with different masses along the Z direction: $5\,\mathrm{m_e}$ for d_{xy}, and $0.3\,m_e$ for $d_{zx/yz}$. Furthermore, the in-plane masses in KTO are lighter than that with similar orbital symmetries in STO, so that a higher mobility can be expected. As discussed in section 2, this causes these orbitals to shift in energy at the interface by a value inversely proportional to their mass along the z axis. The symmetries of the different bands of the 2DEG then change depending on the k_y value (Fig. 4.10b), in contrast to the STO bands that retained their orbital characters far from the avoided crossings (Fig. 4.5d). The change of symmetry of the KTO bands leads to a new set of bands. The lowest lying band is denoted α, and has a strong d_{xy} character with a mass $0.25\,m_e$ along the Y direction. The second band in energy is denoted β and is heavier ($0.5\,m_e$) with an equal admixture of d_{xz} and d_{yz} character, but however remains k-dependent (Fig. 4.10c). The split-off band γ is an equal admixture of all the t_{2g} bands. The γ band sits 400 meV above the other and is above the Fermi energy so that is has not been observed in ARPES measurements. This mass renormalization of the KTO bands in the 2DEG and their k-dependent orbital character is a specificity of the KTO based 2DEG.

In the next paragraph, I will demonstrate the formation of a similar 2DEG by deposition of an ultrathin Al film on KTO, and measure its spin-charge properties. Similarly to the case of STO, the formation of the 2DEG was monitored by XPS for an increasing Al thickness, supported by ARPES which revealed a 2DEG multiband structure compatible with the theoretical description. We then conducted SP-FMR measurements in this 2DEG, and observed a spin-charge conversion with an efficiency comparable to that of STO/LAO.

4.3.2 Measurement of the spin-charge interconversion in the 2DEG at the surface of $\mathrm{KTaO_3}$

Figure 4.11a–c shows the result of in situ XPS measurement of the 4f levels of Ta in KTO, before (Figure 4.11a) and after (Figure 4.11b and 4.11c) the deposition of Al by sputtering. For the pristine KTO substrate, the spectrum can be well fitted by two components corresponding to $\mathrm{Ta^{5+}}$ ions, as expected from the stoichiometry. After depositing 10 Å of Al (Figure 4.11b), some spectral contributions appear at low binding energies, which reflect the reduction of $\mathrm{Ta^{5+}}$ into $\mathrm{Ta^{4+}}$ and $\mathrm{Ta^{2+}}$. This gives a measure of the population of the Ta 5d levels and points to the generation of an electron gas. The relative fraction of these reduced species increases for 21 Å of Al (Figure 14c). Similar measurements were performed for additional Al thicknesses and the results are displayed in Figure 4.11d. The relative fractions of $\mathrm{Ta^{4+}}$ and $\mathrm{Ta^{2+}}$ increase with the Al thickness at the expense of $\mathrm{Ta^{5+}}$, which indicates that the electron density in the 5d bands of Ta increases for thicker Al. XPS of the Al 2p levels for 21 Å of Al showed that the Al was almost fully oxidized after exposing the samples to atmosphere, which is consistent with the XPS results obtained on STO/Al (section 2).

Complementary photoemission experiments were performed at the Cassiopée beamline of Synchrotron SOLEIL. KTO/Al samples were prepared by growing a film of Al in a molecular beam epitaxy chamber that is connected under ultra-high vacuum to the ARPES chamber. Figure 4.11g presents the band dispersions near Γ_{002} probed by ARPES, which resemble those measured for KTO(001) surfaces [194, 191]. Measurements at different photon energies confirmed that such electronic states are confined to the interface, as they do not disperse with k_z. Three parabolic bands are visible. The dotted lines indicate the positions of the bands predicted by Santander-Syro et al.[191]. The bottom band labelled $E_\alpha^{n=1}$ has an effective mass of $m = 0.23\,m_e$, the second band ($E_\alpha^{n=2}$) has $m = 0.23\,m_e$, and the third band ($E_\beta^{n=1}$) has a mass $m = 0.52\,m_e$. Recent calculations suggest that $E_\beta^{n=1}$ should display a substantial Rashba splitting ($\Delta \sim$30 meV) [187], three times larger than that of STO [187] due to the large spin-orbit coupling in Ta when compared to Ti. This feature however cannot be resolved here and was not detected in previous ARPES experiments [194, 191]. The corresponding energy cuts at the Fermi level are shown in Figure 2h, which show evidence of pseudocircular Fermi surfaces (FSs). The dotted lines correspond to the FSs adapted from ref. [191]. From the ARPES data, we estimate that the carrier densities of bands $E_\alpha^{n=1}$, $E_\alpha^{n=2}$ and $E_\beta^{n=1}$ are around $4.1 \cdot 10^{13}$, $1.9 \cdot 10^{13}$, and $1.3 \cdot 10^{13}$ $\mathrm{cm^{-2}}$, respectively. This yields a total carrier density $n_s = 7.3 \cdot 10^{13}\,\mathrm{cm^{-2}}$, which is lower than that for the free surface ($n_s = 1.26 \cdot 10^{14}\,\mathrm{cm^{-2}}$ in ref. [191] or $n_s = 2 \cdot 10^{14}\,\mathrm{cm^{-2}}$ in ref. [194]).

The presence of a conductive interface between KTO and $\mathrm{AlO_x}$ has been controlled by performing sheet resistance (R_s) measurement versus temperature, for different thicknesses of Al. The residual resistivity ratio is above 10, and the low temperature R_s shows a general decrease with increasing Al thickness (Fig. 4.12a), reaching values as small as 150-200 Ω/sq. The Hall measurements performed in these systems exhibit non-linear variations with the magnetic field, which suggest the presence of at least two conducting channels. Fitting the data with a two-band model yields the carrier density n_{s1} and n_{s2} plotted in Fig. 4.12b and the corresponding mobilities μ_1 and μ_2 shown in Fig. 4.12c. This highlights the multi-orbital transport expected from ARPES measurements and band structure calculations. For both bands, the carrier densities and mobilities tend to increase with the Al thickness. The majority carriers (with density n_{s1}) have relatively low mobilities, in the $100 - 500\,\mathrm{cm^2V^{-1}s^{-1}}$ range, while the minority carriers (with density n_{s2}) have mobilities reaching $\approx 2000\,\mathrm{cm^2V^{-1}s^{-1}}$. The maximum total carrier density extracted from the Hall data reaches

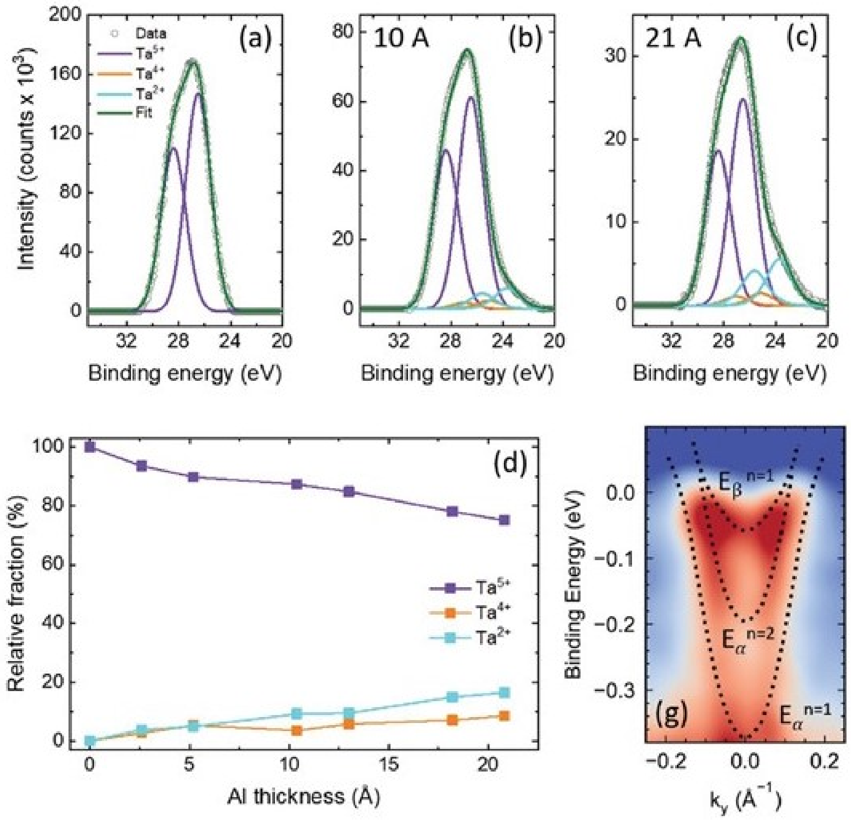

Figure 4.11: (a) XPS spectrum of the Ta 4f levels for a virgin KTO substrate. (b) XPS after deposition of 10 Å of Al. (c) XPS after deposition of 21 Å of Al. (d) Dependence of the relative fraction of the different Ta valence states with the Al thickness. (g) Dispersion curves measured by ARPES for a KTO/Al(2 Å) sample. The dotted lines highlight the positions of the bands, which are labelled following the convention of ref. [191].

$\approx 1.3 \cdot 10^{13}$ cm^{-2}, and is thus slightly lower than that found in ARPES. This is possibly due to some reoxidation of the KTO when the samples are exposed to the atmosphere. One can also ascribe the high-mobility minority carriers to the $E_\beta^{n=1}$ band and the lower-mobility minority carriers to the $E_\alpha^{n=1}$ and $E_\alpha^{n=2}$ bands. The apparent inconsistency between the high mobility and the larger effective mass of carriers from the $E_\beta^{n=1}$ band has previously been seen in STO 2DEGs, and is ascribed to the larger distance of these carriers from the physical interface [177], which leads to longer scattering times τ (here in the range of $\tau_2 \approx 0.6\,ps$, versus $\tau_1 \approx 0.04\,ps$ for the low-mobility carriers from bands $E_\alpha^{n=1}$ and $E_\alpha^{n=2}$).

To probe spin–charge conversion by SP-FMR experiments, we prepared KTO/Al(0.9 nm)/NiFe/AlO$_x$ samples where the AlO$_x$-capped NiFe layer was grown in the same chamber without breaking vacuum between the different deposition. The NiFe thickness was 20 nm, but we also grew samples with a 2.5 nm thick NiFe layer. We performed magnetotransport measurements to extract the carrier densities and mobilities in the 2DEG, [196, 197] from which we found a total carrier density of about $1 \cdot 10^{14}$cm^{-2}. Similarly to the case of STO/Al described in section 2, a back gate was applied during the SP-FMR measurement to check the possibility to modulate the interconversion by changing the position of the Fermi level into the 2DEG band structure. The SP-FMR measurements and the FMR signals obtained for different applied gate voltages are shown in Fig. 4.13a. The FMR measurements displayed a secondary peak that possibly originates from an insufficient Al capping thickness. This could result in a partial oxidization of the top of the NiFe layer, which would change locally the FMR properties resulting in this secondary peak. Since this concerns a part of the NiFe layer that is not in contact with the 2DEG, this should not influence the interconversion measurements. As expected, the FMR signal does not vary with the back-gate voltage. The electrical signals shown in the lower panel display a gate-dependent signal with symmetric and asymmetric Lorentzian components. The symmetric part of the Lorentzian reverses when changing the direction of the applied magnetic field, which matches the expected symmetries of the interconversion signal. Contrarily to the case of the STO/Al system however, the sign of the interconversion signal does not change over

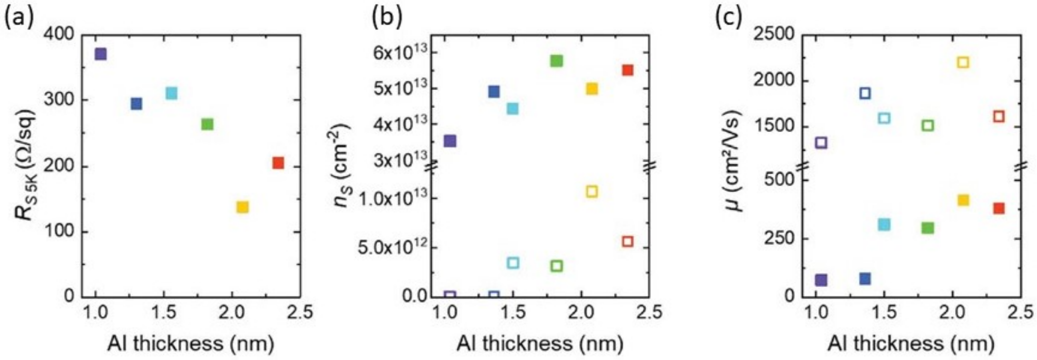

Figure 4.12: (a) Sheet resistance at 5 K, (b) sheet carrier density (n_{s1}: filled symbol, n_{s2} open symbols) and (c) electron mobilities (μ_1: filled symbol, μ_2 open symbols) as a function of the Al thickness.

an applied gate ranging from -200 V to +200 V (Fig. 4.13b). We also note that the sign of the conversion is opposite to that of STO/LAO and STO/Al at large negative gate voltages [168], which would correspond here to a negative Rashba coefficient. From the extra damping induced by the 2DEG with respect to the damping of a reference NiFe layer, the spin current density injected into the 2DEG can be calculated and used to estimate the spin–charge conversion efficiency λ_{IEE}. Its value is found here to be up to $\lambda_{IEE} = -3.5$ nm, comparable to the 6.4 nm measured in STO/LAO-based 2DEGs, which is among the largest value reported to date, albeit lower than that for STO/Al. We also note that the produced raw current is of the order of 40 nA, i.e., much higher than the value of 1 nA reported in thermal spin injection experiments [195].

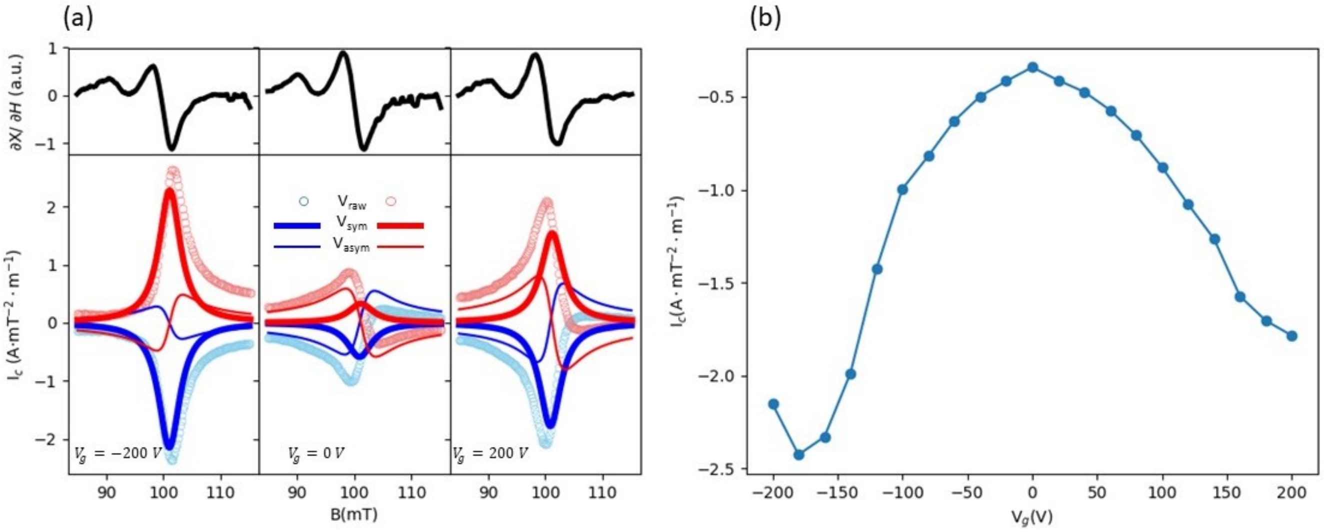

Figure 4.13: (a) FMR (top) and electrical signals (bottom) measured during SP-FMR experiments at different gate voltages. The blue and red curves correspond to opposite static magnetic field directions. The light colors are the raw data, while the heavy ones corresponds to the symmetric (large lines) and asymmetric (thin lines) components of the electrical signal. (b) Gate evolution of the produced charge current measured by SP-FMR.

The Rashba parameter of the KTO/Al 2DEG has been estimated by Bilinear Magnetoresistance measurements [198] (not shown here) performed at CNRS/Thales. A $\alpha \approx$ -70 meV A, i.e., two to three times higher (in absolute value) than the value found for STO 2DEGs was extracted assuming that the interconversion is mostly driven by the high mobility band $E_\beta^{n=1}$. This value of the Rashba coefficient agrees well with the value extracted from weak-antilocalization data, $|\alpha_R| \approx 100$ meV Å [187] and from Shubnikov-de Haas oscillations, $|\alpha_R| = 86$ meV Å [199]. Note that in contrast to other techniques used to determine the Rashba coefficients, the BMR allows its sign to be determined. The value of α_R can be used to calculate $\lambda_{IEE} = \alpha_R \tau/\hbar$, which with $\tau = 0.6$ ps yields $\lambda_{IEE} \approx -6$ nm, in good agreement with the values extracted from SP-FMR when taking into account the additional spin-relaxation channels opened by the presence of a FMs on top of the 2DEG, as discussed in section 2.

Despite being smaller than the very high spin-charge efficiencies reported in STO, the Edelstein length remains among the highest reported so far [200]. Furthermore, several possibilities remain to optimize this efficiency. The dielectric constant of KTO, despite being large, remains smaller than that of STO. Consequently, the Fermi level tuning by applying a back-gate voltage may not allow positioning the Fermi level at the avoided crossing points, and thus achieving the optimal interconversion observed in STO (Fig. 4.7). This issue can be solved either by using a top-gate, as already done in other systems [282], or by forming a 2DEG on KTO by depositing different materials to tune the position of the Fermi level, as discussed in the end of section 2.3.2. Finally, the interconversion in KTO could also be optimized by enhancing the mobility of the 2DEG, that is to say by increasing the electronic scattering time, providing that it remains smaller than the escape time through the oxidized metallic barrier. Finally, the fabrication of a 2DEG on top of KTO, and the measurement of a spin-charge interconversion allows to study the non-trivial effect of spin-orbit coupling on the complex multi-orbital transport. This indicates that their presence could be a universal feature of complex oxides, so that such systems could be achieved on the surface of ferroelectric oxides [29, 283], providing an ideal platform for the spin-logic devices discussed in the next chapter of this manuscript.

Chapter 5

Spin-orbit read-out of a ferroelectric state

The spin-orbit interaction opens possibilities to create full spin-logic architectures for ultralow power computing [28]. This requires the optimization of spin to charge interconversion signals in nanodevices and its study in novel multifunctional materials. The spin to charge interconversion signal optimization can be achieved by the development of alternatives to the lateral spin valves used in Chapter 2 for the measurement of the interconversion [315]. A careful geometrical optimization of the signal in these devices must then be done. Furthermore, the spin-current injection [127] plays a crucial role in the magnitude of the interconversion signal, meaning that the properties of the interfaces between the ferromagnetic current source and the spin-orbit material must be carefully evaluated for future optimization. Finally, large interconversion signals can also be achieved by moving to novel spin-charge interconversion materials.

In the first section of this Chapter, I will discuss the spin-charge interconversion signal optimization in a spin-orbit read-out device used to read the ferroelectric state in the so-called magnetoelectric spin-orbit device [27]. I will show that this can be achieved either by tuning the resistivities and dimensions in the spin-orbit read-out device using platinum as a spin-charge interconversion material, but also by interface engineering. I will then show that large spin to charge interconversion signal can be achieved in these devices by replacing platinum with the topological insulator Sb_2Te_3. In the second section, I will discuss the ferroelectric spin-orbit device, and present preliminary results regarding the patterning and interconversion in multifunctional materials which combine spin to charge interconversion with ferroelectric properties.

5.1 A device for the spin-orbit read-out

In this first section, I will introduce the MESO device, and show that its read-out block corresponds to a *spin-orbit read-out device* (sometimes called a local detection device) used to detect locally the spin to charge interconversion. I will then show how the output spin to charge interconversion signal in a spin-orbit read-out device can be optimized.

5.1.1 MESO device

The basic principle of the MESO device (Fig. 5.1a) is to store the information in the ferroelectric order. This presents two advantages: when compared to transistors, the remnance of the ferroelectric polarization removes the need to apply continuously a voltage to store the information. This non-volatility is an advantage shared with several spin devices such as the MRAM family. However, it is expected that the energy needed to write an information in the MESO device by switching a ferroelectric polarization, i.e. the writing energy, strongly decreases when compared to the magnetization switching by STT or SOT [28]. The energy cost of carrying out a logic operation in these devices could then be reduced to the atojoule scale, which is several order of magnitudes smaller than that of current spintronics solutions. The main difficulty here concerns the reading of the ferroelectric polarization. The solution proposed by Manipatruni *et al.* in ref. [284] is to couple the ferroelectric polarization to the magnetization of a nearby ferromagnetic material, through the magnetoelectric effect (Fig. 5.1c). In this way, the ferroelectric polarization is associated to a magnetization direction. The ferromagnet is then used to produce a spin current with a polarization along its magnetization direction (Fig. 5.1b). The spin current subsequently flows through a material with spin-orbit coupling, which converts it into a charge current (Fig. 5.1b and 5.1c). Since, as discussed before, the direction of the produced charge current depends on the polarization direction, this creates an output voltage with a sign that depends on the magnetization direction, and therefore on the ferroelectric polarization.

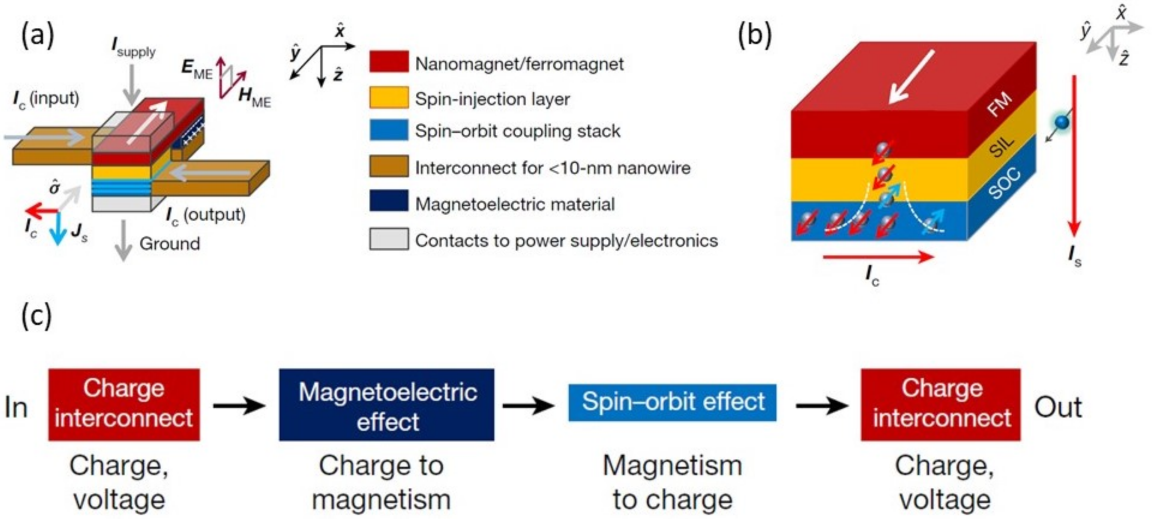

Figure 5.1: (a) Concept of the MESO device. An input charge current is used to manipulate the polarization of a magnetoelectronic material, thus writing the information. This material is coupled to a ferromagnet, so that its polarization state is recorded in the magnetization. A supply current is applied vertically and passes through the ferromagnet, so that it creates a spin current. This spin current is injected in a spin-orbit coupling material, generating an output charge current thanks to a spin to charge conversion process. (b) Principle of the MESO reading block, in which the supply current is converted into a charge current that depends on the magnetization direction. (c) Sketch of the working principle of a MESO device. Images from Ref. [284].

This device concept raises two important challenges. One is to achieve an efficient coupling between the ferroelectric and magnetic order, with a magnetoelectric switching using a minimal voltage. Research is under way in the material science community, targeting a 100 mV switching of the polarization of BiFeO_3, a material used to achieve a magnetoelectric coupling with metallic ferromagnets such as CoFe [285, 286, 287]. The second challenge, with which we are concerned here, is the optimization of the signal output in the reading part of the MESO device. Indeed, the realization of a spintronics logic circuit requires the cascading of MESO devices, in which the output signal of one device would switch the ferroelectric polarization of the next device. This means that these devices necessitate a 100 mV interconversion signal from a $\sim$100 μA bias current, 5 to 6 order of magnitude larger than the commonly achieved microvolts produced through spin-charge interconversion in heavy metals such as platinum [271]. I will address this second challenge in the rest of this section, both from a device geometry and a material perspective.

5.1.2 The spin-orbit read-out device

The Lateral spin valve devices presented in Chapter 2 allow for a simple and straightforward measurement of the spin-charge interconversion, using a pure spin-current and thus without the parasitic charge-related effects observed in other interconversion-measurement systems [275, 300, 301]. Furthermore, they also allow the study of the direct and inverse spin-charge conversion effects on the same device [315]. Due to these advantages, the lateral spin valves have been extensively used for the study of the Spin Hall Effect in heavy metals. The use of these devices for applications such as the MESO device is however limited by several important drawbacks. One is the complexity of the fabrication, which requires a minimum of three electronic lithography steps. This multiplicity of steps is accompanied by a large number of metallic interfaces, whose spin transport properties can strongly modify the measured signal as described in Chapter 1, 2 and 3. More importantly, as observed in Chapter 3 and in literature on metallic lateral spin valves, the amplitude of the measured signals goes from 0.1 to 1 mΩ, which for the usual applied bias currents $\sim$ 100 μA brings the detected voltages close to the usual lock-in detection limit of 10 nV. The smallness of the measured signals then has the effect of hiding important physical features in the measurement noise, and makes impossible the application of such devices for the spin-logic devices.

The interconversion signals measured in LSVs remain small due to the need to separate the spin current injection point, from which the charge current flows, from the SHE material, by a metallic channel in which the spin current relaxes. Recent device developments made in the Spintec laboratory [271] have however shown that this spin diffusion channel is not necessary to the observation of the SHE. This new class of SHE-measurement devices is called a spin-orbit read-out device, and will be described in this paragraph.

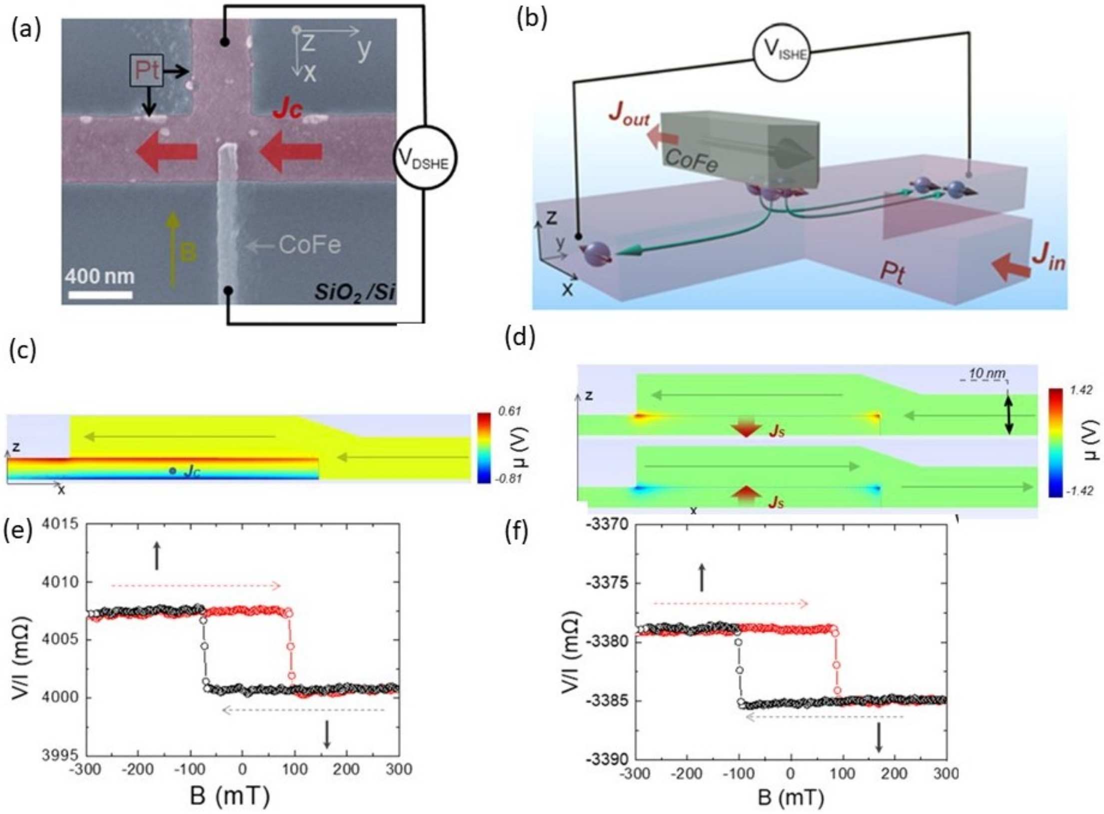

Figure 5.2: (a) Colored SEM image of a spin-orbit read-out device using a direct measurement configuration of the spin Hall effect. (b) Sketch of a spin-orbit read-out device and set up for an inverse measurement configuration of the spin Hall effect. (c) Map of the spin accumulation below the ferromagnetic electrode, in the direct measurement configuration. (d) Map of the spin accumulation in and below the ferromagnetic electrode, in the inverse measurement configuration, for two directions of the bias charge current. (e) Typical signal obtained in a spin-orbit read-out device using a direct measurement configuration and (f) an inverse measurement configuration. The red of black dots corresponds to different directions of the field sweep, and the two resistance states to opposite directions of the ferromagnetic electrode magnetization orientation. Image modified from Ref. [315].

A colored SEM image of spin-orbit read-out device is shown in Fig. 5.2a with a Direct Spin Hall Effect (DSHE) measurement configuration. In this geometry, a ferromagnetic (FM) electrode is deposited on top of a T-shape heavy metal (here Pt) structure. A charge current is then flown between the two outer branches of the heavy metal level, while a transverse potential drop is measured between the T-shaped structure inner branch and the FM electrode. When flowing into platinum, the spin current generates opposite spin accumulations at the edges of the Pt wire (Fig. 5.2c), polarized along the easy magnetization axis of the electrode (X), with different electrochemical potentials for the majority and minority spins ($\mu_\uparrow$ and $\mu_\downarrow$). The Fermi level of the ferromagnetic electrode then aligns with the majority (minority) spin accumulation when its magnetization is along +X (-X). This causes a net positive (negative) electrical potential drop between the electrode and the platinum. The magnetization of the electrode is switched from the +X to the -X direction using a magnetic field along X. The measured transverse potential drop has then a squared shape (Fig. 5.2e), with two lines that corresponds to the different direction of the electrode magnetization. This measurement geometry can also be used to measure the Inverse Spin Hall Effect (ISHE), as shown in Fig. 5.2b. Flowing a charge current from the FM electrode to the platinum inner branch creates a spin accumulation at their interface (Fig. 5.2d), in a mechanism that corresponds to the spin current injection described in Chapter 1. The spin accumulation then diffuses into platinum, generating a spin current into this material, with a polarization along the electrode magnetization. This spin current generates in turn a charge current into a direction that depends on its polarization (Fig. 5.2b), leading to a potential drop between the two outer branches of the T-shaped platinum wire. When reversing the magnetization of the electrode using a magnetic field along X, the polarization of the spin current and the spin accumulation direction reverse (Fig. 5.2d). This leads to an electrical signal at zero field dependent on the electrode magnetization direction (Fig. 5.2f). Importantly, two aspects of the obtained signals must be noted. One is that the DSHE and ISHE signals have the same amplitude, which is expected from the Onsager reciprocity relation [76]. The other one is that their amplitude is of $7\,\mathrm{m}\Omega$, one order of magnitude higher than those obtained for the interconversion measurement in platinum using lateral spin valves.

The spin-orbit read-out device could constitute the reading part of the MESO device. However, their $\sim 10\,\mathrm{m}\Omega$ output signal is still not enough to switch the ME order and cascade the MESO devices into a spin-logic circuit. Indeed, for the typically $100\,\mu$A current, the output voltage is of the order of $1\,\mu$V, far below the minimum 100 mV needed for the logical operation in these devices. The output signal of the spin-orbit read-out device therefore needs to be optimized. This can be done from several progression axis which will be described in the next paragraph.

5.2 Signal optimization for the spin-orbit read-out in heavy metals

A possible way to increase the output signal of a spin-orbit read-out device could be given by the study of its scalability, *e.g.* the evolution of the signal while reducing its size. This is also a crucial parameter for its integration into logic circuits. Progresses can also be done from the point of view of the spin-injection. Indeed, as discussed previously in this manuscript, injecting a spin current into a given material is not straightforward, since several depolarization effects such as the spin memory loss [46] and spin backflow [121] can severely reduce the spin current polarization, and therefore the produced charge current obtained from the ISHE. This clearly calls for interfacial engineering. Finally, the question of the signal optimization can be addressed by looking to materials with optimized spin-charge interconversion efficiencies and higher resistivities, such as topological insulators and Rashba interfaces [200]. I will start by discussing the question of scalability and interface engineering for the measured ISHE signal optimization in the next section, before moving to the realization of a MESO reading block using a topological insulator in the following one.

5.2.1 Scaling properties

We consider in this paragraph a spin-orbit read-out device similar to that presented in section 5.1.2, with a T-shape Pt structure and a CoFe electrode placed on top. In such a device, the ISHE and DSHE signals can be written as [312]:

$$\Delta R_{SHE} = G\lambda_{eff} \tag{5.1}$$

Which is obtained from a one dimensional analysis based on the Valet-Fert equation [35], with G and λ_{eff} describing distinct contributions to the signal. G is termed the *geometrical factor*, and writes [271]:

$$G = \frac{1}{(\frac{t_{CoFe}}{\rho_{CoFe}} + \frac{t_{Pt}}{\rho_{Pt}})w_{Pt}} \tag{5.2}$$

when assuming a transparent interface between the electrode and the Pt structure. The dimensions of the devices are indicated in Fig. 5.3a. This term relates to the transverse resistance of the device, given by the dimensions and resistivities of the Pt structure and of the CoFe absorber. It is related to the shunting effect already mentioned in Chapter 3, that tends to decrease the measured interconversion signal, and which has already been widely discussed in literature on non-local measurement of the ISHE in lateral spin valves [228]. In the ISHE configuration, the shunting described a process through which the charge current produced in Pt will be partially shunted through the CoFe electrode, leading to a reduction of the measured potential drop. Similarly, in the DSHE measurement configuration, only the charge current that flows within a distance equal to the spin diffusion length of Pt l_{sf}^{Pt} from the CoFe/Pt interface contributes to the spin accumulation built up that generates the interconversion signal. The rest of the charge current is shunted by the CoFe electrode and Pt layer bottom, without contributing to the interconversion. This leads to a decrease of the interconversion signal described by the geometrical factor. Importantly, due to the complexity of the shunted charge current lines, a proper evaluation of the G-factor requires Finite Element simulations [228], as was done in Chapter 3, and the analytical formula given in eq. 5.2 remains a qualitatively correct but rough evaluation of its effect on the signal.

The second term of eq. 5.1 is the *efficiency factor* λ_{eff}. In the limit where the thicknesses of CoFe and Pt are much

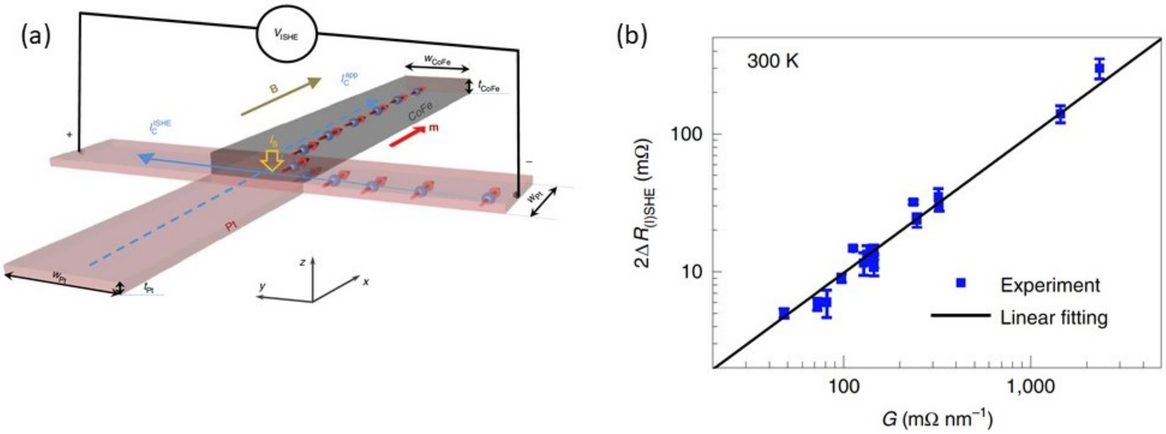

Figure 5.3: (a) Sketch of the spin-orbit read-out device used in the Ref. [312], with the measurement configuration and the geometrical quantities used in eq. 5.2. (b) Evolution on the ISHE signal with the geometrical factor of equation 2. Images from Ref. [312].

larger than their spin diffusion lengths, this term writes [271]:

$$\lambda_{eff} = \theta_{SHE} l_{sf}^{Pt} \frac{\beta_{CoFe}}{1 + \frac{l_{sf}^{Pt}\rho_{Pt}}{l_{sf}^{CoFe}\rho_{CoFe}}} \tag{5.3}$$

with θ_{SHE} and ρ_{CoFe} the spin Hall angle and resistivity of Pt, while β_{CoFe}, l_{sf}^{CoFe} and ρ_{CoFe} are the polarization, spin diffusion length and resistivity of the CoFe electrode. The efficiency factor is the product of the spin-charge interconversion efficiency $\theta_{SHE} l_{sf}$ introduced in Chapter 3, times the spin injection efficiency that takes into account the spin backflow term. In this paragraph I will focus on the optimization of the spin signal by tuning the geometrical factor, demonstrated by V.T. Pham *et al.* in Ref. [312]. The G-factor can indeed be increased by reducing the sizes and thicknesses of the device components, and by modifying the deposition conditions of CoFe and Pt to change their resistivity. By changing these parameters, the authors indeed evaluated that they could increase the geometrical factor by two order of magnitude. They also observed a linear dependence between the geometrical factor and the interconversion signal ΔR, which also spanned over two order of magnitude (Fig. 5.3b). They observed signals ranging from 4 mΩ for the devices presenting the largest width of the T-shape Pt structure, and the thickest and less resistive CoFe and Pt layers, to 300 mΩ for the smallest devices and with more resistive materials. These results thus present a guideline for a geometrical optimization of the spin-orbit read-out device output signal.

Despite the large achieved signals, which went up to 3 mΩ by replacing Pt by Ta, the target of $\Delta R = 1\mathrm{k}\omega$ needed to achieve the 100 mV output for a 100 μA bias current is still far from being achieved. Since in metals the product ρl_{sf} is roughly constant, the dimension and resistivity tuning of the spin-orbit read-out devices presented in this paragraph has however not modified the efficiency factor λ_{eff}, since the spin injection term has been left untouched. It has been observed in materials as graphene [325] or topological insulators [326] that a polarized resistive interface can optimize the spin injection by reducing the spin impedance mismatch, as illustrated in Chapter 1 of this manuscript. In the next paragraph, I will therefore report results published over the course of my PhD as a letter in Physical review B [56], which describes the effect of such an interface on the spin interconversion signal in spin-orbit read-out devices, by evaluating the interface resistance and spin scattering asymmetry at FM/Pt interfaces. This will provide new guidelines for the signal optimization in these devices.

5.2.2 Role of the FM/HM interface

Beyond the conversion rate by spin-orbit coupling, the interface is another key element to be optimized. Indeed, the spin memory loss [46, 125], the disorder at the interface [125, 55], the spin reflection/spin backflow [313, 314] due to the spin impedance mismatch and the interfacial-SOC-based spin-transparency [126] have been identified as key factors in the process of spin-charge interconversion in simple FM/SOC bilayers. The spin memory loss decreases the spin current effectively injected, while the disorder at the interface can actually lead to high interface resistances [125]. Together with the relaxation by the injecting element, they are both detrimental to the spin injection. For instance, a high spin transmission increases the spin current crossing the interface but also the spin backflow. We measured electrically the DSHE and ISHE in FM/Pt nanostructures made of different FM materials [315, 271]. We found that the amplitude of SHE signals depends drastically on the magnetic materials ($Co_{60}Cu_{40}$, Co, and $Ni_{81}Fe_{19}$). Using finite-element method simulations and assuming the interface to be transparent, we extracted effective spin Hall angles varying strongly with the FMs, with high values in line with ST-FMR experiments [313, 86]. The values of the interface resistances are then carefully estimated for each FM/Pt interface. This measured spin-independent additional resistance should lead to the decrease of the spin signals, which is inconsistent with our observations. We show that the interfacial scattering asymmetry has thus to be taken into account for the estimation of the spin-charge interconversion. Although it is usually overlooked in spinorbitronics, it allows completing the spin transport picture, with a major role in our metallic FM/SOC nanostructures. Contrarily to what could be expected, resistive FM/Pt interfaces can favorably enhance the spin Hall signal, which is useful for the spin-orbit magnetic state readout [312, 27]. This study was carried out using a slightly different geometry for the local detection of the SHE than that of the first section of this chapter. Instead of having only one detecting/injecting electrode (Fig. 5.1a), the considered devices have two FM electrodes (Fig. 5.4a). Similarly to the case presented in the first section, however, a charge current flowing into the Pt wire creates a transverse spin current density with two opposite spin accumulations localized at the top and bottom surfaces of the Pt wire. The associated electrochemical potential landscape is sketched on the right of Fig. 5.4a. The spin accumulation aligns the Fermi energy of the electrodes on the minority or majority spins, depending on their magnetization direction (Fig. 5.4b(i)). The voltage between the two electrodes thus depends on their magnetic configurations (parallel or antiparallel). A resistive FM/Pt interface can contribute to probe the spin accumulation (Fig. 5.4b(ii)), and an additional electrochemical potential appears at the interface, due the continuity of the spin current through the resistive interface. When the two FMs have parallel magnetizations, the same electrochemical potential is probed, and the voltage between the two FMs is zero. In the antiparallel states, the two FMs are probing opposite electrochemical potentials, and a nonzero voltage is measured. Note that there are opposite signs of this voltage for the head to head and tail to tail magnetic configurations [315, 271]. The spin Hall signal, in ohm, is the measured voltage divided by the applied current. The amplitude of the SHE signal is defined as the difference of the measured resistance between the antiparallel and parallel magnetic states.

Devices	β	$\theta_{SHE}^{Pt} l_{sf}^{Pt}$ (trans.) (nm)	RA (fΩm^2)	$\theta_{SHE}^{Pt} l_{sf}^{Pt}$ (RA) (nm)	γ
CoFe/Pt	0.48	0.60	9.6 ± 1.5	1.83 ± 0.10	0.46 ± 0.05
Co/Pt	0.17	0.81	13.5 ± 2.0	2.28 ± 0.10	0.17 ± 0.03
Py/Pt	0.22 ± 0.1	0.22	29.0 ± 2.5	0.93 ± 0.10	0.070 ± 0.015

Table 5.1: Parameters and retrieved values in the different FM/Pt systems. β is the polarization of the bulk FMs estimated using the spin absorption technique [67]. $\theta_{SHE}^{Pt} l_{sf}^{Pt}$ (trans.) is the effective $\theta_{SHE}^{Pt} l_{sf}^{Pt}$, estimated by FEM simulation when assuming transparent interfaces. RA is the interfacial RA estimated from the experiments (Fig. 5.5). $\theta_{SHE}^{Pt} l_{sf}^{Pt}$ (RA) corresponds to the extracted values of the effective $\theta_{SHE}^{Pt} l_{sf}^{Pt}$ when the measured RA and $\gamma = 0$ are introduced in the FEM simulations. γ is the extracted value of the interfacial spin scattering asymmetry, calculated with the measured RAs and assuming that the intrinsic value of $\theta_{SHE}^{Pt} l_{sf}^{Pt}$ is 0.19 nm.

As expected, the observed spin signals are asymmetric, as observed in Fig. 5.4d-5.4f for CoFe/Pt, Co/Pt, and NiFe/Pt, respectively. The signal amplitudes are found to vary with the FM material, with values for CoFe/Pt, Co/Pt, and Py/Pt of 8.0 ± 0.5, 4.1 ± 0.5 and $1.7 \pm 0.4\,\mathrm{m}\Omega$, respectively. Note that in these experiments, we can measure either the direct SHE or the inverse SHE, and that they both give exactly the same signal amplitude [315, 271].

The efficiency of the spin-charge interconversion in Pt is related to the product of the spin Hall angle by the spin-diffusion length, $\theta_{SHE}^{Pt} l_{sf}^{Pt}$ [200]. Despite the fact that the SHA depends on the Pt resistivity, the product $\theta_{SHE}^{Pt} l_{sf}^{Pt}$ is expected to be independent of the resistivity, because of the intrinsic origin of the SHE in Pt at room temperature [79, 316]. Using spin-pumping–FMR techniques, $\theta_{SHE}^{Pt} l_{sf}^{Pt}$ values in the range of 0.17 to 0.24 nm are usually extracted [46, 79, 317]. In particular, a value of $\theta_{SHE}^{Pt} l_{sf}^{Pt} = 0.19$ nm has been extracted by spin pumping measurement in our group [46] using the same deposition technique, and will be taken as a reference in this study. Note that these values of $\theta_{SHE}^{Pt} l_{sf}^{Pt}$ are in line with first-principles calculations of the Pt spin Hall conductivity [73, 229]. If the Elliott-Yafet mechanism [318] is dominant, the spin-diffusion length can be estimated from the resistivity value (ρ_{Pt}). For our Pt wires, $l_{sf}^{Pt} = 2.6$ nm and $\theta_{SHE}^{Pt} = 0.073$ are calculated from the measured $\rho_{Pt} = 28.0\,\mu\Omega$cm. Using FEM simulations in the case of transparent interfaces (Ref. [271]) and the transport parameters we have previously estimated in our nanostructures (Ref. [67] and Chapter 1), we extract quite different values of effective $\theta_{SHE}^{Pt} l_{sf}^{Pt}$ for the different FMs, as shown in column 2 of table 5.1. Although we take into account the variations of the spin polarizations and the other transport parameters in FMs, we do not obtain a consistent value of $\theta_{SHE}^{Pt} l_{sf}^{Pt}$. The corresponding effective SHA of Pt would be 0.19, 0.34, and 0.10 for CoFe, Co, and NiFe electrodes, respectively. These scattered values imply that this analysis fails to describe the spin-charge interconversion in these systems, and that the resistance at the FM/Pt interface

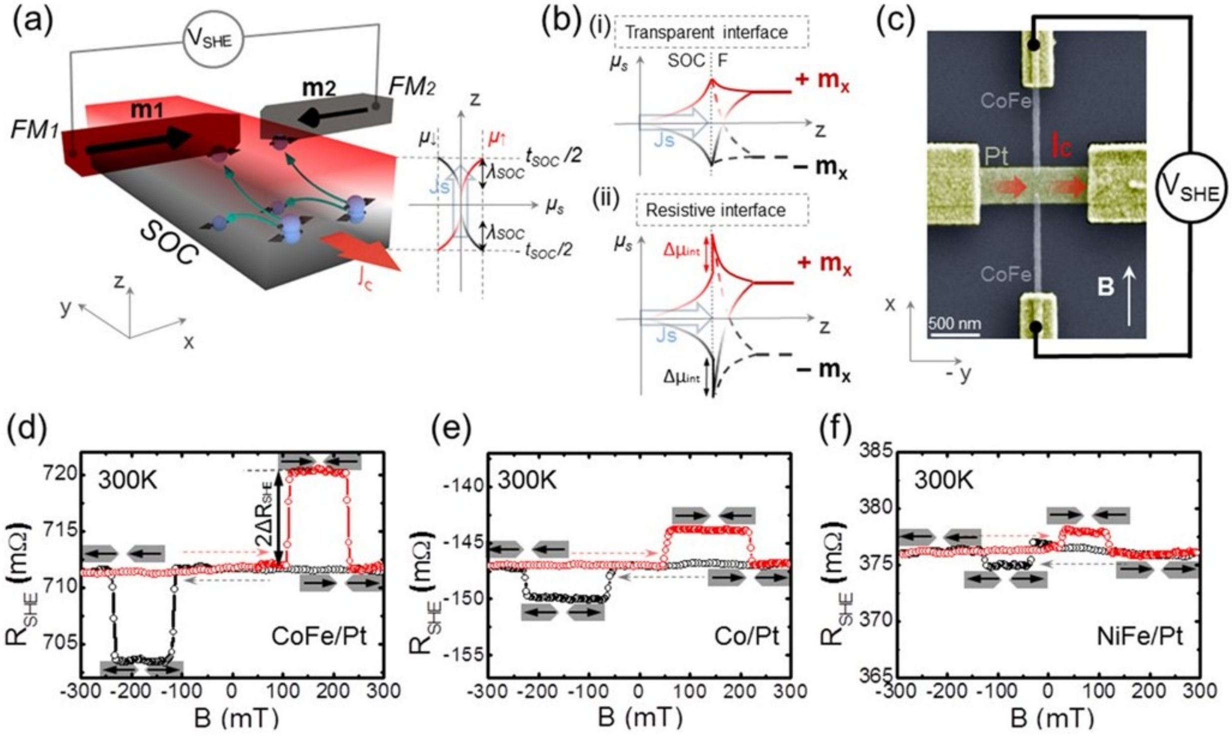

Figure 5.4: (a) Sketch of the direct SHE measurement principle using the FM/SOC nanostructure. Left: Two FM electrodes probe the spin accumulation induced at the top surface of a SOC wire by the direct SHE. The red volume is spin-up rich (+x polarization) while the grey one is spin-down rich (-x polarization). The black arrows indicate the vector magnetization of the electrodes ($-\boldsymbol{m}_x/\boldsymbol{m}_x$). Right: electrochemical potential landscape within the SOC material. (b) Electrochemical potential landscape at one FM/SOC interface of the device, in the case of a transparent interface (i), and in the case of a resistive interface with an interfacial spin asymmetry (ii). The red and black curves correspond to the electrochemical potential of electrons whose spins are polarized along x and -x, respectively. In (ii), $\Delta\mu_{int}$ is an additional electrochemical potential, due to the resistive interface, that contributes to the spin detection. (c) Scanning electron microscopy (SEM) image of a CoFe/Pt sample, with a sketch of the direct SHE measurement configuration. (d), (e), and (f) are the experimental field sweep loops measured along x on CoFe/Pt, Co/Pt, and NiFe/Pt samples, respectively. The geometrical parameters are identical for all the devices, with nanowire widths of w_{Pt} = 400 nm and w_{FM} = 50 nm and thicknesses t_{Pt} = 7 nm and t_{FM} = 15 nm. The black arrows indicate the configuration of the magnetic electrodes when sweeping the magnetic field.

must be taken into account.

In order to clarify the role of the interface in the spin signals, we measured the FM/Pt interface resistances. The samples consist of simple cross made of a thick FM wire (CoFe, Co, and NiFe), patterned transversely on top of a Pt wire (Fig. 5.5a). A current is applied from a Pt branch to a FM branch, so that it flows through the interface. The voltage drop is probed in-between the two other branches, which sum up the voltage drops due to the volumes and to the interface. We used 3D FEM modeling to take into account the contribution of the bulk resistances and the strong inhomogeneity of the current lines through the interface, so that the interface resistance can be estimated [319]. The interface-specific resistance is defined by the product of its area by its resistance, RA, and is varied in the FEM simulations. As shown in Fig. 5.5b, the current lines crossing the interface for a large RA are more homogeneous, while for lower RA values the current lines are more complex. Experimental and simulated values are plotted in Figs. 5.5c–5.5e for CoFe, Co, and Py, respectively. The obtained values of RA products (table 5.1) are quite large, in the range of $10 - 30\,\mathrm{f}\Omega \cdot m$. This is more than one order of magnitude larger than that of the Pt/Cu interface [319], and than the minimum RA value at the FM/Cu interface, equal to the Sharvin resistance estimated in Chapter 1. A possible contribution to these high RA values is the additional scattering due to the disorder at the interface [320, 321, 322]. For instance, the measured RA value of the NiFe/Pt interface agrees well with that calculated by Liu *et al.* [125], which shows that it is proportional to ρ_{Pt}. Correspondingly, the measured RAs of the Co/Pt and CoFe/Pt interfaces are about one order of magnitude larger to previously reported values [322, 323, 324] and might be attributed to an increased

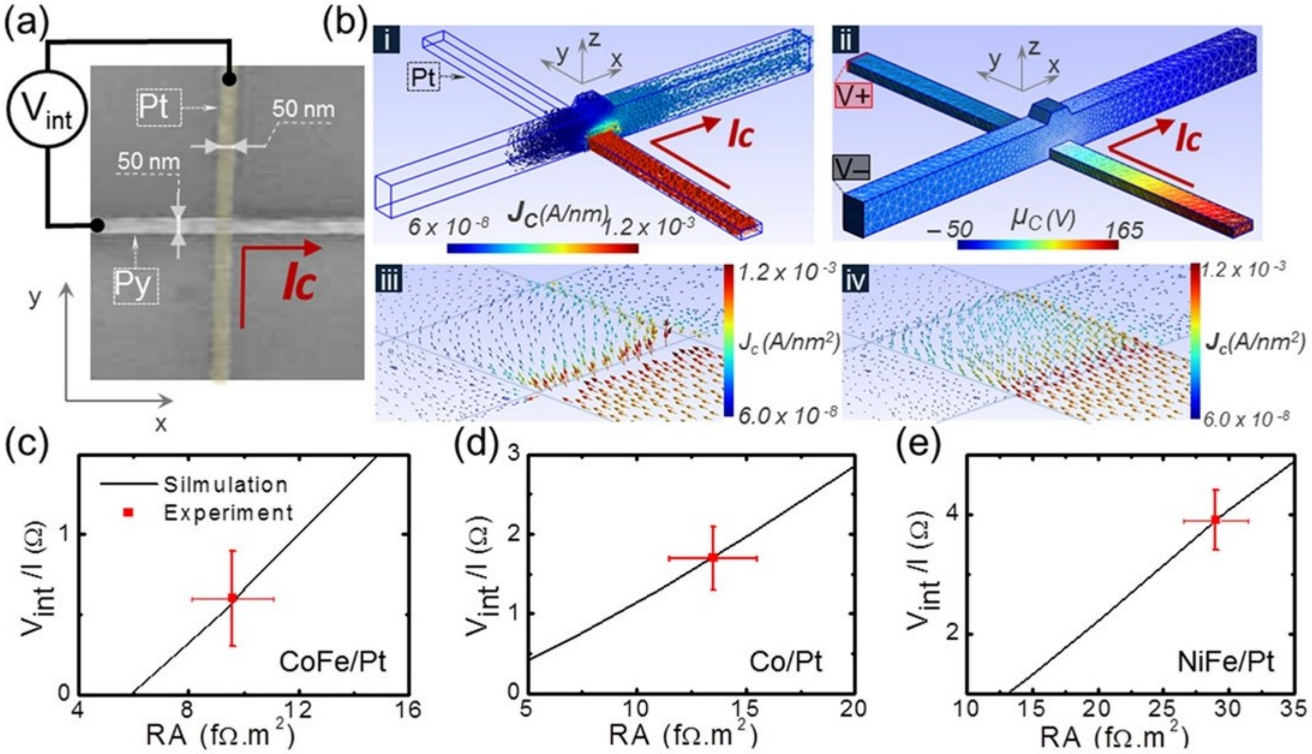

Figure 5.5: (a) SEM image of a NiFe/Pt cross, and sketch of the electrical setup for interface resistance measurements. (b) 3D-FEM simulation results of charge transport through the interface: (i) and (ii) are the distributions of the charge-current density (J_c) and potential (μ_c) landscape, (iii) and (iv) show the charge current distribution in the interface plane, for a transparent interface (iii) and an interface resistance of 29 $\text{f}\Omega \cdot \text{m}^2$ (iv). (c), (d), and (e) are the expected resistances as a function of the interfacial RA of CoFe/Pt, Co/Pt, and NiFe/Pt systems, respectively. The measured V_{int}/I value is an average of measurements obtained on three to five different nanostructures. From the simulation curves and from the measured V_{int}/I value, we then deduced the interface RA.

disorder at the interface [130]. The role of the interface resistance in the SHE measurement can be implemented in the 3D FEM simulations using the procedure described in the appendix. The two quantities, the measured RA and the interface polarization γ, are introduced as the boundary condition described in the section 1.1.3, where γ originates from the difference of interfacial conductivity between the two spin species with opposite directions, and acts as a source of spin polarization.

Figure 5.6b plots the amplitude of the simulated spin signal as a function of RA for the CoFe/Pt system, with and without spin-scattering asymmetry. If the parameter γ is set to zero, the spin signal drastically decreases as the interface resistance increases (green line in Fig. 5.6b). Indeed, the electron transit time through the interface becomes larger than the spin-relaxation time in the FM, and thus the spin accumulation disappears [127]. To fit the experimental data, this would require increasing the $\theta_{SHE}^{Pt} l_{sf}^{Pt}$ value by roughly a factor of 10 with respect to the transparent interface case. Using this assumption of a nonpolarized interface resistance, we obtain $\theta_{SHE}^{Pt} l_{sf}^{Pt}$ values of the order of 1.83 nm, or equivalently a SHA of 0.74 for a l_{sf}^{Pt} of 2.6 nm and a room-temperature Pt resistivity ($\rho_{Pt} = 28\,\mu\Omega\text{cm}$) [67]. This effective value of the SHA is in line with a recent report [313], which underestimates the spin transmission by simply taking into account the spin backflow due to the spin-resistance mismatch. The SHA can be even unrealistic for the case of Co/Pt ($\theta_{SHE} \approx 1$). Furthermore, the extracted values are different in the three systems (table 5.1). This means that the interface polarization needs to be taken into account to describe the spin injection in Pt. Indeed, the spin resistances determine the strength of the spin injection/detection by a ferromagnet. The measured RAs are in the 10–30 $\text{f}\Omega\text{m}^2$ range, whereas the FM spin resistances are on the order of a few $\text{f}\Omega\text{m}^2$ (1.98, 1.61, and 1.63 $\text{ff}\Omega\text{m}^2$ for Co, CoFe, and NiFe, respectively). It turns out that the injected spin current is mainly determined by the interface contribution, and thus by the spin-asymmetry parameter.

Figures 5.7a-5.7c plot the amplitude of the simulated and experimental spin signals, as a function of the Pt wire

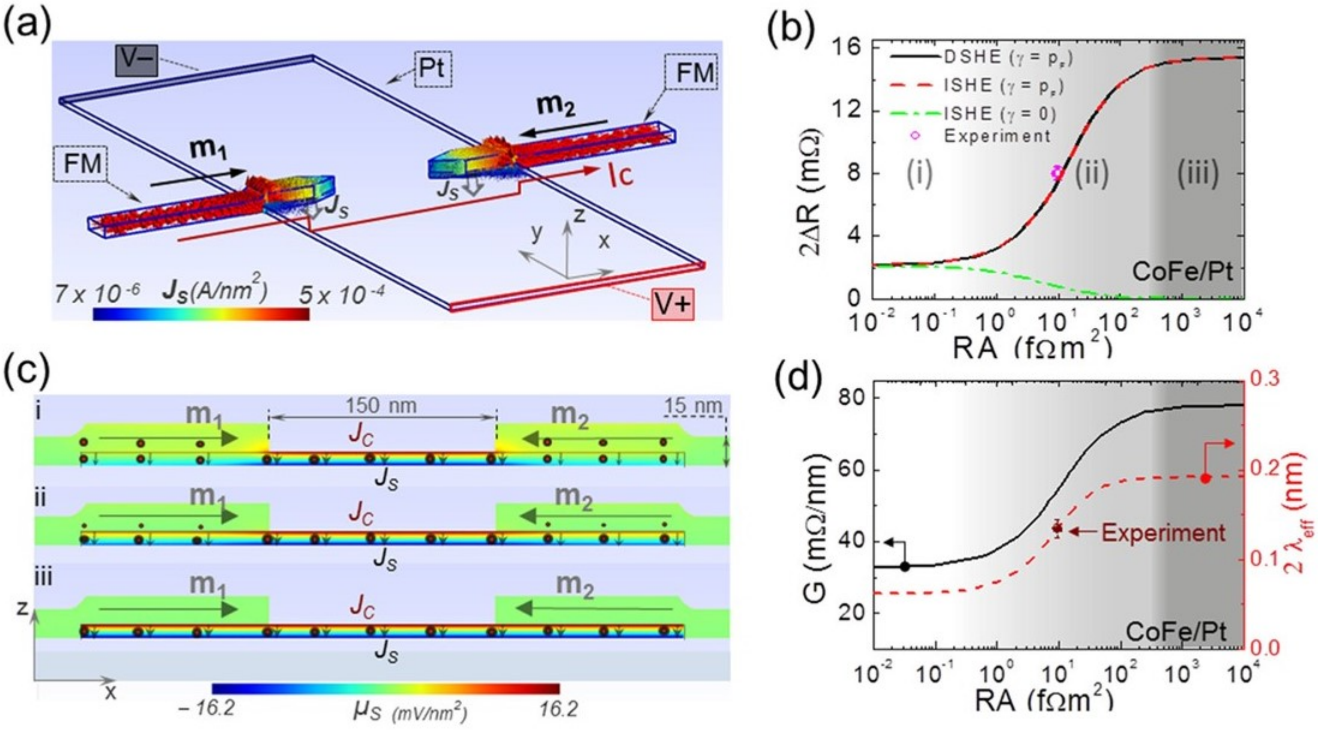

Figure 5.6: (a) Example of FEM simulation for the spin-orbit read-out device in the inverse SHE configuration, with the geometrical parameters of Fig. 1. A charge current I_c is applied in between the ferromagnetic electrodes, which possess antiparallel magnetizations to inject a spin-current density (j_s) into Pt. The inverse SHE converts the spin current flowing in the z direction (j_s) into a charge current along the Pt wire (y direction). (b) Spin signal amplitudes as a function of RA for CoFe/Pt. The simulation indicates three regions corresponding to three regimes of the interface: transparent (i), intermediate (ii), and resistive (iii). (c) x-z cross section at the sample center of the electrochemical potential distribution (proportional to the spin density). It presents the spin accumulation profile in the direct SHE configuration, for values of RA corresponding to the three cases (i, ii, and iii). The applied charge current density (J_c) is in the -y direction (red-black dots in different size shows the different local J_c due to the electrical shunting by FM). The SHE creates a spin current in the z direction (J_s) (small black arrows in Pt; the different size corresponds to different produced local J_s). m_1 and m_2 are the magnetizations of the FMs. (d) Plots of the geometry factor (G) and of the effective spin-charge conversion rate (λ_{eff}) as a function of RA, for $\gamma = p_F$, i.e., the spin polarization of the FM electrode is kept at the interface.

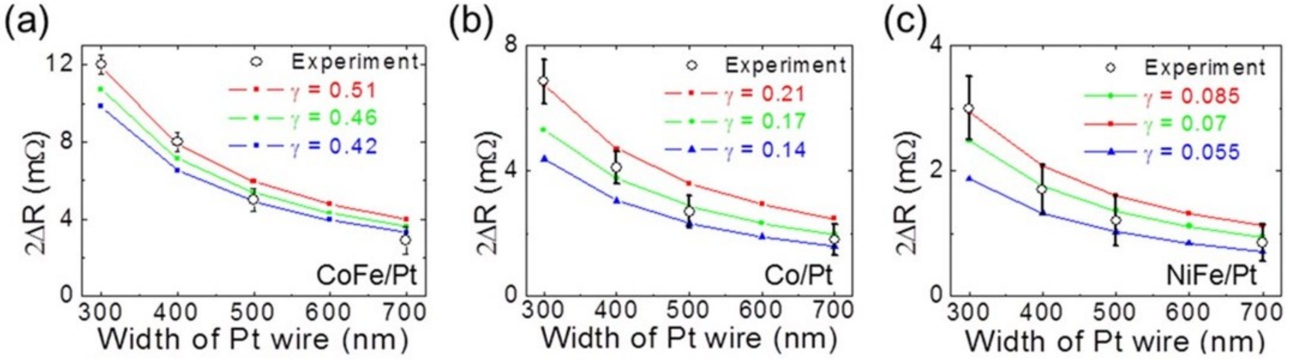

Figure 5.7: Simulated and experimental values of the amplitude of SHE signals vs. Pt wire width, in CoFe/Pt (a), Co/Pt (b), and NiFe/Pt (c). The simulations are performed assuming the same Pt SHE efficiency ($\theta^{Pt}_{SHE} l^{Pt}_{sf} = 0.19$ nm)

width, in the three systems [315, 271]. Here, we keep assuming that $\theta_{SHE}^{Pt} l_{sf}^{Pt}$ is of the order of 0.19 nm. Using the experimentally measured RA values at the FM/Pt interface reported in table 5.1, the single free parameter, γ, that allows this consistent extraction of $\theta_{SHE}^{Pt} l_{sf}^{Pt}$ is then found to be 0.46, 0.17, and 0.07 for CoFe/Pt, Co/Pt, and Py/Pt interfaces, respectively. The results match quite well with the polarization of the bulk ferromagnets [323], except for the NiFe/Pt interface, which is a footprint of the high spin-memory loss at this interface. Particularly, if the spin-flip ratio of $\delta = 3.8$ from Ref. [125] is introduced, the effective spin resistance of the interface is decreased and consequently γ becomes similar to the value of P_F of bulk NiFe. Note that a factor of 3 between the bulk polarization and γ has been theoretically predicted by Gupta *et al.* [55], which has taken into account the magnetic disorder at the NiFe/Pt interface. Our results tend to prove that large interface resistances and nonzero γ values are at the origin of the large and scattered values of the effective SHA, usually extracted assuming either completely transparent interfaces or resistive interfaces without taking into account γ.

These results thus allowed us to extract the RA and interface polarization at the Co/Pt, CoFe/Pt and NiFe/Pt interfaces. Furthermore, they show that these interface properties provide a guideline to the optimization of the output signal at the read-out block of the MESO device. Indeed, an increased interface resistance with $\gamma = 0$ leads to a drop in the interconversion signal (Fig. 5.6b). However, when $\gamma \neq 0$, the output signal increases. The Fig. 5.6d shows the mechanism behind this effect. As described in the previous paragraph of this section, the interconversion signal writes $\Delta R = G\lambda_{eff}$. The efficiency factor λ_{eff} increases with RA when $\gamma = P_{eff}$. This is because a polarized resistive interface favors the spin injection by decreasing the spin backflow, as described in the section 1.1.3. More difficult to understand is the increase of the geometrical factor G with RA. As previously mentioned, the geometrical factor depends on the transverse resistance R_{trans} of the device through $G = R_{trans}/w_F$, where w_F is the width of the FM electrode. This allows computing the evolution of G, by evaluating using FEM simulations the potential drop when imposing a charge current through the device, as illustrated in Fig. 5.8a. For a low FM/Pt interface resistance, the charge current is free to flow through both the Pt wire and the electrode (Fig. 5.8b). When the interface resistance is included (Fig. 5.8c), the charge current is constrained to stay in the Pt wire, leading to an increase of R_{trans}, and therefore of G. This effect is also the reason for the non-monotonic behavior of the non-local interconversion signal simulated in Fig. 3.13, and it is independent of the interface polarization.

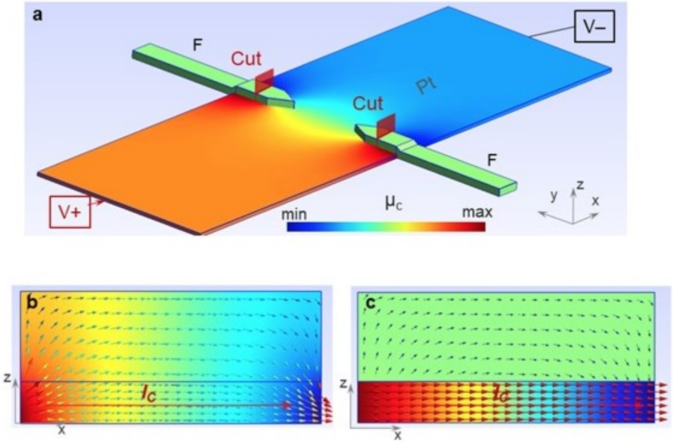

Figure 5.8: Example of 3D FEM simulations used to calculate the factor G. (a) 3D electrical potential distribution (μ_m) in the device with application of the charge current between the two ends of the Pt strip. Repartition of the charge current in the xz-cut-planes (indicated in red in (a) of the electrical potentials and of the current density for transparent (b) and resistive (c) interfaces between the ferromagnetic electrode and Pt.

In conclusion for this section, scaling down the spin-orbit read-out device and including polarized resistive interfaces between a heavy metal and the FM electrode should allow optimizing the ISHE output signal. Furthermore, increasing the resistivity of the spin-charge interconversion materials also leads to an increased signal. However, even though these methods allows to increase the spin signal ΔR, *i.e.* the ratio of the output signal divided by the bias current, they do not necessarily allow for a strong increase of the output voltage. Indeed, smaller devices with highly resistive components are more fragile and cannot accommodate large bias currents.

This means that, in addition to the downscalling and to the interface engineering previously described, materials with higher spin-charge interconversion efficiencies must be considered to obtain a large output voltage. This can be achieved by replacing Pt with topological insulators or two dimensional electron gases. Indeed, while the spin charge efficiency $\theta_{SHE}l_{sf}$ of Pt has been estimated to be 0.2 nm, the Edelstein length, which is the corresponding quantity for two dimensional systems, as been measured to be up to 60 nm in STO-based 2DEG at low temperature [29], and of 2 nm at room temperature in the topological insulator α-Sn [109]. The use of these materials for integrable MESO devices is however impeded by their low industry compatibility and the lack of large scale deposit processes of high quality materials. In the next section, I will demonstrate the fabrication of a MESO device building block using the topological insulator Sb_2Te_3 deposited on a large scale with a high structural quality.

5.3 Topological insulator-based spin-orbit read-out device

Sb_2Te_3 is a well known narrow gap (0.1 eV) layered semi-conductor, which has been intensively studied for its room temperature thermoelectric properties [339]. More recently, it has been predicted [103] and observed [295] that it is also a three dimensional topological insulator, along with Bi_2Se_3 and Bi_2Te_3. Recently, a relatively large spin-charge interconversion efficiency has been observed in this material ($\lambda_{IEE} \sim 0.3$ nm) [336]. This, combined to the development of large scale deposition processes driven by the potential use of Sb_2Te_3 for phase change memory application [340], makes Sb_2Te_3 an appealing material for the realization of integrable MESO devices read-out block. Topological insulators grown on large scales have already been used for spintronics applications such as SOT switching [292]. Their poor crystal quality and high density of defects cause however their electronic properties to be greatly different of those observed in high quality MBE-deposited topological insulator. This raises concerns regarding the possibility for such highly disordered materials to harbor topological surface states [337]. In addition to these material fabrication issues, the patterning of three dimensional topological insulators is a difficult task, due to their sensitivity to basic clean room solvents such as water. Furthermore, it has been observed that even the micrometer-scale patterning of topological insulators can induce defects and degrade their transport properties [338]. Finally, attributing the measured signals to the spin-charge interconversion in topological insulator-based spin-orbit read-out devices remains a challenges, due to the enhancement of spurious effects which can produce a signal with similar symmetries [271, 299].

In this section, I will discuss the measurement of the spin-charge interconversion in the large-scale grown topological insulator Sb_2Te_3. After shortly presenting its high structural quality, I will discuss its transport properties. I will then show how this material was patterned into a nanoscale spin-orbit read-out device, that we used to measure the spin-charge interconversion.

5.3.1 Characterization of a large-scale deposited thin film of Sb_2Te_3

The Sb_2Te_3 thin films were deposited on 300 mm Si/SiO_2 wafers by magnetron sputtering [344], in the group of P. Noé from LETI. Structural characterization of the films were performed using X-Ray Diffraction (XRD) measurements by P. Noël, on films produced in a first deposition campaign [297]. These measurements confirmed the Sb_2Te_3 stoichiometry of the film, and their 001 crystal orientation. A vertical grain thickness of 9.1 nm and a 0.7 nm roughness has been observed for a 10 nm films. The high structural quality of the film was further confirmed by Transverse Electron Microscopy (TEM), and an in-plane average grain size of 100 nm has been observed by Atomic Force Microscopy (AFM). These results show that our thin film have a much higher structural quality than previous attempts of depositing topological insulators by magnetron sputtering, which can be non-stoichiometric [292], have a nanometer grain size [290, 292] or even be amorphous [288].

In addition to this structural study, we performed magnetotransport measurements. Importantly, the thin films used for the structural characterization and the magnetotransport and interconversion measurement have been obtained from different deposition campaigns. Additional measurements are currently being performed by the group of P. Noé to make sure that the structural qualities of the films used for the electrical measurement presented in this section are the same as the ones studied in ref. [297]. The electrical characterization was performed using lock-in detection on a 15 nm thick Sb_2Te_3 non-patterned film, with gold contacts at the corners. The sheet resistance displays a monotonic decrease (Fig. 5.9a), indicating a metallic behavior of its bulk. The carrier density was extracted from Hall measurements. It is estimated to be $n_s = 10^{20}\text{cm}^{-3}$, with a hole character, and it is mostly independent with the temperature (Fig. 5.9c), while the low temperature mobility is $\mu = 10\,\text{cm}^2 \cdot \text{V}^{-1} \cdot \text{s}^{-1}$. The metallic behavior of Sb_2Te_3 has also been observed in MBE-deposited films [295], and is attributed to the presence of thermodynamically favoured Sb-Te antisite defects, which pushes the Fermi level into the valence bands of Sb_2Te_3, thus rendering its bulk conducting. The carrier density is one order of magnitude higher than that measured in MBE-deposited films of similar thicknesses [106, 289]. This shows that our magnetron sputtering deposited films present a larger density of defects [111]. This density is however closer to that of MBE films than what has been achieved in widely studied topological insulators such as Bi_2Se_3, in which a

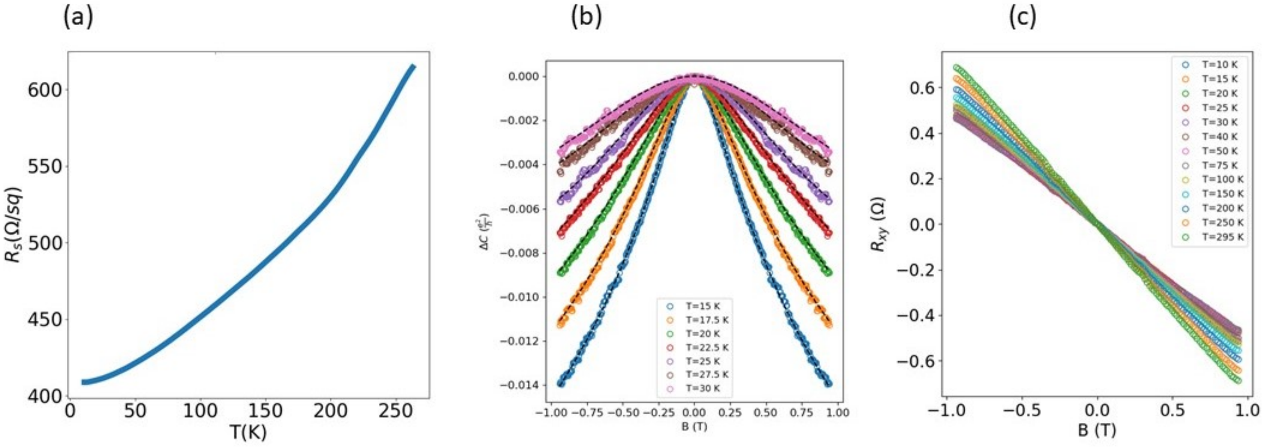

Figure 5.9: (a) Resistance area versus temperature of a 15 nm thick Sb_2Te_3 film. (b) Variation of the normalized conductance for an out-of-plane applied magnetic field and (c) Hall signal versus temperature of a 15 nm thick Sb_2Te_3 film.

two orders of magnitude difference in carrier density between sputtered [290, 291] and MBE films [293, 294] has been observed. The mobility of our film is low when compared to MBE-deposited films [295], which can be understood by estimating the Ioffe-Regel parameter $k_F\lambda_t$ that was found to be close to unity, thus indicating an intermediate level of disorder that decreases the mobility [111]. Finally, Weak Antilocalization (WAL) measurements where performed (Fig. 5.9b), where we observed a linear-in-field modulation of the conductivity C at 10 K, which becomes progressively quadratic upon increasing the temperature up to 30 K. We fitted the WAL signals using the HLN formula [296]:

$$\Delta C = -\frac{\alpha e^2}{2\pi^2\hbar}\left[\Psi\left(\frac{\hbar}{4eBl_\phi^2}+\frac{1}{2}\right)-\ln\left(\frac{\hbar}{4eBl_\phi^2}\right)\right] \tag{5.4}$$

with B the out-of-plane applied magnetic field, l_ϕ the coherence length and α a prefactor that gives the number of coherent channels participating to the transport, and Ψ the digamma function. From our fit we extracted a α of 0.1, and a coherence length of up to 50 nm at 10 K. Importantly, while our fit of l_ϕ is reliable, as it depends mostly of the low field conductivity variation with magnetic field, this is not the case of the extracted α value, which would require higher fields to be evaluated correctly. Such a measurement with magnetic fields of up to 9 T has been performed in ref. [297], on a Sb_2Te_3 10 nm films deposited in the first campaign by the group of P. Noé. Similar values of the coherence length have been found, which confirm our results, while a α of 0.5 has been extracted. This is in good agreement with the conducting nature of the bulk of Sb_2Te_3, since the surface and bulk states would then behave as a single conducting channel [111]. Overall, these results indicate that our Sb_2Te_3 films have structural and transport properties that match with the existing literature, so that even though we could not perform ARPES observation of our material band structure, we may expect the presence of topological surface states in our Sb_2Te_3 thin films [298, 295].

5.3.2 Local detection of the interconversion in Sb_2Te_3

We fabricated spin-orbit read-out devices with the geometry presented in Fig. 5.10a, where the platinum of the devices displayed in Fig. 5.3a has been replaced by Sb_2Te_3 as the spin-charge interconversion material. We first patterned a T-shaped 15 nm-thick Sb_2Te_3 structure, by Electron-Beam Lithography (EBL) and subsequent deposition of a TiO_x(2 nm)/CoFe(3 nm) hard mask. These materials where deposited by evaporation, and the Ti layer was oxidized in the chamber prior to the CoFe deposition. The uncovered Sb_2Te_3 was subsequently removed by Ion Beam Etching (IBE). The ferromagnetic electrode is then EBL-patterned in a second step, followed by the deposition of 20 nm of CoFe. The 2 nm layer of CoFe is removed by IBE prior to the deposition. In a final step, the CoFe hard mask is removed by IBE, leaving only the TiO_x layer on top of the T-shape Sb_2Te_3 structure. We also fabricated devices without TiO_x spacer between Sb_2Te_3 and the CoFe electrode. Each etching step was controlled by Electron dispersive X-ray (EDX) spectroscopy. A SEM image of the final device is shown in Fig. 5.10b, with an electrical contact configuration corresponding to the spin-to-charge interconversion measurement. Importantly, the magnetotransport results obtained in these nanodevices are similar to those obtained on the non-patterned films, indicating that our fabrication process do not modify the quality of the material.

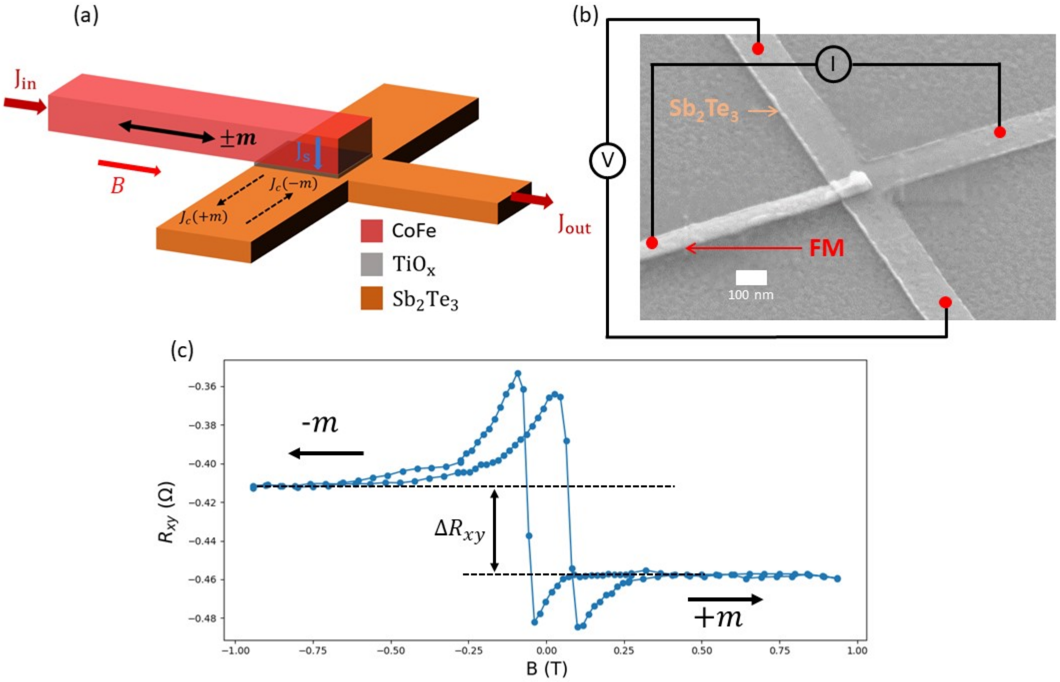

Figure 5.10: (a) Schematics of the spin-orbit magnetization read-out device. The charge current is injected between the ferromagnetic electrode in red and the inner branch of the T-shape Sb_2Te_3 structure (orange). The polarization of the spin current generated at the interface between the electrode and Sb_2Te_3 is along the magnetization $\pm \boldsymbol{m}$ of the electrode (black arrows). The interconversion in the surface states of Sb_2Te_3 creates a charge current in the two outer branches of the Sb_2Te_3 structure with a sign that depends on the magnetization direction. (b) Scanning Electron Microscopy image of the device presented in (a) with the connections used to flow the charge current and measure the transverse resistance R_{xy}. (c) Signal measured at 12 K with the connection set-up presented in (c). The black arrows correspond to the different orientations of the FM electrode magnetization. The difference between the high field lines corresponds to the transverse signal ΔR_{xy}.

Using this configuration, we used a standard 123 Hz lock-in detection technique to measure the transverse $R_{xy} = V/I$ resistance, by flowing a $100\,\mu$A bias current between the ferromagnetic electrode and the central branch of the Sb_2Te_3 structure. This was done while applying a magnetic field along the easy axis of the ferromagnetic electrode. A typical R_{xy} versus field evolution is shown in Fig. 5.10. At high positive and negative fields, the signal displays two different stable values, which correspond to the saturated magnetization directions of the FM electrode. Their difference ΔR_{xy} corresponds to the transverse resistance amplitude. The baseline of the signal most-likely originates from a misalignement between the T-shape Sb_2Te_3 structure and the FM electrode [312]. The signal peaks at low field are similar to those observed in Ref. [300], which attributes them to the Planar Hall Effect. This effect contributes to the signal during the magnetization reversal, i.e. when its direction is not collinear to that of the bias current [275]. In our Sb_2Te_3 devices, this low field feature is much larger than when using platinum. This could be attributed to the fact that the resistivity of Sb_2Te_3 ($6000\,\Omega\cdot$nm) is larger than that of Pt ($130\,\Omega\cdot$nm [67]). Consequently, most of the current flowing from the FM electrode to the Sb_2Te_3 goes through the tip of the electrode. The magnetization in this region of the electrode most likely presents a vortex states, which is progressively expelled when applying a magnetic field. As a consequence, the magnetization tip progressively rotates to align with the magnetic field, leading to the presence of a strong planar Hall effect with a clear signal modification of the signal corresponding to the expulsions of the vortex from the tip. We also measured the transverse signal in the spin-to-charge interconversion measurement configuration presented in Fig. 5.2a, and observed a signal with a similar shape and amplitude. In the devices witout the TiO_x spacer between Sb_2Te_3 and the CoFe electrode, ΔR_{xy} vanishes and only the low field peaks can be observed.

At this stage, it is difficult to attribute the observed ΔR_{xy} signal to a spin-charge interconversion effect. Indeed, the

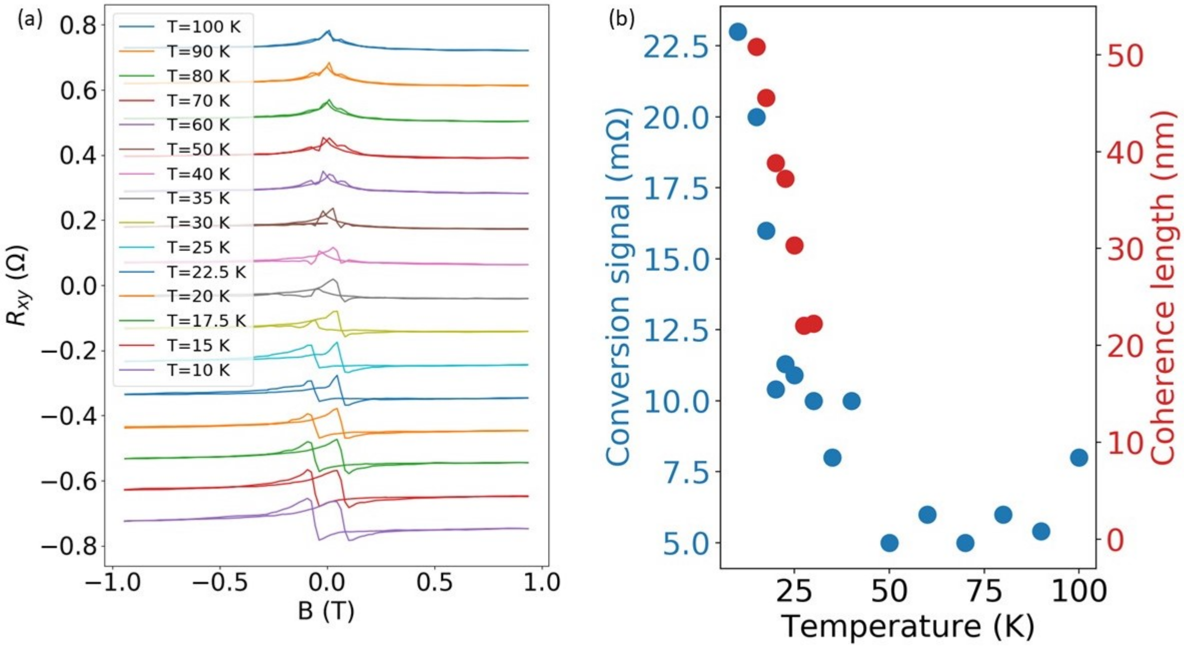

Figure 5.11: (a) Evolution of the interconversion signal with temperature. (b) Spin-charge interconversion signal ΔR_{xy} and coherence length versus temperature.

AHE produced by the charge current flowing vertically in the electrode, and the Ordinary Hall effect (OHE) originating from the stray fields produced by the fringes of the ferromagnetic electrodes can both produce a signal, with symmetries similar to that of the spin-charge interconversion [299, 275]. The latter effect is expected to be especially strong in topological insulators when compared to platinum, as the low carrier density can lead to the production of a large OHE-related transverse signal.

We ruled out these two contributions by performing temperature-dependent measurements. The R_{xy} signal measured for different temperatures between 10 K and 100 K is shown in Fig. 5.11a. A clear separation ΔR_{xy} is observed between the high field branches below 30 K. Above this temperature, the signal reduces to the low field deformations. This temperature corresponds to that at which the WAL vanishes (Fig. 5.10c), and the interconversion signal ΔR_{xy} appears to be correlated with the coherence length L_ϕ, as shown in Fig. 5.11b. This temperature dependence allows us to rule out the AHE contribution to R_{xy}, since the AHE angle of 3d ferromagnets does not vanish when increasing the temperature [96]. Secondly, our observation of a near-independence of the Hall signal with the temperature (Fig. 5.9c) also shows that the OHE does not contribute to the transverse signal, thus confirming the spin-charge interconversion origin of the measured ΔR_{xy}. The absence of contribution from the AHE and OHE is further supported by the zero transverse signal in the absence of a TiO_x spacer, which also shows that direct contact between these two materials needs to be avoided as it is predicted to lead to an intermixing at the interface that would modify the interfacial properties [302].

In conclusion, we observed a low temperature spin-charge interconversion in a spin-orbit read-out device using the topological insulator Sb_2Te_3. The use of this material for the read-out block of MESO devices is however, at this stage, still impeded by the disappearance of the transverse signal at high temperature, and its relative smallness.

The decrease of the interconversion signal when increasing the temperature has already been reported in several studies dealing with the charge-compensated topological insulators $Bi_{1.5}Sb_{0.5}Te_{1.7}Se_{1.3}$ [330, 331]. It has been attributed to the opening of bulk scattering channels, that causes a relaxation of the topological surface states [332], as also observed in thickness dependence of the interconversion using the topological insulator HgTe [104]. The coupling between the bulk and surface states causes a reduction of the surface state mean free path [333], thus leading to a reduction of the spin-charge interconversion efficiency [112, 110]. This also causes a decrease in the coherence length [334], thus explaining the correlation between the spin coherence length and the interconversion signal observed in ref. [331]. Even though the bulk of our Sb_2Te_3 thin film is conducting, an increase of the coupling between the surface and bulk state is possible when going to high temperature, since it is mediated by phonon modes [335]. This would explain the results shown in Fig. 5.11. A consequence of these results is therefore that an efficient use of topological insulator for the read-out block of the MESO device at room temperature requires the bulk conduction to remain negligible at room temperature, which for now remains a challenging prospect for magnetron sputtering deposited topological insulator.

5.4 From MESO to FESO

Beyond the need for a large spin-charge interconversion for the read-out, the MESO device relies on complex magnetoelectric coupling effects to convey the information from the ferroelectric polarization to the ferromagnetic electrode magnetization. This additional difficulty may render difficult both the experimental realization of the device and its integrability. In this section, I will present a simpler device proposed by our team, with similar functionalities but without the requirement for magnetoelectric switching.

5.4.1 The FESO device

The MESO device relies on a multifunctional material combining the magnetic and the ferroelectric order to store and read the information. Other multifunctional materials, which combine the ferroelectric order and spin-charge interconversion, have been developed recently [327, 328]. In particular, materials with a chiral spin texture in their surface or bulk provide an interesting plateform for such multifunctional behavior, since in some of them it is expected that the spin texture changes chirality with the polarization, thus providing a possibility to manipulate the spin to charge interconversion sign using the ferroelectric polarization [166]. This class of material could then be used to realize the so-called Ferroelectric Spin-Orbit (FESO) device (Fig. 5.12) which is a patented invention by SPINTEC/CNRS Thales. In the FESO device, the information is stored in the ferroelectric polarization, which can be reversed using a back-gate voltage. The read-out of the information is achieved by applying a bias charge current, between the ferroelectric material and a ferromagnetic electrode which produces a spin-current at their interface. The spin current is then converted into a charge current, with a sign that depends on the ferroelectric polarization direction.

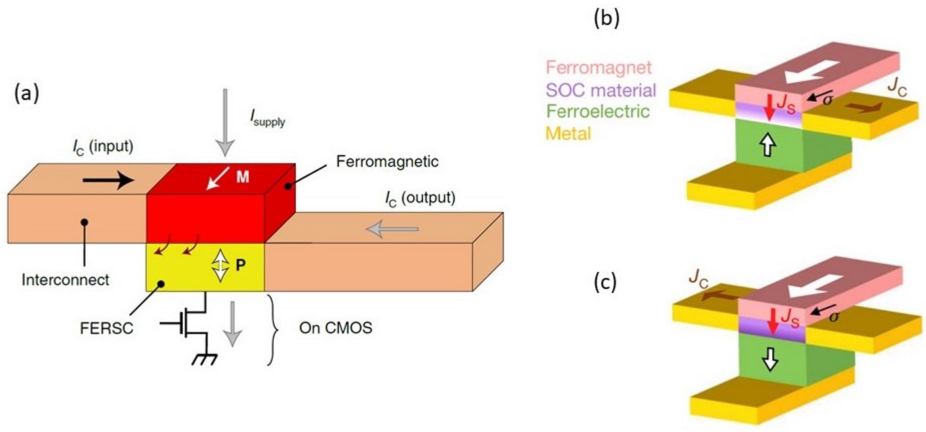

Figure 5.12: (a) Concept of FESO device using a ferroelectric material with bulk spin-charge interconversion. The supply current is used to inject a spin current into a Ferroelectric Rashba Semiconductor (FERSC). This spin current is converted into the output charge current, with a direction which depends on the polarization direction. The input current is used to control the polarization direction. (b) FESO device based on the control of the interconversion in a SOC material, by proximity effect with a ferroelectric material. The SOC-material is chosen so that the sign of the interconversion changes when the ferroelectric polarization goes from the upward (b) to the downward direction (c) using a gate voltage.

While the need for an efficient magnetoelectric coupling between the ferromagnetic electrode and the ferroelectric material has been removed, the challenge of producing a high output voltage from the spin to charge interconversion remains, in order to cascade the FESO devices and build a spin-logic circuit. Furthermore, systems in which the sign of the interconversion depends on the ferroelectric polarization direction must be developed and integrated into nanodevices. In this section, I will present the nano-fabrication of FESO-like devices using two class of systems. The first one corresponds to ferroelectric materials which harbor a bulk spin-charge interconversion (Fig. 5.12a). I will discuss the case of GeTe in the first part of this section. In the second part, I will discuss a situation in which the change of the interconversion sign is controlled by the ferroelectric polarization of a material in contact with the spin-charge interconversion material (Fig. 5.12b and 5.12c). This is for instance the case for a two dimensional electron gas at the surface of $SrTiO_3$.

5.4.2 GeTe: a ferroelectric semi-conductor for the realization of the FESO device

Ferroelectricity and interconversion in GeTe

GeTe is a small band gap (0.5 eV [303]) semiconducting materials. Below a critical temperature of around 700°C, it takes a rhomboedral crystal structure (Fig. 5.13a), with a displacement of the Te plane with respect to the Ge plane [304]. This leads to the formation of Ge-Te double layers with strong bonds between the Ge and Te atoms within the layer, and weaker bonds with atoms outside the Ge-Te double layer (Fig. 5.13b). The charge repartition asymmetry created by the different intra and interlayer bond strengths gives rise to a ferroelectric polarization, which makes GeTe one of the simplest known ferroelectric compounds [305]. The polar nature of GeTe leads to a space reversal symmetry breaking and to a Rashba splitting in the top (bottom) of the valence (conduction) bands [303], especially important at the Z high symmetry point of the Brillouin zone (Fig. 5.13c). DFT calculations [306] confirmed by ARPES measurements [307] demonstrated the presence of a giant Rashba bulk splitting of around 200 meV in the band structure, which is two order of magnitude larger than the 5 meV observed in STO-based 2DEG. Importantly, the Rashba splitting of GeTe corresponds to a thermal energy of 2300 k_B (60 k_B for STO), making possible the use of Rashba driven interconversion in GeTe [308] at room temperature. It has also been predicted [303] that the chirality of the Rashba split band is reversed upon polarization reversal (Fig. 5.13d). This means that polarization switching should lead to the reversal of the Rashba driven spin-charge interconversion. The combination of these different functionalities with the possibility to grow GeTe on a large scale, which has been established in the context of studies regarding its application for phase change memories [340], makes GeTe an interesting candidate for the practical realization of the FESO device.

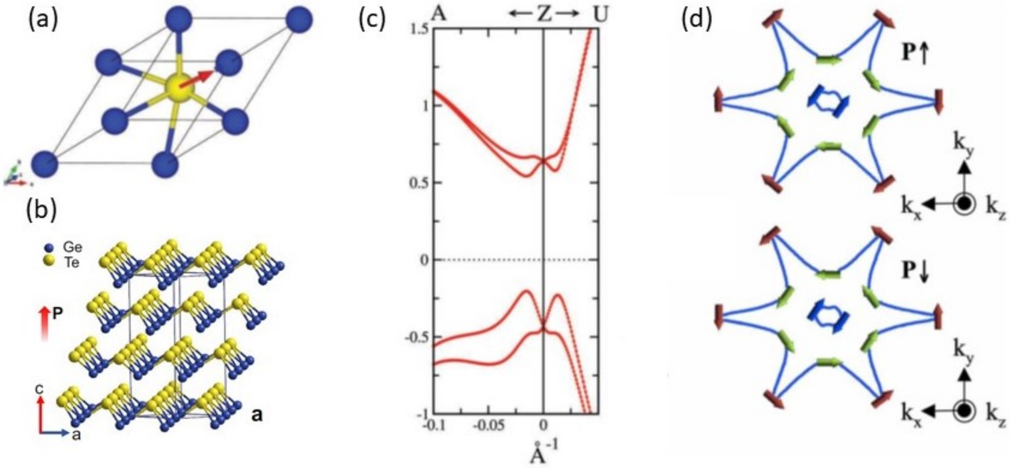

Figure 5.13: (a) Rhomboedral GeTe unit cell, with the displacement of the Te due to the formation of longer and shorter bonds of Ge with the neighbouring Te atoms (image from ref. [305]). (b) The displacement of the Ge and Te sublattices separate into Ge-Te double layers (image from Ref. [308]). (c) Rashba splitting around the Z point in the Brillouin zone of ferroelectric GeTe, and (d) the spin texture around this point and its reversal with the change of the ferroelectric polarization direction (image from Ref. [306]).

Despite these interesting properties, GeTe remains a material difficult to exploit for spintronics applications. Indeed, the presence of a 10% intrinsic Ge vacancies [305] leads to a large carrier density of around 10^{20} cm^{-3} and a relatively low resistivity of around 0.1 mΩ·cm [308]. This causes difficulties for the switching of its polarization, as the mobile carriers screen the applied electric field. Furthermore, the large leakage current associated to the low resistivity prevent the use of standard polarization measurement methods [304]. Finally, regarding the generation of a large output signal from the spin-charge interconversion, the fact that GeTe has a resistivity larger than that of metals leads to a smaller spin conductance. This leads to the spin injection difficulties already experienced in the field of semi-conducting spintronics, due to the spin impedance mismatch [127] between the metallic ferromagnetic electrode and GeTe. These difficulties have been recently circumvented in a study by S. Varotto *et al.* [30] made in our team. the electrical demonstration of a polarization switching was done by measuring the variation of the polarization-dependent interface resistance, which is induced by the modulation of the Schottky barrier height [309] at the interface between Ti and GeTe. In this study, they applied nanosecond voltage pulses of up to 8 V across a Si/GeTe(20 nm)/Ti(100 nm) stack, after which the conductance of the stack was measured. The hysteretic loop displayed by the stack conductance (Fig. 5.14a) indicates that the height of the Schottky barrier changes, from which it was inferred that the polarization of GeTe reversed. They subsequently used SP-FMR to measure the spin-charge interconversion in GeTe along the two high symmetry directions ZA and ZU, while applying electrical pulses across a Si/GeTe/Fe stack in order to polarize GeTe (Fig. 5.14b). In the pristine state of GeTe, no interconversion signal was observed, which was attributed to the random orientation of the ferroelectric domains in GeTe, averaging out the interconversion to zero. Upon applying positive or negative pulses, the sign of the interconversion could be changed without modification of the FMR curve, which indicates that the sign change originates from a change of the GeTe band structure. In ref. [30], the interconversion was however attributed to a spin Hall effect in GeTe, with an interconversion sign that reverses with the polarization. This is due to the change in the band structure induced by the polarization-dependent charge accumulation at the interface. Importantly, the charge current produced by the interconversion in GeTe at room temperature is close to that obtained for platinum using the same technique. This work showed that GeTe is a good candidate for the developments of FESO devices.

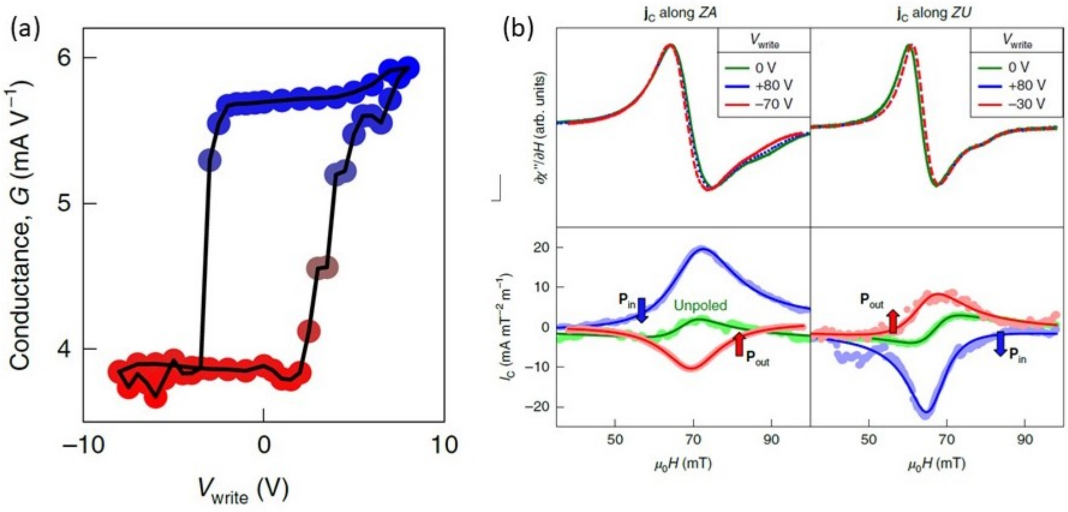

Figure 5.14: (a) Hysteresis loop measured at a Si/GeTe/Ti junction. The junction conductance was measured after the application of a write pulse. (b) Results of SP-FMR measured on a Fe(20 nm)/GeTe(15 nm)/Si stack along the ZA and ZU directions. The top panel corresponds to the FMR curve, while the bottom pannel gives the charge current at the resonance for different polarization states of GeTe (image modified from [30]).

These results have been obtained on MBE-deposited macroscopic samples. The next step in the realisation of a FESO device using GeTe is now to integrate it into a nanodevices. In the following paragraph, I will present the nanopaterning of GeTe-based FESO devices, using GeTe thin films grown on 200 mm wafers by the group of P. Noé in LETI, by magnetron sputtering.

Spin-charge interconversion in a GeTe-based FESO-like device

We patterned FESO-like devices, using the shape presented in Fig. 5.15a. The tip of the FM electrode is deposited on a GeTe square. At the bottom of the structure, a T-shaped TiN metallic back contact is patterned. Here, the charge current is applied between the ferromagnetic electrode and the middle branch of the TiN structure. This creates a spin current at the interface between GeTe and CoFe, which is interconverted into a charge current in GeTe. This charge current is measured as a potential drop between the two outer branches of TiN, using the contact configuration described in Fig. 5.3. In order to take advantage of the interconversion sign reversal with the polarization of GeTe, it is necessary to be able to apply an electric field trough this material. The poling of GeTe is achieved by applying voltage pulses between the TiN and the ferromagnetic electrode.

The devices have been fabricated using TiN(10)/GeTe(10) stacks capped with Sb_2Te_3(5), deposited on Si/SiO_2 (500), with the numbers in parentheses corresponding to the layer thicknesses in nanometers. In a first step we patterned a

T-shaped TiN/GeTe structure, using Reactive Ion Etching with a Ti(2)/CoFe(5) mask, with an IBE removal of the Sb_2Te_3 capping layer prior to the CoFe deposition. The 20 nm thick CoFe ferromagnetic electrode was subsequently deposited using the conditions developed for the fabrication of the spin-orbit read-out devices on Sb_2Te_3 presented in section 5.3. A final IBE step allows to remove the GeTe present outside of the ferromagnetic electrode tip bottom. An example of device produced using this fabrication method is shown in Fig. 5.15b.

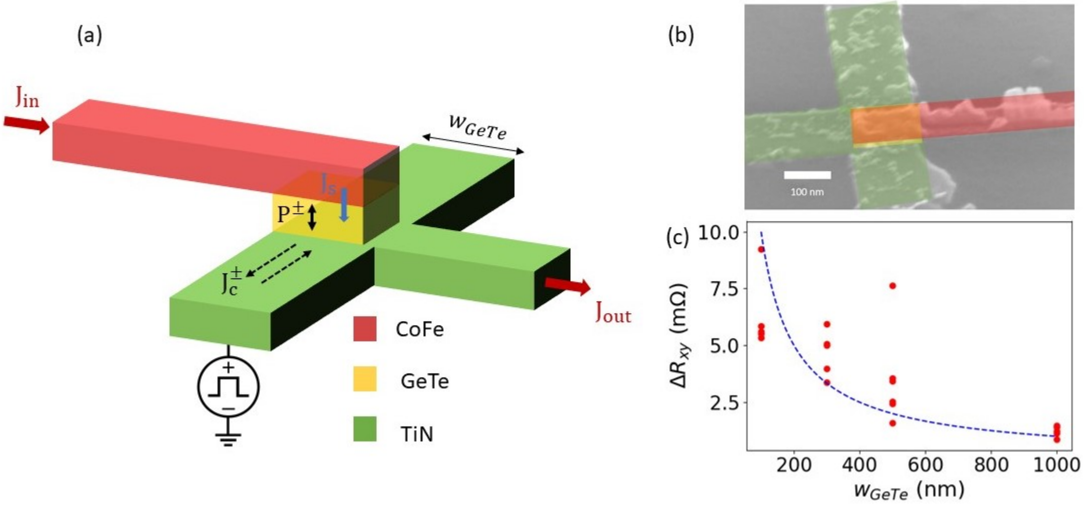

Figure 5.15: (a) Schematics of the fabricated GeTe-based FESO device. (b) SEM image of the GeTe-based FESO device. The material color code corresponds to that of (a). (c) Evolution of the interconversion signal with the width of the GeTe square.

The interconversion in these devices was measured using the lock-in technique described previously. Similarly to the case of Sb_2Te_3 and platinum, a transverse voltage was generated by application of a bias current. This ΔR_{xy} signal scales as $1/w_{GeTe}$ (Fig. 5.15c), as expected from the scaling properties of the output signal of spin-orbit read-out devices, and goes up to 10 mΩ for the smallest devices.

The nanopatterning of these samples is already a considerable achievment. There remain though several points that have to be adressed to claim that these devices are functionnal FESO devices. We will have to check the origin of this signal, since it could also be produced by Ordinary Hall effect induced by stray fields, or coming from the Anomalous Hall effect in the CoFe electrode. The next steps of this project will also be concerned with the output signal optimization, and the polarization switching of GeTe. The output signal optimization can be achieved through the introduction of a tunnel barrier at the interface between CoFe and GeTe. The shunting of the produced charge current by the TiN bottom electrode also leads to a reduction of the output signal, and modifications of the device design are envisioned to reduce its effect. Finally, the FESO device functionalities is to be achieved by poling the GeTe layer through voltage nanosecond pulses. Even though we managed to observed the poling of GeTe in unpatterned Si/GeTe/Fe/Au junctions using a material provided by F. Cheynis and F. Leroy from CINAM, and following the method introduced in Ref. [30], the electrical demonstration of the interconversion control by ferroelectricity in GeTe nanodevices is still lacking. A difficulty originates from the large leakage current induced by the application of a voltage difference between TiN and the CoFe electrode, which tends to cause a breakdown of the device. We however observed a modulation of the signal amplitude when applying voltage pulses, which could originate from the partial reversal of GeTe domains [30]. The optimization of the design and the demonstration of the FESO functionalities of this device are part of the PhD topics of Salvatore Teresi and Paolo Sgarro, in the framework of the ITN SPEAR project.

Other materials have been identified as relevant for the realization of the FESO devices. In particular, complex oxides such as $BiWO_6$ could be used, with large ferroelectric polarizations and giant Rashba splittings, comparable to that of GeTe [310]. Furthermore, owing to their larger band gap, the leakage currents are expected to be smaller, simplifying the polarization switching. The drawback of this material family when used in bulk is the need to introduce electron doping, so that a spin current can be injected in their bulk. This indeed has a detrimental effect on their ferroelectric properties, and decreases their Rashba splitting [310]. The 2DEGs present at the surface of some of these materials can however be used as a spin-to charge interconversion layer, whose properties depend on the ferroelectric state of a nearby ferroelectric material [311, 283].

5.4.3 Ferroelectric STO for FESO devices

STO is a quantum paraelectric at low temperature, meaning that a ferroelectric order can be induced in this material upon application of a large enough electric field [341]. A recent study of my group [29] demonstrated that, when thinning down a 500 μm thick STO substrate to 200 μm, the appearance of a ferroelectric polarization can be induced by applying a 200 V backgate voltage. This results in a remnant control of the carrier density of a 2DEG fabricated by thin Aluminum deposition present at the surface of STO. More importantly, SP-FMR measurements demonstrated that the sign of the spin-charge interconversion, already observed in paraelectric STO-based 2DEG and discussed in Chapter 4 of this manuscript, depends on the polarization direction (Fig. 5.16a). This, combined with the large values of the charge current produced by the interconversion in this system, and the absence of leakage current upon applying a back-gate voltage for the STO polarization switching, makes STO an interesting plateform for the realization of FESO devices. In the course of my PhD, we developed the fabrication of 2DEGs on the surface of STO by metal deposition in SPINTEC, and learned how to patterned nanodevices by e-beam lithography. From this work, we observed a non-volatile control of the spin-orbit torques created by charge to spin interconversion in STO-based 2DEGs, using second harmonic measurements [329]. This fabrication process can also be used for the fabrication of spin-orbit read-out devices based on the interconversion in STO-based 2DEG. This would be a first step towards the realization of oxide-based FESO devices (Fig. 5.16b). The multiple lithography steps involved in this device fabrication process, and the need to engineer a good contact for the spin injection from the ferromagnetic, make the fabrication process slightly more complicated than that used for the spin-orbit torques devices. In this paragraph, I will quickly discuss the fabrication process of spin-orbit read-out devices that I developed over the course of my PhD, as well as some challenges that have to be dealt with for the realization of an oxide-based FESO device.

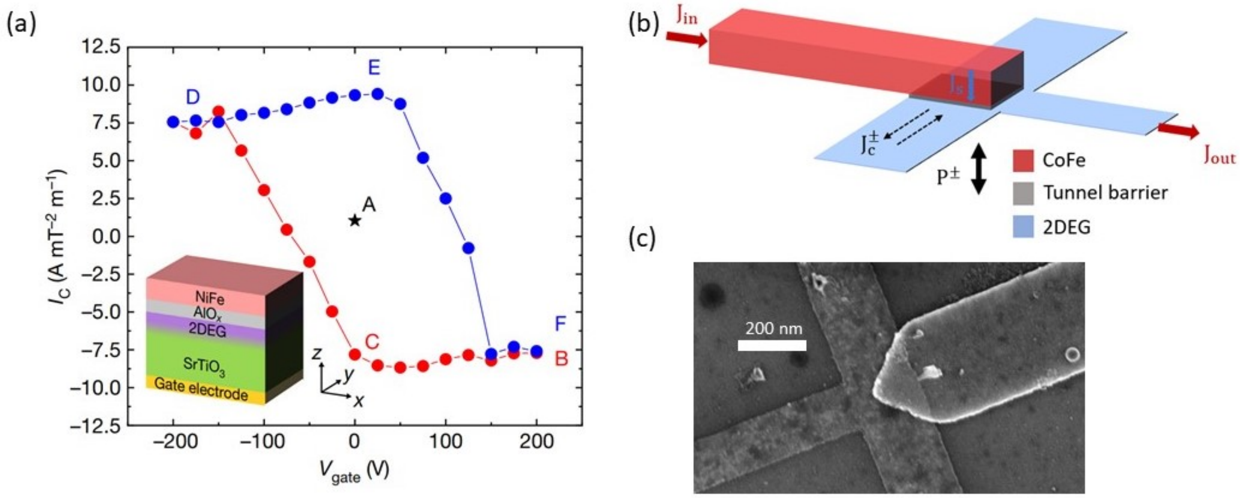

Figure 5.16: (a) Remnant control of the spin-charge interconversion sign on a STO-based 2DEG measured by SP-FMR measurements (image from Ref. [29]). (b) Schematic of the spin-orbit read-out device for the measurement of the spin-charge interconversion in 2DEGs and (c) SEM image of the device presented in (b) and fabricated on STO.

The first step consists in patterning the T-shape 2DEG structure using EBL. The metal/TB/CoFeB/Pt stack is then deposited by magnetron sputtering and followed by a lift off. Here, the metal is used for the formation of the 2DEG, and can be Al, Ta or Y, as discussed in Chapter 4, but also Mg. TB corresponds to a tunneling barrier used to favor the spin injection of the 2DEG. Note that the barrier can directly be the metal used to form the 2DEG, especially in the case of Mg. The 3 nm thick CoFeB layer is used as a seed layer for the ferromagnetic electrode deposition, so that a spin contact can be made with the 2DEG without breaking the vacuum. Finally, the 2 nm Pt layer prevents the stack oxidation and allows for a soft etch removal of the undesirable ferromagnetic parts. In a second EBL step, a CoFe ferromagnetic electrode is deposited, after a soft IBE etch of the Pt layer, at the place of the contact between CoFe and CoFeB. Finally, the full batch is etched, so that the TB/CoFeB/Pt part of the stack not placed under the electrode is removed, leaving only the 2DEG to conduct the bias and the produced charge current. Importantly, the presence of the Pt layer allows to perform this etch using low energy IBE, and therefore prevents the formation of defects in STO that would induce a bulk conductivity by doping this material [342]. A typical device fabricated using this method is shown in Fig. 5.16c. We are currently performing a systematic investigation of the tunnel barrier, that would allow for the injection of a spin current in STO-based 2DEGs. Once a reliable signal has been obtained, this process will be used on other ferroelectric materials harboring a 2DEG at their surface, such as Ca:STO [283], with in view the use of room temperature oxide ferroelectrics such as $BaTiO_3$ [343].

Conclusion

The topic of my PhD was the study of the spin-charge interconversion in various materials, with a special focus on MESO and FESO applications. In **Chapter 1**, I introduced the concepts used throughout this PhD. This included the spin current transport in bulk metallic materials and at metal-metal interfaces, for a spin polarization collinear and transverse to the ferromagnetic components magnetization. This was followed by a presentation of the charge-spin interconversion, by spin Hall effect in metallic materials, and by Edelstein effect in two dimensional systems such as topological insulators and Rashba interfaces. I then discussed the issue of electronic scattering in the surface states and in the adjacent ferromagnetic material, which is essential to find the optimum between the spin injection efficiency and the spin to charge interconversion efficiency. In **Chapter 2**, I presented the measurement of the collinear and transverse spin transport properties in ferromagnets, using lateral spin valves. These measurements demonstrated the high anisotropy of the spin relaxation in the 3d ferromagnets Co, CoFe and NiFe. Furthermore, I extracted from these measurements the spin mixing conductance at the Cu/3d ferromagnetic materials interface, which is a quantity essential for the understanding of exchange of angular momentum between the spin-current and the magnetization. Using these results, I could study in **Chapter 3** the link between the spin Hall effect and the magnetic order. In a first step, I used SP-FMR measurements to measure the spin Hall effect across the ferromagnetic-paramagnetic transition temperature in NiCu. I observed that this material has a large spin Hall angle comparable to the one of platinum, and that its spin Hall angle is independent with the magnetic order. In a second step, I investigated the anisotropy of the spin-charge interconversion in the weak ferromagnetic materials below their Curie temperature, using a new geometry of lateral spin valve. From this study, I observed an unexpected isotropy of the spin Hall effect in these materials. We attribute it to a comparatively low exchange interaction when compared to the spin-orbit interaction NiCu and NiPd, which is a situation that has not been explored in previous studies concerned with the spin Hall effect anisotropy in ferromagnetic materials. These results constitute an important step toward the understanding of the spin-charge interconversion effects, and the device proposed in this chapter should provide a useful platform for the study of these effects.

In **Chapter 4**, I showed how a two dimensional electron gas can be formed by depositing a metal on top on the complex oxides $SrTiO_3$ and $KTaO_3$ by reduction of the Ti or Ta atoms at the interface, and the oxidation of the metal layer. I also explained how the space reversal symmetry breaking at the metal/oxide interface leads to the apparition of a spin chirality in the reciprocal space, which leads to the spin-charge interconversion in this class of two-dimensional systems. I then performed SP-FMR measurements of the spin to charge interconversion in STO/Ta, STO/Y and STO/Al, while varying the Fermi level position of the two dimensional electron gas using a backgate. I observed a difference in the magnitude of the spin-charge interconversion that can be attributed to the different tunneling times of the electron across the oxidized metal layer. I then detailed the difference between the two dimensional electron gases at the STO and KTO interfaces induced by the higher spin-orbit interaction in KTO, and performed a backgate dependent spin-charge interconversion measurement in this system. Finally, in **Chapter 5** I studied the output signal of a spin-orbit read-out device that constitutes the reading part of a MESO device. I showed that it can be optimized by scaling and interface engineering when using platinum as a spin-charge interconversion material. I then demonstrated the fabrication of such a nanodevice using the magnetron sputtering topological insulator Sb_2Te_3 as the spin-charge interconversion material. In the last part of this chapter, I described the fabrication of FESO devices using the ferroelectric Rashba semi-conductor GeTe and two dimensional electron gas at the surface of STO.

Personal contribution

During my PhD I learned and used various nanofabrication techniques. I was trained in UV and electron-beam lithography, and used various kind of direct and inverted resists, for the micro and nanopatterning of devices requiring multiple lithography steps. The electron-beam lithography has been performed with a definition down to 50 nanometer and a

10-nanometer overlay alignment. I was also trained to physical vapor deposition by evaporation. I also performed Ion Beam Etching controlled by Secondary Emission Ion Mass Spectrometer and Reactive Ion Etching. Over the course of the nanofabrication processes, I controlled the different nanofabrication steps, using a mechanical profilometer, and Scanning Electron Microscopy associated with Energy-dispersive X-ray spectroscopy. I used these techniques to perform and develop fabrication process of nanodevices using various classes of materials and on different type of substrates. In Chapter 2 and 3 I presented metallic nanodevices fabricated on thermally oxidized silicon substrates, using a lift-off technique previously developed in my group. In chapter 5, I presented the fabrication of nanodevices using a metallic hard mask from a blanket layer on the semiconducting materials GeTe and Sb_2Te_3. In the same chapter, I also demonstrated the fabrication of spin-orbit read-out devices using STO as an insulating substrate, which necessitated refinements in the electron-beam lithography technique. The device nanofabrication was performed with the help of master and younger PhD students (Salvatore Teresi, Aurélie Kandazoglou, Paolo Sgarro and Nicolas Sebe) whom I trained in nanofabrication. Additionally, I took part in the development of the fabrication process of two dimensional electron gases at the surface of STO, with different orientation, and in other types of complex oxides.

I also developed competencies in experimental physics by using various types of experimental methods. I performed measurements of the spin-charge interconversion using spin-pumping ferromagnetic resonance in cavity, at room and low temperature. I also performed frequency depend ferromagnetic resonance measurement at room temperature using a broadband stripline set-up. The results of these measurements are presented in Chapters 3 and 4. In addition, I performed spin transport and spin-charge interconversion measurements using low-frequency lock-in techniques, with a noise down to 10 nV. This was done in lateral spin valves (Chapter 2 and 3), and in the spin-orbit read-out device presented in Chapter 5, using both homemade magnetotransport set-up and a commercial Physical Property Measurement Set-up. Finally, I had the opportunity to develop my modelling skills. This was done by using the homemade Finite Element Code previously developed in my group, for the analysis of spin transport in complex geometries presented in Chapter 2. I then extended the finite element formulation to include the spin-charge interconversion, magnetoresistive effects and interface parameters in a compact and user friendly manner. Results based on this new formulation are reported in Chapter 3 and 5. Furthermore, I initiated the development of simulation tools for the description of two the dimensional spin-charge interconversion originating from the Edelstein Effect.

Parts of the work presented in this thesis have already been published:

- The results of Chapter 1 concerned with the measurement of the spin diffusion length in Au, Cu and Al has been published in Physical Review B [33], a paper in which I am second author. Those regarding the measurement of the spin polarization and spin diffusion length in Co, CoFe and NiFe are also published in Physical Review B [67].
- The measurement of the spin relaxation anisotropy presented in Chapter 2 has been published in Physical Review Letters [137]; I am the first author of this paper.
- The spin pumping measurements of the interconversion across the Curie temperature of NiCu presented in Chapter 3 have been published in Physical Review Letters [243]; I am the first author (equal contribution) to this paper.
- The interconversion measurements in the two dimensional electron gas at the surface of STO and Al, Y and Ta reported in Chapter 4 have been published in Physical Review material [186]. The interconversion at the surface of KTO presented in the same chapter was published in Advanced Materials [186]. I am co-author of these two papers, for which I performed the spin to charge interconversion measurements.
- The effect of the interface polarization on the spin-charge interconversion efficiency in spin-orbit read-out devices presented in Chapter 5 has been published as a letter in Physical Review B [56] in a paper for which I am second author.

Several other results presented in this manuscript are submitted or will be submitted for publications in which I will be the first author:

- The measurement of the anisotropy of the interconversion in a ferromagnetic material from Chapter 3 has been submitted for publication in Physical Review Letters [345].
- The measurement of the spin-charge interconversion in the topological insulator Sb_2Te_3 reported in Chapter 5 is to be submitted to Applied Physics Letters Material.

In order to reduce the length of the manuscript, I did not include some more minor parts of my work such as:

- The fabrication of two dimensional electron gas at the surface of STO with (111) and (110) orientation, and the associated electrical characterization by magnetotransport experiments in collaboration with A. Kandazoglou and P. Sgarro. This work will be complemented by spin-pumping measurement of the spin to charge interconversion, in order to study the modification of the back.

- Spin pumping measurement in the two dimensional electron at the surface of Ca-doped STO. Even though we observed a relatively large interconversion, as well as clear switchings of the interconversion with the polarization, the hysteretic behavior of the interconversion with a backgate voltage remains unclear, possibly because of the presence of ferroelectric domain walls. The investigation of the interconversion in this system will continue in my group as a collaboration with CNRS/Thales.

Perspectives

The results presented in Chapter 2 and 3 highlight the possibility to obtain large spin Hall angles in light metals. Furthermore, the fact that these high spin-charge interconversion efficiencies take place in ferromagnetic materials raises new and interesting questions. Indeed, in most spintronics studies there is a clear separation of roles between spin-charge interconversion materials and ferromagnets. In the former, the production and transport of the spin current is dominated by the spin-orbit interaction. In the latter, it is usually considered that the transport of a spin current with a polarization transverse to the magnetization will be controlled only by the exchange interaction [64], so that they are not expected to take part in the interconversion. This picture is however currently being challenged by a number of experimental [23] and theoretical works [346, 65], which predict that the interplay between the spin-orbit and exchange interactions can lead to novel spin-transport phenomena. In particular, the modification of the spin-expectation value by the spin-orbit coupling in the band structure of ferromagnetic materials [92] opens the possibility for a spin current to exist in a ferromagnetic material with a magnetization transverse to the spin polarization. This could create new possibilities for the application of bulk spin-orbit torques in ferromagnets with strong spin-orbit interaction, and the possibility to switch the magnetization of a single ferromagnetic layer by the self-induced spin Hall effect [347]. The dilute ferromagnetic materials discussed in Chapter 3 open a wide range of possibilities for the study of such phenomena, since a variation in their composition allows tuning the relative strength of the exchange and spin-orbit interactions. Furthermore, I believe that the device introduced in the second part of this chapter can provide a convenient way to study these phenomena through the measurement of the spin-charge interconversion anisotropy.

The new spin-charge interconversion phenomena observed in ferromagnetic materials originates from the space isotropy symmetry breaking, induced by the presence of a magnetization vector. Another symmetry breaking created by the interface between two materials can also lead to large interconversion efficiencies at the interface between metals and complex oxides, as discussed in Chapter 4. High conversions are also present in ferroelecric Rashba semiconductors such as GeTe. Furthermore, the possibility to read the ferroelectric polarization by spin to charge interconversion [29, 30] opens a wide range of research directions. Indeed, as discussed in Chapter 5, multifunctional materials create new possibilities for spin-orbit logic. In this framework, it is necessary to demonstrate the ferroelectric control of the spin-charge interconversion at room temperature. This has been already achieved in GeTe by spin-pumping measurements, and materials development are under way in CNRS/Thales and in SPINTEC to observe these effects in two dimensional electron gas at the surface of room temperature ferroelectric complex oxides such as BaTiO3. In addition, these effects needs to be demonstrated in nanodevices. This was the object of the second part of Chapter 5, where I described the fabrication of spin-orbit read-out devices, whose structure is similar to that of FESO devices. This point will be the focus of my group for the next years, with several PhD contracts focused around the development of these FESO devices. I hope that the nanofabrication processes and finite elements tools developed over the course of this PhD will be of use to attain this goal.

Bibliography

[1] M. M. Waldrop, "The chips are down for Moores law", Nature News, 530(7589):144, (2016).

[2] Z. Guo, J. Yin, Y. Bai, D. Zhu, K. Shi, G. Wang, K. Cao and W. Zhao, "Spintronics for energy-efficient computing: An overview and outlook", Proc. IEEE 109, 1399 (2021).

[3] M. N. Baibich, J. M. Broto, A. Fert, F. Nguyen Van Dau, F. Petroff, P. Etienne, G. Creuzet, A. Friederich, and J. Chazelas, "Giant Magnetoresistance of (001)Fe/(001)Cr Magnetic Superlattices", Phys. Rev. Lett. 61, 2472 (1988).

[4] G. Binasch, P. Grünberg, F. Saurenbach, and W. Zinn, "Enhanced magnetoresistance in layered magnetic structures with antiferromagnetic interlayer exchange", Phys. Rev. B 39, 4828(R) (1989).

[5] J. S. Moodera, Lisa R. Kinder, Terrilyn M. Wong, and R. Meservey, "Large Magnetoresistance at Room Temperature in Ferromagnetic Thin Film Tunnel Junctions", Phys. Rev. Lett. 74, 3273 (1995).

[6] Everspin “Toggle MRAM Technology”, https://www.everspin.com/toggle-mram-technology accessed 03/07/2016.

[7] L. Berger, "Emission of spin waves by a magnetic multilayer traversed by a current", Phys. Rev. B 54, 9353 (1996).

[8] J.C.Slonczewski, "Current-driven excitation of magnetic multilayers", J. Magn. Magn. Mater. 159, L1–L7 (1996).

[9] Y. Huai, "Spin-transfer torque MRAM (STT-MRAM): Challenges and prospects", AAPPS bulletin, 18(6), 33-40 (2008).

[10] H. Yang, S. O. Valenzuela, M. Chshiev, S. Couet, B. Dieny, B. Dlubak, A. Fert, K. Garello, M. Jamet, D.-E. Jeong, K. Lee, T. Lee, M.-B. Martin, G. Sankar Kar, P. Sénéor, H.-J. Shin and S. Roche, "Two-dimensional materials prospects for non-volatile spintronic memories", Nature 606, 663–673 (2022).

[11] Emerging Non-Volatile Memory 2021 (Yole Développement, 2021); `https://www.i-micronews.com/products/emerging-non-volatile-memory-2021/?utm_source=PR&utm_medium=email&utm_campaign=PR_EMERGING_NON_VOLATILE_MEMORY_YOLE_Market_Update_Feb2021`.

[12] W. S. Zhao, T. Devolder, Y. Lakys, J. O. Klein, C. Chappert, and P. Mazoyer, "Design considerations and strategies for high-reliable STT-MRAM", Microelectron. Reliab. 51, 1454–1458 (2011).

[13] A. Manchon, J. Železný, I.M. Miron, T. Jungwirth, J. Sinova, A. Thiaville, K. Garello, and P. Gambardella, "Current-induced spin-orbit torques in ferromagnetic and antiferromagnetic systems", Rev. Mod. Phys. 91, 035004 (2019).

[14] K. Garello et al, "SOT-MRAM 300 mm integration for low power and ultrafast embedded memories" IEEE Symp. VLSI Circuits 5481–82 (2018).

[15] MRAM info, "ITRI joins forces with TSMC and NYCU to develop next-gen MRAM technologies", `https://www.mram-info.com/itri-joins-forces-tsmc-and-nycu-develop-next-gen-mram-technologies` accessed 03/07/2022.

[16] I. Mihai Miron, K. Garello, G. Gaudin, P.-J. Zermatten, M. V. Costache, S. Auffret, S. Bandiera, B. Rodmacq, A. Schuhl and P. Gambardella, "Perpendicular switching of a single ferromagnetic layer induced by in-plane current injection", Nature 476, 189 (2011).

[17] S. Valenzuela, M. Tinkham, "Direct electronic measurement of the spin Hall effect", Nature 442, 176 (2006).

[18] D.C. Mahendra, R. Grassi, J.-Y. Chen, M. Jamali, D. Reifsnyder Hickey, D. Zhang, Z. Zhao, H. Li, P. Quarterman, Y. Lv, M. Li, A. Manchon, K. Andre Mkhoyan, T. Low and J.-P. Wang "Room-temperature high spin–orbit torque due to quantum confinement in sputtered $\mathrm{Bi_xSe_{1-x}}$ films", Nature Mater. 17, 800 (2018).

[19] D. MacNeill, G. M. Stiehl, M. H. D. Guimaraes, R. A. Buhrman, J. Park and D. C. Ralph, "ontrol of spin–orbit torques through crystal symmetry in WTe2/ferromagnet bilayers", Nature Phys. 13, 300–305 (2017).

[20] D. C. Vaz, P. Noël, A. Johansson, B. Göbel, F. Y. Bruno, G. Singh, S. McKeown-Walker, F. Trier, L. M. Vicente-Arche, A. Sander, S. Valencia, P. Bruneel, M. Vivek, M. Gabay, N. Bergeal, F. Baumberger, H. Okuno, A. Barthélémy, A. Fert, L. Vila, I. Mertig, J.-P. Attané and M. Bibes, "Mapping spin–charge conversion to the band structure in a topological oxide two-dimensional electron gas", Nat. Mater. 18, 1187–1193 (2019).

[21]] Q. Shao, P. Li, L. Liu, H. Yang, S. Fukami, A. Razavi, H. Wu, K. Wang, F. Freimuth, Y. Mokrousov, M. D. Stiles, S. Emori, A. Hoffmann, J. Akerman, K. Roy, J.-P. Wang, S.-H. Yang, K. Garello, and W. Zhang, "Roadmap of spin–orbit torques", IEEE Trans. Magn. 57, 1 (2021).

[22] S. Fukami, C. Zhang, S. DuttaGupta, A. Kurenkov and H. Ohno, "Magnetization switching by spin–orbit torque in an antiferromagnet–ferromagnet bilayer system", Nature Mater 15, 535–541 (2016).

[23] M. Kimata, H. Chen, K. Kondou, S. Sugimoto, P. K. Muduli, M. Ikhlas, Y. Omori, T. Tomita, A.. H. MacDonald, S. Nakatsuji and Y. Otani "Magnetic and magnetic inverse spin Hall effects in a non-collinear antiferromagnet", Nature 565, 627–630 (2019).

[24] Y. Hibino, T. Taniguchi, K. Yakushiji, A. Fukushima, H. Kubota and S. Yuasa "Giant charge-to-spin conversion in ferromagnet via spin-orbit coupling", Nat. Commun. 12, 6254 (2021).

[25] C. Safranski, E. A. Montoya and I. N. Krivorotov, ". Spin–orbit torque driven by a planar Hall current", Nature Nanotech. 14, 27–30 (2019).

[26] B. Dieny, I. L. Prejbeanu, K. Garello, P. Gambardella, P. Freitas, R. Lehndorff, W. Raberg, U. Ebels, S. O. Demokritov, J. Akerman, A. Deac, P. Pirro, C. Adelmann, A. Anane, A. V. Chumak, A. Hirohata, S. Mangin, Sergio O. Valenzuela, M. Cengiz Onbaşlı, M. d'Aquino, G. Prenat, G. Finocchio, L. Lopez-Diaz, R. Chantrell, O. Chubykalo-Fesenko and P. Bortolotti, "Opportunities and challenges for spintronics in the microelectronics industry", Nat. Electron. 3, 446–459 (2020).

[27] S. Manipatruni, D. E. Nikonov, C.-C. Lin, T. A. Gosavi, H. Liu, B. Prasad, Y.-L. Huang, E. Bonturim, R. Ramesh and I. A. Young, "Scalable energy-efficient magnetoelectric spin–orbit logic", Nature 565, 35–42 (2019).

[28] S. Manipatruni, D. E. Nikonov and I. A. Young, "Beyond CMOS computing with spin and polarization", Nature Phys 14, 338–343 (2018).

[29] P. Noël, F. Trier, L. M. Vicente Arche, J. Bréhin, D. C. Vaz, V. Garcia, S. Fusil, A. Barthélémy, L. Vila, M. Bibes and J.-P. Attané, "Non-volatile electric control of spin–charge conversion in a SrTiO3 Rashba system", Nature 580, 483–486 (2020).

[30] S. Varotto, L. Nessi, S. Cecchi, J. Sławińska, P. Noël, S. Petrò, F. Fagiani, A. Novati, M. Cantoni, D. Petti, E. Albisetti, M. Costa, R. Calarco, M. Buongiorno Nardelli, M. Bibes, S. Picozzi, J.-P. Attané, L. Vila, R. Bertacco and C. Rinaldi, "Room-temperature ferroelectric switching of spin-to-charge conversion in germanium telluride", Nat. Electron. 4, 740–747 (2021).

[31] A. Fert and I. A. Campbel "Transport properties of ferromagnetic transition metals", J. Phys. Colloques 32, C1-46 (1971).

[32] P. C. van Son, H. van Kempen, and P. Wyder, "Boundary Resistance of the Ferromagnetic-Nonferromagnetic Metal Interface", Phys. Rev. Lett. 58, 2271 (1987).

[33] P. Laczkowski, M. Cosset-Cheneau, W. Savero-Torres, V. T. Pham, G. Zahnd, H. Jaffrès, N. Reyren, J.-C. Rojas-Sànchez, A. Marty, L. Vila, J.-M. George, and J.-P. Attané, "Spin-dependent transport characterization in metallic lateral spin valves using one-dimensional and three-dimensional modeling", Phys. Rev. B 99, 134436 (2019).

[34] A. Brataas, G. E. Bauer, and P. J. Kelly, "Non-collinear magnetoelectronics", Phys. Rep. 427, 157 (2006).

[35] T. Valet and A. Fert, "Theory of the perpendicular magnetoresistance in magnetic multilayers", Phys. Rev. B 48, 7099 (1993).

[36] R. J. Elliott "Theory of the Effect of Spin-Orbit Coupling on Magnetic Resonance in Some Semiconductors", Phys. Rev. 96, 266 (1954).

[37] M.I.Dyakonov and V.I.Perel, "Current-induced spin orientation of electrons in semiconductors", Phys. Lett. 35, 6 (1971).

[38] R.S. Nair, E. Barati, K. Gupta, Z. Yuan, and P.J. Kelly ”Spin-Flip Diffusion Length in 5d Transition Metal Elements: A First-Principles Benchmark”, Phys. Rev. Lett. 126, 196601 (2021).

[39] E. Villamor, M. Isasa, L. E. Hueso, and F. Casanova, ”Contribution of defects to the spin relaxation in copper nanowires”, Phys. Rev. B 87, 094417 (2013).

[40] J. D. Watts, L. O’Brien, J. S. Jeong, K. A. Mkhoyan, P. A. Crowell, and C. Leighton, ”Magnetic impurities as the origin of the variability in spin relaxation rates in Cu-based spin transport devices”, Phys. Rev. Materials 3, 124409 (2019).

[41] H. Idzuchi, Y. Fukuma, L. Wang, and Y. Otani, ”Spin relaxation mechanism in silver nanowires covered with MgO protection layer”, Appl. Phys. Lett. 101, 022415 (2012).

[42] G. Mihajlović, J. E. Pearson, S. D. Bader, and A. Hoffmann, ”Surface Spin Flip Probability of Mesoscopic Ag Wires”, Phys. Rev. Lett. 104, 237202 (2010).

[43] T. Kimura, T. Sato, and Y. Otani, ”Temperature Evolution of Spin Relaxation in a NiFe/Cu Lateral Spin Valve”, Phys. Rev. Lett. 100, 066602 (2008).

[44] H. Zou and Y. Ji, ”The origin of high surface spin-flip rate in metallic nonlocal spin valves”, Appl. Phys. Lett. 101, 082401 (2012).

[45] J. Bass and W. P Pratt, ”Spin-diffusion lengths in metals and alloys, and spin-flipping at metal/metal interfaces: an experimentalist’s critical review”, J. Phys.: Condens. Matter 19 183201 (2007).

[46] J.-C. Rojas-Sánchez, N. Reyren, P. Laczkowski, W. Savero, J.-P. Attané, C. Deranlot, M. Jamet, J.-M. George, L. Vila, and H. Jaffrès, ”Spin Pumping and Inverse Spin Hall Effect in Platinum: The Essential Role of Spin-Memory Loss at Metallic Interfaces”, Phys. Rev. Lett. 112, 106602 (2014).

[47] N.F. Mott, ”The electrical conductivity of transition metals”, Proc. R. Soc. A 153.880 (1936).

[48] A. Fert and I. A. Campbell ”Electrical resistivity of ferromagnetic nickel and iron based alloys”, J. Phys. F: Met. Phys. 6 849 (1976).

[49] E. Villamor, M. Isasa, Luis E. Hueso, and F. Casanova, ”Temperature dependence of spin polarization in ferromagnetic metals using lateral spin valves”, Phys. Rev. B 88, 184411 (2013).

[50] S. Zhang, P. M. Levy, and A. Fert, ”Mechanisms of Spin-Polarized Current-Driven Magnetization Switching”, Phys. Rev. Lett. 88, 236601 (2002).

[51] S. Zhang, ”Spin Hall Effect in the Presence of Spin Diffusion”, Phys. Rev. Lett. 85, 393 (2000).

[52] W.S. Torres, A. Marty, P. Laczkowski, M. Jamet, L. Vila and J.-P. Attané, ”Calculation method of spin accumulations and spin signals in nanostructures using spin resistors”, Eur. Phys. J. B 91, 37 (2018).

[53] Y. Tserkovnyak, A. Brataas, and G. E. W. Baue ”Spin pumping and magnetization dynamics in metallic multilayers”, Phys. Rev. B 66, 224403 (2002).

[54] W.P.Pratt and J.Bass, ”Perpendicular-current studies of electron transport across metal/metal interfaces”, Appl. Surf. Sci. 256, 399–40 (2009).

[55] K. Gupta et al, ”Disorder Dependence of Interface Spin Memory Loss” Phys. Rev. Lett. 124, 087702 (2020).

[56] V. T. Pham, M. Cosset-Chéneau et al, ”Evidence of interfacial asymmetric spin scattering at ferromagnet-Pt interfaces”, Phys. Rev. B 103, L201403 (2021).

[57] L. Zhu et al, ”Origin of Strong Two-Magnon Scattering in Heavy-Metal/Ferromagnet/Oxide Heterostructures” Phys. Rev. Applied 13, 034038 (2020).

[58] W. Park, D. V. Baxter, S. Steenwyk, I. Moraru, W. P. Pratt, Jr., and J. Bass, ”Measurement of resistance and spin-memory loss (spin relaxation) at interfaces using sputtered current perpendicular-to-plane exchange-biased spin valves”, Phys. Rev. B 62, 1178 (2000).

[59] J. Borge and I. V. Tokatly, ”Boundary conditions for spin and charge diffusion in the presence of interfacial spin-orbit coupling”, Phys. Rev. B 99, 241401(R) (2019).

[60] L. Berger, ”Precession of conduction-electron spins near an interface between normal and magnetic metals” IEEE Trans. Magn. 31, 3871 (1995).

[61] J. C. Slonczewski, "Currents and torques in metallic magnetic multilayers", J. Magn. Magn. Mater. 247, 324 (2002).

[62] M.D. Stiles and A. Zangwill, "Anatomy of spin-transfer torque", Phys. Rev. B 66, 014407 (2002).

[63] V.P. Amin and M D. Stiles, "Spin transport at interfaces with spin-orbit coupling: Formalism", Phys. Rev. B 94, 104419 (2016).

[64] C. Petitjean, D. Luc, and X. Waintal, "Unified DriftDiffusion Theory for Transverse Spin Currents in Spin Valves, Domain Walls, and Other Textured Magnets", Phys. Rev. Lett. 109, 117204 (2012).

[65] C. Ortiz Pauyac, M. Chshiev, A. Manchon, and S. A. Nikolaev "Spin Hall and Spin Swapping Torques in Diffusive Ferromagnets", Phys. Rev. Lett. 120, 176802 (2018).

[66] V.P. Amin and M.D. Stiles, "Spin transport at interfaces with spin-orbit coupling: Phenomenology", Phys. Rev. B 94, 104420 (2016).

[67] G. Zahnd, L. Vila, V. T. Pham, M. Cosset-Cheneau, W. Lim, A. Brenac, P. Laczkowski, A. Marty, and J. P. Attané, "Spin diffusion length and polarization of ferromagnetic metals measured by the spin-absorption technique in lateral spin valves", Phys. Rev. B 98, 174414 (2018).

[68] X. Qiu, W. Legrand, P. He, Y. Wu, J. Yu, R. Ramaswamy, A. Manchon, and H. Yang "Enhanced Spin-Orbit Torque via Modulation of Spin Current Absorption, Phys. Rev. Lett. 117, 217206 (2016).

[69] S. Nonoguchi, T. Nomura, and T. Kimura, "Longitudinal and transverse spin current absorptions in a lateral spin-valve structure", Phys. Rev. B 86, 104417 (2012).

[70] Jairo Sinova, Sergio O. Valenzuela, J. Wunderlich, C.H. Back, and T. Jungwirth, "Spin Hall effects" Rev. Mod. Phys. 87, 1213 (2015).

[71] Y. Niimi, Y. Kawanishi, D. H. Wei, C. Deranlot, H. X. Yang, M. Chshiev, T. Valet, A. Fert, and Y. Otani, "Giant Spin Hall Effect Induced by Skew Scattering from Bismuth Impurities inside Thin Film CuBi Alloys", Phys. Rev. Lett. 109, 156602 (2012).

[72] P. Laczkowski, Y. Fu, H. Yang, J.-C. Rojas-Sánchez, P. Noel, V. T. Pham, G. Zahnd, C. Deranlot, S. Collin, C. Bouard, P. Warin, V. Maurel, M. Chshiev, A. Marty, J.-P. Attané, A. Fert, H. Jaffrès, L. Vila, and J.-M. George, "Large enhancement of the spin Hall effect in Au by side-jump scattering on Ta impurities" Phys. Rev. B 96, 140405(R) (2017).

[73] G. Y. Guo, S. Murakami, T.-W. Chen, and N. Nagaosa, "Intrinsic Spin Hall Effect in Platinum: First-Principles Calculations", Phys. Rev. Lett. 100, 096401 (2008).

[74] N. Niimi and Y. Otani "Reciprocal spin Hall effects in conductors with strong spin–orbit coupling: a review", Rep. Prog. Phys. 78 124501 (2015).

[75] A. Davidson, V. P. Amin, W. S. Aljuaid, P. M. Haney, X. Fan "Perspectives of electrically generated spin currents in ferromagnetic materials", Phys. Lett. A 384, 126228 (2020).

[76] T. Kimura, Y. Otani, T. Sato, S. Takahashi, and S. Maekawa, "Room-Temperature Reversible Spin Hall Effect", Phys. Rev. Lett. 98, 156601 (2007).

[77] K. V. Shanavas, Z. S. Popović, and S. Satpathy, "Theoretical model for Rashba spin-orbit interaction in d electrons", Phys. Rev. B 90, 165108 (2014).

[78] H.L. Wang, C.H. Du, Y. Pu, R. Adur, P.C. Hammel, and F.Y. Yang "Scaling of Spin Hall Angle in 3d, 4d, and 5d Metals from $Y_3Fe_5O_{12}$/Metal Spin Pumping", Phys. Rev. Lett. 112, 197201 (2014).

[79] E. Sagasta, Y. Omori, M. Isasa, M. Gradhand, L. E. Hueso, Y. Niimi, Y. Otani, and F. Casanova, "Tuning the spin Hall effect of Pt from the moderately dirty to the superclean regime", Phys. Rev. B 94, 060412(R) (2016).

[80] M. Morota, Y. Niimi, K. Ohnishi, D. H. Wei, T. Tanaka, H. Kontani, T. Kimura, and Y. Otani, "Indication of intrinsic spin Hall effect in 4d and 5d transition metals", Phys. Rev. B 83, 174405 (2011).

[81] L. Liu, C.-F. Pai, Y. Li, H. W. Tseng, D. C. Ralph, R. A. Buhrman, "Spin-Torque Switching with the Giant Spin Hall Effect of Tantalum", Science 336, 555 (2012).

[82] C.-F. Pai, L. Liu, Y. Li, H. W. Tseng, D. C. Ralph, and R. A. Buhrman, "Spin transfer torque devices utilizing the giant spin Hall effect of tungsten", Appl. Phys. Lett. 101, 122404 (2012).

[83] M. Isasa, E. Villamor, L. E. Hueso, M. Gradhand, and F. Casanova, "Temperature dependence of spin diffusion

length and spin Hall angle in Au and Pt", Phys. Rev. B 91, 024402 (2015).

[84] P. Laczkowski, J.-C. Rojas-Sánchez, W. Savero-Torres, H. Jaffrès, N. Reyren, C. Deranlot1, L. Notin, C. Beigné, A. Marty, J.-P. Attané, L. Vila, J.-M. George, and A. Fert, "Experimental evidences of a large extrinsic spin Hall effect in AuW alloy", Appl. Phys. Lett. 104, 142403 (2014).

[85] Y. Niimi, M. Morota, D. H. Wei, C. Deranlot, M. Basletic, A. Hamzic, A. Fert, and Y. Otani, "Extrinsic Spin Hall Effect Induced by Iridium Impurities in Copper", Phys. Rev. Lett. 106, 126601 (2011).

[86] L. Liu, T. Moriyama, D. C. Ralph, and R. A. Buhrman, "Spin-Torque Ferromagnetic Resonance Induced by the Spin Hall Effect", Phys. Rev. Lett. 106, 036601 (2011).

[87] K. Ando, S. Takahashi, J. Ieda, Y. Kajiwara, H. Nakayama, T. Yoshino, K. Harii, Y. Fujikawa, M. Matsuo, S. Maekawa, and E. Saitoh, "Inverse spin-Hall effect induced by spin pumping in metallic system", J. Appl. Phys. 109, 103913 (2011).

[88] C. Stamm, C. Murer, M. Berritta, J. Feng, M. Gabureac, P.M. Oppeneer, and P. Gambardella, "Magneto-Optical Detection of the Spin Hall Effect in Pt and W Thin Films", Phys. Rev. Lett. 119, 087203 (2017).

[89] L. Vila, T. Kimura, and Y. Otani, "Evolution of the Spin Hall Effect in Pt Nanowires: Size and Temperature Effects", Phys. Rev. Lett. 99, 226604 (2007).

[90] Lesne, E. Non-Equilibrium Spin Accumulation Phenomena at the LaAlO3/SrTiO3 (001) Quasi-Two-Dimensional Electron System. Ph.D. thesis, Université Pierre et Marie Curie (2015).

[91] C. Du, H. Wang, F. Yang, and P. Chris Hammel, "Systematic variation of spin-orbit coupling with d-orbital filling: Large inverse spin Hall effect in 3d transition metals" Phys. Rev. B 90, 140407(R) (2014).

[92] V. P. Amin, Junwen Li, M. D. Stiles, and P. M. Haney, "Intrinsic spin currents in ferromagnets", Phys. Rev. B 99, 220405(R) (2019).

[93] Y. Miura and K. Masuda, "First-principles calculations on the spin anomalous Hall effect of ferromagnetic alloys", Phys. Rev. Materials 5, L101402 (2021).

[94] G. Qu, K. Nakamura, and M. Hayashi, "Magnetization direction dependent spin Hall effect in 3d ferromagnets", Phys. Rev. B 102, 144440 (2020).

[95] T. C. Chuang, D. Qu, S. Y. Huang, and S. F. Lee, "Magnetization-dependent spin Hall effect in a perpendicular magnetized film", Phys. Rev. Research 2, 032053(R) (2020).

[96] Y. Omori, E. Sagasta, Y. Niimi, M. Gradhand, L. E. Hueso, F. Casanova, and Y. Otani, "Relation between spin Hall effect and anomalous Hall effect in 3d ferromagnetic metals", Phys. Rev. B 99, 014403 (2019).

[97] S. LaShell, B. A. McDougall, and E. Jensen, "Spin Splitting of an Au(111) Surface State Band Observed with Angle Resolved Photoelectron Spectroscopy", Phys. Rev. Lett. 77, 3419 (1996).

[98] J. C. Rojas Sánchez, L. Vila, G. Desfonds, S. Gambarelli, J. P. Attané, J. M. De Teresa, C. Magén and A. Fert, "Spin-to-charge conversion using Rashba coupling at the interface between non-magnetic materials", Nat Commun 4, 2944 (2013).

[99] C. Sanz-Fernandez, V. T. Pham, E. Sagasta, L. E. Hueso, I.V. Tokatly, F. Casanova, and F. S. Bergere "Quantification of interfacial spin-charge conversion in hybrid devices with a metal/insulator interface", Appl. Phys. Lett. 117, 142405 (2020).

[100] A. Manchon, H. C. Koo, J. Nitta, S. M. Frolov and R. A. Duine "New perspectives for Rashba spin–orbit coupling", Nature Mater 14, 871–882 (2015).

[101] A. Soumyanarayanan, N. Reyren, A. Fert and C. Panagopoulos "Emergent phenomena induced by spin–orbit coupling at surfaces and interfaces", Nature 539, 509–517 (2016).

[102] Y. Xia, D. Qian, D. Hsieh, L. Wray, A. Pal, H. Lin, A. Bansil, D. Grauer, Y. S. Hor, R. J. Cava and M. Z. Hasan "Observation of a large-gap topological-insulator class with a single Dirac cone on the surface", Nature Phys 5, 398–402 (2009).

[103] H. Zhang, C.-X. Liu, X.-L. Qi, Xi Dai, Zhong Fang and S.-C. Zhang; "Topological insulators in Bi_2Se_3, Bi_2Te_3 and Sb_2Te_3 with a single Dirac cone on the surface" Nature Phys 5, 438–442 (2009).

[104] P. Noel, C. Thomas, Y. Fu, L. Vila, B. Haas, P-H. Jouneau, S. Gambarelli, T. Meunier, P. Ballet, and J.P. Attané

”Highly Efficient Spin-to-Charge Current Conversion in Strained HgTe Surface States Protected by a HgCdTe Layer”, Phys. Rev. Lett. 120, 167201 (2018).

[105] H. Wang, J. Kally, J. Sue Lee, T. Liu, H. Chang, F. Reifsnyder Hickey, K. Andre Mkhoyan, M. Wu, A. Richardella, and N. Samarth ”Surface-State-Dominated Spin-Charge Current Conversion in Topological-Insulator–Ferromagnetic-Insulator Heterostructures”, Phys. Rev. Lett. 117, 076601 (2016).

[106] K. Kondou, R. Yoshimi, A. Tsukazaki, Y. Fukuma, J. Matsuno, K. S. Takahashi, M. Kawasaki, Y. Tokura and Y. Otani ”Fermi-level-dependent charge-to-spin current conversion by Dirac surface states of topological insulators”, Nature Phys 12, 1027–1031 (2016).

[107] S. Hong, V. Diep, S. Datta, and Y. P. Chen; ”Modeling potentiometric measurements in topological insulators including parallel channels”, Phys. Rev. B 86, 085131 (2012).

[108] Y. Wang, D. Zhu, Y. Wu, Y. Yang, J. Yu, R. Ramaswamy, R. Mishra, S. Shi, M. Elyasi, K.-L. Teo, Y. Wu and H. Yang; ”Room temperature magnetization switching in topological insulator-ferromagnet heterostructures by spin-orbit torques”, Nat. Commun. 8, 1364 (2017).

[109] J.-C. Rojas-Sánchez, S. Oyarzún, Y. Fu, A. Marty, C. Vergnaud, S. Gambarelli, L. Vila, M. Jamet, Y. Ohtsubo, A. Taleb-Ibrahimi, P. Le Fèvre, F. Bertran, N. Reyren, J.-M. George, and A. Fert; ”Spin to Charge Conversion at Room Temperature by Spin Pumping into a New Type of Topological Insulator: α-Sn Films” Phys. Rev. Lett. 116, 096602 (2016).

[110] S. Zhang and A. Fert, ”Conversion between spin and charge currents with topological insulators”, Phys. Rev. B 94, 184423 (2016).

[111] M. Brahlek, N. Koirala, N. Bansal, and S. Oh, ”Transport properties of topological insulators: Band bending, bulk metal-to-insulator transition, and weak anti-localization”, Solid State Commun. 215, 54 (2015).

[112] R. Dey, N. Prasad, L. F. Register, and S. K. Banerjee ”Conversion of spin current into charge current in a topological insulator: Role of the interface”, Phys. Rev. B 97, 174406 (2018).

[113] D. C. Ralph and M. D. Stiles, ”Spin transfer torque”, J. Magn. Magn. Mater. 320, 1190 (2008).

[114] I.M. Miron, G. Gaudin, S. Auffret, B. Rodmacq, A. Schuhl, S. Pizzini, J. Vogel and P. Gambardella , ”Current-driven spin torque induced by the Rashba effect in a ferromagnetic metal layer”, Nat. Mater. 9, 230 (2010).

[115] Y. Tserkovnyak, A. Brataas, G.E.W. Bauer, and B.I. Halperin, ”Nonlocal magnetization dynamics in ferromagnetic heterostructures”, Rev. Mod. Phys. 77, 1375 (2015).

[116] K. Uchida, S. Takahashi, K. Harii, J. Ieda, W. Koshibae, K. Ando, S. Maekawa and E. Saitoh, ”Observation of the spin Seebeck effect”, Nature 455, 778–781 (2008).

[117] W. Zhang, V. Vlaminck, J. E. Pearson, R. Divan, S. D. Bader, and A. Hoffmann, ”Determination of the Pt spin diffusion length by spin-pumping and spin Hall effect”, Appl. Phys. Lett. 103, 242414 (2013).

[118] M. Weiler, M. Althammer, M. Schreier, J. Lotze, M. Pernpeintner, S. Meyer, H. Huebl, R. Gross, A. Kamra, J. Xiao, Y.-T. Chen, H. Jiao, G. E. W. Bauer, and S. T. B. Goennenwein, ”Experimental Test of the Spin Mixing Interface Conductivity Concept” Phys. Rev. Lett. 111, 176601 (2013).

[119] Y. Wang, R. Ramaswamy and H. Yang, ”FMR-related phenomena in spintronic devices” J. Phys. D: Appl. Phys. 51, 273002 (2018).

[120] O. Gladii, R. L. Seeger, L. Frangou, G. Forestier, U. Ebels, S. Auffret, and V. Baltz, ”Stacking order-dependent sign-change of microwave phase due to eddy currents in nanometer-scale NiFe/Cu heterostructures”, Appl. Phys. Lett. 115, 032403 (2019).

[121] H. Jiao and G.E.W. Bauer, ”Spin Backflow and ac Voltage Generation by Spin Pumping and the Inverse Spin Hall Effect”, Phys. Rev. Lett. 110, 217602 (2013).

[122] E. Sagasta, Y. Omori, M. Isasa, Y. Otani, L. E. Hueso, and F. Casanova, ”Spin diffusion length of Permalloy using spin absorption in lateral spin valves”, Appl. Phys. Lett. 111, 082407 (2017).

[123] P. Laczkowski, H. Jaffrès, W. Savero-Torres, J.-C. Rojas-Sánchez, Y. Fu, N. Reyren, C. Deranlot, L. Notin, C. Beigné, J.-P. Attané, L. Vila, J.-M. George, and A. Marty, ”Evaluation of spin diffusion length of AuW alloys using spin absorption experiments in the limit of large spin-orbit interactions”, Phys. Rev. B 92, 214405 (2015).

[124] J.-C. Rojas-Sánchez, N. Reyren, P. Laczkowski, W. Savero, J.-P. Attané, C. Deranlot, M. Jamet, J.-M. George, L.

Vila, and H. Jaffrès, "Spin Pumping and Inverse Spin Hall Effect in Platinum: The Essential Role of Spin-Memory Loss at Metallic Interfaces", Phys. Rev. Lett. 112, 106602 (2014).

[125] Y. Liu, Z. Yuan, R.J.H. Wesselink, A.A. Starikov, and P.J. Kelly, "Interface Enhancement of Gilbert Damping from First Principles", Phys. Rev. Lett. 113, 207202 (2014).

[126] L. Zhu, D.C. Ralph, and R.A. Buhrman, "Spin-Orbit Torques in Heavy-Metal–Ferromagnet Bilayers with Varying Strengths of Interfacial Spin-Orbit Coupling" Phys. Rev. Lett. 122, 077201 (2019).

[127] A. Fert and H. Jaffrès, "Conditions for efficient spin injection from a ferromagnetic metal into a semiconductor", Phys. Rev. B 64, 184420 (2001).

[128] F. L. Bakker, A. Slachter, J.-P. Adam, and B. J. van Wees "Interplay of Peltier and Seebeck Effects in Nanoscale Nonlocal Spin Valves", Phys. Rev. Lett. 105, 136601 (2010).

[129] T. Kimura, J. Hamrle, and Y. Otani, "Estimation of spin-diffusion length from the magnitude of spin-current absorption: Multiterminal ferromagnetic/nonferromagnetic hybrid structures", Phys. Rev. B 72, 014461 (2005).

[130] K. Gupta, R. J. H. Wesselink, Z. Yuan, and P. J. Kelly "Spin transport at finite temperatures: A first-principles study for ferromagnetic/nonmagnetic interfaces' Phys. Rev. B 104, 205426 (2021).

[131] G. Zahnd, L. Vila, V. T. Pham, F. Rortais, M. Cosset-Cheneau, C. Vergnaud, M. Jamet, P. Noel, T. Gushi, A. Brenac, A. Marty, and J. P. Attané, "Observation of the Hanle effect in giant magnetoresistance measurements", Appl. Phys. Lett. 112, 232405 (2018).

[132] H. Idzuchi, Y. Fukuma, S. Takahashi, S. Maekawa, and Y. Otani, "Effect of anisotropic spin absorption on the Hanle effect in lateral spin valves", s, Phys. Rev. B 89, 081308(R) (2014).

[133] Y.-T. Chen, S. Takahashi, H. Nakayama, M. Althammer, S. T. B. Goennenwein, E. Saitoh, and G.E.W. Bauer, "Theory of spin Hall magnetoresistance", Phys. Rev. B 87, 144411 (2013).

[134] M.-G. Kang, G. Go, K.-W. Kim, J.-G. Choi, B.-G. Park and K.-J. Lee, "Negative spin Hall magnetoresistance of normal metal/ferromagnet bilayers", Nat Commun 11, 3619 (2020).

[135] A. Ghosh, S. Auffret, U. Ebels, and W. E. Bailey, "Penetration Depth of Transverse Spin Current in Ultrathin Ferromagnets", Phys. Rev. Lett. 109, 127202 (2012).

[136] M. J. Donahue and D. G. Porter, OOMMF User's Guide Nat. Inst. Stand. Technol., Gaithersburg, MD, Tech. Rep. NISTIR 6376, 1999, Version 1.0.

[137] M. Cosset-Chéneau, L. Vila, G. Zahnd, D. Gusakova, V.T. Pham, C. Grèzes, X. Waintal, A. Marty, H. Jaffrès, and J.-P. Attané, "Measurement of the Spin Absorption Anisotropy in Lateral Spin Valves", Phys. Rev. Lett. 126, 027201 (2021).

[138] H. Jaffrès, J.-M. George, and A. Fert, "Spin transport in multiterminal devices: Large spin signals in devices with confined geometry", Phys. Rev. B 82, 140408(R) (2010).

[139] J. Borge, and I. V. Tokatly, "Ballistic spin transport in the presence of interfaces with strong spin-orbit coupling", *Phys. Rev. B* 96, 115445 (2017).

[140] Kyoung-Whan Kim, Kyung-Jin Lee, Jairo Sinova, Hyun-Woo Lee, and M. D. Stiles, "Spin-orbit torques from interfacial spin-orbit coupling for various interfaces", *Phys. Rev. B* 96, 104438 (2017).

[141] K. Xia, P. J. Kelly, G. E. W. Bauer, A. Brataas, and I. Turek, "Spin torques in ferromagnetic/normal-metal structures", Phys. Rev. B 65, 220401(R) (2002).

[142] G. E. W. Bauer, K. M Schep, K. Xia and P. J. Kelly, "Scattering theory of interface resistance in magnetic multilayers", J. Phys. D: Appl. Phys. 35 2410 (2002).

[143] S. Karube, K. Kondou and Y. Otani, "Experimental observation of spin-to-charge current conversion at non-magnetic metal/Bi_2O_3 interfaces", Appl. Phys. Express 9 033001 (2016).

[144] V.M. Edelstein, "Spin polarization of conduction electrons induced by electric current in two-dimensional asymmetric electron systems", Solid State Commun. 73, 233 (1990).

[145] G. Manchon, S. Ghosh, C. Barreteau, and A. Manchon, "Semirealistic tight-binding model for spin-orbit torques", Phys. Rev. B 101, 174423 (2020).

[146] G. Go, D. Jo, C. Kim, and H.-W. Lee, "Intrinsic Spin and Orbital Hall Effects from Orbital Texture", Phys. Rev.

Lett. 121, 086602 (2018).

[147] A. Johansson, B. Göbel, J. Henk, M. Bibes, and I. Mertig, "Spin and orbital Edelstein effects in a two-dimensional electron gas: Theory and application to $SrTiO_3$ interfaces" Phys. Rev. Research 3, 013275 (2021).

[148] H. E. Weaver, "Dielectric properties of single crystals of SrTiO3 at low temperatures", J. Phys. Chem. Solid 11, 274 (1959).

[149] A. Pojani, F. Finocchi, and C. Noguera, "Polarity on the $SrTiO_3$ (111) and (110) surfaces", Surf. Sci. 442, 179 (1999).

[150] S. McKeown Walker, F. Y. Bruno, F. Baumberger, "Spectroscopy of Complex Oxide Interfaces" (Eds: C. Cancellieri, V. Strocov), Springer, Cham 2018.

[151] H. Y. Hwang, Y. Iwasa, M. Kawasaki, B. Keimer, N. Nagaosa and Y. Tokura, "Emergent phenomena at oxide interfaces", Nature Mater 11, 103–113 (2012).

[152] A. F. Santander-Syro, O. Copie, T. Kondo, F. Fortuna, S. Pailhès, R. Weht, X. G. Qiu, F. Bertran, A. Nicolaou, A. Taleb-Ibrahimi, P. Le Fèvre, G. Herranz, M. Bibes, N. Reyren, Y. Apertet, P. Lecoeur, A. Barthélémy and M. J. Rozenberg, "Two-dimensional electron gas with universal subbands at the surface of SrTiO3", Nature 469, 189–193 (2011).

[153] A. Ohtomo, A. and H.Y. Hwang, " high-mobility electron gas at the LaAlO3/ SrTiO3 heterointerface", Nature 427, 423–426 (2004).

[154] W. Meevasana, P. D. C. King, R. H. He, S-K. Mo, M. Hashimoto, A. Tamai, P. Songsiriritthigul, F. Baumberger and Z-X. Shen "Creation and control of a two-dimensional electron liquid at the bare SrTiO3 surface", Nature Mater 10, 114–118 (2011).

[155] T. C. Rödel, F. Fortuna, S. Sengupta, E. Frantzeskakis, P. Le Fèvre, F. Bertran, B. Mercey, S. Matzen, G. Agnus, T. Maroutian, P. Lecoeur, A. F. Santander-Syro, "Universal fabrication of 2D electron systems in functional oxides", Adv. Mater. 28, 1976–1980 (2016).

[156] Z. Wang, S. McKeown Walker, A. Tamai, Y. Wang, Z. Ristic, F. Y. Bruno, A. de la Torre, S. Riccò, N. C. Plumb, M. Shi, P. Hlawenka, J. Sánchez-Barriga, A. Varykhalov, T. K. Kim, M. Hoesch, P. D. C. King, W. Meevasana, U. Diebold, J. Mesot, B. Moritz, T. P. Devereaux, M. Radovic and F. Baumberger, "Tailoring the nature and strength of electron–phonon interactions in the $SrTiO_3(001)$ 2D electron liquid", Nature Mater. 15, 835–839 (2016).

[157] P. D. C. King, S. McKeown Walker, A. Tamai, A. de la Torre, T. Eknapakul, P. Buaphet, S.-K. Mo, W. Meevasana, M. S. Bahramy and F. Baumberger, "Quasiparticle dynamics and spin–orbital texture of the SrTiO3 two-dimensional electron gas", Nat. Commun. 5, 3414 (2014).

[158] A. D. Caviglia, M. Gabay, S. Gariglio, N. Reyren, C. Cancellieri, and J.-M. Triscone, "Tunable Rashba Spin-Orbit Interaction at Oxide Interfaces", Phys. Rev. Lett. 104, 126803 (2010).

[159] A. Joshua, S. Pecker, J. Ruhman, E. Altman and S. Ilani "A universal critical density underlying the physics of electrons at the $SrTiO_3/LaAlO_3$ interface", Nat Commun 3, 1129 (2012).

[160] H. Liang, L. Cheng, L. Wei, Z. Luo, G. Yu, C. Zeng, and Z. Zhang "Nonmonotonically tunable Rashba spin-orbit coupling by multiple-band filling control in $SrTiO_3$-based interfacial d-electron gases" Phys. Rev. B 92, 075309 (2015).

[161] D. C. Vaz, F. Trier, A. Dyrdał, A. Johansson, K. Garcia, A. Barthélémy, I. Mertig, J. Barnaś, A. Fert, and M. Bibes, "Determining the Rashba parameter from the bilinear magnetoresistance response in a two-dimensional electron gas", Phys. Rev. Materials 4, 071001(R) (2020).

[162] G. Khalsa, B. Lee, and A. H. MacDonald "Theory of t_{2g} electron-gas Rashba interactions" Phys. Rev. B 88, 041302(R) (2013).

[163] Z. Zhong, A. Toth, and K. Held, "Theory of spin-orbit coupling at $SrTiO_3/LaAlO_3$ interfaces and $SrTiO_3$ surfaces", Phys. Rev. B 87, 161102(R) (2013).

[164] P. Kim, K. Tae Kang, G. Go, and J. H. Han "Nature of orbital and spin Rashba coupling in the surface bands of $SrTiO_3$ and $KTaO_3$" Phys. Rev. B 90, 205423 (2014).

[165] L. L. Tao and J. Wang, "Strain-tunable ferroelectricity and its control of Rashba effect in $KTaO_3$", J. Appl. Phys. 120, 234101 (2016).

[166] L. L. Tao and E. Y. Tsymbal, "Perspectives of spin-textured ferroelectrics", J. Phys. D: Appl. Phys. 54 113001

(2021).

[167] A. D. Caviglia, S. Gariglio, N. Reyren, D. Jaccard, T. Schneider, M. Gabay, S. Thiel, G. Hammerl, J. Mannhart and J.-M. Triscone, " Electric feld control of the LaAlO3/SrTiO3 interface ground state" Nature 456, 624–627 (2008).

[168] E. Lesne, Yu Fu, S. Oyarzun, J. C. Rojas-Sánchez, D. C. Vaz, H. Naganuma, G. Sicoli, J.-P. Attané, M. Jamet, E. Jacquet, J.-M. George, A. Barthélémy, H. Jaffrès, A. Fert, M. Bibes and L. Vila, "Highly efficient and tunable spin-to-charge conversion through Rashba coupling at oxide interfaces", Nature Mater 15, 1261–1266 (2016).

[169] Diogo Castro Vaz, Spin-to-charge current conversion in SrTiO3-based two-dimensional electron gases, Condensed Matter. Sorbonne Université, 2018.

[170] V. T. Pham, H. Yang, W. Y. Choi, A. Marty, I. Groen, A. Chuvilin, F. S. Bergeret, L. E. Hueso, I. V. Tokatly, and F. Casanova, "Large spin-charge interconversion induced by interfacial spin-orbit coupling in a highly conducting all-metallic system", Phys. Rev. B 104, 184410 (2021).

[171] M. Isasa, M. C. Martínez-Velarte, E. Villamor, C. Magén, L. Morellón, J. M. De Teresa, M. R. Ibarra, G. Vignale, E. V. Chulkov, E. E. Krasovskii, L. E. Hueso, and F. Casanova, "Origin of inverse Rashba-Edelstein effect detected at the Cu/Bi interface using lateral spin valves", Phys. Rev. B 93, 014420 (2016).

[172] L. M. Vicente-Arche, S. Mallik, M. Cosset-Chéneau, P. Noël, D.C. Vaz, F. Trier, T.A. Gosavi, C.-C. Lin, D.E. Nikonov, I.A. Young, A. Sander, A. Barthélémy, J.-P. Attané, L. Vila, and M. Bibes, "Metal/$SrTiO_3$ two-dimensional electron gases for spin-to-charge conversion" Phys. Rev. Materials 5, 064005 (2021).

[173] A. B. Posadas, K. J. Kormondy, W. Guo, P. Ponath, J. GelerKremer, T. Hadamek, and A. A. Demkov, "Scavenging of oxygen from SrTiO3 during oxide thin film deposition and the formation of interfacial 2DEGs", J. Appl. Phys. 121, 105302 (2017).

[174] R. Nakamura, T. Toda, S. Tsukui, M. Tane, M. Ishimaru, T. Suzuki, and H. Nakajima, "Diffusion of oxygen in amorphous Al_2O_3, Ta_2O_5, and Nb_2O_5", J. Appl. Phys. 116, 033504 (2014).

[175] Y. Ikuma, Y. Tsubaki, Y. Nakao, Y. Yokogawa, and M. Yoshimura, "Oxygen diffusion in the fluorite-related phases of Y_2O_3 Ta_2O_5 and Ho_2O_3 Ta_2O_5 systems", Solid State Ionics 40–41, 258 (1990).

[176] A. Asgari and M. Kalafi, "The control of two-dimensional-electron-gas density and mobility in AlGaN/GaN heterostructures with Schottky gate" Mater. Sci. Eng. C 26, 898 (2006).

[177] P. Delugas, A. Filippetti, V. Fiorentini, D. I. Bilc, D. Fontaine, P. Ghosez, "Spontaneous 2-Dimensional Carrier Confinement at the n-type $SrTiO_3$/$LaAlO_3$ interface", Phys. Rev. Lett. 106, 166807 (2011).

[178] J. Biscaras, S. Hurand, C. Feuillet-Palma, A. Rastogi, R. C. Budhani, N. Reyren, E. Lesne, J. Lesueur and N. Bergeal, "Limit of the electrostatic doping in two-dimensional electron gases of $LaXO_3$(X = Al, Ti)/$SrTiO_3$ Sci Rep 4, 6788 (2014).

[179] S. McKeown Walker, M. Boselli, E. A. Martínez, S. Gariglio, F. Y. Bruno, F. Baumberger, "A Laser-ARPES View of the 2D Electron Systems at $LaAlO_3$/$SrTiO_3$ and Al/$SrTiO_3$ Interfaces", Adv. Elec. Mater. 2101376 (2022).

[180] T. Dimopoulos, G. Gieres, S. Colis, J. Wecker, Y. Luo, and K. Samwer, "Magnetic tunnel junctions with yttrium oxide barrier", Appl. Phys. Lett. 83, 3338 (2003).

[181] T. Dimopoulos, G. Gieres, S. Colis, R. Lopez, M. Vieth, J. Wecker, Y. Luo, and K. Samwer "Tunnel junctions with yttrium oxide barrier and various ferromagnetic electrodes", IEEE Trans. Magn. 40, 2296 (2004).

[182] K. Komatsu, S. Kasai, S.-L. Li, S. Nakaharai, N. Mitoma, M. Yamamoto, and K. Tsukagoshi "Spin injection and detection in a graphene lateral spin valve using an yttrium-oxide tunneling barrier", Appl. Phys. Express 7, 085101 (2014).

[183] S. McKeown Walker, A. de la Torre, F.Y. Bruno, A. Tamai, T.K. Kim, M. Hoesch, M. Shi, M.S. Bahramy, P.D.C. King F. Baumberger, "Control of a two-dimensional electron gas on SrTiO3(111) by atomic oxygen" Phys. Rev. Lett. 113, 177601 (2014).

[184] Z. Wang, Z. Zhong, X. Hao, S. Gerhold, B. Stöger, M. Schmid, J. Sánchez-Barriga, A. Varykhalov, C. Franchini, K. Held, U. Diebold, "Anisotropic two-dimensional electron gas at SrTiO3(110)", Proc. Natl. Acad. Sci. U.S. Am. 111, 3933–3937 (2014).

[185] K. Zou, S. Ismail-Beigi, K. Kisslinger, X. Shen, D. Su, F. J. Walker, and C. H. Ahn, "$LaTiO_3$/$KTaO_3$ interfaces: A new two-dimensional electron gas system" APL Mater. 3, 036104 (2015).

[186] Luis M. Vicente-Arche, J. Bréhin, S. Varotto, M. Cosset-Chéneau, S. Mallik, R. Salazar, P. Noël, D. C. Vaz, F. Trier, S. Bhattacharya, A. Sander, P. Le Fèvre, F. Bertran, G. Saiz, G. Ménard, N. Bergeal, A. Barthélémy, H. Li, C.-C. Lin, D. E. Nikonov, I. A. Young, J. E. Rault, L. Vila, J.-P. Attané, and M. Bibes, "Spin–Charge Interconversion in KTaO3 2D Electron Gases", Adv.Mater. 33, 2102102 (2021).

[187] H. Zhang, X. Yan, X. Zhang, S. Wang, C. Xiong, H. Zhang, S. Qi, J. Zhang, F. Han, N. Wu, B. Liu, Y. Chen, B. Shen, and J. Sun, "Unusual Electric and Optical Tuning of $KTaO_3$-Based Two-Dimensional Electron Gases with 5d Orbitals", ACS Nano 13, 1, 609–615 (2019).

[188] C. Ang and Z. Yu, "dc electric-field dependence of the dielectric constant in polar dielectrics: Multipolarization mechanism model", Phys. Rev. B 69, 174109 (2004).

[189] S. K. Ojha, S. K. Gogoi, P. Mandal, S. D. Kaushik, J. W. Freeland, M. Jain, and S. Middey, "Oxygen vacancy induced electronic structure modification of KTaO3" Phys. Rev. B 103, 085120 (2021).

[190] H. Nakamura and T. Kimura "Electric field tuning of spin-orbit coupling in KTaO3 field-effect transistors" Phys. Rev. B 80, 121308(R) (2009).

[191] A. F. Santander-Syro, C. Bareille, F. Fortuna, O. Copie, M. Gabay, F. Bertran, A. Taleb-Ibrahimi, P. Le Fèvre, G. Herranz, N. Reyren, M. Bibes, A. Barthélémy, P. Lecoeur, J. Guevara, M. J. Rozenberg, "Orbital symmetry reconstruction and strong mass renormalization in the two-dimensional electron gas at the surface of $KTaO_3$", Phys. Rev. B 86, 121107 (2012).

[192] A. Gupta, H. Silotia, A. Kumari, M. Dumen, S. Goyal, R. Tomar, N. Wadehra, P. Ayyub, and S. Chakraverty, "KTaO3—The New Kid on the Spintronics Block", Adv.Mater. 34, 2106481 (2022).

[193] C. Bareille, F. Fortuna, T. C. Rödel, F. Bertran, M. Gabay, O. Hijano Cubelos, A. Taleb-Ibrahimi, P. Le Fèvre, M. Bibes, A. Barthélémy, T. Maroutian, P. Lecoeur, M. J. Rozenberg and A. F. Santander-Syro, "Two-dimensional electron gas with six-fold symmetry at the (111) surface of KTaO3" Sci Rep 4, 3586 (2014).

[194] P. D. C. King, R. H. He, T. Eknapakul, P. Buaphet, S.-K. Mo, Y. Kaneko, S. Harashima, Y. Hikita, M. S. Bahramy, C. Bell, Z. Hussain, Y. Tokura, Z.-X. Shen, H. Y. Hwang, F. Baumberger, and W. Meevasana, "Subband Structure of a Two-Dimensional Electron Gas Formed at the Polar Surface of the Strong Spin-Orbit Perovskite $KTaO_3$" Phys. Rev. Lett. 108, 117602 (2012).

[195] H. Zhang, Y. Ma, H. Zhang, X. Chen, S. Wang, G. Li, Y. Yun, X. Yan, Y. Chen, F. Hu, J. Cai, B. Shen, W. Han, J. Sun, "Thermal Spin Injection and Inverse Edelstein Effect of the Two-Dimensional Electron Gas at EuO–$KTaO_3$ Interfaces", Nano Lett. 19, 1605 (2019).

[196] E. Lesne, N. Reyren, D. Doennig, R. Mattana, H. Jaffrès, V. Cros, F. Petroff, F. Choueikani, P. Ohresser, R. Pentcheva, A. Barthélémy, M. Bibes, "Suppression of the critical thickness threshold for conductivity at the $LaAlO_3/SrTiO_3$ interface", Nat. Commun. 5, 4291 (2014).

[197] D. C. Vaz, E. Lesne, A. Sander, H. Naganuma, E. Jacquet, J. Santamaria, A. Barthélémy, M. Bibes, "Tuning Up or Down the Critical Thickness in $LaAlO_3/SrTiO_3$ through In Situ Deposition of Metal Overlayers", Adv. Mater. 29, 1700486 (2017).

[198] D. C. Vaz, F. Trier, A. Dyrdał, A. Johansson, K. Garcia, A. Barthélémy, I. Mertig, J. Barnaś, A. Fert, and M. Bibes, "Determining the Rashba parameter from the bilinear magnetoresistance response in a two-dimensional electron gas", Phys. Rev. Materials 4, 071001(R) (2020).

[199] N. Kumar, N. Wadehra, R. Tomar, Shama, S. Kumar, Y. Singh,S. Dattagupta, and S. Chakraverty, "Observation of Shubnikov–de Haas Oscillations, Planar Hall Effect, and Anisotropic Magnetoresistance at the Conducting Interface of EuO–KTaO3", Adv Quantum Tech 4, 2000081 (2021).

[200] J.-C. Rojas-Sánchez and A. Fert, "Compared Efficiencies of Conversions between Charge and Spin Current by Spin-Orbit Interactions in Two- and Three-Dimensional Systems", Phys. Rev. Applied 11, 054049 (2019).

[201] I. A. Campbell, A. Fert, and O. Jaoul, "The spontaneous resistivity anisotropy in Ni-based alloys", J. Phys. C 3, S95 (1970).

[202] T. Greber, T. J. Kreutz, and J. Osterwalder, "Photoemission above the Fermi Level: The Top of the Minority d Band in Nickel", Phys. Rev. Lett. 79, 4465 (1997).

[203] M. W. Keller, K. S. Gerace, M. Arora, E. K. Delczeg Czirjak, J. M. Shaw, and T. J. Silva, "ear-unity spin Hall ratio in Ni_xCu_{1-x} alloys" Phys. Rev. B 99, 214411 (2019).

[204] S. Eich, M. Plotzing, M. Rollinger, S. Emmerich, R. Adam, C. Chen, H. Cornelius Kapteyn, M. M. Murnane, L. Plucinski, D. Steil, B. Stadtmüller, M. Cinchetti, M. Aeschlimann, C. M. Schneider and S. Mathias "Band structure evolution during the ultrafast ferromagnetic-paramagnetic phase transition in cobalt", Sci. Adv. 3, e1602094 (2017).

[205] I. Turek and K. Carva, "Spin-mixing conductances of metallic and half metallic magnetic layers", J. Phys.: Condens. Matter 19 365203 (2007).

[206] A. M. Abdul-Lettif, "Investigation of interdiffusion in copper–nickel bilayer thin films", Physica (Amsterdam) 388B, 107 (2007).

[207] M. Caminale, A. Ghosh, S. Auffret, U. Ebels, K. Ollefs, F. Wilhelm, A. Rogalev, and W. E. Bailey, "Spin pumping damping and magnetic proximity effect in Pd and Pt spin-sink layers" Phys. Rev. B 94, 014414 (2016).

[208] S. Andersson and V. Korenivski, "Exchange coupling and magnetoresistance in CoFe/NiCu/CoFe spin valves near the Curie point of the spacer", J. Appl. Phys. 107, 09D711 (2010).

[209] H. Y. T. Nguyen, R. Acharyya, W. P. Pratt, and J. Bass, "Conduction electron spin–flipping at sputtered $Co_{90}Fe_{10}$/Cu interfaces", J. Appl. Phys. 109, 07C903 (2011).

[210] B. Dassonneville, R. Acharyya, H. Y. T. Nguyen, R. Loloee, W. P. Pratt Jr., and J. Bass "A way to measure electron spin-flipping at ferromagnetic/nonmagnetic interfaces and application to Co/Cu", Appl. Phys. Lett. 96, 022509 (2010).

[211] J. Lindner and K. Baberschke, "In situ ferromagnetic resonance: an ultimate tool to investigate the coupling in ultrathin magnetic films" J. Phys. Condens. Matter 15, R193 (2003).

[212] B. Heinrich, Y. Tserkovnyak, G. Woltersdorf, A. Brataas, R. Urban, and G. E. W. Bauer "Dynamic Exchange Coupling in Magnetic Bilayers", Phys. Rev. Lett. 90, 187601 (2003).

[213] M. Hayashi, J. Kim, M. Yamanouchi, and H. Ohno, "Quantitative characterization of the spin-orbit torque using harmonic Hall voltage measurements", Phys. Rev. B 89, 144425 (2014).

[214] D.H. Wei, Y. Niimi, B. Gu, T. Ziman, S. Maekawa and Y. Otani, "The spin Hall effect as a probe of nonlinear spin fluctuations", Nat Commun 3, 1058 (2012).

[215] T. Taniguchi, J. Grollier, and M.D. Stiles, "Spin-Transfer Torques Generated by the Anomalous Hall Effect and Anisotropic Magnetoresistance", Phys. Rev. Applied 3, 044001 (2015).

[216] N. Nagaosa, J. Sinova, S. Onoda, A. H. MacDonald, and N. P. Ong "Anomalous Hall effect", Rev. Mod. Phys. 82, 1539 (2010).

[217] M. Harder, Y. Gui, C.-M. Hu, "Electrical detection of magnetization dynamics via spin rectification effects", Phys. Rep. 661, 1 (2016).

[218] L. Hodges, H. Ehrenreich, and N. D. Lang, "Interpolation Scheme for Band Structure of Noble and Transition Metals: Ferromagnetism and Neutron Diffraction in Ni", Phys. Rev. 152, 505 (1966).

[219] G. Qu, K. Nakamura, and M. Hayashi, "Magnetization direction dependent spin Hall effect in 3d ferromagnets", Phys. Rev. B 102, 144440 (2020).

[220] T. J. Kreutz, T. Greber, P. Aebi, and J. Osterwalder, "Temperature-dependent electronic structure of nickel metal", Phys. Rev. B 58, 1300 (1998).

[221] L. Landau and E. Lifshitz, "On the theory of dispersion of magnetic permeability in ferromagnetic bodies", , Phys. Z. Sowjet 8(153-169) (1935).

[222] B. Khodadadi, A. Rai, A. Sapkota, A. Srivastava, B. Nepal, Y. Lim, D.A. Smith, C. Mewes, S. Budhathoki, A.J. Hauser, M. Gao, J.-F. Li, D.D. V., Z. Jiang, J.J. Heremans, P.V. Balachandran, T. Mewes, and S. Emori, "Conductivitylike Gilbert Damping due to Intraband Scattering in Epitaxial Iron", Phys. Rev. Lett. 124, 157201 (2020).

[223] C. Kittel, "Ferromagnetic resonance", Journal de Physique et le Radium, 12(3)(291-302)(1951).

[224] E. Saitoh, M. Ueda, and H. Miyajima, "Conversion of spin current into charge current at room temperature : Inverse spin-Hall effect", Appl. Phys. Lett. 88, 182509 (2006).

[225] Iguchi and E. Saitoh, "Measurement of spin pumping voltage separated from extrinsic microwave effects", J. Phys. Soc. Jpn. 86, 011003 (2017).

[226] J.-C. Rojas-Sánchez, M. Cubukcu, A. Jain, C. Vergnaud, C. Portemont, C. Ducruet, A. Barski, A. Marty, L. Vila, J.-P. Attané, E. Augendre, G. Desfonds, S. Gambarelli, H. Jaffrès, J.-M. George, and M. Jamet, "Spin pumping and inverse spin Hall effect in germanium", Phys. Rev. B 88, 064403 (2013).

[227] P. Noël, M. Cosset-Chéneau, V. Haspot, V. Maurel, C. Lombard, M. Bibes, A. Barthelemy, L. Vila, and J.-P. Attané, "Negligible thermal contributions to the spin pumping signal in ferromagnetic metal–platinum bilayers", J. Appl. Phys. 127, 163907 (2020).

[228] L. Liu, R. A. Buhrman, D. C. Ralph, "Review and Analysis of Measurements of the Spin Hall Effect in Platinum", arXiv:1111.3702 (2012).

[229] T. Tanaka, H. Kontani, M. Naito, T. Naito, D. S. Hirashima, K. Yamada, and J. Inoue, "Intrinsic spin Hall effect and orbital Hall effect in 4d and 5d transition metals" Phys. Rev. B 77, 165117 (2008).

[230] Albert Fert and Peter M. Levy, "Spin Hall Effect Induced by Resonant Scattering on Impurities in Metals", Phys. Rev. Lett. 106, 157208 (2011).

[231] C. Du, H. Wang, F. Yang, and P. C. Hammel, "Systematic variation of spin-orbit coupling with d-orbital filling: Large inverse spin Hall effect in 3d transition metals", Phys. Rev. B 90, 140407(R) (2014).

[232] B. F. Miao, S. Y. Huang, D. Qu, and C. L. Chien, "Inverse Spin Hall Effect in a Ferromagnetic Metal", Phys. Rev. Lett. 111, 066602 (2013).

[233] D. Tian, Y. Li, D. Qu, S. Y. Huang, X. Jin, and C. L. Chien, "Manipulation of pure spin current in ferromagnetic metals independent of magnetization", Phys. Rev. B 94, 020403(R) (2016).

[234] S.-H. C. Baek, V. P. Amin, Y.-W. Oh, G. Go, S.-J. Lee, G.-H. Lee, K.-J. Kim, M. D. Stiles, B.-Guk Park and K.-J. Lee, "Spin currents and spin–orbit torques in ferromagnetic trilayers", Nat. Mater. 17, 509 (2018).

[235] Y. Ou, D.C. Ralph, and R.A. Buhrman, "Strong Enhancement of the Spin Hall Effect by Spin Fluctuations near the Curie Point of $\mathrm{Fe_xPt_{1-x}}$ Alloys" Phys. Rev. Lett. 120, 097203 (2018).

[236] B. Gu, T. Ziman, and S. Maekawa, "Theory of the spin Hall effect, and its inverse, in a ferromagnetic metal near the Curie temperature" Phys. Rev. B 86, 241303(R) (2012).

[237] B. Zimmermann, K. Chadova, D. Ködderitzsch, S. Blügel, H. Ebert, D. V. Fedorov, N. H. Long, P. Mavropoulos, I. Mertig, Y. Mokrousov, and M. Gradhand "Skew scattering in dilute ferromagnetic alloys", Phys. Rev. B 90, 220403(R) (2014).

[238] C. Safranski, E. A. Montoya and I. N. Krivorotov "Spin–orbit torque driven by a planar Hall current", Nature Nanotech 14, 27–30 (2019).

[239] A. Okada, S. He, B. Gu, S. Kanai, A. Soumyanarayanan, S. Ter Lim, M. Tran, M. Mori, S. Maekawa, and F. Matsukura, "Magnetization dynamics and its scattering mechanism in thin CoFeB films with interfacial anisotropy", Proc. Natl. Acad. Sci. U.S.A. 114, 3815 (2017).

[240] O. Gladii, L. Frangou, A. Hallal, R. L. Seeger, P. Noël, G. Forestier, S. Auffret, M. Rubio-Roy, P. Warin, L. Vila, S. Wimmer, H. Ebert, S. Gambarelli, M. Chshiev, and V. Baltz, "Self-induced inverse spin Hall effect in ferromagnets: Demonstration through nonmonotonic temperature dependence in permalloy", Phys. Rev. B 100, 174409 (2019).

[241] G. Zahnd, L. Vila, V.T. Pham, A. Marty, P. Laczkowski, W. Savero Torres, C. Beigné, C. Vergnaud, M. Jamet, and J.-P. Attané, "Comparison of the use of NiFe and CoFe as electrodes for metallic lateral spin valves", Nanotechnology 27 035201 (2016).

[242] M. Cosset-Chéneau, L. Vila, G. Zahnd, D. Gusakova, V.T. Pham, C. Grèzes, X. Waintal, A. Marty, H. Jaffrès, and J.-P. Attané, "Measurement of the Spin Absorption Anisotropy in Lateral Spin Valves", Phys. Rev. Lett. 126, 027201 (2021).

[243] S. Varotto, M. Cosset-Chéneau, C. Grèzes, Y. Fu, P. Warin, A. Brenac, J.-F. Jacquot, S. Gambarelli, C. Rinaldi, V. Baltz, J.-P. Attané, L. Vila, and P. Noël, "Independence of the Inverse Spin Hall Effect with the Magnetic Phase in Thin NiCu Films", Phys. Rev. Lett. 125, 267204 (2020).

[244] V. T. Pham , M. Cosset-Chéneau, A. Brenac, O. Boulle, A. Marty, J.-P. Attané, and L. Vila, "Evidence of interfacial asymmetric spin scattering at ferromagnet-Pt interfaces", Phys. Rev. B 103, L201403 (2021).

[245]] P. Dular and C. Geuzaine, GetDP reference manual: The documentation for GetDP, a general environment for the treatment of discrete problems, http://www.geuz.org/getdp/.

[246] P. Dular, C. Geuzaine, A. Genon, and W. Legros, An evolutive software environment for teaching finite element methods in electromagnetism, IEEE Trans. Magn. 35, 1682 (1999).

[247] V. D. Nguyen, L. Vila, P. Laczkowski, A. Marty, T. Faivre, and J. P. Attané, "Detection of domain-wall position and magnetization reversal in nanostructures using the magnon contribution to the resistivity", Phys. Rev. Lett. 107, 136605 (2011).

[248] A. P. Mihai, J. P. Attané, A. Marty, P. Warin, and Y. Samson, "Electron-magnon diffusion and magnetization reversal detection in FePt thin films", Phys. Rev. B 77, 060401(R) (2008).

[249] H. Z. Arham, Trupti S. Khaire, R. Loloee, W. P. Pratt, Jr., and N. O. Birge, "Measurement of spin memory lengths in PdNi and PdFe ferromagnetic alloys", Phys. Rev. B 80, 174515 (2009).

[250] Z. Zhu, X. Zheng, G. Li, H. Bai, J. Su, Y. Zhang and J.-W. Cai, "Strong spin orientation-dependent spin current diffusion and inverse spin Hall effect in a ferromagnetic metal", NPG Asia Mater 12, 12 (2020).

[251] C. Gonzalez-Fuentes, R. Henriquez, C. García, R. K. Dumas, B. Bozzo, and A. Pomar, "Spin diffusion length associated with out-of-plane conductivity of Pt in spin pumping experiments" Phys. Rev. B 103, 224403 (2021).

[252] V.P. Amin, J. Zemen, and M.D. Stiles, "Interface-Generated Spin Currents" Phys. Rev. Lett. 121, 136805 (2018).

[253] A. F. Kravets, A. N. Timoshevskii, B. Z. Yanchitsky, O. Yu. Salyuk, S. O. Yablonovskii, S. Andersson, and V. Korenivski, "Exchange-induced phase separation in Ni–Cu films", J. Magn. Magn. Mater. 324, 2131 (2012).

[254] W. Wang, T. Wang, V. P. Amin, Y. Wang, A. Radhakrishnan, A. Davidson, S. R. Allen, T. J. Silva, H. Ohldag, D. Balzar et al., "Anomalous spin–orbit torques in magnetic single-layer films", Nat. Nanotechnol. 14, 819 (2019).

[255] H. Hopster, R. Raue, G. Güntherodt, E. Kisker, R. Clauberg, and M. Campagna, "Temperature Dependence of the Exchange Splitting in Ni Studied by Spin-Polarized Photoemission", Phys. Rev. Lett. 51, 829 (1983).

[256] K.-P. Kämper, W. Schmitt, and G. Güntherodt, "Temperature and wave-vector dependence of the spin-split band structure of Ni(111) along the Γ-L line" Phys. Rev. B 42, 10696 (1990).

[257] M. Pickel, A. B. Schmidt, M. Weinelt, and M. Donath, "Magnetic Exchange Splitting in Fe above the Curie Temperature", Phys. Rev. Lett. 104, 237204 (2010).

[258] D. E. Shai, C. Adamo, D. W. Shen, C. M. Brooks, J. W. Harter, E. J. Monkman, B. Burganov, D. G. Schlom, and K. M. Shen, "Quasiparticle Mass Enhancement and Temperature Dependence of the Electronic Structure of Ferromagnetic $SrRuO_3$ Thin Films" Phys. Rev. Lett. 110, 087004 (2013).

[259] T. J. Hicks, B. Rainford, J. S. Kouvel, G. G. Low, and J. B. Comly, "Giant Moments in Ni-Cu Alloys Near the Critical Composition", Phys. Rev. Lett. 22, 531 (1969).

[260] Y. Ito and J. Akimitsu, "The Behavior of Localized Moment of Ni in Ni-Cu Alloy System", J. Phys. Soc. Jpn. 35, 1000 (1973).

[261]] M. Wahler, N. Homonnay, T. Richter, A. Müller, C. Eisenschmidt, B. Fuhrmann, and G. Schmidt, "Inverse spin Hall effect in a complex ferromagnetic oxide heterostructure" Sci. Rep. 6, 28727 (2016).

[262] I. Turek , J. Kudrnovsky , V. Drchal and P. Bruno "Exchange interactions, spin waves, and transition temperatures in itinerant magnets" Philos. Mag. 86:12, 1713-1752 (2006).

[263] X. Zhang, Y. Lao, J. Sklenar, N. S. Bingham, J. T. Batley, J. D. Watts, C. Nisoli, C. Leighton, and P. Schiffer, "Understanding thermal annealing of artificial spin ice", APL Materials 7, 111112 (2019).

[264] T. Wimmer, B. Coester, S. Geprag, R. Gross, S.T.B. Goennenwein, H. Huebl, and M. Althammer, "Anomalous spin Hall angle of metallic ferromagnet determined by a multiterminal spin injection/detection device" Appl. Phys. 115, 092404 (2019).

[265] K. S. Das, W.Y. Schoemaker, B.J. van Wees, and I.J.Vera-Marun, "Spin injection and detection via the anomalous spin Hall effect of a ferromagnetic metal", Phys. Rev. B 96, 220408(R) (2017).

[266] T.R. McGuire and R.I. Potter, "Anisotropic Magnetoresistance in Ferromagnetic 3d alloys" IEEE Trans. Magn. 11, 4 (1975).

[267] C. Swindells and D. Atkinson, "Interface enhanced precessional damping in spintronic multilayers: A perspective", : J. Appl. Phys. 131, 170902 (2022).

[268] Paul Noël, "Dynamical spin injection and spin to charge current conversion in oxide-based Rashba interfaces and

topological insulators". PhD thesis, Grenoble University, 2020.

[269] Y. Ou, Z. Wang, C.S. Chang, H. P. Nair, H. Paik, N. Reynolds, D. C. Ralph, D. A. Muller, D. G. Schlom, and R. A. Buhrman, "Exceptionally High, Strongly Temperature Dependent, Spin Hall Conductivity of SrRuO3", Nano Lett., 19, 6, 3663 (2019).

[270] J. D. Gibbons, D. MacNeill, R. A. Buhrman, and D. C. Ralph, "Reorientable Spin Direction for Spin Current Produced by the Anomalous Hall Effect" Phys. Rev. Applied 9, 064033 (2018).

[271] V.T. Pham, L. Vila, G. Zahnd, A. Marty, W. Savero-Torres, M. Jamet and J.P. Attane, "Ferromagnetic/nonmagnetic nanostructures for the electrical measurement of the spin Hall effect", Nano Lett. 16, 11, 6755 (2016).

[272] S. O. Valenzuela and M. Tinkham "Direct electronic measurement of the spin Hall effect", Nature 442, 176 (2006).

[273] J. Kim, P. Sheng, S. Takahashi, S. Mitani, and M. Hayashi "Spin Hall Magnetoresistance in Metallic Bilayers", Phys. Rev. Lett. 116, 097201 (2016).

[274] H. Mizuno, H. Isshiki, K. Kondou, Y. Zhu, and Y. Otani, "Influence of planar Hall effect on the output signal in a T-shaped spin conversion device", Appl. Phys. Lett. 119, 092401 (2021).

[275] I. Groen, V.T. Pham, N. Leo, A. Marty, L. E. Hueso, and F. Casanova, "Disentangling Spin, Anomalous, and Planar Hall Effects in Ferromagnet-Heavy-Metal Nanostructures", Phys. Rev. Applied 15, 044010 (2021).

[276] J. Cramer, A. Ross, S. Jaiswal, L. Baldrati, R. Lebrun, and M. Klaui "Orientation-dependent direct and inverse spin Hall effects in $Co_{60}Fe_{20}B_{20}$", Phys. Rev. B 99, 104414 (2019).

[277] DE Lacheisserie, Etienne du Trémolet. Magnétisme. EDP sciences, 2012.

[278] C. Herring, "The State of d Electrons in Transition Metals", J. Appl. Phys. 31, 3S (1960).

[279] M. B. Stearns, "Why is iron magnetic?", Physics Today 31, 4, 34 (1978).

[280] V. Flovik, F. Macia, A. D. Kent, and E. Wahlstrom, "Eddy current interactions in a ferromagnet-normal metal bilayer structure, and its impact on ferromagnetic resonance lineshapes", J. Appl. Phys. 117, 143902 (2015).

[281] S.Mizukami, Y.Ando, T.Miyazaki, "Magnetic relaxation of normal-metal (NM)/80NiFe/NM films", J. Magn. Magn. Mater. 239 (2002) 42 (2002).

[282] Y. Fu, J. Li, J. Papin, P. Noel, C. Grezes, M. Cosset-Cheneau, T. Guillet, C. Thomas, Y.-M. Niquet, P. Ballet, T. Meunier, J.-P. Attane, A. Fert and L. Vila, "Bilinear magnetoresistance in HgTe topological insulator: opposite signs at opposite interfaces demonstrated by gate control", arXiv:2111.15594 (2021).

[283] J. Bréhin, F. Trier, L. M. Vicente-Arche, P. Hemme, P. Noël, M. Cosset-Chéneau, J.-P. Attané, L. Vila, A. Sander, Y. Gallais, A. Sacuto, B. Dkhil, V. Garcia, S. Fusil, A. Barthélémy, M. Cazayous, and M. Bibes, "Switchable two-dimensional electron gas based on ferroelectric Ca:$SrTiO_3$", Phys. Rev. Materials 4, 041002(R) (2020).

[284] S. Manipatruni, D. E. Nikonov, C.-C. Lin, T. A. Gosavi, H. Liu, B. Prasad, Y.-L. Huang, E. Bonturim, R. Ramesh and I. A. Young, "Scalable energy-efficient magnetoelectric spin–orbit logic", Nature 565, 35–42 (2019).

[285] J. T. Heron, J. L. Bosse, Q. He, Y. Gao, M. Trassin, L. Ye, J. D. Clarkson, C. Wang, Jian Liu, S. Salahuddin, D. C. Ralph, D. G. Schlom, J. Íñiguez, B. D. Huey and R. Ramesh, "Deterministic switching of ferromagnetism at room temperature using an electric field", Nature 516, 370–373 (2014).

[286] R. Ramesh, S. Manipatruni, "Electric field control of magnetism", Proc. R. Soc. A 477: 20200942 (2021).

[287] B. Prasad, Y.-L. Huang, R. V. Chopdekar, Z. Chen, J. Steffes, S. Das, Q. Li, M. Yang, C.-C. Lin, T. Gosavi, D. E. Nikonov, Z. Q. Qiu, L. W. Martin, B. D. Huey, I. Young, J. Íñiguez, S. Manipatruni, and R. Ramesh, "Ultralow Voltage Manipulation of Ferromagnetism", Adv. Mater. 32, 2001943 (2020).

[288] R. Ramaswamy, T. Dutta, S. Liang, G. Yang, M. S. M. Saifullah and H. Yang, "Spin orbit torque driven magnetization switching with sputtered Bi_2Se_3 spin current source", J. Phys. D: Appl. Phys. 52 224001 (2019).

[289] X. Zhang, Z. Zeng, C. Shen, Z. Zhang, Z. Wang, C. Lin, and Z. Hu, "Investigation on the electrical transport properties of highly (00l)-textured Sb_2Te_3 films deposited by molecular beam epitaxy", J. Appl. Phys. 115, 024307 (2014).

[290] P. Sahu, J.-Y. Chen J. C. Myers, and J.-P. Wang, "Weak antilocalization and low-temperature characterization of sputtered polycrystalline bismuth selenide", Appl. Phys. Lett. 112, 122402 (2018).

[291] D.C. Mahendra, T. Liu, J.-Y. Chen, T. Peterson, P. Sahu, H. Li, Z. Zhao, M. Wu, and J.-P. Wang, ”Room-temperature spin-to-charge conversion in sputtered bismuth selenide thin films via spin pumping from yttrium iron garnet”, Appl. Phys. Lett. 114, 102401 (2019).

[292] D.C. Mahendra et al, ”Room-temperature high spin–orbit torque due to quantum confinement in sputtered $\mathrm{Bi_xSe_{1-x}}$ films”, Nature Materials 17, 800 (2018).

[293] P. Deorani, J. Son, K. Banerjee, N. Koirala, M. Brahlek, S. Oh, and H. Yang, ”Observation of inverse spin Hall effect in bismuth selenide”, Phys. Rev. B 90, 094403 (2014).

[294] S.-K. Jerng, K. Joo, Y. Kim, S.-M. Yoon, J. H. Lee, M. Kim, J. S. Kim, E. Yoon, S.-H. Chuna and Y. Seung Kim, ”Ordered growth of topological insulator Bi2Se3 thin films on dielectric amorphous SiO2 by MBE”, Nanoscale, 5, 10618 (2013).

[295] J. Zhang, C.-Z. Chang, Z. Zhang, J. Wen, X. Feng, K. Li, M. Liu, K. He, L. Wang, X. Chen, Q.-K. Xue, X. Ma and Y. Wang, ”Band structure engineering in $\mathrm{(Bi_{1-x}Sb_x)_2Te_3}$ ternary topological insulators”, Nat Commun 2, 574 (2011).

[296] S. Hikami et al, ”Spin-Orbit Interaction and Magnetoresistance in the Two Dimensional Random System”, Prog. Theor. Phys. 63, 707 (1980).

[297] Noel, P. (2019). Dynamical spin injection and spin to charge current conversion in oxide-based Rashba interfaces and topological insulators (Doctoral dissertation, Université Grenoble Alpes).

[298] D. Kong, Y. Chen, J. J. Cha, Q. Zhang, J. G. Analytis, K. Lai, Z. Liu, S. S. Hong, K. J. Koski, S.-K. Mo, Z. Hussain, I. R. Fisher, Z.-X. Shen and Y. Cui ”Ambipolar field effect in the ternary topological insulator $\mathrm{(Bi_xSb_{1-x})_2Te_3}$ by composition tuning”, Nature Nanotech 6, 705 (2011).

[299] E. K. de Vries, A. M. Kamerbeek, N. Koirala, M. Brahlek, M. Salehi, S. Oh, B. J. van Wees, and T. Banerjee, ”Towards the understanding of the origin of charge-current-induced spin voltage signals in the topological insulator $\mathrm{Bi_2Se_3}$ ” Phys. Rev. B 92, 201102(R) (2016).

[300] H. Mizuno, H. Isshiki, K. Kondou, Y. Zhu, and Y. Otani, ”Influence of planar Hall effect on the output signal in a T-shaped spin conversion device”, Appl. Phys. Lett. 119, 092401 (2021).

[301] R. Iguchi, and E. Saitoh, ”Measurement of Spin Pumping Voltage Separated from Extrinsic Microwave Effects”, J. Phys. Soc. Jpn. 86, 011003 (2017).

[302] F. Bonell, M. Goto, G. Sauthier, J. F. Sierra, A. I. Figueroa, M. V. Costache, S. Miwa, Y. Suzuki, and S. O. Valenzuela, ”Control of Spin–Orbit Torques by Interface Engineering in Topological Insulator Heterostructures”, Nano Lett. 20, 5893 (2020).

[303] D. Di Sante , P. Barone , R. Bertacco , and S. Picozzi, ”Electric Control of the Giant Rashba Effect in Bulk GeTe”, Adv. Mater. 25, 509–513 (2013).

[304] A. V. Kolobov, D. J. Kim, A. Giussani,3 P. Fons, J. Tominaga, R. Calarco, and A. Gruverman, ”Ferroelectric switching in epitaxial GeTe films”, APL Mater. 2, 066101 (2014).

[305] J. E. Boschker, R. Wang and R. Calarco, ”GeTe: a simple compound blessed with a plethora of properties”, CrystEngComm 19, 5324 (2017).

[306] S. Picozzi, ”Ferroelectric Rashba semiconductors as a novel class of multifunctional materials”, Front. Phys. 2, 10 (2014).

[307] M. Liebmann, C. Rinaldi, D. Di Sante, J. Kellner, C. Pauly, R. Ning Wang, J. Emiel Boschker, A. Giussani, S. Bertoli, M. Cantoni, L. Baldrati, M. Asa, I. Vobornik, G. Panaccione, D. Marchenko, J. Sánchez-Barriga, O. Rader, R. Calarco, S. Picozzi, R. Bertacco, M. Morgenstern, ”Giant Rashba-Type Spin Splitting in Ferroelectric GeTe(111)”, Adv.Mater. 28, 560–565 (2016).

[308] Y. Li, Y. Li, P. Li, B. Fang, X. Yang, Y. Wen, D.-X. Zheng, C.-H. Zhang, X. He, A. Manchon, Z.-H. Cheng and X.-X. Zhang, ”Nonreciprocal charge transport up to room temperature in bulk Rashba semiconductor α-GeTe”, Nat Commun 12, 540 (2021).

[309] P. W. M. Blom, R. M. Wolf, J. F. M. Cillessen, and M. P. C. M. Krijn, ”Ferroelectric Schottky Diode”, Phys. Rev. Lett. 73, 2107 (1994).

[310] H. Djani, A. C. Garcia-Castro, W.-Y. Tong, P. Barone, E. Bousquet, S. Picozzi and P. Ghosez, ”Rationalizing and

engineering Rashba spin-splitting in ferroelectric oxides", npj Quantum Mater. 4, 51 (2019).

[311] S. Wang, Y. Bai, L. Xie, C. Li, J. D. Key, D. Wu, P. Wang, and X. Pan, "Ferroelectric Polarization-Modulated Interfacial Fine Structures Involving Two-Dimensional Electron Gases in Pb(Zr, Ti)O_3/$LaAlO_3$/$SrTiO_3$ Heterostructures" ACS Appl. Mater. Interfaces, 10, 1374 (2018).

[312] V. T. Pham, I. Groen, S. Manipatruni, W. Y. Choi, D. E. Nikonov, E. Sagasta, C.-C. Lin, T. Gosavi, A. Marty, L. E. Hueso, I. Young, and F. Casanova, "Spin–orbit magnetic state readout in scaled ferromagnetic/heavy metal nanostructures", Nat. Electron. 3, 309 (2020).

[313] W. Zhang, W. Han, S.-H. Yang, X. Jiang, and S. S. P. Parkin, "Role of transparency of platinum–ferromagnet interfaces in determining the intrinsic magnitude of the spin Hall effect", Nat. Phys. 11, 496 (2015).

[314] L. Zhu, L. Zhu, M. Sui, D. C. Ralph, and R. A. Buhrman, "Variation of the giant intrinsic spin Hall conductivity of Pt with carrier lifetime", Science Adv. 5, eaav8025 (2019).

[315] V. T. Pham, L. Vila, G. Zahnd, P. Noël, A. Marty, and J. P. Attané, "Cross-shaped nanostructures for the study of spin to charge inter-conversion using spin-orbit coupling in non-magnetic materials", Appl. Phys. Lett. 114, 222401 (2019).

[316] Y. Tian, L. Ye, and X. Jin, Proper Scaling of the Anomalous Hall Effect, Phys. Rev. Lett. 103, 087206 (2009).

[317] X. Tao, Q. Liu, B. Miao, R. Yu, Z. Feng, L. Sun, B. You, J. Du, K. Chen, S. Zhang, L. Zhang, Z. Yuan, D. Wu, and H. Ding, "Self-consistent determination of spin Hall angle and spin diffusion length in Pt and Pd: The role of the interface spin loss", Science Adv. 4, eaat1670 (2018).

[318] M.-H. Nguyen, D. C. Ralph, and R. A. Buhrman, "Spin Torque Study of the Spin Hall Conductivity and Spin Diffusion Length in Platinum Thin Films with Varying Resistivity", Phys. Rev. Lett. 116, 126601 (2016).

[319] W. Savero Torres, V. T. Pham, G. Zahnd, P. Laczkowski, V. D. Nguyen, C. Beigné, L. Notin, M. Jamet, A. Marty, L. Vila, and J. P. Attané, "Using domain walls to perform non-local measurements with high spin signal amplitudes", Appl. Phys. Lett. 109, 042405 (2016).

[320] K. M. Schep, Jeroen B. A. N. van Hoof, P. J. Kelly, G. E. W. Bauer, and J. E. Inglesfield, "Interface resistances of magnetic multilayers", Phys. Rev. B 56, 10805 (1997).

[321] B. P. Vodopyanov and L. R. Tagirov "Boundary resistance in magnetic multilayers", J. Phys.: Condens. Matter 18, 1545 (2006).

[322] K. Xia, P. J. Kelly, G. E. W. Bauer, I. Turek, J. Kudrnovský, and V. Drchal, "Interface resistance of disordered magnetic multilayers", Phys. Rev. B 63, 064407(2001).

[323] H. Y. T. Nguyen Jr., W. P. Pratt, and J. Bass, "Spin-flipping in Pt and at Co/Pt interfaces", J. Magn. Magn. Mater. 361, 30 (2014).

[324] A. Sharma, J. A. Romero, N. Theodoropoulou, R. Loloee, W. P. Pratt Jr., and J. Bass, "Specific resistance and scattering asymmetry of Py/Pd, Fe/V, Fe/Nb, and Co/Pt interfaces", J. Appl. Phys. 102, 113916 (2007).

[325] W. Han, K. Pi, K. M. McCreary, Yan Li, Jared J. I. Wong, A. G. Swartz, and R. K. Kawakami, "Tunneling Spin Injection into Single Layer Graphene", Phys. Rev. Lett. 105, 167202 (2010).

[326] L. Liu, A. Richardella, I. Garate, Y. Zhu, N. Samarth, and C.-T. Chen "Spin-polarized tunneling study of spin-momentum locking in topological insulators", Phys. Rev. B 91, 235437 (2015).

[327] X. Xu, L. Zhang, L. Zou, M. Li, and H. Wang, "Regulating Interfacial Spin Hall Conductivity with Ferroelectricity", J. Phys. Chem. Lett. 13, 15, 3310 (2022).

[328] M. Fang, W. Zhang, X. Wu, W. Guo, H. Xia, Y. Wang, W. Wang, and J. Shen, "Recent advances in tunable spin–orbit coupling using ferroelectricity", APL Mater. 9, 060704 (2021).

[329] C. Grezes, A. Kandazoglou, M. Cosset-Cheneau, L. Arche, P. Noël, P. Sgarro, S. Auffret, K. Garello, M. Bibes, L. Vila, J.-P. Attané, "Non-volatile electric control of spin-orbit torques in an oxide two-dimensional electron gas", arXiv:2206.03068 (2022).

[330] K. T. Yamamoto, Y. Shiomi, Kouji Segawa, Yoichi Ando, and E. Saitoh, "Universal scaling for the spin-electricity conversion on surface states of topological insulators", Phys. Rev. B 94, 024404 (2016).

[331] A. Dankert, P. Bhaskar, D. Khokhriakov, I. H. Rodrigues, B. Karpiak, M. V. Kamalakar, S. Charpentier, I. Garate,

and S. P. Dash "Origin and evolution of surface spin current in topological insulators", Phys. Rev. B 97, 125414 (2018).

[332] A. Nomura, N. Nasaka, T. Tashiro, T. Sasagawa, and K. Ando, "Absorption of diffusive spin current in surface and bulk states of a topological insulator", Phys. Rev. B 96, 214440 (2017).

[333] R. Giraud,J. Dufouleur, "Quantum Transport in Nanostructures of 3D Topological Insulators", Phys. Status Solidi B,258, 2000066 (2021).

[334] J. Dufouleur, L. Veyrat, B. Dassonneville, C. Nowka, S. Hampel, P. Leksin, B. Eichler, O. G. Schmidt, B. Büchner, and R. Giraud, "Enhanced Mobility of Spin-Helical Dirac Fermions in Disordered 3D Topological Insulators", Nano Lett. 16, 11, 6733 (2016).

[335] J.A. Sobota, S.-L. Yang, D. Leuenberger, A.F. Kemper, J.G. Analytis, I.R. Fisher, P.S. Kirchmann, T.P. Devereaux, and Z.-X. Shen, "Distinguishing Bulk and Surface Electron-Phonon Coupling in the Topological Insulator Bi_2Se_3 Using Time-Resolved Photoemission Spectroscopy", Phys. Rev. Lett. 113, 157401 (2014).

[336] E. Longo, M. Belli, M. Alia, M. Rimoldi, R. Cecchini, M. Longo, C. Wiemer, L. Locatelli, P. Tsipas, A. Dimoulas, G. Gubbiotti, M. Fanciulli, and R. Mantovan, "Large Spin-to-Charge Conversion at Room Temperature in Extended Epitaxial Sb_2Te_3 Topological Insulator Chemically Grown on Silicon", Adv. Funct. Mater. 32, 2109361 (2022).

[337] G. Schubert, H. Fehske, L. Fritz, and M. Vojta, "Fate of topological-insulator surface states under strong disorder", Phys. Rev. B 85, 201105(R) (2012).

[338] C. H. Li, O. M. J. van't Erve, Y.Y. Li, L. Li and B.T. Jonker, "Electrical Detection of the Helical Spin Texture in a p-type Topological Insulator Sb_2Te_3", Sci Rep 6, 29533 (2016).

[339] T. Thonhauser, T. J. Scheidemantel, J. O. Sofo, J. V. Badding, and G. D. Mahan, "Thermoelectric properties of Sb_2Te_3 under pressure and uniaxial stress", Phys. Rev. B 68, 085201 (2003).

[340] R. E. Simpson, P. Fons, A. V. Kolobov, T. Fukaya, M. Krbal, T. Yagi and J. Tominaga, "Interfacial phase-change memory", Nature Nanotech 6, 501 (2011).

[341] J. Hemberger, M. Nicklas, R. Viana, P. Lunkenheimer, A. Loidl, and R. Böhmer, "Quantum paraelectric and induced ferroelectric states in $SrTiO_3$" J. Phys.: Condens. Matter 8 4673 (1996).

[342] G. Herranz, O. Copie, A. Gentils, E. Tafra, M. Basletić, F. Fortuna, K. Bouzehouane, S. Fusil, É. Jacquet, C. Carrétéro, M. Bibes, A. Hamzić, and A. Barthélémy, "Vacancy defect and carrier distributions in the high mobility electron gas formed at ion-irradiated SrTiO3 surfaces", J. Appl. Phys. 107, 103704 (2010).

[343] M. Acosta, N. Novak, V. Rojas, S. Patel, R. Vaish, J. Koruza, G. A. Rossetti, Jr., and J. Rodel , "$BaTiO_3$-based piezoelectrics: Fundamentals, current status, and perspectives", : Appl. Phys. Rev. 4, 041305 (2017).

[344] P. Kowalczyk, F. Hippert, N. Bernier, C. Mocuta, C. Sabbione, W. BatistaPessoa, and P. Noé, "Impact of Stoichiometry on the Structure of van der Waals Layered GeTe/Sb_2Te_3 Superlattices Used in Interfacial Phase-Change Memory (iPCM) Devices" Small 14(24), 1704514 (2018).

[345] M. Cosset-Chéneau, M. Husien Fahmy, A. Kandazoglou, C. Grezes, A. Brenac, S. Teresi, P. Sgarro, P. Warin, A. Marty, V.T. Pham, J.-P. Attané, L. Vila "Electrical measurement of the Spin Hall Effect isotropy in a ferromagnet", arXiv:2205.15651 (2022).

[346] K.-W. Kim and K.-J. Lee, "Generalized Spin Drift-Diffusion Formalism in the Presence of Spin-Orbit Interaction of Ferromagnets", Phys. Rev. Lett. 125, 207205 (2020).

[347] L. Liu, C. Zhou, T. Zhao, B. Yao, J. Zhou, X. Shu, S. Chen, S. Shi, S. Xi, D. Lan, W. Lin, Q. Xie, L. Ren, Z. Luo, C. Sun, P. Yang, E.-J. Guo, Z. Dong, A. Manchon and J. Chen, "Current-induced self-switching of perpendicular magnetization in CoPt single layer", Nat. Commun. 13, 3539 (2022).

Appendix

Analytical computations of the spin accumulation and of spin currents in metallic systems

The spin resistor model

The spin resistor model, developed by A. Marty in SPINTEC [52], allows for the computation of spin current and accumulation in collinear nanostructures, where the magnetization of all of the ferromagnetic component are collinear to one another. This model uses the formalism of electrical resistances in which the circuit is divided into parts of different impedances. Each element of the structure (copper channel, electrodes...) is modelled by a monodimensionnal rod (that I call a resistor in the following), in which the spin accumulation changes along its length (X-direction) (Fig. 5.17a and 5.17b). The resistors are separated by nodes (Fig. 5.17c and 5.17d). The spin current then has only one polarization and one flow direction, and can therefore be modelled by a scalar j_s. Similarly, the charge current is modelled by the scalar j_c. The idea of this method is to relate the spin accumulation in the nodes at the two extremities of each nodes, using the spin/charge current continuity equations and generalized Ohm's law, in which all the spin/charge current and electrical potential/spin accumulation depends only on x. The spin/charge transport equation system can then be written in a matrix form

$$\partial_x \begin{pmatrix} \mu \\ j_s - \beta j_c \end{pmatrix} = \begin{pmatrix} 0 & -1/\sigma^\star \\ -\sigma^\star/{l_{sf}}^2 & 0 \end{pmatrix} \begin{pmatrix} \mu \\ j_s - \beta j_c \end{pmatrix} \tag{5.5}$$

This allows expressing the spin current and accumulation at the $x = L$ extremity of the resistor as a function of its value at the $x = 0$ extremity by taking the matrix exponential. Introducing the notation $I^{c(s)} = j_{c(s)}A$ with A the section of the resistor, and the spin resistance $R = l_{sf}/A\sigma^\star$:

$$I^s(0) = \frac{1}{R}\left(\frac{\mu(0)}{\tanh(L/l_{sf})} - \frac{\mu(L)}{\sinh(L/l_{sf})}\right) + \beta I_c \tag{5.6}$$

$$I^s(L) = \frac{1}{R}\left(\frac{\mu(0)}{\sinh(L/l_{sf})} - \frac{\mu(L)}{\tanh(L/l_{sf})}\right) + \beta I_c \tag{5.7}$$

Each resistor is indexed by the two nodes at its extremities. The resistors connected to an outside electrical contact are approximated as infinitely long ($L \gg l_{sf}$). The spin current going from the i node to the resistor delimited by the nodes i and j is denoted by $I_{i \to ij}$. we assume that the spin current is conserved at the node i so that:

$$\sum_{j \in v(i)} I_{i \to ij} = 0 \tag{5.8}$$

Where $v(i)$ are the set of nodes linked to i by a resistor. This conservation law is valid for all the nodes of the system, and gives a linear relation between the spin accumulations and each nodes:

$$\begin{pmatrix} \sum_{j \in v(1)} \left(\frac{1}{R\tanh(L/l_{sf})}\right)_{1j} \alpha_{1j} & \left(\frac{-1}{R\sinh(L/l_{sf})}\right)_{12} \alpha_{12} & \dots \\ \left(\frac{-1}{R\sinh(L/l_{sf})}\right)_{12} \alpha_{12} & \sum_{j \in v(2)} \left(\frac{2}{R\tanh(L/l_{sf})}\right)_{2j} \alpha_{2j} & \dots \\ \dots & \dots & \dots \end{pmatrix} \begin{pmatrix} \mu_1 \\ \mu_2 \\ \dots \end{pmatrix} = I_0 \begin{pmatrix} \Delta\beta_1 \\ \Delta\beta_2 \\ \dots \end{pmatrix} \tag{5.9}$$

With μ_i the spin accumulation at the i node and I_0 the charge current flowing through the circuit. $\Delta\beta_i = \beta_{i>} - \beta_{i<}$ denotes the polarization difference of the resistors attached to the i node that belong to the entering (denoted $i >$) and exiting (denoted $i <$) charge current path I_0. If the i node does not belong to the charge current path, $\Delta\beta_i = 0$. Finally, $\alpha_{ij} = 1$ if $j \in v(i)$ and 0 otherwise. The ij indexes of the parenthesis indicates that the physical quantities in the parenthesis are associated to the resistor comprised between the nodes i and j. The electrical tension between two contacts is obtained by integrating the Ohm's law with $\rho = 1/\sigma$: $\partial_x \mu_m = -\rho j_s - \beta \partial_x \mu$ on the voltage path $ch_v = V_+ \rightarrow V_-$. That connects the two voltage measurement points:

$$V_+ - V_- = \int_{ch} -\partial_x \mu_m \, \mathrm{d}x = I_0 \sum_{p \in ch_v} R_p + \sum_{p \in ch_v} \beta_p [\mu(L_p) - \mu(0)] \tag{5.10}$$

with the p indices referring to a resistor denoted p through which a charge current is flowing. Assuming its section to be A_p, its length L_p and resistivity ρ_p, then $R_p = \rho_p L_p / A_p$ is its electrical resistance. The spin accumulations are expressed at the extremities of the resistors. Rather that indexing the resistors, it is more convenient to index the spin accumulations on the nodes belonging to ch_v. The previous equation therefore rewrites:

$$\Delta R = \frac{V_+ - V_-}{I_0} - R_{ch} = \sum_{i \in ch_v} \Delta\beta_i \mu_i \tag{5.11}$$

where $R_{ch} = \sum_{p \in ch} R_p$. The spin accumulations in this equation are obtained from equation 5.9. From this method, one can obtain easily spin signals in an arbitrarily complicated geometry, provided that it is possible to assume the homogeneity of the spin accumulation at the interface between the different resistors.

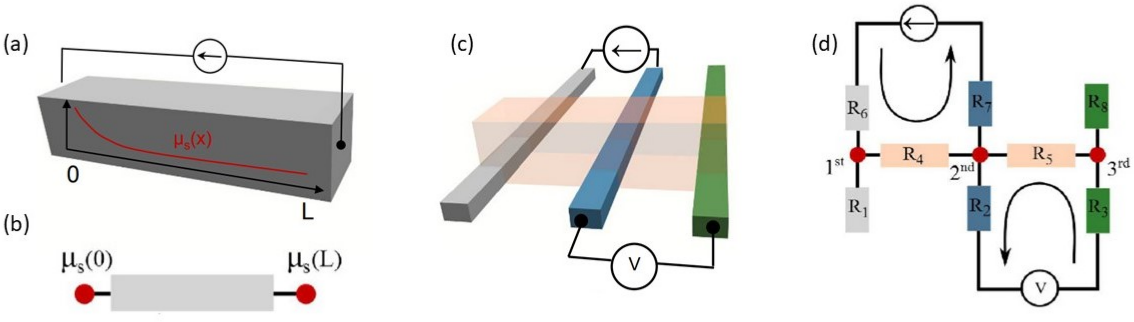

Figure 5.17: (a) Spin accumulation diffusion into a metallic wire and (b) modelization by a spin resistor in which the spin accumulations at the two extremities of the wire are reported in nodes at the extremities of the wire. (c) Example of a structure made of several wires, modeled by the spin resistor model depicted in (d). Image from Ref. [52].

This model has been used to obtain analytical solutions of the spin signals in lateral spin valves presented in section 2. In the next subsection, I detail the model used to compute the spin accumulation and spin current in a FM/NM bilayer system with a resistive spin-polarized interface with spin memory loss.

Spin transport in the FM/NM bilayer

As in section 1.1.3, the interface between the FM and the NM is set at $z = 0$. The length of the NM and the FM (L^N and L^F) are much larger than their respective spin diffusion lengths. The spin accumulation in the NM ($z > 0$) therefore writes:

$$\mu_s(z) = \frac{\sinh\left(\frac{L^N - z}{l_{sf}^N}\right)}{\sinh\left(\frac{L^N}{l_{sf}^N}\right)} \mu(0^+) \tag{5.12}$$

and in the FM ($z < 0$)

$$\mu_s(z) = \frac{\sinh\left(\frac{L^F + z}{l_{sf}^F}\right)}{\sinh\left(\frac{L^F}{l_{sf}^F}\right)} \mu(0^-) \tag{5.13}$$

in which $\mu_s(0^+)$ and $\mu_s(0^-)$ are the spin accumulations at the two sides of the interfaces. Obtaining the spin current is straightforward from eq. 5.9:

$$j_s(z>0) = \frac{1}{R_N} \frac{\cosh\left(\frac{L^N - x}{l^N_{sf}}\right)}{\sinh\left(\frac{L^N}{l^N_{sf}}\right)} \mu(0^+) \tag{5.14}$$

in the NM and

$$j_s(z<0) = \frac{1}{R_N} \frac{\cosh\left(\frac{L^F + x}{l^F_{sf}}\right)}{\sinh\left(\frac{L^F}{l^F_{sf}}\right)} \mu(0^-) + \beta I_c \tag{5.15}$$

in the FM. It is then necessary to obtain the spin accumulations $\mu_s(0^+)$ and $\mu_s(0^+)$, which can be done by a straightforward application of the model described in the previous section.

The spin resistor system used for the calculations of section 1.1.3 is described in Fig. 5.18. The FM and NM are described by resistors with their associated polarizations, spin diffusion length and resistivities. Their interface is described by a set of three resistors. The central resistor represents the spin resistance and polarization of the interface. The spin memory loss is modelled by two spin sink with spin resistances $1/G_{SML}$. The equation 5.9 can be written in a more compact form:

$$A\boldsymbol{\mu} = \boldsymbol{B}_{cur} I_c \tag{5.16}$$

in which the matrix A represent the matrix that fully characterize the system. $\boldsymbol{\mu}$ is the spin accumulation vectors and $\boldsymbol{B}_{cur}$ the polarization vector. In this particular system, $\boldsymbol{\mu} = (\mu_s(0^-), \mu_s(0^+))^T$, so that we get the spin accumulations at the two modes surrounding the interface resistor simply by inverting the A matrix: $\boldsymbol{\mu} = A^{-1} B_{cur} I_c$. The matrix of the system shown in Fig. 5.18 is:

$$A = \begin{pmatrix} \frac{1}{R_F} + (1-\gamma^2)G_{int} + G_{SML} & -(1-\gamma^2)G_{int} \\ -(1-\gamma^2)G_{int} & \frac{1}{R_F} + (1-\gamma^2)G_{int} + G_{SML} \end{pmatrix} \tag{5.17}$$

while $\boldsymbol{B}_{cur} = (\beta - \gamma, \gamma)^T$ so that:

$$\mu(0^-) = \frac{(\beta-\gamma)\left[\frac{1}{R_N} + (1-\gamma^2)G_{int} + G_{SML}\right] + \gamma(1-\gamma^2)G_{int}}{\left[\frac{1}{R_F} + (1-\gamma^2)G_{int} + G_{SML}\right]\left[\frac{1}{R_N} + (1-\gamma^2)G_{int} + G_{SML}\right] - (1-\gamma^2)^2 G_{int}^2} I_c \tag{5.18}$$

and

$$\mu(0^+) = \frac{\gamma\left[\frac{1}{R_F} + (1-\gamma^2)G_{int} + G_{SML}\right] + (\beta-\gamma)(1-\gamma^2)G_{int}}{\left[\frac{1}{R_F} + (1-\gamma^2)G_{int} + G_{SML}\right]\left[\frac{1}{R_N} + (1-\gamma^2)G_{int} + G_{SML}\right] - (1-\gamma^2)^2 G_{int}^2} I_c \tag{5.19}$$

These calculations yields the results in the Fig. 1.2 of section 1.1.3. Even though this model works well for the structure described in section 1.1.3, its interest is limited for more complex structures, and to describe the interconversion by the Spin Hall Effect its fail to take into account geometrical corrections to the produced charge current such as the shunting by the channel in lateral spin valves, or by the injecting electrode in local detection schemes. It is then necessary to solve the Valet-Fert equations using Finite Element Method simulations, described in the next section.

Finite element simulations of the spin transport in metallic systems

Formulation

In the following section, we will use the following notations. The greek letters $\alpha \in \{x, y, z\}$ represents the real space indices. The roman letters $i \in \{0, 1\}$ correspond to the charge ($i = 0$) and spin ($i = 1$) space. We coonsider here only the collinear case, but the non-collinear case can be extended by using the equations given in [64], and by adding two other subscripts to describe the spin components in the three directions of space.

The degree of freedom for the simulations will be the electrical and electrochemical potentials $\mu_{i=0,1}$. The associated currents write $J_{i,\alpha}$, representing the current of charge or spin flowing in the direction α. The transport equations in the volume write:

$$J_{i\alpha} = -[\sigma]^{\alpha\beta}_{ij} \partial_\beta \mu_j$$

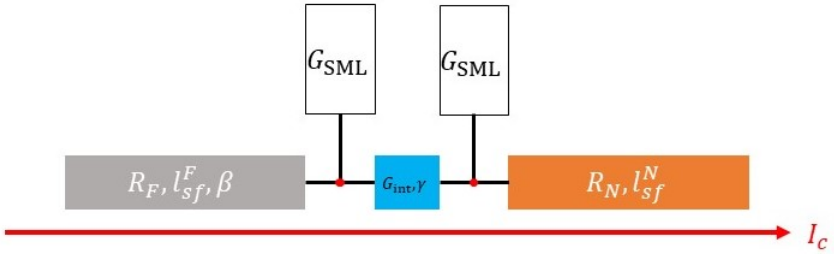

Figure 5.18: Spin resistor model of the system described in Fig. 1.2.

$$\partial_\alpha J_{i\alpha} = -[P]_{ij}\mu_j$$

Where $[\sigma]$ is a 6×6 matrix that contains the drift-diffusion and the interconversion processes, while $[P]$ is a 2×2 matrix representing the relaxation of the spin current.
The boundary condition at an interface with a normal material along z on which the spin current relaxes writes:

$$J_{iz} = [G_s]_{ij}\mu_j$$

with $[G_s]$ a spin conductance matrix and μ_j the spin accumulation at the interface. At the interface between two volumes a and b with electrochemical potentials μ^a and μ^b at each side of the interface, the spin current incident on the interface at the a volume side writes:

$$J_{iz}^a = [G_{int}]_{ij}(\mu_j^a - \mu_j^b)$$

G_{int} is the interface conductance.

Let us consider two spaces a and b. The test functions of this spaces write w_i^a and w_i^b. To obtain the formulation, we used the Galerkin method for the discretization of the problem. To do this, we need to take the scalar product of the conservation equation. Let us consider the case of space a. The scalar product writes:

$$\int_{V^a} \mathrm{d}V w_i^a \partial_\alpha J_{i\alpha} + \int_{V^a} \mathrm{d}V [P]_{ij}\mu_j w_i^a = 0$$

and after integrating by parts:

$$\int_{S^a} \mathrm{d}S_\alpha w_i^a J_{i\alpha} + \int_{V^a} \mathrm{d}V \partial_\alpha w_i^a [\sigma]_{ij}^{\alpha\beta} \partial_\beta \mu_j + \int_{V^a} \mathrm{d}V [P]_{ij} w_1^a \mu_j = 0$$

The first term represents the surface terms on the volume a. Several situations must be considered: At the current injection points, the surface integral writes:

$$\int_{S_{inj}^a} \mathrm{d}S w_0^a \epsilon \frac{I_0}{S_{inj}^a} + \int_{S_{inj}^a} \mathrm{d}S w_1^a \epsilon \frac{\beta I_0}{S_{inj}^a}$$

with β the polarization of the volume a, and $\epsilon = -1$ if the current enters, $\epsilon = 1$ if the current leaves the volume.
At a spin relaxation interface orthogonal to z, the surface term writes:

$$\int_{S^a} \mathrm{d}S w_i J_{iz} = \int_{S^a} \mathrm{d}S w_i [G_s]_{ij}\mu_j$$

Finally, at the interface between a and b,

$$\int_{S^{a/b}} \mathrm{d}S w_i J_{iz} = \int_{S^{a/b}} \mathrm{d}S w_i [G_{int}]_{ij}(\mu_j^b - \mu_j^a)$$

The formulation is the same in space b, with a simple inversion of indices a and b.

The model must then be completed by writing the matrix $[\sigma]$, $[G_s]$, $[G_{int}]$ and $[P]$.

Modelling

From the Valet-Fert model, the $[P]$ matrix simply writes:

$$[P] = \frac{1-\beta^2}{\rho l_{sf}^2} \begin{pmatrix} 0 & 0 \\ 0 & 1 \end{pmatrix}$$

The conductivity contains several terms:
A drift term:

$$[\sigma] = \frac{1}{\rho} \begin{pmatrix} I_3 & 0_3 \\ 0_3 & I_3 \end{pmatrix} + \frac{\beta}{\rho} m \begin{pmatrix} 0_3 & I_3 \\ I_3 & 0_3 \end{pmatrix}$$

with $m = \pm 1$ the magnetization direction in the collinear configuration. 0_3 and I_3 are the zero and identity 3×3 matrix. Each of the matrix 3×3 block will be indexed by $i = 0, 1$ since they correspond to the charge and spin channels, while the indices of the block themselves will be given by Greek letters.

The currents created by the Spin Hall Effect writes

$$J_{i,\alpha} = -\frac{\theta_{SHE}}{\rho} [\boldsymbol{\sigma} \times \partial_{\boldsymbol{r}} \mu_i]_\alpha$$

$\boldsymbol{\sigma} = (\sigma_x, \sigma_y, \sigma_z)^T$ is the direction of the spin currents polarization. The currents can then be written $J_{i\alpha} = -[\sigma_{SHE}]_{ij}^{\alpha\beta} \partial_\beta \mu_j$ with

$$[\sigma_{SHE}] = \frac{\theta_{SHE}}{\rho} \begin{pmatrix} 0_3 & \boldsymbol{\sigma} \cdot \boldsymbol{S} \\ \boldsymbol{\sigma} \cdot \boldsymbol{S} & 0_3 \end{pmatrix}$$

and $\boldsymbol{S} = ([S_x], [S_y], [S_z])^T$, while:

$$[S_x] = \begin{pmatrix} 0 & 0 & 0 \\ 0 & 0 & -1 \\ 0 & 1 & 0 \end{pmatrix}$$

$$[S_y] = \begin{pmatrix} 0 & 0 & 1 \\ 0 & 0 & 0 \\ -1 & 0 & 0 \end{pmatrix}$$

$$[S_z] = \begin{pmatrix} 0 & 1 & 0 \\ -1 & 0 & 0 \\ 0 & 0 & 0 \end{pmatrix}$$

Finally, the Anomalous Hall Effect writes:

$$J_{i\alpha} = -\frac{\theta_{AHE}}{\rho} [\partial_{\boldsymbol{r}} \mu_i \times \boldsymbol{m}]_\alpha$$

with $\boldsymbol{m}$ the magnetization direction. The current then writes $J_{i\alpha} = -[\sigma_{AHE}]_{ij}^{\alpha\beta} \partial_\beta \mu_j$ with

$$[\sigma_{SHE}] = \frac{\theta_{AHE}}{\rho} \begin{pmatrix} -\boldsymbol{m} \cdot \boldsymbol{S} & 0_3 \\ 0_3 & -\boldsymbol{m} \cdot \boldsymbol{S} \end{pmatrix}$$

using the notation for $\boldsymbol{S}$ used in the case of the SHE.

Regarding the interface terms, the conservation of the charge current imposes for the spin absorption term $J_{iz} = [G]_{ij}\mu_j$:

$$[G] = G_{SML}\begin{pmatrix} 0 & 0 \\ 0 & 1 \end{pmatrix}$$

While the interface resistance term $[G_{int}]$ writes for a non-polarized interface:

$$[G_{int}] = G_{int}\begin{pmatrix} 1 & \gamma \\ \gamma & 1 \end{pmatrix}$$

I_2 being the 2 × 2 identity matrix.